International Association of Geodesy Symposia
149

Jeffrey T. Freymueller
Laura Sánchez *Editors*

International Symposium on Advancing Geodesy in a Changing World

Proceedings of the IAG Scientific Assembly, Kobe, Japan, July 30 – August 4, 2017

Springer

International Association of Geodesy Symposia

Jeffrey T. Freymueller, Series Editor
Laura Sánchez, Series Assistant Editor

International Association of Geodesy Symposia

Jeffrey T. Freymueller, Series Editor
Laura Sánchez, Series Assistant Editor

Symposium 108: Application of Geodesy to Engineering
Symposium 109: Permanent Satellite Tracking Networks for Geodesy and Geodynamics
Symposium 110: From Mars to Greenland: Charting Gravity with Space and Airborne Instruments
Symposium 111: Recent Geodetic and Gravimetric Research in Latin America
Symposium 112: Geodesy and Physics of the Earth: Geodetic Contributions to Geodynamics
Symposium 113: Gravity and Geoid
Symposium 114: Geodetic Theory Today
Symposium 115: GPS Trends in Precise Terrestrial, Airborne, and Spaceborne Applications
Symposium 116: Global Gravity Field and Its Temporal Variations
Symposium 117: Gravity, Geoid and Marine Geodesy
Symposium 118: Advances in Positioning and Reference Frames
Symposium 119: Geodesy on the Move
Symposium 120: Towards an Integrated Global Geodetic Observation System (IGGOS)
Symposium 121: Geodesy Beyond 2000: The Challenges of the First Decade
Symposium 122: IV Hotine-Marussi Symposium on Mathematical Geodesy
Symposium 123: Gravity, Geoid and Geodynamics 2000
Symposium 124: Vertical Reference Systems
Symposium 125: Vistas for Geodesy in the New Millennium
Symposium 126: Satellite Altimetry for Geodesy, Geophysics and Oceanography
Symposium 127: V Hotine Marussi Symposium on Mathematical Geodesy
Symposium 128: A Window on the Future of Geodesy
Symposium 129: Gravity, Geoid and Space Missions
Symposium 130: Dynamic Planet - Monitoring and Understanding . . .
Symposium 131: Geodetic Deformation Monitoring: From Geophysical to Engineering Roles
Symposium 132: VI Hotine-Marussi Symposium on Theoretical and Computational Geodesy
Symposium 133: Observing our Changing Earth
Symposium 134: Geodetic Reference Frames
Symposium 135: Gravity, Geoid and Earth Observation
Symposium 136: Geodesy for Planet Earth
Symposium 137: VII Hotine-Marussi Symposium on Mathematical Geodesy
Symposium 138: Reference Frames for Applications in Geosciences
Symposium 139: Earth on the Edge: Science for a sustainable Planet
Symposium 140: The 1st International Workshop on the Quality of Geodetic Observation and Monitoring Systems (QuGOMS'11)
Symposium 141: Gravity, Geoid and Height systems (GGHS2012)
Symposium 142: VIII Hotine-Marussi Symposium on Mathematical Geodesy
Symposium 143: Scientific Assembly of the International Association of Geodesy, 150 Years
Symposium 144: 3rd International Gravity Field Service (IGFS)
Symposium 145: International Symposium on Geodesy for Earthquake and Natural Hazards (GENAH)
Symposium 146: Reference Frames for Applications in Geosciences (REFAG2014)
Symposium 147: Earth and Environmental Sciences for Future Generations
Symposium 148: Gravity, Geoid and Height Systems 2016 (GGHS2016)
Symposium 149: Advancing Geodesy in a Changing World

More information about this series at http://www.springer.com/series/1345

International Symposium on Advancing Geodesy in a Changing World

Proceedings of the IAG Scientific Assembly,
Kobe, Japan, July 30 – August 4, 2017

Edited by

Jeffrey T. Freymueller, Laura Sánchez

Springer

ISSN 0939-9585
International Association of Geodesy Symposia
ISBN 978-3-030-12914-9
https://doi.org/10.1007/978-3-030-12915-6

ISSN 2197-9359 (electronic)

ISBN 978-3-030-12915-6 (eBook)

Library of Congress Control Number: 2019930832

This Springer imprint is published by the registered company Springer Nature Switzerland AG
The registered company address is: Gewerbestrasse 11, 6330 Cham, Switzerland

Preface

The quadrennial Scientific Assembly of the International Association of Geodesy (IAG) was held together with the International Association of Seismology and Physics of the Earth's Interior (IASPEI) in Kobe, Japan, from 30 July to 4 August 2017. The theme of the scientific assembly was "Advancing Geodesy in a Changing World", and it explored a broad range of science and applications in geodesy and seismology. The joint assembly had 1,107 participants from 63 countries and featured a total of 1,119 presentations. Of these, 254 were in IAG symposia and 301 in joint symposia; so about half of the presentations in total involved geodesy. There were 7 IAG symposia and 9 joint symposia.

The seven IAG symposia were structured according to the four IAG commissions and the three GGOS focus areas:

1. Reference frames
2. Static gravity field
3. Time variable gravity field
4. Earth rotation and geodynamics
5. Multi-signal positioning: Theory and applications
6. Geodetic remote sensing
7. Global Geodetic Observing System (GGOS) and Earth monitoring services

The joint symposia supported by the IAG were:

- Monitoring of the cryosphere
- Recent large and destructive earthquakes
- Deformation of the lithosphere: Integrating seismology and geodesy through modelling
- Geohazard early warning systems
- Crustal dynamics: multidisciplinary approach to seismogenesis
- The spectrum of fault-zone deformation processes (from slow slip to earthquake)
- Tracking the seafloor in motion
- Imaging and interpreting lithospheric structures using seismic and geodetic approaches
- Geodesy and seismology general contributions

This volume contains peer-reviewed papers contributed from all of the symposia related to IAG. We warmly recognize the contributions and support of the associated editors and reviewers (see the list in later pages).

East Lansing, MI, USA — Jeffrey T. Freymueller
Munich, Germany — Laura Sánchez

Contents

Part I

Reference Frames

DGFI-TUM Analysis and Scale Investigations of the Latest Terrestrial Reference Frame Realizations

Mathis Bloßfeld, Detlef Angermann, and Manuela Seitz

Abstract

Solutions for the most recent realization of the International Terrestrial Reference System (ITRS) were computed by the three ITRS Combination Centers (CCs) of the International Earth Rotation and Reference Systems Service (IERS), namely the IGN in Paris (France), the JPL in Pasadena (USA), and the DGFI-TUM in Munich (Germany). Thereby, the solutions of IGN and DGFI-TUM comprise conventional parameters of the ITRS (station coordinates and velocities) at a reference epoch as defined in the IERS Conventions 2010. Although the two solutions are based on identical input data, there exist systematic differences between them.

Within all ITRS realizations, the scale is realized as a mean scale between SLR (satellite laser ranging) and VLBI (very long baseline interferometry). If the combined scale is compared to the scale realized by both techniques itself, the IGN solution reveals significant differences between SLR and VLBI whereas the DGFI-TUM solution shows much smaller differences.

When the combined solutions of IGN and DGFI-TUM as well as the single-technique solutions of both institutions are investigated and compared, a significant scale difference between SLR and VLBI is only visible in the IGN analysis but not in the results of the two other ITRS CCs. It is also found that the scale analysis via Helmert parameter is very difficult since the results are quite sensitive w.r.t. particular station networks. In addition, scale comparisons of the IVS and ILRS CCs also do not confirm a systematic scale offset.

Keywords

DTRF2014 · ITRF2014 · JTRF2014 · Local ties · TRF scale · VLBI and SLR co-locations

1 Introduction

Three Combination Centres (CCs) of the International Earth Rotation and Reference Systems Service (IERS) are in charge of computing a realization of the International Terrestrial Reference System (ITRS). The most recent realizations are called DTRF2014 (Seitz et al. 2016), which was computed using the combination scheme described in Seitz et al. (2012), ITRF2014 (Altamimi et al. 2016), and JTRF2014 (Wu et al. 2015). The advantage of multiple realizations using identical input data is, that errors or systematics caused by the combination approach, the analyst, or the software can be identified.

An example for such a systematic effect is the potential scale difference between SLR and VLBI. By comparing the ITRS realizations of DGFI-TUM and IGN via a 14-parameter similarity (Helmert) transformation, a significant scale difference between the SLR and VLBI subnet of the DTRF2014 and the ITRF2014 of about 0.6 ppb (opposite sign for both techniques) and nearly no scale rate is found.

M. Bloßfeld (✉) · D. Angermann · M. Seitz
Deutsches Geodätisches Forschungsinstitut, Technische Universität München (DGFI-TUM), Munich, Germany
e-mail: mathis.blossfeld@tum.de

J. T. Freymueller, L. Sánchez (eds.), *International Symposium on Advancing Geodesy in a Changing World*,
International Association of Geodesy Symposia 149, https://doi.org/10.1007/1345_2018_47

This leads to a scale difference of about **1.2 ppb** which is equivalent to a height change of about 7.5 mm at the Earth's surface. This result (at least the order of magnitude) is confirmed by the analysis of the IGN where the ITRF2014 solution reveals a significant scale bias between VLBI and SLR of **1.37 ppb** (rate: 0.02 ppb/yr) (Altamimi et al. 2016). In contrast to this, the DTRF2014 does not show such a large scale discrepancy (up to 3.3 mm, depending on the test scenario).

This paper focuses on dedicated investigations of a potential scale bias between SLR and VLBI by applying various test scenarios. A major goal is to quantify its magnitude and to study the impact of different transformations to assess the reliability of the results. In Sect. 2, the following comparisons based on Helmert transformations using only stable and well-performing stations (low scatter, few discontinuities, long observation time span, etc.) are discussed:

(Section 2.1) SLR and VLBI single-technique solutions provided by DGFI-TUM and IGN,
(Section 2.2) DGFI-TUM's SLR and VLBI single-technique solutions using local ties between co-located instruments (direct approach),
(Section 2.3) DGFI-TUM's SLR and VLBI single-technique solutions via GNSS co-locations (indirect approach),
(Section 2.4) combined IVS solutions w.r.t. different TRF realizations (test done by IVS CC at BKG, Germany),
(Section 2.5) combined ILRSA solutions w.r.t. different TRF realizations (test done by ILRSA CC at ASI, Italy).

2 Scale Investigations: Test Scenarios

Here, we test if there is a significant scale difference between SLR and VLBI and we assess the reliability of the transformations used to determine a scale bias. Therefore, internal as well as external comparisons of the DGFI-TUM and the IGN solution are provided in this paper. The secular ITRS realizations comprise station positions and velocities, which can be compared by 14-parameter Helmert transformations in terms of estimated scale offset and rate between SLR and VLBI. In contrast to them, the JPL solution provides epoch-wise (sub-secular) station position estimates which are investigated in Sects. 2.4 and 2.5.

2.1 Comparison of Single-Technique Solutions

In this sub-section, the single-technique SLR and VLBI solutions provided by DGFI-TUM and IGN are compared

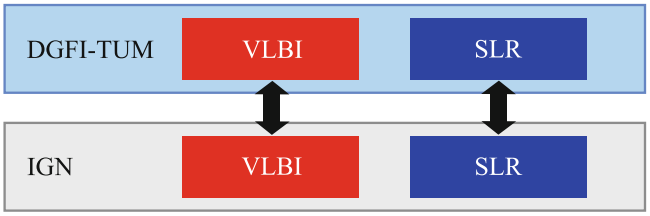

Fig. 1 Comparison of the SLR and VLBI single-technique solutions of DGFI-TUM and IGN. The black arrows indicate the Helmert transformations

Table 1 Scale offsets and rates obtained by 14-parameter Helmert transformations of SLR and VLBI single-technique solutions of DGFI-TUM and IGN

Technique (IGN w.r.t. DGFI-TUM)	epoch	VLBI	SLR
Scale offset [mm]	2000.0	0.2 ± 0.20	2.2 ± 1.00
	2010.0	1.5 ± 0.50	0.7 ± 0.90
Scale rate [mm/yr]	2000.0	0.1 ± 0.04	-0.1 ± 0.11
	2010.0	0.0 ± 0.05	0.0 ± 0.07
Number of stations (used for transformation)		22	19

The transformations are computed at two different epochs 2000.0 and 2010.0

(Fig. 1). All solutions are based on identical input data without any deformation due to the inter-technique combination. The solutions are obtained after epoch-wise input data were accumulated and the geodetic datum was realized. These steps had been performed by the respective institutes. In case of the DGFI-TUM VLBI-only solution, datum-free normal equations (NEQs) were accumulated, station velocities were introduced and No-Net-Translation (NNT) as well as No-Net-Rotation (NNR) conditions were applied to the station coordinates and velocities to realize the origin and the orientation of the VLBI TRF. In case of the DGFI-TUM SLR-only solution, only the orientation has to be realized. This study allows to test if either SLR or VLBI are solely responsible for the scale bias between SLR and VLBI seen in the ITRF. The transformation results are listed in Table 1.

We find that there is neither a prominent scale offset nor rate between the DGFI-TUM and IGN single-technique solutions for SLR and VLBI as found for the ITRF. If the transformation epoch is changed from 2000.0 to 2010.0, the scale offset increases from 0.2 to 1.5 mm (0.2 ppb) which still does not explain the large bias seen by Altamimi et al. (2016). The opposite behavior is achieved in case of the SLR transformation. Here, the scale bias decreases from 2.2 mm at 2000.0 to 0.7 mm (0.1 ppb) at 2010.0. The small scale biases between the single-technique solutions might be caused by the fact that IGN accumulates the epoch-wise VLBI and SLR solutions while introducing Helmert parameters whereas DGFI-TUM directly combines datum-free NEQs. This point needs further investigations. For the

transformation, the technique-specific core station networks are used. As a conclusion, we can state that the scale bias reported for the ITRF is not present in the technique-specific input data which indicates that this effect might be caused by the inter-technique combination.

2.2 Comparison of Single-Technique Solutions: Direct Via Local Ties

In this test we transform a selected VLBI network on the co-located SLR network. Since SLR and VLBI observations refer to different reference points, we use local tie vectors (terrestrially measured vectors between instrument's reference points) to compute a "VLBI reference point" at an SLR marker. Afterwards, we can directly compare the transformed VLBI-only solution (referred to the SLR marker) with the SLR-only solution (see Fig. 2).

Important issues in this investigation are the number, the quality, and the global distribution of co-locations between SLR and VLBI. A high number of co-locations is necessary to achieve stable transformation results. In addition, also the quality of the co-locations impacts the transformation. Thereby, the common observation time span of SLR and VLBI should be as long as possible to get reliable results.

In Fig. 3 (upper panel), the SLR observation time spans (blue bars) for 19 possible co-location sites between SLR and VLBI are shown together with the VLBI observation time spans (red bars) and the common observation time spans of both techniques (green bars). Out of 19 sites, only 9 have a common observation time span longer than 5 years. An example for a high quality co-location station is Hartebeesthoek in South Africa (left panel in Fig. 3) which provides 22 years of parallel SLR and VLBI observations. Even if there are 5 years of common observations, these observations could also be made more than 20 years ago (e.g., Quincy, USA, middle panel). Any error in the velocity estimation of the SLR or VLBI reference point would result in large errors at the transformation epoch (e.g., 2010.0) when the old local tie measurement is used to derive the marker coordinates. The example in the right panel of Fig. 3 shows Yarragadee in Australia which provides 3 years of parallel observations during the most recent years which are far away from the transformation epoch 2000.0 (large interpolation error).

Besides the common observation time interval and the quality of the co-locations, also their global distribution affects the transformation. Figure 4 shows the global distribution of 19 co-locations (Fig. 3) according to their common observation time span. The longer the common time span of SLR and VLBI observations is, the more reliable is the computation of the "VLBI reference point". First of all, a clear inequality of the number of co-locations on the northern hemisphere compared to the southern hemisphere can be found. Secondly, the importance of Hartebeesthoek (South Africa) for the global coverage becomes visible.

Table 2 shows the transformation parameters between the SLR and the VLBI single-technique solutions using local ties obtained for the DTRF2014. The transformation parameters of three different station networks are compared at three different epochs. In summary, we can say that in test case A, the scale offset is between 3 and 4 mm for all epochs using the 9 co-locations (out of 19 possible ones). If we add Yarragadee to the transformation network (test case B), we see a significant impact of this station on the obtained offsets (as well as on the rates) with a small scale offset at the epoch 2010.0. This is caused by the fact that the VLBI telescope starts operation around 2012 which is 2 years away to the newest transformation epoch (including the LT measurement epoch). Test case C shows that the extrapolation of Quincy from 1991 over 9 years to all transformation epochs is problematic. In that case, a clear scale bias between SLR and VLBI is visible. This effect is a consequence of the velocity handling within the DTRF2014 computation. If two velocities are statistically not equal, they are not equalized in our solution with the consequence that the reference points drift away from each other with time.

The conclusion of this sub-section is that the results of a direct comparison between SLR and VLBI are quite sensitive w.r.t. particular stations used in the transformations. However, the most stable transformation with 9 co-locations does not explain the large scale bias between the SLR and the VLBI solutions of ITRF2014.

Fig. 2 Direct comparison of DGFI-TUM's VLBI and SLR single-technique solutions by using local ties between co-located instruments

2.3 Comparison of Single-Technique Solutions: Indirect Via GNSS

In this section, we describe the indirect transformation approach between SLR and VLBI using the co-locations to GNSS. One big advantage of this indirect approach is the improved network geometry. Whereas there are only 9 long-term (more than 5 years common observations) co-locations

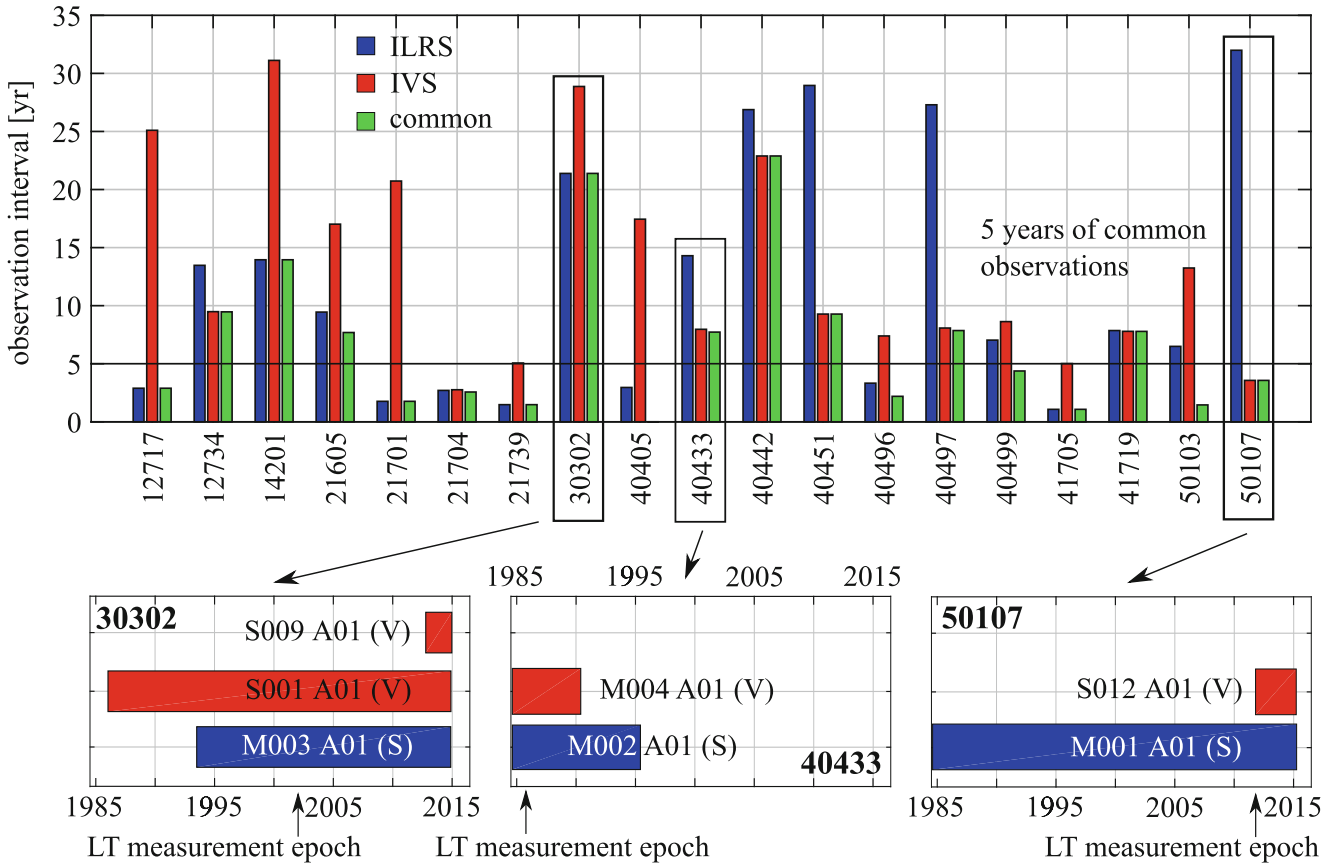

Fig. 3 Time span of SLR (blue) and VLBI (red) observations and common time span of both techniques (green). In the lower panels, selected examples for the stations in Hartebeesthoek (South Africa, left panel), Quincy (USA, middle panel), and Yarragadee (Australia, right panel) are shown together with the local tie (LT) measurement epochs

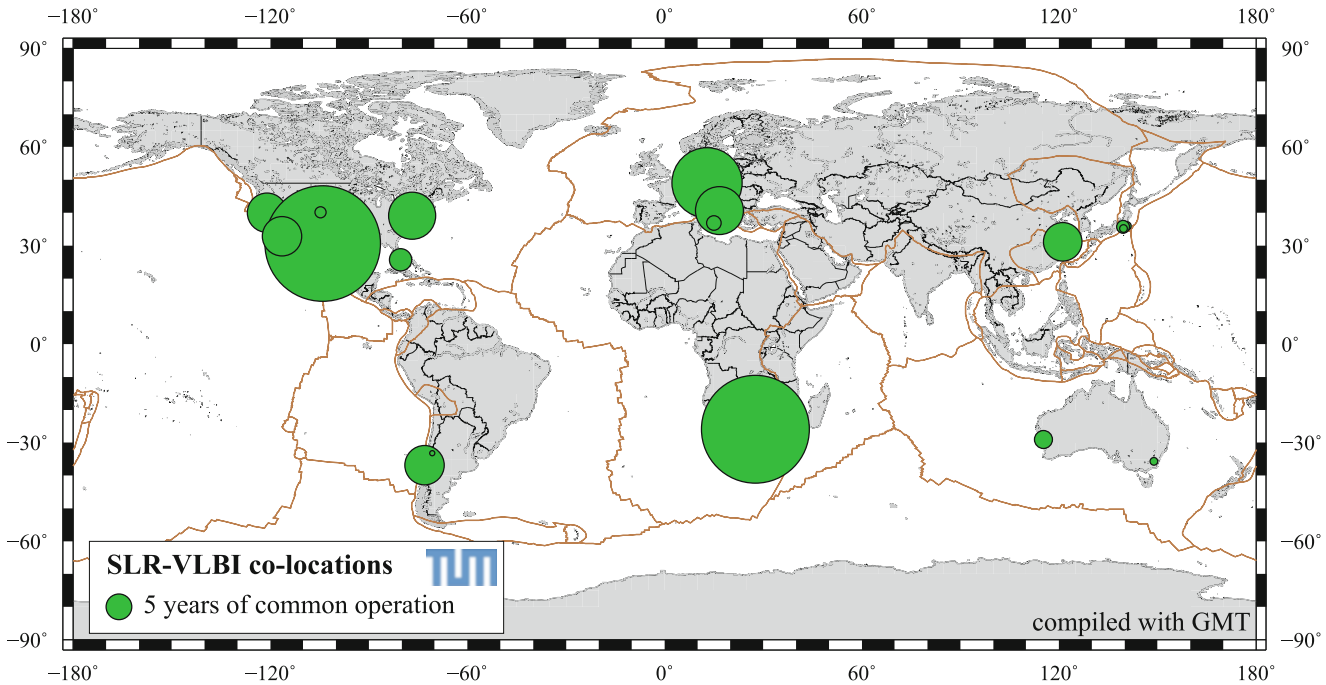

Fig. 4 Global distribution of VLBI and SLR co-location sites. The radii of the circles indicate the common observation time span of VLBI and SLR

Table 2 Scale offsets [mm] obtained from 14-parameter Helmert transformations of SLR and VLBI single-technique solutions of DGFI-TUM

Test	Co-locations	2000.0	2005.0	2010.0
A	9 "stable"	3.2 ± 1.9	2.9 ± 1.8	4.0 ± 3.7
B	9 + Ya.	-6.8 ± 3.7	-3.2 ± 3.2	0.3 ± 2.6
C	9 + Ya. + Qu.	-9.8 ± 3.9	-8.0 ± 4.0	-6.1 ± 5.3

The transformations are computed directly for three different epochs using local ties (see Fig. 2). "Ya." means Yarragadee, "Qu." means Quincy. The obtained scale rates are small and not shown here

between SLR and VLBI directly (see Sect. 2.2), we have up to 31 co-locations between SLR and GNSS and up to 36 between VLBI and GNSS, respectively, if a threshold of 25 mm is applied for the local tie accuracy. In analogy to Sect. 2.2, we use the local ties to GNSS to compute GNSS markers from SLR and VLBI reference points (see Fig. 5). After the marker computation, we transform the GNSS markers to the GNSS-only solution of DGFI-TUM at the epoch 2000.0 and subtract the obtained transformation parameters. At the end, we achieve an indirect estimate of the scale difference between SLR and VLBI using the improved network geometry of the GNSS station network.

Table 3 summarizes the scale differences between SLR and VLBI using the indirect approach via the GNSS co-locations. To test the robustness of this comparison, we use four different local tie thresholds for the discrepancy between the single-technique coordinates of the reference points and the measured local tie vectors. As we can see, a restrictive local tie selection (e.g., 7 mm threshold) results in the smallest number of transformation stations (20 for VLBI, 15 for SLR) and a scale bias of **0.1 ppb** (0.7 mm at the Earth's crust). If the threshold is increased to 25 mm, also the number of transformation stations increases to 36 stations, but a scale bias of **−0.5 ppb** (−3.3 mm) is obtained. This large threshold primarily deform the SLR network since the scale bias increases by nearly 5 mm. In total, three test scenarios show VLBI and SLR scale differences below 0.15 ppb (1 mm). Although the better network geometry gives more stable transformation results, it should also be noticed here that the large number of GNSS discontinuities is a critical issue for the scale comparison since co-locations in the past might not be transferred properly to the transformation epoch. In other words, a measured local tie is not valid any more if a discontinuity is introduced.

2.4 VLBI Scale Comparisons Performed by IVS CC

A different approach to assess the scale bias between SLR and VLBI is to look a the scale differences which the Combination Centre (CC) of the International VLBI Service for Geodesy and Astrometry (IVS) located at BKG (Germany) obtained. They compared the estimated scale parameters of the epoch-wise IVS combined solutions (VLBI-only) to several different TRF realizations (see Fig. 6). The results indicate that the DTRF2008, the DTRF2014, the JTRF2014, and the quarterly VLBI-only TRF solution VTRF2015q2 agree well with the IVS combined solutions in terms of scale offsets showing a mean value close to zero. The ITRF2008 as well as the ITRF2014 reveal a mean offset of about −0.5 ppb (−3.4 mm) by construction. The mean value of both ITRF solutions w.r.t. the IVS combined solutions can be explained by the obtained scale bias between SLR and VLBI in the ITRF solutions. Since the ITRF scale is a mean of the SLR and the VLBI scale, each technique-only solution must show an offset w.r.t. the ITRFs. Despite this fact, all other solutions do not show any long-term mean offset which means that the VLBI-only station networks within these combined solutions realize a scale which is identical scale to the VLBI-only scale.

2.5 SLR Scale Comparisons Performed by ILRS CC

Similarly to the VLBI-only scale, this sub-section focuses on the external comparison of the SLR-only scale. Therefore, the primary (A) CC of the International Laser Ranging Service (ILRS) located at ASI (Italy) named ILRSA in the following provided epoch-wise estimated scale differences of the weekly combined ILRSA solutions w.r.t. the most recent ITRS realizations (Fig. 7). Again, the DTRF2014 as well as the JTRF2014 do not show a long-term mean offset w.r.t. the SLR-only solutions whereas there is a mean scale

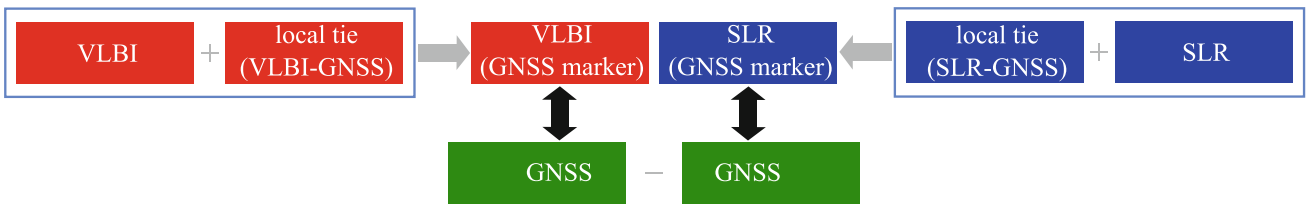

Fig. 5 Transformation of DGFI-TUM's VLBI and SLR single-technique solutions via GNSS co-locations (indirect approach, but improved network geometry). After the transformation, the obtained transformation parameters are subtracted from each other

Table 3 Scale offsets [mm] obtained from 14-parameter Helmert transformations of GNSS markers computed using local ties (LTs) from SLR and VLBI reference points (DTRF2014 single-technique solutions) at the epoch 2000.0 (see Fig. 5)

LT threshold	VLBI w.r.t. GNSS [mm]	Number of stations	SLR w.r.t. GNSS [mm]	Number of stations	Δ scale (VLBI w.r.t. SLR) [mm]
7 mm	0.3 ± 0.8	20	-0.4 ± 0.7	15	0.7 ± 1.1
10 mm	0.9 ± 0.7	26	0.3 ± 0.6	19	0.6 ± 0.9
15 mm	1.4 ± 0.6	34	1.3 ± 0.7	23	0.1 ± 0.9
25 mm	1.2 ± 0.7	36	4.5 ± 0.9	31	-3.3 ± 1.1

The scale rates are all nearly zero and not listed in this table. For the LTs, different thresholds are tested (see also Seitz et al. 2012)

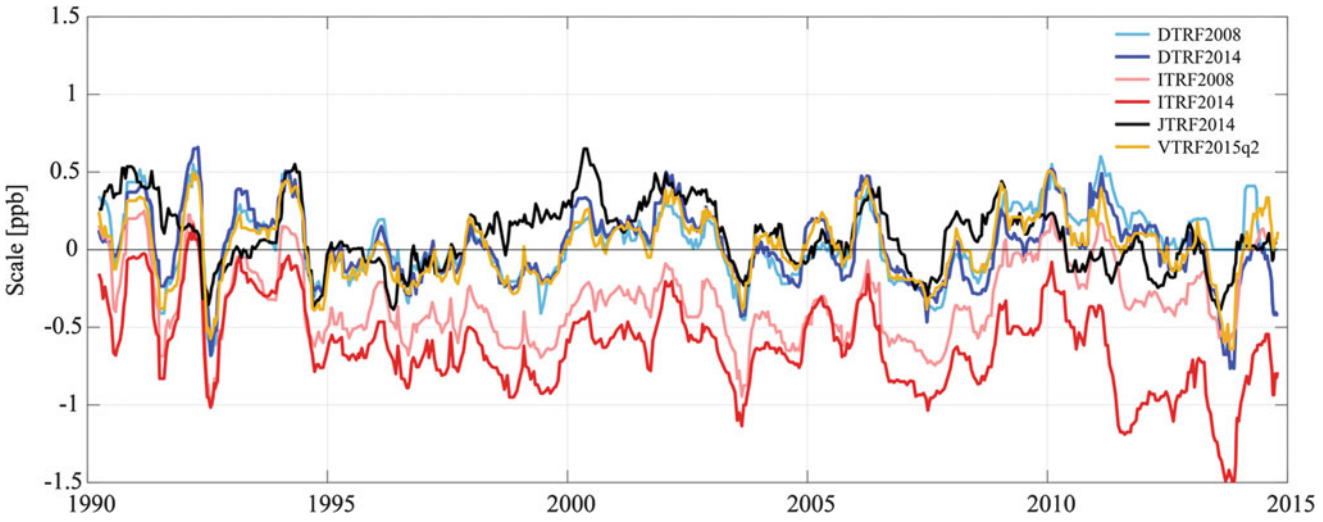

Fig. 6 Scale of combined IVS solutions w.r.t. different ITRS realizations. This plot has been kindly provided by S. Bachmann (IVS CC at BKG, Germany)

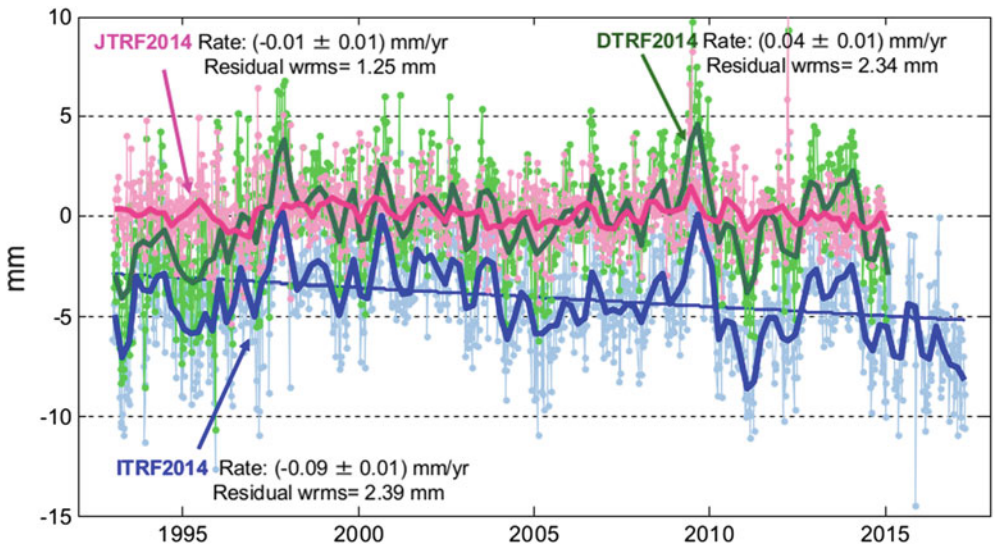

Fig. 7 Scale of combined ILRSA solutions w.r.t. different ITRS realizations. This plot has been kindly provided by C. Luceri (ILRSA CC at ASI, Italy)

offset of about -0.6 ppb (-4.0 mm) for the ITRF2014. The sign of this offset depends on the transformation direction (the opposite sign will be used to quantify the scale offset between SLR and VLBI). This means that the DTRF2014 and the JTRF2014 do not adjust the scale of the SLR subnet since it is implicitly included in the SLR-only NEQ. The same behavior was found for the VLBI subnet in the previous section. Thus, the results of the

comparisons done by the IVS and ILRSA CCs do confirm the 1.2 ppb (−0.5 ppb for VLBI in Sect. 2.4 and 0.6 ppb for SLR) apparent scale bias between the SLR and the VLBI ITRF2014 solutions. Up to now, no explicit explanation can be found for this behavior but most likely, the scale difference might be explained by the combination procedure (adjusting scale parameters for SLR and VLBI or not) or the local tie and velocity tie handling within the ITRF solutions.

3 Summary and Conclusions

The three most recent realizations of the ITRS, namely the DTRF2014, the ITRF2014, and the JTRF2014 provide a valuable basis to measure the consistency of the combination processes of the terrestrial reference frame. In this paper, the SLR and VLBI scale bias investigation was brought into focus triggered by a bias of 1.37 ppb reported by IGN for the ITRF2014 which cannot be confirmed by the two other ITRS CCs and the IVS and ILRSA CCs. To verify the results, we defined several test scenarios to (1) quantify a possible scale bias and (2) to assess the reliability of the obtained results. In the following, the major findings of this investigation are summarized:

- The single-technique SLR and VLBI solutions do not show a significant scale offset or rate difference between IGN and DGFI-TUM.
- A direct comparison between SLR and VLBI (via Helmert transformations) is quite sensitive w.r.t. particular stations used in the transformation. If the most stable transformation with 9 co-locations is used, the large scale bias observed by IGN between SLR and VLBI is not confirmed.
- Transformations via the GNSS network using local ties provide a much better geometry for the Helmert transformation. If a reasonable local tie selection is used, only mean scale offsets of up to 1 mm are found.
- The IVS and ILRSA results show a good agreement of the VLBI and SLR scale w.r.t. the DTRF solutions and the JTRF2014, but reveal a bias and a drift w.r.t. ITRF2014.

As a final conclusion, we can only state that a scale bias between VLBI and SLR cannot be explained by our results. As a consequence, the apparent scale issue seems to be an effect inherent in ITRF2014 only. Since the single-technique secular solutions agree quite well to each other (between DGFI-TUM and IGN), the reason for the scale bias in the ITRF2014 might be caused in the inter-technique combination procedure.

In addition, one has to mention that all results presented in this paper do not converge to a clear and evident statement if there is a scale bias between SLR and VLBI or not. This paper tries to extend the common analysis by applying different strategies to resolve a potential scale bias. Unfortunately, further investigations are still necessary to finally answer this question in an unambiguous way.

References

Altamimi Z, Rebischung P, Metivier P et al (2016) ITRF2014: A new release of the International Terrestrial Reference Frame modeling non-linear station motions. J Geophys Res 121(8):6109–6131. https://doi.org/0.1002/2016JB013098

Seitz M, Angermann D, Bloßfeld M et al (2012) The 2008 DGFI realization of the ITRS: DTRF2008. J Geod 86(12):1097–1123. https://doi.org/10.1007/s00190-012-0567-2

Seitz M, Bloßfeld M, Angermann D et al (2016) The new DGFI-TUM realization of the ITRS: DTRF2014 (data). Deutsches Geodätisches Forschungsinstitut, Munich. https://doi.org/10.1594/PANGAEA.864046 (Open Access)

Wu X, Abbondanza C, Altamimi Z et al (2015) KALREF-a Kalman filter and time series approach to the International Terrestrial Reference Frame realization. J Geophys Res Solid Earth 3775–3802. https://doi.org/10.1002/2014JB011622

Impact of Different ITRS Realizations on VLBI Combined EOP and Scale

Sabine Bachmann and Daniela Thaller

Abstract

In this paper we investigate the impact of using the three ITRS realizations DTRF2014, ITRF2014, and JTRF2014 as a priori TRF for the VLBI combination on EOP and scale. The scale factor between the IVS routine combined solution and DTRF2014, ITRF2014, and JTRF2014 shows a significant offset of −0.59 ppb with respect to ITRF2014 and of 0.19 ppb with respect to JTRF2014. No significant offset was found for the DTRF2014-based solution. The investigation of the EOP of all four TRF-based solutions (DTRF2014-, ITRF2014-, JTRF2014- and VTRF2015q2-based) shows specific effects when comparing to the reference time series IERS 14C04, IGS, and ILRS. Relative to the VTRF2015q2-based solution, x-pole differences with respect to the DTRF2014-based solution (positive trend) and JTRF2014-based solution (scatter and negative trend), as well as an offset concerning the y-pole for all three TRF-based solutions with an additional scatter for the JTRF2014-based solution are recognized. No significant differences were found for pole rates, nutation, and LOD, but using ITRF2014 or JTRF2014 leads to marginal larger scatter with respect to the VTRF-based EOP series for LOD. In addition, a significant impact was found when comparing dUT1. All three TRF-based solutions show a significant offset comparing to IERS 14C04, whereas no offset is detected for the VTRF2015q2-based solution.

Keywords

Earth orientation parameters · ITRS realizations · Scale factor · VLBI

1 Introduction and Input Contributions

In the framework of the latest realization of the International Terrestrial Reference System (ITRS), each of the three ITRS Combination Centers of the International Earth Rotation and Reference System Service (IERS) provides an inter-technique combined terrestrial reference frame (TRF) using different station coordinate parameterizations. The German Geodetic Research Institute/Technical University of Munich (DGFI-TUM) (Seitz et al. 2016) provides the DTRF2014, using a piece-wise linear station model with improved geophysical modeling. The official ITRF solution, ITRF2014, is provided by Institut national de l'information géographique et forestière (IGN, France) (Altamimi et al. 2016), using a piece-wise linear station model and an additional post-seismic deformation model. Finally, Jet Propulsion Laboratory (JPL, USA) (Abbondanza et al. 2017) provides the JTRF2014, using Kalman filtered weekly estimations of station coordinates.

In our study we investigate the impact on VLBI combined Earth Orientation Parameter (EOP) and scale when using these three TRF solutions as a priori station coordinates. The combination is performed session-wise on the normal equation level using the contributions provided by the Analysis Centers (AC) of the International VLBI Service for

S. Bachmann (✉) · D. Thaller
Federal Agency for Cartography and Geodesy, Frankfurt am Main, Germany
e-mail: sabine.bachmann@bkg.bund.de

J. T. Freymueller, L. Sánchez (eds.), *International Symposium on Advancing Geodesy in a Changing World*,
International Association of Geodesy Symposia 149, https://doi.org/10.1007/1345_2018_36

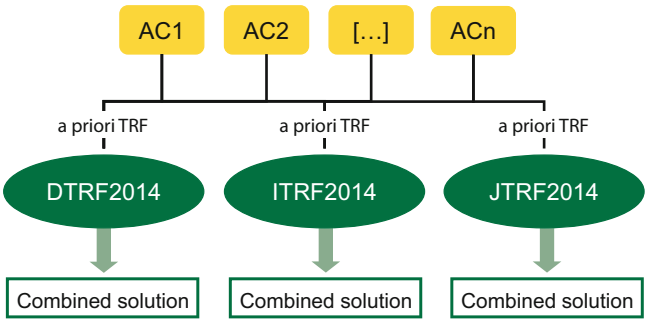

Fig. 1 AC input contributions and processing scheme to make a solution based on a given a priori TRF

Geodesy and Astrometry (IVS).[1] The combination process is sketched in Fig. 1. Datum free normal equations from the IVS ACs are stacked and the datum is applied to the combined contributions by fixing the station coordinates to their a priori values coming from each of the three TRF solutions. A detailed description of the combination process is described in Bachmann et al. (2016). Overall, we generate three different combined EOP solutions, using DTRF2014, ITRF2014, and JTRF2014 as a priori station coordinates, denoted here as DTRF2014-based, ITRF2014-based and JTRF2014-based solution, respectively. Additionally, we include a fourth solution in our comparisons, which is a routine VLBI-only combined quarterly TRF solution called VTRF2015q2 (aligned to ITRF2008).

In Sect. 2, we compare the scale parameter between different ITRS realizations and the routine VLBI combined solution. This parameter is particularly interesting, since VLBI – together with Satellite Laser Ranging (SLR) – are the only space geodetic techniques with reliable access to this parameter. Therefore, investigating the scale is of vital interest in VLBI. EOP comparisons follow in Sect. 3, a conclusion is drawn in Sect. 4.

2 Scale Parameter Comparison

We evaluate the scale parameter by estimating a seven-parameter Helmert transformation between the session-wise routine VLBI combined solution (VTRF2015q2 as a priori TRF) and each of the ITRS realizations. Sessions observed between 1990.0 and 2015.0 are taken into account, i.e., that time-span with good VLBI sessions that is also used as input for the ITRF2014. By default, all stations included in the respective network are used for the Helmert transformation datum definition, taking into account the smaller networks containing only three or four stations. However, stations with discontinuities (e.g. caused by earthquakes) are excluded from the datum definition in the period after the earthquake took place.

Figure 2 shows the 90-days median-smoothed scale (7 days overlap) between the three ITRS realizations and the VLBI combined solution. Additionally, previous ITRS realizations, like DTRF2008 and ITRF2008, as well as the VTRF2015q2 are shown. The peculiarities that can be seen in each of the scale plots before 1994, around 2004 and 2014 can be explained by unfavorable VLBI network geometry. The figure shows a good agreement of the scale with respect to the two DTRF solutions (DTRF2008, DTRF2014), the VTRF2015q2 solution, and the JTRF2014 solution, scattering around the zero line. Between about 1998 and 2002 a variation of the scale with respect to JTRF2014 can be observed. We see a noticeable offset for the scale with respect to the two ITRF solutions (ITRF2008 and ITRF2014), and a trend with respect to the ITRF2014 solution. Table 1 shows the weighted mean of the scale time series as presented in Fig. 2. The weighted mean for the two DGFI solutions as well as the VTRF solution is not significant. For the JTRF2014, a weighted mean of 0.19 ppb is estimated, mainly resulting from the scale irregularities between 1998 and 2002. The weighted mean compared to ITRF2008 is −0.38 ppb, and compared to ITRF2014 −0.59 ppb, i.e., −3.8 mm on the Earth's surface. This value corresponds well with the scale factor between VLBI and SLR of 1.37 ppb found by Altamimi et al. (2016) and the offset of the SLR solution with respect to the ITRF2014 of about 0.7 ppb as found by V. Luceri for the SLR intra-technique combined solution (personal communication[2]) (opposite transformation direction causing inverted sign). Looking at the WRMS of the scale time series, the scale factor with respect to JTRF2014 shows the smallest value of 0.78 ppb, which can be most likely explained by the Kalman filter approach in JTRF2014, which allows the best-possible adaption on a weekly basis. The highest value of 1.02 ppb has been detected for scale factor with respect to ITRF2008. Possible reasons for the differences between the ITRF and DTRF scale factors are equating station velocities, treatment of local ties, and parameter estimation within the inter-technique combination process.

3 EOP Comparison

In this section we investigate the impact of the various ITRS realizations on the VLBI-derived EOP. Therefore, in Sect. 3.1 we compare the EOP resulting from the VLBI combination (as described in Sect. 1) with external EOP series from IERS 14C04 (a combined solution including VLBI, GNSS, and SLR EOP time series aligned to ITRF2014) (Bizouard et al.

[1] https://ivscc.gsfc.nasa.gov/.

[2] https://ilrs.cddis.eosdis.nasa.gov/docs/2017/ILRS_ASC_EGU2017_PRESENTATIONS.pdf.

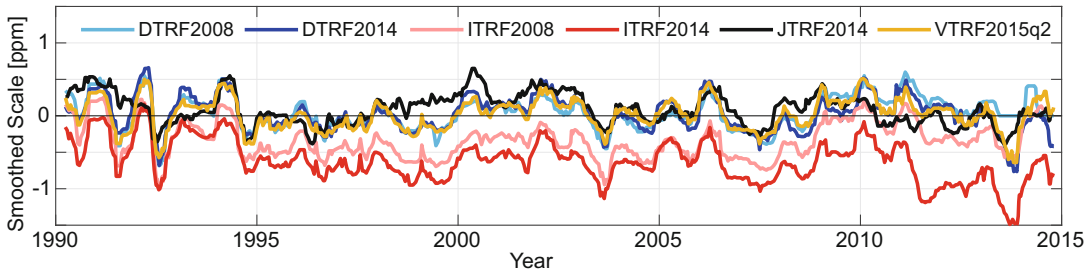

Fig. 2 90-Days median-smoothed scale between the different ITRS realizations and the session-wise VLBI combined solution: DTRF2008 (light blue), DTRF2014 (dark blue), ITRF2008 (light red), ITRF2014 (dark red), JTRF2014 (black) and VTRF2015q2 (ocher)

Table 1 Weighted mean and WRMS of the scale time series

ITRS realization	Weighted mean [ppb]	WRMS [ppb]
DTRF2014	−0.01 ±0.01 (−0.1 mm)	0.88
ITRF2014	−0.59 ±0.02 (−3.8 mm)	0.95
JTRF2014	0.19 ±0.01 (1.2 mm)	0.78
VTRF2015q2	0.01 ±0.01 (−0.1 mm)	0.91
DTRF2008	0.02 ±0.02 (0.1 mm)	0.98
ITRF2008	−0.38 ±0.02 (−2.4 mm)	1.02

2017), IGS finals and ILRS combined EOP time series resulting from the ILRS input contribution to ITRF2014. Additionally, we compare dUT1 to IERS 08C04 (aligned to ITRF2008). In Sect. 3.2 we use the EOP time series which are commonly estimated with the respective ITRS realizations, i.e., DTRF2014, ITRF2014 and JTRF2014 (denoted DGFI, IGN and JPL hereafter). These external EOP time series are provided by the IERS ITRS Combination Centers along with the respective TRF. We compare these EOP time series with the IVS EOP long-term combined time series using the VTRF2015q2 for a priori station coordinates.

3.1 Comparison to IERS 14C04, IGS and ILRS

The x-pole comparison in Fig. 3 with respect to the IERS 14C04 series (upper left figure) shows no evident characteristics and a scatter about zero commonly for each of the EOP solutions. The same yields for the comparison to the ILRS solution (lower right figure), except for a characteristic peak around 2010/2011 (leaving aside the early, less accurate years before 2000). In contrast, for the comparison to the IGS finals (upper right figure) we observe a slope between the years around 2002 and 2015. This slope is associated with IGS analysis only, since it is not visible in ILRS comparisons. We notice an offset and a larger scatter of the JTRF2014-based EOP until 2007 comparing to the IVS VTRF2015q2-based solution (lower right figure). Also, the differences between the various TRF solutions become larger again from 2013 on. Furthermore, we see a drift for the differences with respect to the DTRF2014-based solution, but no significant characteristic for the ITRF2014-based solution is visible. The reason for the drift remains unclear. In Table 2 the correlation coefficients r between the EOP time series are shown. We used the 14C04 solution as reference to reduce the EOP for long-term periods. It states, that the DTRF2014-based, ITRF2014-based, and VTRF2015q2-based solutions are highly correlated with r between 0.93 and 0.96, whereas the JTRF2014-based solution is lowly correlated (r between 0.23 and 0.24).

Figure 4 shows the comparison of the y-pole. Comparing each EOP solution to IERS 14C04 (upper left) and IGS (upper right figure) we see a peculiarity around 2006. Whereas the comparison to IERS 14C04 shows a scatter about zero with no visible characteristics, we observe a drift in the IGS comparison starting around 2011 and an offset from 2010/2011 on in comparison with the ILRS solution (lower left figure). These characteristics are common for each of the EOP solutions. According to SLR analysts, this offset is due to modifications in the network configuration, and not induced by earthquake affected stations. Common to the x-pole comparison, the differences between the three TRF solutions become larger from 2013 on. As already observed for the x-pole, the inter-TRF-based comparisons for the y-pole shows an offset of the JTRF2014-based EOP, as well (lower right figure), with negative sign before 2002/2003 and positive sign afterward. Also, a larger scatter can be seen than for the DTRF2014- and ITRF2014-based solutions. The latter two solutions show a small offset of about 50 µas. This behavior is also reflected in the correlation coefficients between the respective EOP solutions. As Table 2 shows, the y-pole is highly correlated between the DTRF2014-, ITRF2014-, and VTRF2015q2-based solutions (r between 0.88 and 0.92), but moderately correlated to the JTRF2014-based EOP (0.47–0.50).

Contrary to the pole coordinates, the comparison of LOD shows little characteristic differences with a regular scatter about zero commonly for all EOP solutions in comparisons to IERS 14C04, IGS, and ILRS (not shown). Also, the comparison with the VTRF2015q2-based IVS solution

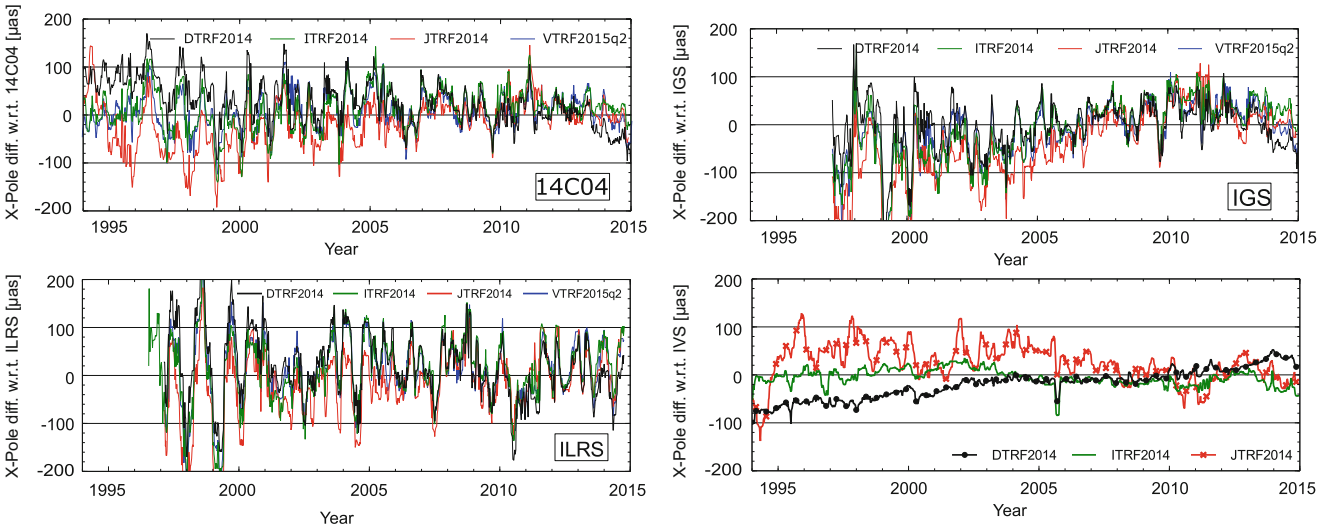

Fig. 3 X-pole differences between the solutions based on the different TRFs and IERS 14C04 (upper left), IGS finals (upper right), ILRS input for ITRF2014 (lower left). Additionally, the differences to the VTRF2015q2-based IVS solution are shown (lower right). 90 days median smoothed values are shown

Table 2 Correlation coefficients r for x-, and y-pole, and dUT1 between the investigated EOP time series based on DTRF2014, ITRF2014, JTRF2014, and VTRF2015q2 (IERS 14C04 series subtracted)

Correlation coefficient r	x-pole	y-pole	dUT1
DTRF2014, ITRF2014	0.93	0.90	0.78
DTRF2014, JTRF2014	0.23	0.50	0.41
DTRF2014, VTRF2015q2	0.96	0.92	0.91
ITRF2014, JTRF2014	0.23	0.47	0.40
ITRF2014, VTRF2015q2	0.95	0.88	0.83
JTRF2014, VTRF2015q2	0.24	0.50	0.42

shows a homogeneous scatter about zero with a moderately larger amplitude for both ITRF2014-, and JTRF2014-based solutions as shown in Fig. 5. This is also reflected in the correlation coefficient between these solutions, where r is between 0.98 and 0.99 for each correlation, i.e., highly correlated (not included in Table 2). This means, that other effects than the choice of the a priori TRF impact the estimated LOD parameter.

In contrast to the comparison of LOD estimates, the dUT1 parameter shows significant differences comparing to IERS 14C04 as shown in Fig. 6 (left figure). The DTRF2014- and ITRF2014-based solutions show an offset of about 5 µs and strong variations between the years 2000 and 2015. The JTRF2014-based solution shows an offset of about 2 µs and strong variations between 2000 and 2015, as well. However, the VTRF2015q2-based IVS solution shows no noticeable offset and a regular scatter about zero. For the dUT1 comparison, significant differences between the IERS 14C04 (aligned to ITRF2014) and 08C04 (aligned to ITRF2008) are visible. We see a discontinuity in 2000 for the IERS 08C04 comparison (right figure) for each of the EOP solutions. This discontinuity disappears when comparing the dUT1 time series with the IERS 14C04 series. It is somehow surprising that this discontinuity disappears for the VTRF2015q2-based solution as well, since this solution is aligned to ITRF2008. We assume that this discontinuity is related to the IERS 08C04 series itself and not depending on the a priori TRF used for the EOP generation. As expected from the left figure, offsets for all three EOP solutions can be observed in comparison to the VTRF2015q2-based dUT1, as well as a larger scatter for the JTRF2014-based solution. Again, the correlation coefficient r for the JTRF2014-based solution shows lowly correlation to the other three solutions with r between 0.4 and 0.42. Contrary, the DTRF2014-, ITRF2014-, and VTRF2015q2-based solution show a correlation coefficient between 0.78 and 0.91 (see Table 2).

3.2 Comparison to TRF EOP

In this section we investigate the EOP time series that are generated commonly with the ITRS realizations and which are provided by DGFI, IGN and JPL, respectively. We compare these external EOP solutions to the VTRF2015q2-based combined EOP solution and to IERS 14C04 series. The pole coordinates show no peculiarities and are not shown here. For the dUT1 differences, the most noticeable is an offset of all the three EOP time series of about −5 µs with respect to the VLBI-only combined dUT1 solution, similar to the results seen in Fig. 6. Furthermore, a systematic time dependent signal can be accounted for all three EOP differences in

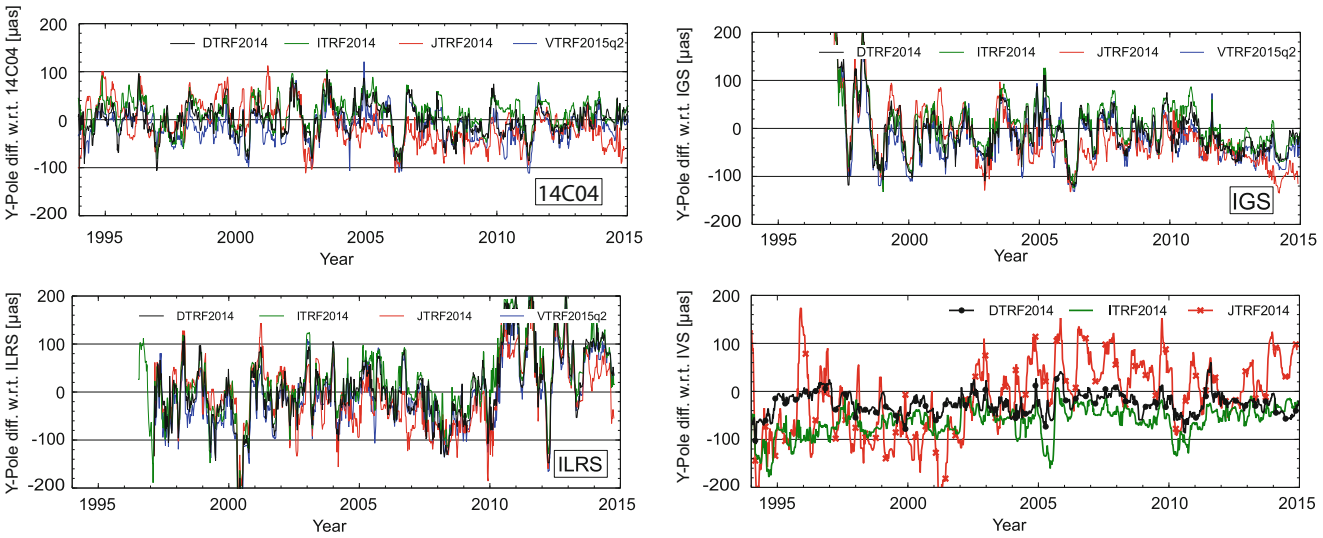

Fig. 4 Y-pole differences between the solutions based on the different TRFs and IERS 14C04 (upper left), IGS finals (upper right), ILRS input for ITRF2014 (lower left). Additionally, the differences to the VTRF2015q2-based IVS solution are shown (lower right). 90 days median smoothed values are shown

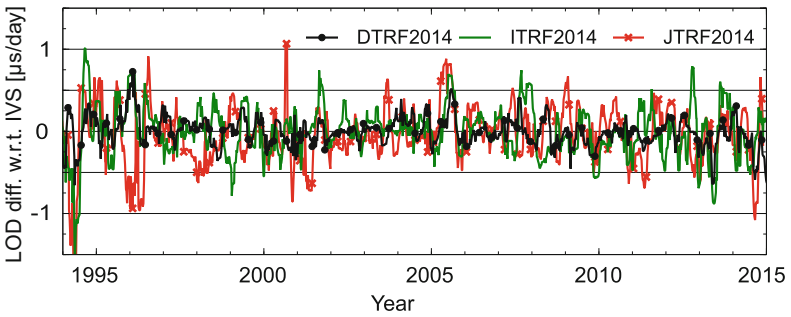

Fig. 5 LOD differences between the solutions based on the different TRFs and the VTRF2015q2-based IVS solution are shown. 90 days median smoothed values are shown

a range of about $\pm 5\,\mu$s (not shown). The reason for the offset is not clear, yet. We observe a noticeable difference with respect to the VTRF2015q2-based solution for all LOD solutions as shown in Fig. 7 (left figure). It shows significant larger variations of the DGFI LOD up to $20\,\mu$s/day (black line), while the LOD differences for the IGN and the JPL EOP solutions agree very well (overlapping).

To investigate the origin of the elevated scatter of the DGFI LOD solution, we perform comparisons to the IERS 14C04 series, and here, the DGFI solution shows smaller variations in comparison to the IGN, JPL and VTRF2015q2-based solution (right figure). The reason for these differences can be explained with the inter-technique combination procedure applied at the different IERS ITRS Combination Centers. Contrary to the combination procedure applied at IGN and JPL (where solely VLBI is used for the determination of LOD), all space geodetic techniques are incorporated in the LOD combination at DGFI. This leads to higher differences when comparing to intra-technique VLBI-only EOP (Fig. 7, left figure). At the same time, the DGFI LOD parameter shows a better accordance to the IERS 14C04 series (Fig. 7, right figure), which is a combination of IGS and ILRS contributions aligned to IVS dUT1 time derivatives (cf. Bizouard et al. 2017), which is the reasons for the LOD differences.

4 Conclusion

In Bachmann and Thaller (2017) we showed that no significant differences were found for station coordinate estimation and repeatabilities (WRMS/RMS) using the three ITRS realizations as datum information for the VLBI combination. In this paper we found significant differences in the scale factor when comparing the routine VLBI combined solution to DTRF2014, ITRF2014, and JTRF2014. The scale factor with respect to ITRF2014 shows a significant offset of -0.59 ppb, whereas the scale factor with respect to DTRF2014 is not significant. The scale factor with respect to JTRF2014 is 0.19 ppb, which is mainly influenced by an offset between 1998 and 2002. At the same time, it shows the smallest WRMS value of all ITRS realizations of 0.78 ppb.

The analysis of the TRF-based combined x- and y-pole, shows specific effects common for all TRF-based solutions

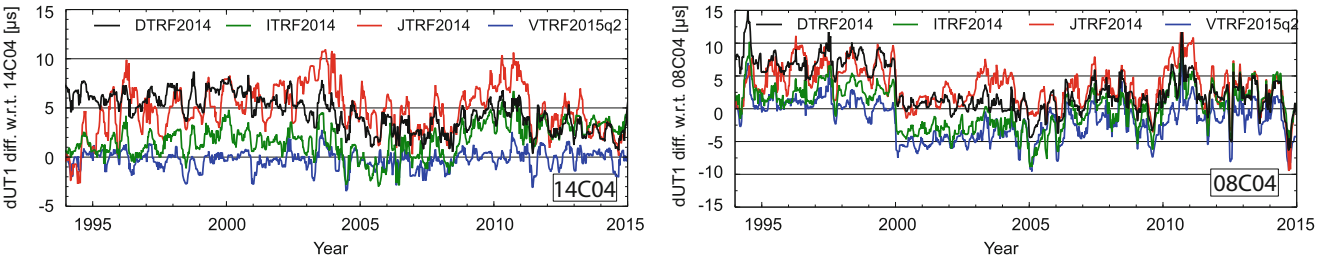

Fig. 6 dUT1 differences between the solutions based on the different TRFs and IERS 14C04 (left), and IERS 08C04 (right). 90 days median smoothed values are shown

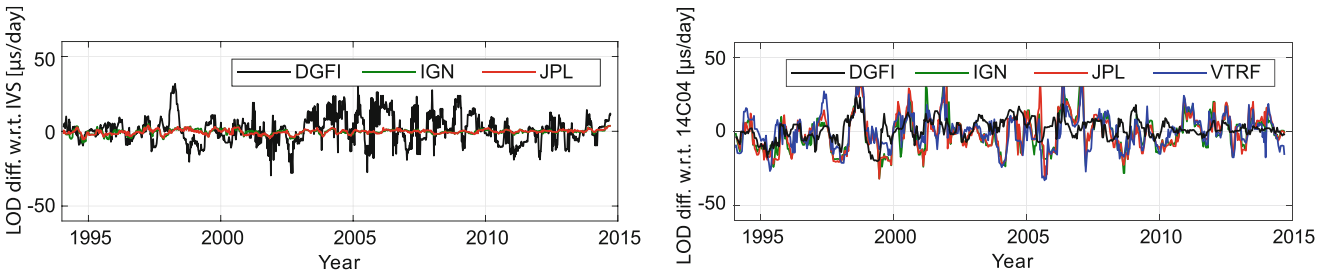

Fig. 7 Differences between the DGFI (black), IGN (green) and JPL (red) LOD with respect to the VTRF015q3-based solution (left) and to IERS 14C04 (right). 90 days median smoothed values are shown

when comparing to IERS 14C04, IGS and ILRS EOP series. The JTRF2014-based EOP solution shows a slight offset compared to the other solutions. For the pole coordinate rates, nutation, and LOD, we found no significant differences between the different TRF-based EOP time series and the reference EOP series, i.e., the choice of the a priori TRF is secondary. Using ITRF2014 or JTRF2014 leads to marginal larger scatter with respect to the VTRF-based EOP series. The most significant impact can be seen comparing dUT1. All three TRF-based solutions show a significant offset comparing to IERS 14C04, while the VTRF-based IVS solution shows no offset. The reason for the offsets with respect to IERS 14C04 series remains unclear, especially against the background that the IERS 14C04 dUT1 series are generated using solely VLBI contributions. In contrast, comparing to IERS 08C04, a significant discontinuity for each EOP series was found in 2000, but no offset for DTRF2014 and JTRF2014 afterward. The comparison of the EOP time series provided by the ITRS Product Centers along with the TRFs shows a significant difference for LOD for the DGFI series. This difference can be explained by the combination procedure (see Sect. 3.2) as it disappears when comparing these EOP series to IERS 14C04.

Based on our results found in this paper, we conclude our investigation with the following recommendations: for VLBI analysis focusing on scale we recommend to use the DTRF2014 or JTRF2014 solution as long as the ITRF2014 shows larger differences. For pole coordinate analysis either DTRF2014 or ITRF2014 are performing equally, JTRF2014 shows larger scatter and slight offsets comparing to the DTRF2014-, and ITRF2014-based EOP. The EOP time derivatives including LOD, as well as nutation, each of the different ITRS realizations performs equally. The JTRF2014 Kalman filter approach allows the best-possible adaption on a weekly basis. Using it as a priori TRF results in EOP time series that are independent (uncorrelated) comparing to piece-wise linear station coordinate modeling, and at the same time lead to larger scatter. Unfortunately, it is not extendable into the future beyond 2015.0 (no regular updates available yet). The same holds for the non-tidal loading models available for the DTRF2014, which are not provided after 2015.0 (and thus not used in this study). For future investigations we plan to focus on the origin of the dUT1 differences with respect to IERS 14C04 and to include non-tidal loading models provided for DTRF2014 and ITRF2014 and their impact on VLBI combined EOP.

Acknowledgements We thank Vincenza Luceri for providing the ILRS combined EOP time series for our comparisons.

References

Abbondanza C, Chin TM, Gross RS, Heflin MB, Parker J, Soja BS, van Dam T, Wu X (2017) JTRF2014, the JPL Kalman filter, and smoother realization of the international terrestrial reference system. J Geophys Res Solid Earth 122:8474–8510. https://doi.org/10.1002/2017JB014360

Altamimi Z, Rebischung P, Métivier L, Collilieux X (2016) ITRF2014: a new release of the international terrestrial reference frame modeling nonlinear station motions. J Geophys Res Solid Earth 121:6109–6131. https://doi.org/10.1002/2016JB013098

Bachmann S, Thaller D (2017) ITRS realizations in the framework of ITRF2014: impact of different TRF parameterizations on VLBI combined products. In: Haas R, Elgered G (eds) Proceedings of the 23rd European VLBI Group for Geodesy and Astrometry Working Meeting, pp 157–161. ISBN: 978-91-88041-10-4

Bachmann S, Thaller D, Roggenbuck O, Lösler M, Messerschmitt L (2016) IVS contribution to ITRF2014. J Geod 90:631–654. https://doi.org/10.1007/s00190-016-0899-4

Bizouard C, Lambert S, Becker O, Richard JY (2017) Combined solution C04 for earth rotation parameters consistent with international terrestrial reference frame 2014. Observatoire de Paris, SYRTE, 61 av. de l'Observatoire, Paris. http://hpiers.obspm.fr/eoppc/eop/eopc04/C04.guide.pdf

Seitz M, Bloßfeld M, Angermann D, Schmid R, Gerstl M, Seitz F (2016) The new DGFI-TUM realization of the ITRS: DTRF2014 (data). Deutsches Geodätisches Forschungsinstitut, Munich (2016). https://doi.org/10.1594/PANGAEA.864046

Testing Special Relativity with Geodetic VLBI

Oleg Titov and Hana Krásná

Abstract

Geodetic Very Long Baseline Interferometry (VLBI) measures the group delay in the barycentric reference frame. As the Earth is orbiting around the Solar system barycentre with the velocity V of 30 km/s, VLBI proves to be a handy tool to detect the subtle effects of the special and general relativity theory with a magnitude of $(V/c)^2$. The theoretical correction for the second order terms reaches up to 300 ps, and it is implemented in the geodetic VLBI group delay model. The total contribution of the second order terms splits into two effects – the variation of the Earth scale, and the deflection of the apparent position of the radio source. The Robertson-Mansouri-Sexl (RMS) generalization of the Lorenz transformation is used for many modern tests of the special relativity theory. We develop an alteration of the RMS formalism to probe the Lorenz invariance with the geodetic VLBI data. The kinematic approach implies three parameters (as a function of the moving reference frame velocity) and the standard Einstein synchronisation. A generalised relativistic model of geodetic VLBI data includes all three parameters that could be estimated. Though, since the modern laboratory Michelson-Morley and Kennedy-Thorndike experiments are more accurate than VLBI technique, the presented equations may be used to test the VLBI group delay model itself.

Keywords

Lorentz invariance · Special relativity · VLBI

1 Introduction

The Very Long Baseline Interferometry (VLBI) technique measures time delay – the difference between times of the signal arrival on two radio telescopes separated by a long baseline. All measurements are referred to the Solar system barycentre, which moves around the Sun with an orbital velocity about 30 km/s. This makes the Earth a natural flying platform and VLBI a very effective tool to detect a tiny effect of special relativity. Each baseline of thousand kilometres length may serve as a "flying rod", which is traditionally used for theoretical calculation. Precision of each single group delay is about 10 mm and since many observations are collected over a long period of time (20 years or more) the estimate of the time dilation effect will be very accurate.

Geodetic VLBI has been used to test general relativity theory either in the frame of the Parameterized Post-Newtonian (PPN) formalism or the Standard-Model Extension (SME) (e.g., Robertson and Carter 1984, Shapiro et al. 2004, Lambert and Le Poncin-Lafitte 2009, or Le Poncin-Lafitte et al. 2016). However, it has not been considered for testing special relativity in spite of its interferometric nature directly

O. Titov
Geoscience Australia, Canberra, ACT, Australia
e-mail: Oleg.Titov@ga.gov.au

H. Krásná (✉)
Technische Universität Wien, Vienna, Austria

Astronomical Institute, Czech Academy of Sciences, Prague, Czech Republic
e-mail: hana.krasna@tuwien.ac.at

J. T. Freymueller, L. Sánchez (eds.), *International Symposium on Advancing Geodesy in a Changing World*,
International Association of Geodesy Symposia 149, https://doi.org/10.1007/1345_2018_48

linked to the Michelson-Morley and Kennedy-Thorndike interferometers yet. In this paper we show a possible application of the geodetic VLBI to this experimental work.

The conventional group delay τ_g model to approximate the observed VLBI data is given by Petit and Luzum (2010, chap. 11) as

$$\tau_g = \frac{-\frac{(\boldsymbol{b}\cdot\boldsymbol{s})}{\mathrm{c}}\left(1-\frac{2GM}{\mathrm{c}^2R}-\frac{|\boldsymbol{V}|^2}{2\mathrm{c}^2}-\frac{(\boldsymbol{V}\cdot\boldsymbol{w}_2)}{\mathrm{c}^2}\right)-\frac{(\boldsymbol{b}\cdot\boldsymbol{V})}{\mathrm{c}^2}\left(1+\frac{(\boldsymbol{s}\cdot\boldsymbol{V})}{2\mathrm{c}}\right)}{1+\frac{\boldsymbol{s}\cdot(\boldsymbol{V}+\boldsymbol{w}_2)}{\mathrm{c}}} \tag{1}$$

where $\boldsymbol{b}$ is the vector of baseline $\boldsymbol{b} = \boldsymbol{r_2} - \boldsymbol{r_1}$, $\boldsymbol{s}$ is the barycentric unit vector of radio source, $\boldsymbol{V}$ is the barycentric velocity of the geocentre, $\boldsymbol{w}_2$ is the geocentric velocity of the second station, c is the speed of light, G is the gravitational constant, M is the mass of the Sun, and R is the geocentric distance to the Sun.

The term $\frac{2GM}{\mathrm{c}^2R}$ is related to the general relativity effect and we won't focus on it in this note. The impact of $\boldsymbol{w}_2$ is small and may be ignored for the sake of simplicity. After these alterations, Eq. (1) is given by

$$\tau_g = \frac{-\frac{(\boldsymbol{b}\cdot\boldsymbol{s})}{\mathrm{c}}\left(1-\frac{|\boldsymbol{V}|^2}{2\mathrm{c}^2}\right)-\frac{1}{\mathrm{c}^2}(\boldsymbol{b}\cdot\boldsymbol{V})\left(1+\frac{(\boldsymbol{s}\cdot\boldsymbol{V})}{2\mathrm{c}}\right)}{1+\frac{1}{\mathrm{c}}(\boldsymbol{s}\cdot\boldsymbol{V})}. \tag{2}$$

Using the Taylor series expansion $(1+x)^{-1} = 1-x+x^2$ for $\left(1+\frac{(\boldsymbol{s}\cdot\boldsymbol{V})}{\mathrm{c}}\right)^{-1}$ and noting the $\frac{|\boldsymbol{V}|^2}{\mathrm{c}^2}$ terms only, Eq. (2) reduces to

$$\begin{aligned}
\tau_g =& \frac{(\boldsymbol{b}\cdot\boldsymbol{s})}{\mathrm{c}}\frac{|\boldsymbol{V}|^2}{2\mathrm{c}^2}-\frac{1}{\mathrm{c}^2}(\boldsymbol{b}\cdot\boldsymbol{V})\frac{(\boldsymbol{s}\cdot\boldsymbol{V})}{2\mathrm{c}}- \\
&-\frac{(\boldsymbol{b}\cdot\boldsymbol{s})(\boldsymbol{s}\cdot\boldsymbol{V})^2}{\mathrm{c}^3}+\frac{1}{\mathrm{c}^2}(\boldsymbol{b}\cdot\boldsymbol{V})\frac{(\boldsymbol{s}\cdot\boldsymbol{V})}{\mathrm{c}}= \\
=&\frac{(\boldsymbol{b}\cdot\boldsymbol{s})|\boldsymbol{V}|^2}{2\mathrm{c}^3}-\frac{(\boldsymbol{b}\cdot\boldsymbol{s})(\boldsymbol{s}\cdot\boldsymbol{V})^2}{2\mathrm{c}^3} \\
&-\frac{(\boldsymbol{b}\cdot\boldsymbol{V})(\boldsymbol{s}\cdot\boldsymbol{V})}{2\mathrm{c}^3}+\frac{(\boldsymbol{b}\cdot\boldsymbol{V})(\boldsymbol{s}\cdot\boldsymbol{V})}{\mathrm{c}^3}-\frac{(\boldsymbol{b}\cdot\boldsymbol{s})(\boldsymbol{s}\cdot\boldsymbol{V})^2}{2\mathrm{c}^3}= \\
=&\frac{(\boldsymbol{b}\cdot\boldsymbol{s})\left(|\boldsymbol{V}|^2-(\boldsymbol{s}\cdot\boldsymbol{V})^2\right)}{2\mathrm{c}^3}+\frac{(\boldsymbol{s}\cdot\boldsymbol{V})\left((\boldsymbol{b}\cdot\boldsymbol{V})-(\boldsymbol{b}\cdot\boldsymbol{s})(\boldsymbol{s}\cdot\boldsymbol{V})\right)}{2\mathrm{c}^3}.
\end{aligned} \tag{3}$$

In Fig. 1 we introduce the following angles $|\boldsymbol{V}|\cos\theta = (\boldsymbol{s}\cdot\boldsymbol{V})$, $|\boldsymbol{b}|\cos\varphi = (\boldsymbol{b}\cdot\boldsymbol{s})$ and $|\boldsymbol{b}||\boldsymbol{V}|\cos\psi = (\boldsymbol{b}\cdot\boldsymbol{V})$, and from the equation of spherical trigonometry we get $\cos\psi = \cos\theta\cos\varphi + \sin\theta\sin\varphi\cos A$. After applying the substitution

$$\begin{aligned}
(\boldsymbol{b}\cdot\boldsymbol{s})\left(|\boldsymbol{V}|^2-(\boldsymbol{s}\cdot\boldsymbol{V})^2\right) =& |\boldsymbol{b}|\cos\varphi\left(|\boldsymbol{V}|^2-|\boldsymbol{V}|^2\cos^2\theta\right)= \\
=&|\boldsymbol{b}||\boldsymbol{V}|^2\cos\varphi\sin^2\theta
\end{aligned} \tag{4}$$

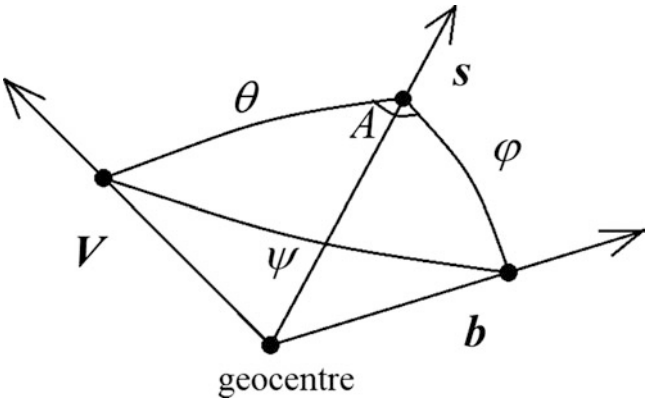

Fig. 1 Schematic view of the introduced angles with vectors placed in the geocentre

and

$$\begin{aligned}
&(\boldsymbol{s}\cdot\boldsymbol{V})\left((\boldsymbol{b}\cdot\boldsymbol{V})-(\boldsymbol{b}\cdot\boldsymbol{s})(\boldsymbol{s}\cdot\boldsymbol{V})\right)= \\
&=|\boldsymbol{V}|\cos\theta\left(|\boldsymbol{b}||\boldsymbol{V}|\cos\psi-(|\boldsymbol{b}|\cos\varphi)(|\boldsymbol{V}|\cos\theta)\right)= \\
&=|\boldsymbol{b}||\boldsymbol{V}|^2\cos\theta\left(\cos\theta\cos\varphi+\sin\theta\sin\varphi\cos A-\cos\theta\cos\varphi\right)
\end{aligned} \tag{5}$$

we get Eq. (3) in the following form

$$\tau_g = \frac{|\boldsymbol{b}||\boldsymbol{V}|^2}{2\mathrm{c}^3}\cos\varphi\sin^2\theta+\frac{|\boldsymbol{b}||\boldsymbol{V}|^2}{2\mathrm{c}^3}\sin\varphi\sin\theta\cos\theta\cos A. \tag{6}$$

The major term of the geometric delay is

$$\tau_g = -\frac{(\boldsymbol{b}\cdot\boldsymbol{s})}{\mathrm{c}} = -\frac{|\boldsymbol{b}|\cos\varphi}{\mathrm{c}}. \tag{7}$$

The components of the baseline vector $\boldsymbol{b}$ and the source position vector $\boldsymbol{s}$ can be estimated from a large set of data within an adjustment. The observational delay from a correlator is approximated by the theoretical delay (Eq. (1)), and the difference between the observational and the theoretical delay is modelled as follows:

$$\tau_{obs}-\tau_{calc} = \frac{\partial\tau}{\partial b}\Delta b+\frac{\partial\tau}{\partial s}\Delta s \tag{8}$$

or, by applying Eq. (7) one gets

$$\tau_{obs}-\tau_{calc} = -\Delta b\frac{1}{\mathrm{c}}\cos\varphi+\Delta s\frac{|\boldsymbol{b}|}{\mathrm{c}}\sin\varphi \tag{9}$$

which means that the corrections to the baseline vector components are calculated with the partials proportional to $\cos\varphi$ and corrections to the source vector components

need partials proportional to $\sin\varphi$. Therefore, the first part of Eq. (6) is a variation of the baseline vector (i.e., of the Earth scale) as it is proportional to the factor $(|\boldsymbol{b}|\cos\varphi)$, and the second part is a variation of the source positions $(|\boldsymbol{b}|\sin\varphi)$.

2 Lorenz Transformation

There are many approaches to generalise the standard Lorenz transformation. The first known is the Robertson-Mansouri-Sexl (RMS) formalism (Robertson 1949; Mansouri and Sexl 1977a,b) that assumes a possibility of anisotropic speed of light, i.e., tantamount of a preferred reference frame existing. For the sake of simplicity, we develop a new functional form of three functions $A(V), B(V)$, and $D(V)$ instead of the original RMS formalism.

Let's consider the Lorenz transformation in a general form between the preferred reference frame $S(\boldsymbol{x}, t)$ and another reference frame $S'(\boldsymbol{x'}, t')$ moving with a relative velocity $\boldsymbol{V}$

$$\begin{aligned} \boldsymbol{x'} &= D\boldsymbol{x} - (D-B)\frac{(\boldsymbol{Vx})\boldsymbol{V}}{|\boldsymbol{V}|^2} - B\boldsymbol{V}t \\ t' &= A\left(t - \frac{\boldsymbol{V}}{\mathrm{c}^2}\boldsymbol{x}\right). \end{aligned} \tag{10}$$

Here, we adopt the Einstein synchronisation here. In special relativity $A(V) = B(V) = \left(\sqrt{1-\frac{|\boldsymbol{V}|^2}{\mathrm{c}^2}}\right)^{-1} = \gamma$ and $D(V) = 1$. This form of generalisation is similar to those proposed by Will (1992) with some alterations.

The velocity transformation between frames S' and S may be derived from Eq. (10) as $\boldsymbol{v'_x} = \frac{\boldsymbol{dx'}}{dt'}$ and $\boldsymbol{v_x} = \frac{\boldsymbol{dx}}{dt}$

$$\begin{aligned} \boldsymbol{dx'} &= D\boldsymbol{dx} - (D-B)\frac{(\boldsymbol{V}\,\boldsymbol{dx})\boldsymbol{V}}{|\boldsymbol{V}|^2} - B\boldsymbol{V}\,dt \\ dt' &= A\left(dt - \frac{\boldsymbol{V}}{\mathrm{c}^2}\boldsymbol{dx}\right) \end{aligned} \tag{11}$$

$$\begin{aligned} \boldsymbol{v'_x} &= \frac{\boldsymbol{dx'}}{dt'} = \frac{D\frac{\boldsymbol{dx}}{dt} - (D-B)\frac{\left(\boldsymbol{V}\frac{\boldsymbol{dx}}{dt}\right)\boldsymbol{V}}{|\boldsymbol{V}|^2} - B\boldsymbol{V}}{A\left(1 - \frac{\boldsymbol{V}\frac{\boldsymbol{dx}}{dt}}{\mathrm{c}^2}\right)} \\ &= \frac{D\boldsymbol{v_x} - (D-B)\frac{(\boldsymbol{V}\boldsymbol{v_x})\boldsymbol{V}}{|\boldsymbol{V}|^2} - B\boldsymbol{V}}{A\left(1 - \frac{\boldsymbol{V}\boldsymbol{v_x}}{\mathrm{c}^2}\right)}. \end{aligned} \tag{12}$$

For the propagation of light from an extragalactic radio source one has to assign the unit vector in the direction of the source apparent position (moving system S') as $\boldsymbol{s'} = -\frac{\boldsymbol{v'_x}}{\mathrm{c}}$, and in the preferred reference frame as $\boldsymbol{s} = -\frac{\boldsymbol{v_x}}{\mathrm{c}}$. Therefore, the transformation between $\boldsymbol{s'}$ and $\boldsymbol{s}$ is given by

$$\boldsymbol{s'} = \frac{D\boldsymbol{s} - (D-B)\frac{(\boldsymbol{Vs})\boldsymbol{V}}{|\boldsymbol{V}|^2} + \frac{B\boldsymbol{V}}{\mathrm{c}}}{A\left(1 + \frac{(\boldsymbol{Vs})}{\mathrm{c}}\right)}. \tag{13}$$

Now we apply the traditional expansion (Mansouri and Sexl 1977a; Will 1992):

$$\begin{aligned} A(V) &= 1 + \alpha\frac{|\boldsymbol{V}|^2}{\mathrm{c}^2} + \ldots \\ B(V) &= 1 + \beta\frac{|\boldsymbol{V}|^2}{\mathrm{c}^2} + \ldots \\ D(V) &= 1 + \delta\frac{|\boldsymbol{V}|^2}{\mathrm{c}^2} + \ldots \end{aligned} \tag{14}$$

to Eq. (13) which gives

$$\boldsymbol{s'} = \frac{\left(1 + \delta\frac{|\boldsymbol{V}|^2}{\mathrm{c}^2}\right)\boldsymbol{s} + \left(\beta - \delta\right)\frac{(\boldsymbol{Vs})\boldsymbol{V}}{\mathrm{c}^2} + \left(1 + \beta\frac{|\boldsymbol{V}|^2}{\mathrm{c}^2}\right)\frac{\boldsymbol{V}}{\mathrm{c}}}{\left(1 + \alpha\frac{|\boldsymbol{V}|^2}{\mathrm{c}^2}\right)\left(1 + \frac{(\boldsymbol{Vs})}{\mathrm{c}}\right)}. \tag{15}$$

With the help of the Taylor series expansion $(1+x)^{-1} = 1 - x + x^2$ and keeping the terms to $\frac{V^2}{\mathrm{c}^2}$ only, we obtain from Eq. (15)

$$\begin{aligned} \boldsymbol{s'} &= \boldsymbol{s} + \frac{\boldsymbol{V} - \boldsymbol{s}(\boldsymbol{Vs})}{\mathrm{c}} + \frac{\boldsymbol{s}\left(|\boldsymbol{V}|^2(\delta-\alpha) + (\boldsymbol{Vs})^2\right)}{\mathrm{c}^2} \\ &\quad + \frac{(\beta - \delta - 1)\boldsymbol{V}(\boldsymbol{Vs})}{\mathrm{c}^2}. \end{aligned} \tag{16}$$

The second term $\sim \frac{V}{\mathrm{c}}$ represents the annual aberration. The third term (proportional to the vector $\boldsymbol{s}$ only) does not affect the apparent position of the celestial objects. It could be ignored by the traditional observational astrometric techniques but it is essential for the geodetic VLBI. Finally, the last term in Eq. (16) describes the second order correction $(\sim \frac{|\boldsymbol{V}|^2}{\mathrm{c}^2})$ in the radio source positions.

Now we convert Eq. (16) to the geometric delay τ

$$\begin{aligned} \tau &= -\frac{(\boldsymbol{b}(\boldsymbol{s'} - \boldsymbol{s}))}{\mathrm{c}} = -\frac{(\boldsymbol{bV}) - (\boldsymbol{bs})(\boldsymbol{Vs})}{\mathrm{c}^2} \\ &\quad - \frac{(\boldsymbol{bs})(|\boldsymbol{V}|^2(\delta-\alpha) + (\boldsymbol{Vs})^2)}{\mathrm{c}^3} - \frac{(\beta - \delta - 1)(\boldsymbol{bV})(\boldsymbol{Vs})}{\mathrm{c}^3}. \end{aligned} \tag{17}$$

Since in special relativity $\alpha = \frac{1}{2}, \beta = \frac{1}{2}$ and $\delta = 0$, Eq. (17) may be presented as

$$\begin{aligned}\tau =& -\frac{(\boldsymbol{b}(\boldsymbol{s}'-\boldsymbol{s}))}{\mathrm{c}} = -\frac{(\boldsymbol{bV})-(\boldsymbol{bs})(\boldsymbol{Vs})}{\mathrm{c}^2} \\ &- \frac{(\boldsymbol{bs})\Big(-\frac{1}{2}|\boldsymbol{V}|^2+(\boldsymbol{Vs})^2\Big)}{\mathrm{c}^3} + \frac{(\boldsymbol{bV})(\boldsymbol{Vs})}{2\mathrm{c}^3} \\ =& -\frac{(\boldsymbol{bV})-(\boldsymbol{bs})(\boldsymbol{Vs})}{\mathrm{c}^2} + \frac{(\boldsymbol{bs})\Big(|\boldsymbol{V}|^2-(\boldsymbol{Vs})^2\Big)}{2\mathrm{c}^3} \\ &+ \frac{(\boldsymbol{bV})(\boldsymbol{Vs})}{2\mathrm{c}^3} - \frac{(\boldsymbol{bs})(\boldsymbol{Vs})^2}{2\mathrm{c}^3}\end{aligned} \tag{18}$$

where the terms $\sim \frac{|\boldsymbol{V}|^2}{\mathrm{c}^2}$ coincide to Eq. (3).

It is essential to note that the sum of the two last terms in Eq. (17)

$$\begin{aligned}\Delta\tau =& \frac{(\boldsymbol{bs})|\boldsymbol{V}|^2(\alpha-\delta)}{\mathrm{c}^3} - \frac{(\boldsymbol{bs})+(\boldsymbol{Vs})^2}{\mathrm{c}^3} - \frac{(\beta-\delta-1)(\boldsymbol{bV})(\boldsymbol{Vs})}{\mathrm{c}^3} \\ =& \frac{|\boldsymbol{b}||\boldsymbol{V}|^2(\alpha-\delta)}{\mathrm{c}^3}\cos\varphi - \frac{|\boldsymbol{b}||\boldsymbol{V}|^2}{\mathrm{c}^3}\cos\varphi\cos^2\theta \\ &- \frac{|\boldsymbol{b}||\boldsymbol{V}|^2(\beta-\delta-1)}{\mathrm{c}^3}(\cos\varphi\cos^2\theta - \sin\theta\cos\theta\sin\varphi\cos A) \\ =& \frac{|\boldsymbol{b}||\boldsymbol{V}|^2(\alpha-\delta)}{\mathrm{c}^3}\cos\varphi - \frac{|\boldsymbol{b}||\boldsymbol{V}|^2(\beta-\delta)}{\mathrm{c}^3}\cos\varphi\cos^2\theta \\ &+ \frac{|\boldsymbol{b}||\boldsymbol{V}|^2(\beta-\delta-1)}{\mathrm{c}^3}\sin\theta\cos\theta\sin\varphi\cos A \\ =& \frac{|\boldsymbol{b}||\boldsymbol{V}|^2(\alpha-\beta)}{\mathrm{c}^3}\cos\varphi + \frac{|\boldsymbol{b}||\boldsymbol{V}|^2(\beta-\delta)}{\mathrm{c}^3}\cos\varphi\sin^2\theta \\ &+ \frac{|\boldsymbol{b}||\boldsymbol{V}|^2(\beta-\delta-1)}{\mathrm{c}^3}\sin\theta\cos\theta\sin\varphi\cos A\end{aligned} \tag{19}$$

manifests itself as a combination of the Kennedy-Thorndike experiment testing the factor $(\alpha-\beta+1)$ and the Michelson-Morley experiment testing the factor $(\beta+\delta-\frac{1}{2})$ (Michelson and Morley 1887; Kennedy and Thorndike 1932; Mansouri and Sexl 1977b). In special relativity, the factors equal to $(\alpha-\beta)=0$ and $(\beta-\delta)=\frac{1}{2}$, therefore only the two last terms are included in Eq. (1) describing the group delay. The difference $(\beta-\delta)$ is tested twice, once with the geodetic parameters (second term in Eq. (19)), and another time with the apparent displacement of the extragalactic radio sources (third term in Eq. (19)). Thus, the second order aberration effect in the source positions is an alteration of the Michelson-Morley experiment, which was already noted in Klioner et al. (2012).

If $(\alpha-\beta)\neq 0$ in Eq. (19), the Earth scale factor estimated from geodetic VLBI data would differ from unity by the factor $\frac{|\boldsymbol{V}|^2(\alpha-\beta)}{\mathrm{c}^2}$. In this context, the discrepancy between the VLBI and the SLR (Satellite Laser Ranging) scale factor (1.37 ± 0.10 ppb), reported by Altamimi et al. (2016) for the International Terrestrial Reference Frame ITRF2014, may be interpreted as the violation of the local Lorenz invariance at the level of $(\alpha-\beta)\approx 0.14\pm0.01$. However, the modern laboratory Kennedy-Thorndike tests of the Lorenz invariance (e.g., Herrmann et al. 2009) rule this interpretation out.

All three terms in Eq. (19) can be presented in the form of Eq. (9), i.e., as a combination of estimated parameters and partial derivatives. Therefore, the corrections Δb and Δs are given by the following equations (note, that the angle A shows the difference of directions from the source to vectors $\boldsymbol{b}$ and $\boldsymbol{V}$, and therefore the function $\cos A$ is a part of the partial derivative):

$$\begin{aligned}\Delta b =& -\frac{|\boldsymbol{b}||\boldsymbol{V}|^2(\alpha-\beta)}{\mathrm{c}^2} - \frac{|\boldsymbol{b}||\boldsymbol{V}|^2(\beta-\delta)}{\mathrm{c}^2}\sin^2\theta \\ \Delta s =& \frac{|\boldsymbol{V}|^2(\beta-\delta-1)}{\mathrm{c}^2}\sin\theta\cos\theta.\end{aligned} \tag{20}$$

The barycentric velocity $\boldsymbol{V}$ is well-known from the high-precision Solar system ephemerids. Therefore, Eq. (20) is a standard part of the delay model, i.e., Eq. (1).

Let's apply Eq. (20) to a hypothetical preferred reference frame. In this preferred reference frame (e.g., Cosmic Microwave Background (CMB)) the direction of the velocity vector $\boldsymbol{V}$ is constant. Therefore, if $(\beta-\delta)\neq\frac{1}{2}$ the shift in source positions depends on the angle θ only, i.e., the systematic shift across the sky would show a quadrupole pattern.

If we define the vector $\boldsymbol{s}=(\cos\hat{\alpha}\cos\hat{\delta}, \sin\hat{\alpha}\cos\hat{\delta}, \sin\hat{\delta})$ where $\hat{\alpha}$ and $\hat{\delta}$ are the right ascension and declination of the source, respectively, and the vector $\boldsymbol{V}=(V_x, V_y, V_z)$, we can further reformulate Eq. (20) for Δs using the relationship $|\boldsymbol{V}|\cos\theta=(\boldsymbol{s}\cdot\boldsymbol{V})$, the spherical law of cosine for the angle θ, and the division of $\sin\theta$ in two equations which gives us the corresponding corrections to the source coordinates $\Delta\hat{\alpha}\cos\hat{\delta}$ and $\Delta\hat{\delta}$ as

$$\begin{aligned}\Delta\hat{\alpha}\cos\hat{\delta} =& \frac{(\beta-\delta-1)}{\mathrm{c}^2}\Big(\Big(V_y^2-V_x^2\Big)\cos\hat{\delta}\sin\hat{\alpha}\cos\hat{\alpha} \\ &+ V_xV_y\cos 2\hat{\alpha}\cos\hat{\delta} - V_xV_z\sin\hat{\alpha}\sin\hat{\delta} \\ &+ V_yV_z\cos\hat{\alpha}\sin\hat{\delta}\Big)\end{aligned} \tag{21}$$

and

$$\begin{aligned}\Delta\hat{\delta} =& \frac{(\beta-\delta-1)}{\mathrm{c}^2}\Big(-\frac{1}{2}V_x^2\sin 2\hat{\delta}\cos^2\hat{\alpha} - \frac{1}{2}V_y^2\sin 2\hat{\delta}\sin^2\hat{\alpha} \\ &+ \frac{1}{2}V_z^2\sin 2\hat{\delta} - \frac{1}{2}V_xV_y\sin 2\hat{\delta}\sin 2\hat{\alpha} \\ &+ V_xV_z\cos 2\hat{\delta}\cos\hat{\alpha} + V_yV_z\cos 2\hat{\delta}\sin\hat{\alpha}\Big).\end{aligned} \tag{22}$$

A similar equation is developed for the scale factor from the Δb in Eq. (20) using the formula $\sin^2\theta = 1 - \cos^2\theta$ in addition:

$$\begin{aligned}\Delta b = &- \frac{|\boldsymbol{b}||\boldsymbol{V}|^2(\alpha-\beta)}{\mathrm{c}^2} - \frac{|\boldsymbol{b}|(\beta-\delta)}{\mathrm{c}^2} \\ &\Bigg(- V_x^2\cos^2\hat{\alpha}\cos^2\hat{\delta} - V_y^2\sin^2\hat{\alpha}\cos^2\hat{\delta} \\ &- V_z^2\sin^2\hat{\delta} - V_xV_y\cos^2\hat{\delta}\sin 2\hat{\alpha} \\ &- \frac{1}{2}V_xV_z\cos\hat{\alpha}\sin 2\hat{\delta} - \frac{1}{2}V_yV_z\sin\hat{\alpha}\sin 2\hat{\delta}\Bigg)\end{aligned} \tag{23}$$

which means that the scale factor magnitude depends on the equatorial coordinates of the observed radio sources.

3 Methodology Comments

Additional consideration of the special relativity in the geodetic VLBI may be developed in a form of an arbitrary synchronization of clock instead of the Einstein synchronization adopted in Eq. (10) or equivalent to the introduction of the preferred reference frame as in Klioner et al. (2012).

Any non-Einstein synchronisation comes down to replacement of the velocity $\boldsymbol{V}$ in the second equation of Eq. (10) by a function $\varepsilon(\boldsymbol{V}) \neq \boldsymbol{V}$. In this sense, the geodetic velocity of the second station $\boldsymbol{w}_2$, so far ignored throughout this paper, could be explicitly introduced to modify the equation for the time transformation in Eq. (10) as follows:

$$t' = A\left(t - \frac{\boldsymbol{V}+\boldsymbol{w}_2}{\mathrm{c}^2}\boldsymbol{x}\right). \tag{24}$$

This modification immediately results in the appearance of additional terms in equation of the relativistic time delay:

$$\Delta\tau_g = -\frac{(\boldsymbol{b}\cdot\boldsymbol{s})}{\mathrm{c}}\cdot\frac{(\boldsymbol{w}_2\cdot\boldsymbol{s})}{\mathrm{c}} \tag{25}$$

as a part of Eq. (1) and in addition to Eq. (2). This correction changes the VLBI scale factor only and it is not relevant to astrometric positions of reference radio sources, therefore, it is not part of the final equation by Klioner et al. (2012). Further analysis of this term is essential because it lies besides the traditional discussion on the clock synchronization (see, for example, discussion by Cole 1976).

Therefore, there is no need in the introduction of the preferred reference frame explicitly in the VLBI relativistic group delay equation. The barycentric and geocentric celestial reference systems (BCRS and GCRS) are fully sufficient to test the Lorentz invariance. The fact of the matter is that GCRS is moving with respect to BCRS along with the Earth. Therefore, direction of the relative velocity of GCRS with respect to BCRS changes as time progresses. This effectively introduces a set of different inertial reference frames along the Earth's orbit. So, introduction of BCRS and GCRS does not mean that we deal with only two frames. Instead of that an infinite number of the inertial frames along the Earth's orbit are introduced. Therefore, tracking the consistency of VLBI time-delay residuals over one orbital revolution allows to compare VLBI observations conducted at different time of year from different locations of GCRS moving in various directions and, thus, to test Lorentz invariance.

4 Conclusions

We can conclude that a variety of opportunities is allowed by the geodetic VLBI technique to test the Lorenz invariance in a frame of the kinematic RMS formalism. However, precision of the ground based VLBI measurements is not competitive to the laboratory experiments. While the geodetic VLBI is able to reach an accuracy of the estimation of the α, β and δ parameters at the level of $\sim 10^{-2}$ using the barycentric velocity of the Earth in approximation (Smoot et al. 1977), the laboratory tests set bounds on the anisotropy of the speed of light to $\sim 10^{-12}$ with the Michelson-Morley experiments (Herrmann et al. 2009) and to $\sim 10^{-8}$ with the Kennedy-Thorndike experiments (Tobar et al. 2010) using the velocity of the Sun with respect to the CMB which is about $\sim$370 km/s (Smoot et al. 1977). Theoretically, space VLBI observations within, e.g., the RadioAstron mission at baselines $\sim$50 times longer than the Earth radius reduced to the CMB reference frame (as proposed by Klioner et al. 2012) may provide an accuracy of $\sim 10^{-6}$ for the α, β and δ parameter combinations.

Acknowledgements The authors thank the anonymous reviewers for their suggestions and comments which helped to improve the manuscript significantly. We acknowledge the IVS and all its components for providing VLBI data (Nothnagel et al. 2015). Hana Krásná works within the Hertha Firnberg position T697-N29, funded by the Austrian Science Fund (FWF). This paper has been published with the permission of the Geoscience Australia CEO.

References

Altamimi Z, Rebischung P, Métivier L, Collilieux X (2016) ITRF2014: a new release of the international terrestrial reference frame modeling nonlinear station motions. J Geophys Res Solid Earth 121:6109–6131. https://doi.org/10.1002/2016JB013098

Cole TW (1976) Astronomical tests for the presence of an ether. Mon Not R Astron Soc 175(1):93P–96P. https://doi.org/10.1093/mnras/175.1.93P

Herrmann S, Senger A, Möhle K, Nagel M, Kovalchuk EV, Peters A (2009) Rotating optical cavity experiment testing lorentz invariance at the 10^{-17} level. Phys Rev D 80:105,011. https://doi.org/10.1103/PhysRevD.80.105011

Kennedy RJ, Thorndike EM (1932) Experimental establishment of the relativity of time. Phys Rev 42:400–418. https://doi.org/10.1103/PhysRev.42.400

Klioner S, Zschocke S, Soffel M, Butkevich A (2012) Testing local Lorentz invariance with high-accuracy astrometric observations. In: The twelfth Marcel Grossmann meeting, pp 1478–1480. https://doi.org/10.1142/9789814374552_0251

Lambert SB, Le Poncin-Lafitte C (2009) Determining the relativistic parameter gamma using very long baseline interferometry. Astron Astrophys 499(1):331–335. https://doi.org/10.1051/0004-6361/200911714

Le Poncin-Lafitte C, Hees A, Lambert S (2016) Lorentz symmetry and very long baseline interferometry. Phys Rev D 94:125,030. https://doi.org/10.1103/PhysRevD.94.125030

Mansouri R, Sexl R (1977a) A test theory of special relativity: I. Simultaneity and clock synchronization. Gen Relativ Gravit 8(7):497–513. https://doi.org/10.1007/BF00762634

Mansouri R, Sexl R (1977b) A test theory of special relativity: III. Second-order tests. Gen Relativ Gravit 8(10):809–814. https://doi.org/10.1007/BF00759585

Michelson A, Morley E (1887) On the relative motion of the earth and the luminiferous ether. Am J Sci 34(203):333–345. https://doi.org/10.2475/ajs.s3-34.203.333

Nothnagel A, Alef W, Amagai J, Andersen PH, Andreeva T, Artz T, Bachmann S, Barache C, Baudry A, Bauernfeind E et al (2015) The IVS data input to ITRF2014. GFZ Data Services, Helmoltz Centre, Potsdam, Germany. https://doi.org/10.5880/GFZ.1.1.2015.002

Petit G, Luzum B (2010) IERS Conventions 2010. IERS Technical Note No. 36

Robertson H (1949) Postulate versus observation in the special theory of relativity. Rev Mod Phys 21:378–382. https://doi.org/10.1103/RevModPhys.21.378

Robertson DS, Carter WE (1984) Relativistic deflection of radio signals in the solar gravitational field measured with VLBI. Nature 310:572–574. https://doi.org/10.1038/310572a0

Shapiro SS, Davis JL, Lebach DE, Gregory JS (2004) Measurement of the solar gravitational deflection of radio waves using geodetic very-long-baseline interferometry data, 1979–1999. Phys Rev Lett 92:121,101. https://doi.org/10.1103/PhysRevLett.92.121101

Smoot GF, Gorenstein MV, Muller RA (1977) Detection of anisotropy in the cosmic blackbody radiation. Phys Rev Lett 39:898–901. https://doi.org/10.1103/PhysRevLett.39.898

Tobar ME, Wolf P, Bize S, Santarelli G, Flambaum V (2010) Testing local lorentz and position invariance and variation of fundamental constants by searching the derivative of the comparison frequency between a cryogenic sapphire oscillator and hydrogen maser. Phys Rev D 81:022,003. https://doi.org/10.1103/PhysRevD.81.022003

Will CM (1992) Clock synchronization and isotropy of the one-way speed of light. Phys Rev D 45:403–411. https://doi.org/10.1103/PhysRevD.45.403

Development of Wideband Antennas

H. Ujihara, K. Takefuji, M. Sekido, and R. Ichikawa

Abstract

Wideband antennas for VLBI have been under development in NICT Kashima and the status of the project was reported in the poster session. An aim of this wideband observing system is Time and Frequency Transfer, the comparison of atomic clocks separated by long distances of several hundred or thousand kilometers with VLBI, as reported in "Broadband VLBI System GALA-V" by M. Sekido et al. This report focuses on our wideband antenna systems.

Keywords

VGOS · VLBI · Wideband

1 Introduction

Very long baseline interferometery, shortened as VLBI, is used for various scientific observations, such as astronomy with high angular resolution, geodesy and comparison of remote atomic clocks with high resolution of delay time in each station. The latter is known as Time and Frequency Transfer (TFT) and is our aim in developing this wideband VLBI system, that can avoid the need for very long optical fiber connections, or the cost of a two-way satellite transmission link for TFT. The sensitivity of a VLBI station pair in continuum observation with bandwidth of B and integration time T, is described by the SNR as in,

$$SNR \propto \sqrt{BT\frac{\eta_1 A_1 \eta_2 A_2}{Tsys_1 Tsys_2}} \tag{1}$$

$$\sigma_{\tau 12} \propto \frac{1}{SNR} \tag{2}$$

Here, A is the physical surface area of the antenna aperture. Aperture efficiency η of the large aperture reflector antenna is defined as the ratio of effective surface area to A, or simply, the ratio of measured gain to the calculated gain with ideal illumination. T_{sys} is the system noise temperature and σ_τ is the resolution of the delay time of received signals from a celestial radio source between the antenna pair. The integration time T is limited by the fluctuation of the atmosphere and instrumental instability, and T_{sys} is mainly associated to LNA noise. So wider bandwidth brings better sensitivity and is a more cost effective way than reducing T_{sys} or improving η, except for spectrum line observations in astronomy.

2 Development of the Wideband Antennas

In geodesy, VGOS/VLBI2010 typically uses a newly constructed 12 m dish and compact wideband feeds with a wide opening angle and beam width. Compactness of the feed efficiently reduces the computational resources required for simulation in development. However, such a feed cannot be used to simply upgrade a conventional large aperture

H. Ujihara (✉) · K. Takefuji · M. Sekido
National Institute of Information and Communications Technology (NICT), Hirai, Kashima, Japan
e-mail: ujihara@nict.go.jp

R. Ichikawa
NICT/Headquarter, Nukui-Kitamachi, Koganei, Japan

J. T. Freymueller, L. Sánchez (eds.), *International Symposium on Advancing Geodesy in a Changing World*,
International Association of Geodesy Symposia 149, https://doi.org/10.1007/1345_2018_41

radio telescope with Cassegrain optics. Our Kashima 34 m antenna of this type and, also unfortunately, our budget is not sufficient for the construction of a new VGOS antenna. So the first wideband feeds with narrow beam for the Cassegrain optics were developed to refurbish Kashima 34 m antenna. Also wideband Orthogonal Mode Transducer (OMT)s were newly developed for the feeds to be capable receiving two linear polarizations simultaneously. So now, Kashima 34 m antenna and its accompanying small portable VLBI stations named MARBLE are ready for wideband VLBI observations in the 3.2–14.4 GHz frequency range. These wideband feeds with bandwidth of 3.2–14.4 GHz were named as NINJA Feed and used for our VLBI TFT project, named Gala-V (Sekido et al. 2016; Kondo and Takefuji 2016). Also 6.5–15 GHz feeds were developed (named as IGUANA-H (Ujihara 2017)) and used only in the 34 m antenna for wideband geodetic observation, simultaneous observations of both the 6.7 GHz and 12.2 GHz methanol maser transitions without switching feeds for each band as in conventional way, and other various wideband radio astronomical observations.

2.1 Development of the Wideband Feeds

Developed wideband feeds for Gala-V are listed in Table 1. The IGUANA feeds are multimode horns and the NINJA feeds (shown in Fig. 1) are corrugated horns with lenses. Apparent radius, angular size of the sub-reflector from the focus of Kashima 34 m antenna is about 17° and the MARBLEs (Fig. 2) need a 26° beam. Beam width of NINJA feeds are adjustable for various optics in the 15–55° range through the arrangement of the structure. They were developed with a commercial 3D electric and magnetic field simulator, COMSOL. These feeds can receive both of two linear polarizations with wideband Orthogonal Mode Transducer (OMT) developed in same time. Measured return loss of the NINJA Feed with OMT is near or less than −10 dB typically.

2.2 Measurement of the Wideband Antennas

With NINJA feed, measured aperture efficiency of MARBLE 2 placed in NICT Koganei are shown in Fig. 3. This figure shows the typical band performance now, but efforts to increase the efficiency will be continued with a target of 50% or more. Radio Frequency Interference (RFI) is a serious problem for wideband observations. The lowest frequency of Gala-V was defined 3.2 GHz based on RFI surveys in advance. Strong RFI may cause increase of T_{sys} through intermodulation noise or saturation of the low noise amplifier. So, the cutoff frequency of the NINJA is designed around 3 GHz to avoid RFI from WLAN from near by houses or cellular phones. Radars or radio communication for satellites are not so strong to overcome the power of signals from celestial radio sources in the case of broadband VLBI observations, because they are well removed in the correlator if they are not so strong that they saturate the receiver or sampler. However, astronomers may require further reduction of RFI as they need to observe very weak sources. Thus, the necessity of filters depends on the site and aims of observations. MARBLE 1 at Tsukuba needs no filters. but MARBLE 2 at Koganei needs filter banks designed for Gala-V. Kashima 34 m antenna required a OMT with more sharp cutoff because of cellular phones.

Table 1 Developed wideband feeds

Name	Frequency	Year	Used in
IGUANA-H	6.5–15 GHz	2013-	34 m antenna (Kashima)
NINJA	3.2–14.4 GHz	2015-	34 m antenna (Kashima)
		2016-	MARBLE2 (Koganei)
		2017-	MARBLE1 (Tsukuba)

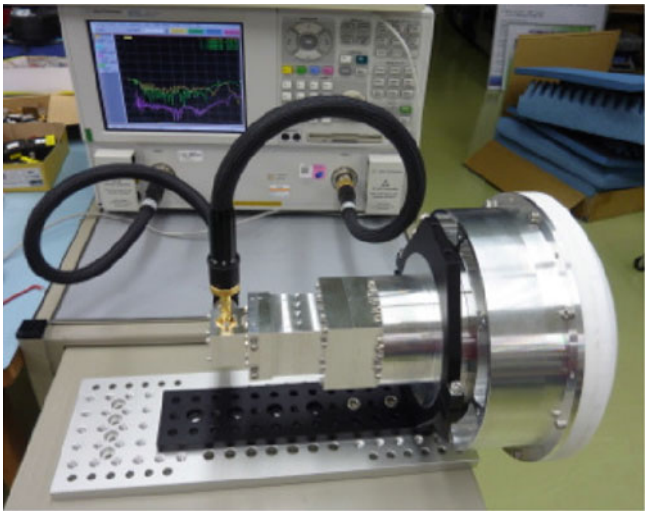

Fig. 1 A NINJA feed in measurement of return loss

3 Conclusions and Future Development Plan

Wideband feeds were newly developed for conventional Cassegrain antennas and we could successfully start our TFT project named Gala-V with them. Kashima 34 m antenna was refurbished as a wideband radio telescope. We are using these feeds for geodesy and astronomical observations. Efficiency of the wideband feeds is increasing and also the bandwidth of the feeds will be expanded. Wideband feeds on the 34 m antenna may have super-conductive filters for astronomical observations in the future.

Fig. 2 MARBLE with 2.4 m dish and the NINJA feed

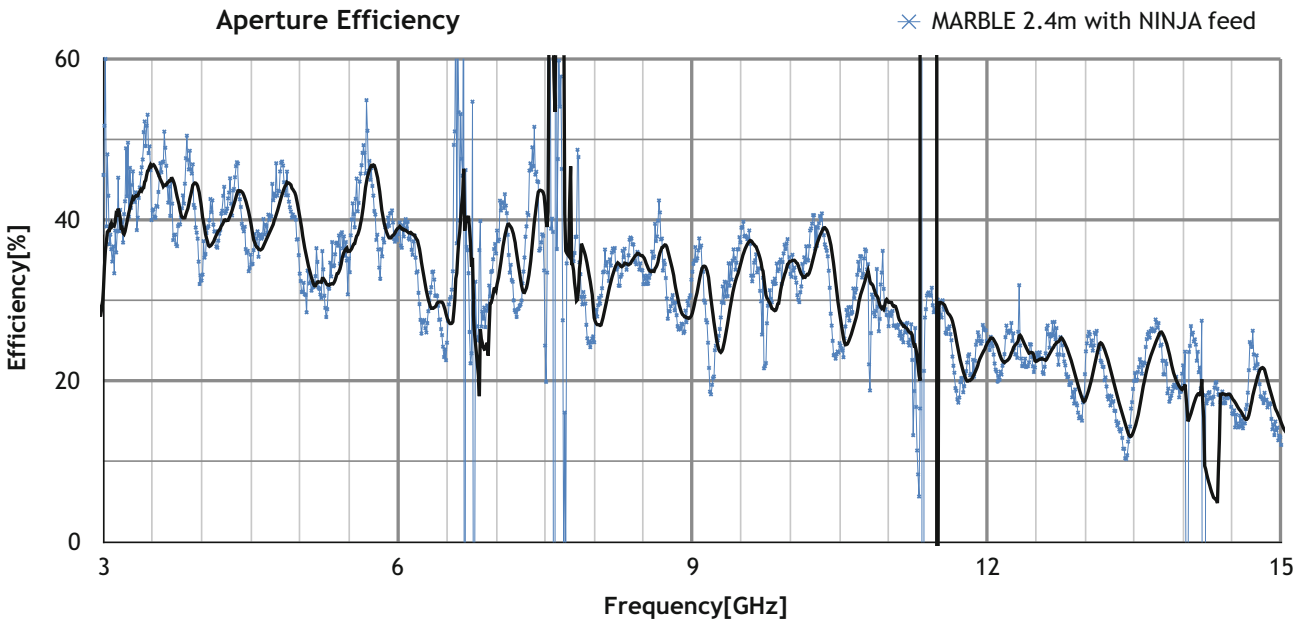

Fig. 3 Measured efficiency of MARBLE2 with NINJA feed

Acknowledgements Development of wideband feeds were supported by the grant of Joint Development Research of National Astronomical Observatory of Japan (NAOJ) in 2013–2014.

References

Kondo T, Takefuji K (2016) An algorithm of wideband bandwidth synthesis for geodetic VLBI. Radio Sci 51. https://doi.org/10.1002/2016RS006070

Sekido M et al (2016) An overview of the Japanese GALA-V wideband VLBI system. In: Behrend D, Baver KD, Armstrong KL (eds) IVS 2016 general meeting proceedings new horizons with VGOS NASA/CP-2016-219016, pp 25–33

Ujihara H (2017) Development of wideband feed for Kashima 34m antenna. Radio Sci 52. https://doi.org/10.1002/2016RS006071

Part II

Static Gravity Field

Boundary Complexity and Kernel Functions in Classical and Variational Concepts of Solving Geodetic Boundary Value Problems

Petr Holota and Otakar Nesvadba

Abstract

In gravity field studies the complex structure of the Earth's surface makes the solution of geodetic boundary value problems quite challenging. This equally concerns classical methods of potential theory as well as modern methods often based on a (variational or) weak solution concept. Aspects of this nature are reflected in the content of the paper. In case of a spherical Neumann problem the focus is on the classical Green's function method and on the use of reproducing kernel and elementary potentials in generating function bases for Galerkin's approximations. Similarly, the construction of Neumann's function – Green's function of the second kind and of entries in Galerkin's matrix for basis functions generated by the reproducing kernel and by elementary potentials is also highlighted when solving Neumann's problem in the exterior of an oblate ellipsoid of revolution. In this connection the role of elliptic integrals is pointed out. Finally, two concepts applied to the solution of the linear gravimetric boundary value problem are mentioned. They represent an approach based on variational methods and on the use of a transformation of coordinates offering an alternative between the boundary complexity and the complexity of the coefficients of the partial differential equation governing the solution. Successive approximations are involved in both the cases.

Keywords

Elliptic integrals · Galerkin's system · Green's function · Laplace's operator · Reproducing kernel · Transformation of coordinates

1 Introduction

The complexity of the Earth's surface gives great importance to the choice of mathematical apparatus suitable for solving geodetic boundary-value problems. Tools and techniques that can be used represent a rich mathematical equipment. Regarding its development, a broader view may be interesting. Efforts to have a closed form representation for the solution of mathematical problems, even in more complex cases, were always given considerable attention. Nevertheless, they have not led to full success. Various methods for finding a suitable approximate solution started to develop, especially finite difference methods, variational methods (weak solution concept) and boundary element methods, see e.g. Nečas (1967), Rektorys (1974) and Klees (1997).

Returning to geodetic boundary value problems, we can see that the solution often rests on a mathematical apparatus that actually was developed for a spherical boundary. On the one hand, this makes the way to the closed form representation of the solution simpler and has also an instructive value. In addition, the relation to the apparatus

P. Holota (✉)
Research Institute of Geodesy, Topography and Cartography, Prague-East, Czech Republic
e-mail: petr.holota@pecny.cz

O. Nesvadba
Land Survey Office, Prague 8, Czech Republic
e-mail: nesvadba@sky.cz

J. T. Freymueller, L. Sánchez (eds.), *International Symposium on Advancing Geodesy in a Changing World*, International Association of Geodesy Symposia 149, https://doi.org/10.1007/1345_2018_34

of spherical harmonics, which is often used in geodesy, is quite straightforward in this case. On the other hand, however, a sphere is rather far from the real shape of the Earth, which has a negative effect on any attempt to bridge the deviation of the Earth's surface from the sphere by means of an iteration procedure. We, therefore, tried to discuss the transition from the sphere to a more complicated boundary.

As an intermediate step we used an oblate ellipsoid of revolution. For the construction of the apparatus we apply ellipsoidal harmonics with the aim to follow an analogy to the role of spherical harmonics in the spherical case.

In this paper we follow the classical as well as the weak (variational) solution concept. Our aim is to focus on some of the main construction steps associated with the solution of Neumann's and the oblique derivative boundary value problem. Concerning the notation, x_i, i=1, 2, 3, mean rectangular Cartesian co-ordinates of the general point $\boldsymbol{x}=(x_1, x_2, x_3)$ in 3D Euclidean space $\boldsymbol{R}^3$ and $|\,\boldsymbol{x}\,| = \left(\sum_{i=1}^{3} x_i^2\right)^{1/2}$.

2 Spherical Boundary

In this section we suppose that the solution domain is given by the exterior S_R of a sphere of radius R. An assumption like this represents a suitable level for an initial presentation of the methods discussed. In the realm of the classical concept we definitely find the integral representation of the solution and the Green's function method, see e.g. Roach (1982). For instance Green's function of the second kind (or Neumann's function) $N(\boldsymbol{x},\boldsymbol{y})$ is associated with the problem to find u such that

$$\Delta u = g \quad \text{in} \quad S_R \tag{1}$$

and

$$\frac{\partial u}{\partial n} = -f \quad \text{on} \quad \partial S_R, \tag{2}$$

where Δ is Laplace's differential operator, ∂S_R is the boundary of S_R and $\partial/\partial n$ means the derivative in the direction of the unit (outer) normal $\boldsymbol{n}$ of ∂S_R. The function $N(\boldsymbol{x},\boldsymbol{y})$ enables to express the solution of the above exterior Neumann problem by means of the following integral formula

$$\begin{aligned} u(\boldsymbol{y}) \;=\; & \frac{1}{4\pi} \int\limits_{\boldsymbol{x}\in\partial S_R} N(\boldsymbol{x},\boldsymbol{y})\; f(\boldsymbol{x})\; d_x S \\ & - \frac{1}{4\pi} \int\limits_{\boldsymbol{x}\in S_R} N(\boldsymbol{x},\boldsymbol{y})\, g(\boldsymbol{x})\, d\boldsymbol{x}, \end{aligned} \tag{3}$$

where $d\boldsymbol{x}=dx_1dx_2dx_3$ represents the volume element and dS is the surface element of ∂S_R. In addition in the spherical case Neumann's function can be nicely expressed in a closed form. We have

$$\begin{aligned} N(\boldsymbol{x},\boldsymbol{y}) = & \frac{1}{|\,\boldsymbol{x}-\boldsymbol{y}\,|} + \frac{R}{|\,\boldsymbol{x}\,|}\frac{1}{|\,\overline{\boldsymbol{x}}-\boldsymbol{y}\,|} \\ & - \frac{1}{R}\ln\frac{|\,\overline{\boldsymbol{x}}-\boldsymbol{y}\,| + |\,\overline{\boldsymbol{x}}\,| - |\,\boldsymbol{y}\,|\cos\psi}{|\,\boldsymbol{y}\,|\,(1-\cos\psi)}, \end{aligned} \tag{4}$$

where

$$\overline{\boldsymbol{x}} = \frac{R^2}{|\boldsymbol{x}|^2}\boldsymbol{x} \quad \text{and} \quad |\,\boldsymbol{x}\,||\,\overline{\boldsymbol{x}}\,| = R^2 \tag{5}$$

and ψ is the angle between the position vectors $\boldsymbol{x}$ and $\boldsymbol{y}$, see Holota (2003, 2004).

In physical geodesy for g=0 in S_R the problem given by Eqs. (1) and (2) is often interpreted as an approximate formulation of the so-called linear (or linearized) gravimetric boundary value problem. Thus in gravity field studies it gives a way to the determination (though in spherical and constant radius approximation) of the disturbing potential T. For $|\,\boldsymbol{x}\,| = |\,\boldsymbol{y}\,| = \boldsymbol{R}$ the restriction of the kernel function $N(\boldsymbol{x},\boldsymbol{y})$ can be found, e.g., in Hotine (1969), Pick et al. (1973) and Hofmann-Wellenhof and Moritz (2005).

Of course, kernel functions have their position also in the weak solution concept applied to boundary value problems. A good example is the reproducing kernel. Its construction corresponds not only to the geometry of the solution domain, but also to the scalar product associated with the particular Hilbert space of functions used as the functional analytic background of the problem solved. Consider, e.g., the space $H_2^{(1)}(S_R)$ of functions harmonic in S_R that is equipped with the scalar product

$$(u,v)_1 = A(u,v),\, A(u,v) = \sum_{i=1}^{3} \int\limits_{S_R} \frac{\partial u}{\partial x_i}\frac{\partial v}{\partial x_i}\; d\boldsymbol{x}. \tag{6}$$

One can show that there exists a function $K(\boldsymbol{x},\boldsymbol{y})$ which is an element of $H_2^{(1)}(S_R)$ for every $\boldsymbol{x} \in S_R$ (or symmetrically every $\boldsymbol{y} \in S_R$) and such that

$$\sum_{i=1}^{3} \int\limits_{S_R} \frac{\partial K(\boldsymbol{x},\boldsymbol{y})}{\partial x_i}\; \frac{\partial v(\boldsymbol{x})}{\partial x_i}\; d\boldsymbol{x} = v(\boldsymbol{y}) \tag{7}$$

holds for all $v \in H_2^{(1)}(S_R)$.

In this case

$$K(\boldsymbol{x},\boldsymbol{y}) = \frac{1}{4\pi R}\sum_{n=0}^{\infty}\frac{2n+1}{n+1}z^{n+1}P_n(\cos\psi), \quad z = \frac{R^2}{|\boldsymbol{x}||\boldsymbol{y}|}, \tag{8}$$

where P_n is the usual Legendre's polynomial of degree n, see Holota (2004, 2011). Moreover, it is not extremely difficult to find that

$$K(\boldsymbol{x},\boldsymbol{y}) = \frac{1}{4\pi R}\left(\frac{2z}{L} - \ln\frac{L+z-\cos\psi}{1-\cos\psi}\right), \tag{9}$$

where

$$L = \sqrt{1-2z\cos\psi+z^2}, \tag{10}$$

cf. Tscherning (1975) and Neyman (1979).

The advantage of using the reproducing kernel $K(\boldsymbol{x},\boldsymbol{y})$ can be seen from the construction of Galerkin's approximations to the solution of Neumann's problem for functions harmonic in S_R. In the numerical solution the function u is approximated by the linear combinations

$$u_n = \sum_{j=1}^{n} c_j^{(n)} v_j, \tag{11}$$

where v_j are members of a function basis of $H_2^{(1)}(S_R)$ and the coefficients $c_j^{(n)}$ can be obtained from the respective Galerkin's system

$$\sum_{j=1}^{n} c_j^{(n)} A(v_j, v_k) = \int_{\partial S_R} v_k\, f\, dS, \; k = 1,\ldots,n. \tag{12}$$

Putting

$$v_j(\boldsymbol{x}) = K(\boldsymbol{x},\boldsymbol{y}_j), \tag{13}$$

we can immediately deduce that in our Galerkin system the elements $A(v_j, v_k)$ are given by

$$A(v_j, v_k) = K(\boldsymbol{y}_j,\boldsymbol{y}_k), \tag{14}$$

in view of the reproducing property of the kernel, see Holota (2011) and Holota and Nesvadba (2014).

Clearly, Eq. (14) confirms an exceptional role and advantages connected with the $K(\boldsymbol{x},\boldsymbol{y})$ function. Nevertheless, it is tempting to use also elementary potentials for constructing Galerkin's approximations. This means that the basis functions will be of the following form

$$v_j(\boldsymbol{x}) = \frac{1}{|\boldsymbol{x}-\boldsymbol{y}_j|} = \sum_{n=0}^{\infty}\frac{|\boldsymbol{y}_j|^n}{|\boldsymbol{x}|^{n+1}}P_n(\cos\psi_j) \tag{15}$$

with $\boldsymbol{y}_j \in \boldsymbol{R}^3 - S_R \cup \partial S_R$, i.e. outside the closure $\overline{\Omega}_R$ of the domain Ω_R, cf. e.g. Heiskanen and Moritz (1967). For Galerkin's elements we then obtain

$$A(v_j, v_k) = \frac{4\pi}{R}\sum_{n=0}^{\infty}\frac{n+1}{2n+1}q^n P_n(\cos\psi_{jk}), \quad \text{where} \quad q = \frac{|\boldsymbol{y}_j||\boldsymbol{y}_k|}{R^2}. \tag{16}$$

Concerning the diagonal elements, a standard integration yields

$$A(v_j, v_j) = \pi\left(\frac{2R}{R^2-|\boldsymbol{y}_j|^2} + \frac{1}{|\boldsymbol{y}_j|}\ln\frac{R+|\boldsymbol{y}_j|}{R-|\boldsymbol{y}_j|}\right), \tag{17}$$

see an analogue in Holota (1999, 2000). As to the off diagonal elements, the situation is a bit more complex. We get

$$A(v_j, v_k) = \frac{2\pi}{R}\left(\frac{1}{L}+S\right) \quad \text{with} \quad L = \sqrt{1-2q\cos\psi_{jk}+q^2} \tag{18}$$

and

$$S = \sum_{n=0}^{\infty}\frac{1}{2n+1}q^n P_n(\cos\psi_{jk}). \tag{19}$$

However, the problem is to find a closed expression for S. Following Holota and Nesvadba (2014), we can show that

$$S = \frac{1}{2}\left(\tan\frac{\varphi}{2}\right)^{-1}\mathcal{F}(k,\varphi), \quad \text{where} \quad \mathcal{F}(k,\varphi) = \int_0^{\varphi}\frac{d\varphi}{\sqrt{1-k^2\sin^2\varphi}}, \tag{20}$$

q is replaced by a new variable $\varphi \in \langle 0, \pi/2 \rangle$ according to

$$q = \tan^2\frac{\varphi}{2}, \quad k^2 = \cos^2\frac{\psi_{jk}}{2} \tag{21}$$

and $\mathcal{F}(k,\varphi)$ is the Legendre (incomplete) elliptic integral of the first kind expressed in a trigonometric form.

3 Transition to an Ellipsoid

The mathematical apparatus related to the exterior of the sphere is fairly developed and transparent. However, the sphere is rather far from the real surface of the Earth. Therefore, we mention now the construction of an apparatus applicable for the exterior Ω_{ell} of an oblate ellipsoid of revolution. We will suppose that a and b, $a \geq b$, are the semi-axes of the ellipsoid and will consider the ellipsoidal coordinates u, β, λ related to x_1, x_2, x_3 by the equations

$$x_1 = \sqrt{u^2 + E^2}\cos\beta\cos\lambda, \quad x_2 = \sqrt{u^2 + E^2}\cos\beta\sin\lambda,$$
$$x_3 = u\sin\beta, \tag{22}$$

where $E = \sqrt{a^2 - b^2}$ denotes the linear eccentricity. Clearly, the boundary $\partial\Omega_{ell}$ is then defined by $u{=}b$.

Taking $H_2^{(1)}(\Omega_{ell})$ as an analogue to $H_2^{(1)}(S_R)$ and going back to the notion of reproducing kernel, we instead of $K(\boldsymbol{x},\boldsymbol{y})$ will have $K_{ell}(\boldsymbol{x},\boldsymbol{y})$. According to Holota (2004, 2011) we can deduce that

$$K_{ell}(\boldsymbol{x},\boldsymbol{y}) = \tfrac{1}{4\pi b}\sum_{n=0}^{\infty}(2n+1)\left[K_{n0xy}\,P_n(\sin\beta_x)\,P_n(\sin\beta_y) + \right.$$
$$\left. + 2\sum_{m=1}^{n}\frac{(n-m)!}{(n+m)!}K_{nmxy}\,P_{nm}(\sin\beta_x)\,P_{nm}(\sin\beta_y)\cos m(\lambda_x{-}\lambda_y)\right] \tag{23}$$

with

$$K_{nmxy} = \frac{iEb}{a^2}\frac{Q_{nm}(z_x)}{Q_{nm}(z_0)}\frac{Q_{nm}(z_y)}{Q_{nm}(z_0)}\left[\frac{1}{Q_{nm}(z_0)}\frac{dQ_{nm}(z_0)}{dz}\right]^{-1}, \tag{24}$$

where P_{nm} and Q_{nm} are associated Legendre's functions of the first and the second kind, respectively; while

$$z_x = \frac{iu_x}{E}, \quad z_y = \frac{iu_y}{E}, \quad z_0 = \frac{ib}{E} \quad \text{and} \quad i = \sqrt{-1}. \tag{25}$$

Nevertheless, the problem is how to approach the summation of the series representing the reproducing kernel $K_{ell}(\boldsymbol{x},\boldsymbol{y})$. A possible way is to recall that

$$Q_{nm}(z) = (-1)^m\,\frac{2^n n!\,(n+m)!}{(2n+1)!}\,\left(z^2-1\right)^{-\frac{n+1}{2}}$$
$$\times F\left(\frac{n+m+1}{2}, \frac{n-m+1}{2}, \frac{2n+3}{2}; \frac{1}{1-z^2}\right), \tag{26}$$

where F is a hypergeometric function and to follow Holota and Nesvadba (2014). In this manner we can deduce that approximately (terms multiplied by the third and higher powers of the numerical eccentricity $e{=}E/a$ are neglected)

$$K_{ell}(\boldsymbol{x},\boldsymbol{y}) \approx \frac{1}{4\pi b}K^{(1)}(\boldsymbol{x},\boldsymbol{y}) - \frac{E^2}{4\pi ab^2}K^{(2)}(\boldsymbol{x},\boldsymbol{y}) + \frac{E^2}{4\pi ab^2}K^{(3)}(\boldsymbol{x},\boldsymbol{y}), \tag{27}$$

where

$$K^{(1)}(\boldsymbol{x},\boldsymbol{y}) = \sum_{n=0}^{\infty}\frac{2n+1}{n+1}\,\rho^{n+1}P_n(\cos\psi), \tag{28}$$

$$K^{(2)}(\boldsymbol{x},\boldsymbol{y}) = \sum_{n=0}^{\infty}\frac{2n+1}{2n+3}\,\rho^{n+1}P_n(\cos\psi), \tag{29}$$

$$K^{(3)}(\boldsymbol{x},\boldsymbol{y}) = -\sum_{n=1}^{\infty}\frac{2n+1}{(n+1)^2(2n+3)}\,\rho^{n+1}\frac{\partial^2 P_n(\cos\psi)}{\partial\lambda^2}, \tag{30}$$

λ means λ_x or λ_y (the choice has no effect on the result),

$$\rho = \frac{a^2}{\sqrt{u_x^2 + E^2}\sqrt{u_y^2 + E^2}} \tag{31}$$

and ψ denotes the angular distance of points (β_x, λ_x) and (β_y, λ_y) on a sphere, when β and λ are interpreted as spherical latitude and longitude, respectively. Note that in the derivations above an interpretation like this made it possible to apply the well-known Legendre's addition theorem.

Similarly, we now return to the function basis generated by elementary potentials with $\boldsymbol{y}_j \in \boldsymbol{R}^3 - \Omega_{ell} \cup \partial\Omega_{ell}$. In ellipsoidal coordinates, following Hobson (1931, Chap. X, §3), we have

$$v_j(\boldsymbol{x}) = \frac{i}{E}\sum_{n=0}^{\infty}(2n+1)\left[Q_n(z)P_n(z_j)\,P_n(\sin\beta)\,P_n(\sin\beta_j) + \right.$$
$$\left. + 2\sum_{m=1}^{n}(-1)^m\left(\frac{(n-m)!}{(n+m)!}\right)^2 Q_{nm}(z)P_{nm}(z_j)\,P_{nm}(\sin\beta) \times P_{nm}(\sin\beta_j)\cos m(\lambda-\lambda_j)\right], \tag{32}$$

where

$$z = \frac{iu}{E}, \quad z_j = \frac{iu_j}{E} \quad \text{and} \quad i = \sqrt{-1}. \tag{33}$$

We suppose that $u_j < u$, which guarantees the convergence and will focus on Galerkin's element $A(v_j, v_k)$, more

precisely on $A_{ell}(v_j, v_k)$. One can show that

$$A_{ell}\left(v_j, v_k\right) = \frac{4\pi b}{E^2} \sum_{n=0}^{\infty} (2n+1)\left[A_{n0jk} P_n\left(\sin\beta_j\right) P_n\left(\sin\beta_k\right) + \right. \\ + 2 \sum_{m=1}^{n} \left(\frac{(n-m)!}{(n+m)!}\right)^3 A_{nmjk}\ P_{nm}\left(\sin\beta_j\right) \\ \left. \times P_{nm}\left(\sin\beta_k\right) \cos m\left(\lambda_j - \lambda_k\right)\right], \tag{34}$$

where

$$A_{nmjk} = i\frac{a^2}{bE} Q_{nm}\left(z_0\right)\ \frac{dQ_{nm}\left(z_0\right)}{dz}\ P_{nm}\left(z_j\right)\ P_{nm}\left(z_k\right) \\ \text{and } z_0 = \frac{ib}{E}, \tag{35}$$

see Holota and Nesvadba (2017). Again, however, the problem is the summation of the series representing the element $A_{ell}(v_j, v_k)$. To solve this problem we apply the apparatus of hypergeometric functions and series for representing Legendre's functions P_{nm} and Q_{nm}. This enables to deduce that approximately

$$A_{nmjk} \approx \frac{E^2}{a^2}\ \frac{n+1}{(2n+1)^2}\ \left[\frac{(n+m)!}{(n-m)!}\right]^2 q^n \\ \times \left\{1 + \frac{E^2}{b^2}\ \left[\frac{2n^2+n-2}{(2n-1)(2n+3)} + \frac{m^2(2n+5)}{(n+1)(2n-1)(2n+3)}\right]\right\}, \tag{36}$$

where

$$q = \frac{\sqrt{1-z_j}\sqrt{1-z_k}}{1-z_0} = \frac{\sqrt{u_j^2+E^2}\sqrt{u_k^2+E^2}}{a^2} \tag{37}$$

and terms multiplied by the third and higher powers of the numerical eccentricity $e{=}E/a$ were neglected. Note that q is less or equal to one for points $\boldsymbol{y}_j$, $\boldsymbol{y}_k$ on and below the ellipsoid. Hence

$$A_{ell}\left(v_j, v_k\right) \approx \frac{4\pi b}{a^2} A^{(1)}\left(v_j, v_k\right) + \frac{4\pi E^2}{a^2 b} A^{(2)}\left(v_j, v_k\right) \\ + \frac{4\pi E^2}{a^2 b} A^{(3)}\left(v_j, v_k\right) \tag{38}$$

with

$$A^{(1)}\left(v_j, v_k\right) = \sum_{n=0}^{\infty} \frac{n+1}{2n+1} q^n P_n\left(\cos\psi\right), \tag{39}$$

$$A^{(2)}\left(v_j, v_k\right) = \sum_{n=0}^{\infty} \frac{n+1}{2n+1} \frac{2n^2+n-2}{(2n-1)(2n+3)} q^n\ P_n\left(\cos\psi\right), \tag{40}$$

$$A^{(3)}\left(v_j, v_k\right) = -\sum_{n=1}^{\infty} \frac{2n+5}{(2n-1)(2n+1)(2n+3)}\ q^n \\ \times \frac{\partial^2 P_n\left(\cos\psi\right)}{\partial\lambda^2}, \tag{41}$$

where λ means λ_j or λ_k and ψ denotes the angular distance of points (β_j, λ_j) and (β_k, λ_k) on a sphere, when β and λ are interpreted as spherical latitude and longitude, respectively, see Holota and Nesvadba (2017).

Of course, the integral formula (3) has its ellipsoidal analogue too. This means that in Eqs. (1), (2), (3) we substitute S_R and ∂S_R by Ω_{ell} and $\partial\Omega_{ell}$ and have to construct the respective Neumann's function for the domain Ω_{ell}. It is, however, worth mentioning that for Ω_{ell} given by the exterior of the ellipsoid of revolution the approach to the construction of Neumann's function N is not routine as yet in contrast to the spherical case and stimulates discussion. The question also is the closed form representation of N. All this is in full agreement, e.g., with a general observation in Roach (1970) concerning methods for constructing Green's functions (Neumann's function is Green's function of the second kind) in case of more complicated boundaries.

Basically we start with the elementary potential

$$J\left(\boldsymbol{x}, \boldsymbol{y}\right) = \frac{1}{|\ \boldsymbol{x} - \boldsymbol{y}\ |} \tag{42}$$

and construct a harmonic function H_N such that

$$\frac{\partial H_N}{\partial n_x} = \frac{\partial J}{\partial n_x}\ \text{ for }\ u_x = b. \tag{43}$$

Neumann's function N is then given by

$$N\left(\boldsymbol{x}, \boldsymbol{y}\right) = J\left(\boldsymbol{x}, \boldsymbol{y}\right) - H_N\left(\boldsymbol{x}, \boldsymbol{y}\right). \tag{44}$$

Nevertheless, in practical evaluation of the function N it is of advantage to take into play also Green's function of the first kind, here denoted by G and to use the general relation between the kernel functions N, G and K_{ell}, i.e.

$$N\left(\boldsymbol{x}, \boldsymbol{y}\right) = G\left(\boldsymbol{x}, \boldsymbol{y}\right) + 4\pi K_{ell}\left(\boldsymbol{x}, \boldsymbol{y}\right), \tag{45}$$

see Garabedian (1964) or also Holota (2004). Green's function G is given by

$$G\left(\boldsymbol{x}, \boldsymbol{y}\right) = J\left(\boldsymbol{x}, \boldsymbol{y}\right) - H_G\left(\boldsymbol{x}, \boldsymbol{y}\right), \tag{46}$$

but the harmonic function H_G meets Dirichlet's boundary condition

$$H_G = J \quad \text{for} \quad u_x = b. \tag{47}$$

Passing now to ellipsoidal harmonics we have

$$J(\boldsymbol{x},\boldsymbol{y}) = \frac{i}{E}\sum_{n=0}^{\infty}(2n+1)\left[P_n(z_x)\,Q_n(z_y)\,P_n(\sin\beta_x)\,P_n(\sin\beta_y) + \right.$$
$$+2\sum_{m=1}^{n}(-1)^m\left(\frac{(n-m)!}{(n+m)!}\right)^2 P_{nm}(z_x)\,Q_{nm}(z_y)$$
$$\left.\times\, P_{nm}(\sin\beta_x)\,P_{nm}(\sin\beta_y)\cos m(\lambda_x-\lambda_y)\right], \tag{48}$$

where in analogy to Eq. (32)

$$z_x = \frac{iu_x}{E},\quad z_y = \frac{iu_y}{E} \quad \text{and} \quad i = \sqrt{-1}. \tag{49}$$

We suppose that $u_x < u_y$, which guarantees the convergence of the series and from Eq. (47) we can deduce that

$$H_G = H_G(\boldsymbol{x},\boldsymbol{y}) = \frac{i}{E}\sum_{n=0}^{\infty}(2n+1)\left[H_{n0xy}\,P_n(\sin\beta_x)\,P_n(\sin\beta_y) + \right.$$
$$+2\sum_{m=1}^{n}(-1)^m\left(\frac{(n-m)!}{(n+m)!}\right)^2 H_{nmxy}\,P_{nm}(\sin\beta_x)$$
$$\left.\times\, P_{nm}(\sin\beta_y)\cos m(\lambda_x-\lambda_y)\right], \tag{50}$$

where

$$H_{nmxy} = Q_{nm}(z_x)\,Q_{nm}(z_y)\,\frac{P_{nm}(z_0)}{Q_{nm}(z_0)} \quad \text{and} \quad z_0 = \frac{ib}{E}. \tag{51}$$

Finally, we again apply the apparatus of hypergeometric functions and series to represent Legendre's functions P_{nm} and Q_{nm}. This enables us to deduce that approximately (terms multiplied by the third and higher powers of the numerical eccentricity $e{=}E/a$ are neglected)

$$H_G(\boldsymbol{x},\boldsymbol{y}) \approx \frac{1}{a}H_G^{(1)}(\boldsymbol{x},\boldsymbol{y}) - \frac{E^2}{2a^2b}H_G^{(2)}(\boldsymbol{x},\boldsymbol{y}) + \frac{2E^2}{a^2b}H_G^{(3)}(\boldsymbol{x},\boldsymbol{y}), \tag{52}$$

where

$$H_G^{(1)}(\boldsymbol{x},\boldsymbol{y}) = \sum_{n=0}^{\infty}\rho^{n+1}P_n(\cos\psi), \tag{53}$$

$$H_G^{(2)}(\boldsymbol{x},\boldsymbol{y}) = \sum_{n=0}^{\infty}\frac{1}{(2n+3)(2n-1)}\,\rho^{n+1}P_n(\cos\psi), \tag{54}$$

$$H_G^{(3)}(\boldsymbol{x},\boldsymbol{y}) = \sum_{n=1}^{\infty}\frac{1}{(2n+3)(2n-1)}\,\rho^{n+1}\frac{\partial^2 P_n(\cos\psi)}{\partial\lambda^2} \tag{55}$$

and λ means λ_x or λ_y.

4 Key Role of Elliptic Integrals

Inspecting the components $K^{(1)}(\boldsymbol{x},\boldsymbol{y})$, $K^{(2)}(\boldsymbol{x},\boldsymbol{y})$, $K^{(3)}(\boldsymbol{x},\boldsymbol{y})$, $A^{(1)}(v_j,v_k)$, $A^{(2)}(v_j,v_k)$, $A^{(3)}(v_j,v_k)$ and similarly $H_G^{(1)}(\boldsymbol{x},\boldsymbol{y})$, $H_G^{(2)}(\boldsymbol{x},\boldsymbol{y})$, $H_G^{(3)}(\boldsymbol{x},\boldsymbol{y})$ that produce the reproducing kernel $K_{ell}(\boldsymbol{x},\boldsymbol{y})$, Galerkin's element $A_{ell}(v_j,v_k)$ and the harmonic part $H_G(\boldsymbol{x},\boldsymbol{y})$ in our Green function of the first kind, we can show by means of some algebra and decomposition that in essence these components, except for $K^{(1)}$ and $H_G^{(1)}$, rest on the following three different series

$$S = \sum_{n=0}^{\infty}\frac{1}{2n+1}(\,.\,)^n P_n(\cos\psi), \tag{56}$$

$$A = \sum_{n=0}^{\infty}\frac{1}{2n-1}(\,.\,)^n P_n(\cos\psi) \tag{57}$$

and

$$B = \sum_{n=0}^{\infty}\frac{1}{2n+3}(\,.\,)^{n+1} P_n(\cos\psi), \tag{58}$$

with $(\,.\,) < 1$ substituting ρ or q, see Holota and Nesvadba (2014, 2017). For $K^{(1)}$ one can obtain

$$K^{(1)}(\boldsymbol{x},\boldsymbol{y}) = \frac{2\rho}{L} - \ln\frac{L+\rho-\cos\psi}{1-\cos\psi} \tag{59}$$

with

$$L = \sqrt{1-2\rho\cos\psi+\rho^2} \tag{60}$$

in a relatively easy way, cf. Eqs. (8) and (9). Similarly, for $H_G^{(1)}$ we have

$$H_G^{(1)}(\boldsymbol{x},\boldsymbol{y}) = \frac{\rho}{L}. \tag{61}$$

Therefore, it is of key importance for the computation of $K_{ell}(\boldsymbol{x},\boldsymbol{y})$, $A_{ell}(v_j,v_k)$ and $H_G(\boldsymbol{x},\boldsymbol{y})$ that the summation of the series in Eqs. (56), (57), (58) can be made by means of Legendre (incomplete) elliptic integrals of the first and the

second kind

$$\mathcal{F}(k,\varphi) = \int_0^{\varphi} \frac{d\varphi}{\sqrt{1-k^2\sin^2\varphi}} \quad \text{and}$$
$$\mathcal{E}(k,\varphi) = \int_0^{\varphi} \sqrt{1-k^2\sin^2\varphi}\; d\varphi, \tag{62}$$

where

$$(\,.\,) = \tan^2\frac{\varphi}{2} \quad \text{and} \quad k^2 = \cos^2\frac{\psi}{2}. \tag{63}$$

Indeed, we obtain

$$S = \frac{1}{2}\mathcal{F}(k,\varphi)\cot\frac{\varphi}{2}, \tag{64}$$

cf. Eqs. (19) and (20),

$$A = -\sqrt{1-k^2\sin^2\varphi} + \frac{1}{2}\left[\mathcal{F}(k,\varphi) - 2\mathcal{E}\left(k,\varphi\right)\right]\tan\frac{\varphi}{2} \tag{65}$$

and

$$B = \sqrt{1-k^2\sin^2\varphi} + \frac{1}{2}\left[\mathcal{F}(k,\varphi) - 2\mathcal{E}\left(k,\varphi\right)\right]\cot\frac{\varphi}{2}, \tag{66}$$

see Holota and Nesvadba (2014, 2017). It is interesting that in contrast to $A^{(1)}$ for the computation of $K^{(1)}$ and $H_G^{(1)}$ elliptic integrals need not be used.

5 From the Ellipsoid to the Earth's Surface

In reality, the determination of the Earth's gravity potential from surface gravity data represents the gravimetric boundary value problem. Its solution domain Ω is the exterior the Earth. The problem is usually treated in a linearized form. We identify W and U with the gravity and a standard (or normal) potential of the Earth, respectively. Under this notation $\boldsymbol{g} = \boldsymbol{grad}\, W$ is the gravity vector and its length $g = |\,\boldsymbol{grad}\, W\,|$ is the measured gravity. By analogy $\boldsymbol{\gamma} = \boldsymbol{grad}\, U$ and $\gamma = |\,\boldsymbol{grad}\, U\,|$ for the normal gravity. Finally, in the general point $\boldsymbol{x}$ we have $T(\boldsymbol{x}) = W(\boldsymbol{x}) - U(\boldsymbol{x})$ for the disturbing potential and $\delta g(\boldsymbol{x}) = g(\boldsymbol{x}) - \gamma(\boldsymbol{x})$ for the gravity disturbance.

The linear gravimetric boundary value problem then means to find T such that

$$\Delta T = div\, \boldsymbol{grad}\, T = 0 \;\text{ in }\; \Omega, \tag{67}$$

$$\frac{\partial T}{\partial \boldsymbol{s}} = \langle \boldsymbol{s}, \boldsymbol{grad}\, T\rangle = -\,\delta g \;\text{ on }\; \partial\Omega, \tag{68}$$

where $\langle\ ,\ \rangle$ denotes the scalar product, $\partial\Omega$ is the boundary of Ω and

$$\boldsymbol{s} = -\,\frac{1}{\gamma}\,\boldsymbol{grad}\, U, \tag{69}$$

see Koch and Pope (1972), Bjerhammar and Svensson (1983) or Grafarend (1989). Let us add in this connection that the vector $\boldsymbol{s}$ is assumed to be nowhere tangential to $\partial\Omega$ and when denoting by $\boldsymbol{n}$ the unit (outer) normal of $\partial\Omega$, we suppose that the angle between $\boldsymbol{n}$ and $\boldsymbol{s}$ is less than 90°, i.e. $\langle \boldsymbol{s}, \boldsymbol{n}\rangle > 0$.

The formulation above is rather general and it is natural that the step towards mathematical formalization involves a certain idealization. In case of the weak solution concept we assume that $\Omega' = \boldsymbol{R}^3 - \overline{\Omega}$ is a domain with a Lipschitz boundary, for definition see Nečas (1967), Rektorys (1974) or Kufner et al. (1977) and T is sought as a function from Sobolev's space $W_2^{(1)}(\Omega)$, see Holota (1997). Note that $W_2^{(1)}(\Omega)$ as a part contains $H_2^{(1)}(\Omega)$, an analogue to $H_2^{(1)}(S_R)$ and $H_2^{(1)}(\Omega_{ell})$ mentioned in Sects. 2 and 3. Within this concept T is defined by the following integral identity

$$A(T,v) = \int_{\partial\Omega} vf\; dS \tag{70}$$

valid for all $v \in W_2^{(1)}(\Omega)$. The function f is assumed square integrable on $\partial\Omega$ and such that $f = -\gamma(\partial U/\partial n)^{-1}\delta g = \langle \boldsymbol{s}, \boldsymbol{n}\rangle^{-1}\delta g$, where $\partial/\partial n$ means the derivative in the direction of the normal $\boldsymbol{n}$ and $A(u,v)$ is a bilinear form on the Cartesian product $W_2^{(1)}(\Omega) \times W_2^{(1)}(\Omega)$, but of somewhat more complex structure in comparison with Eq. (6). Because the linear gravimetric boundary-value problem is an oblique derivative problem

$$A(u,v) = A_1(u,v) - A_2(u,v)\,, \tag{71}$$

where

$$A_1(u,v) = \int_{\Omega} \langle \boldsymbol{grad}\, u, \boldsymbol{grad}\, v \rangle \, d\boldsymbol{x}, \tag{72}$$

$$\begin{aligned} A_2(u,v) = &\int_{\Omega} \langle \boldsymbol{grad}\, v, \boldsymbol{a} \times \boldsymbol{grad}\, u \rangle \, d\boldsymbol{x} \\ &+ \int_{\Omega} v \, \langle \boldsymbol{curl}\, \boldsymbol{a}, \boldsymbol{grad}\, u \rangle \, d\boldsymbol{x} \end{aligned} \tag{73}$$

and $\boldsymbol{a}=(a_1, a_2, a_3)$ is a vector field such that on the boundary $\partial\Omega$ the vector

$$\boldsymbol{\sigma} = \frac{1}{\langle \boldsymbol{s}, \boldsymbol{n} \rangle} \, \boldsymbol{s} \tag{74}$$

and the field $\boldsymbol{a}$ are coupled by $\boldsymbol{\sigma}=\boldsymbol{n} + \boldsymbol{a} \times \boldsymbol{n}$, see Holota (1997). We believe that the conventional notation $\times$ used here for the vector product will not be a cause of any confusion (cf. Cartesian product above).

The realization of the weak solution concept, including the approximation of $A_1(u, v)$ by a bilinear form

$$A^*(u,v) = \int_{\Omega^*} \langle \boldsymbol{grad}\, u, \boldsymbol{grad}\, v \rangle \quad d\boldsymbol{x}, \tag{75}$$

where Ω^* has a "simpler boundary", the implementation of the respective iteration steps and the representation of the form $A_2(u, v)$, is described (with numerical examples) in Nesvadba et al. (2007) and Holota and Nesvadba (2012). It turned out, e.g., that for basis functions generated by elementary potentials and Ω^* represented by the exterior of a sphere the convergence of the iterations is rather slow but considerably improves for Ω^* being the exterior of an oblate ellipsoid of revolution. This motivated the computations mentioned in Sect. 3.

In the second part of this section we mention still one more approach. The complexity of the boundary can be transformed into the coefficients of the partial differential equation governing the solution. As a starting point for an alternative like this we can use the mapping given by Eq. (22), but with $u=z + h(\beta, \lambda)$, where $h(\beta, \lambda)$ is a function that describes the boundary $\partial\Omega$ with respect to the level ellipsoid $\partial\Omega_{ell}$. We thus have

$$x_1 = \sqrt{[\, z + h(\beta,\lambda)\,]^2 + E^2} \cos\beta \cos\lambda, \tag{76}$$

$$x_2 = \sqrt{[\, z + h(\beta,\lambda)\,]^2 + E^2} \cos\beta \sin\lambda, \tag{77}$$

$$x_3 = [\, z + h(\beta,\lambda)\,] \sin\beta, \tag{78}$$

where z together with β and λ form a system of new curvilinear coordinates. Interpreting z, β, λ as ellipsoidal coordinates again and taking into consideration that $\partial u/\partial z=1$, we immediately see that the transformation is a one-to-one mapping between the original solution domain Ω and the outer space of our oblate ellipsoid of revolution, i.e. Ω_{ell}. It is also obvious that $\partial\Omega$ is defined by $z=b$ and its image coincides with $\partial\Omega_{ell}$. The approach as above represents a generalization of the concept discussed in Holota (1985, 1986, 1989, 1992a, b, 2016). Here we particularly refer to Holota and Nesvadba (2016).

Putting $y_1=z$, $y_2=\beta$, $y_3=\lambda$, we are ready to write Laplace's operator Δ applied on T in terms of the curvilinear coordinates y_i. Within tensor calculus we generally have

$$\begin{aligned} \Delta T &= \frac{1}{\sqrt{g}} \frac{\partial}{\partial y_i} \left(\sqrt{g}\; g^{ij} \frac{\partial T}{\partial y_j} \right) \\ &= g^{ij} \frac{\partial^2 T}{\partial y_i \partial y_j} + \frac{1}{\sqrt{g}} \frac{\partial \sqrt{g}\; g^{ij}}{\partial y_i} \frac{\partial T}{\partial y_j}, \end{aligned} \tag{79}$$

see Sokolnikoff (1971). Here g is the determinant related to the respective metric tensor g_{ij} and g^{ij} means the associate (or conjugate) metric tensor. After some algebra (and a negligible approximation) we obtain

$$\Delta T = \frac{z^2 + E^2 \sin^2\beta}{(z+h)^2 + E^2 \sin^2\beta} \left[\Delta_{ell} T - \delta(T,h) \right], \tag{80}$$

where

$$\begin{aligned} \Delta_{ell} T = \frac{1}{z^2 + E^2 \sin^2\beta} &\left[2z \frac{\partial T}{\partial z} + \left(z^2 + E^2\right) \frac{\partial^2 T}{\partial z^2} + \right. \\ &\left. + \frac{\partial^2 T}{\partial \beta^2} - \frac{\sin\beta}{\cos\beta} \frac{\partial T}{\partial \beta} + \frac{z^2 + E^2 \sin^2\beta}{(z^2 + E^2)\cos^2\beta} \frac{\partial^2 T}{\partial \lambda^2} \right], \end{aligned} \tag{81}$$

$$\begin{aligned} \delta(T,h) = {} & A_1 \tfrac{\partial T}{\partial z} + A_2 \tfrac{\partial^2 T}{\partial z^2} + \\ & + A_3 \tfrac{1}{\sqrt{z^2 + E^2 \sin^2\beta}} \tfrac{\partial^2 T}{\partial z \partial \beta} + A_4 \tfrac{1}{\sqrt{z^2 + E^2}\cos\beta} \tfrac{\partial^2 T}{\partial z \partial \lambda}, \end{aligned} \tag{82}$$

and A_i are topography dependent coefficients given by

$$\begin{aligned} A_1 = {} & \frac{1}{z^2 + E^2 \sin^2\beta} \\ & \times \left[-2h - \frac{\sin\beta}{\cos\beta} \frac{\partial h}{\partial \beta} + \frac{\partial^2 h}{\partial \beta^2} + \frac{z^2 + E^2 \sin^2\beta}{(z^2 + E^2)\cos^2\beta} \frac{\partial^2 h}{\partial \lambda^2} \right], \end{aligned} \tag{83}$$

$$\begin{aligned} A_2 = {} & -\frac{2zh + h^2}{z^2 + E^2 \sin^2\beta} - \frac{1}{z^2 + E^2 \sin^2\beta} \\ & \times \left[\left(\frac{\partial h}{\partial \beta} \right)^2 + \frac{z^2 + E^2 \sin^2\beta}{(z^2 + E^2)\cos^2\beta} \left(\frac{\partial h}{\partial \lambda} \right)^2 \right], \end{aligned} \tag{84}$$

$$A_3 = \frac{2}{\sqrt{z^2 + E^2 \sin^2\beta}} \frac{\partial h}{\partial \beta}, \tag{85}$$

$$A_4 = \frac{2}{\sqrt{z^2 + E^2}\cos\beta} \frac{\partial h}{\partial \lambda}. \tag{86}$$

Obviously, the transformation of coordinates has also an effect on the boundary condition. Indeed, for the normal (Somigliana-Pizzeti) potential U the condition given by Eq. (68) turns into

$$\frac{\partial T}{\partial z} = - \; w\,(z + h, \beta)\,\delta g \;\; \text{for} \;\; z = b, \tag{87}$$

where

$$w\,(z + h, \beta) = \sqrt{\frac{(z+h)^2 + E^2 \sin^2\beta}{(z+h)^2 + E^2}} \tag{88}$$

and it follows from differential geometric considerations that for $\partial/\partial n$ denoting now the derivative in the direction of the unit (outer) normal $\boldsymbol{n}$ of $\partial\Omega_{ell}$

$$\frac{\partial T}{\partial n} = - \; \sqrt{1 + \varepsilon} \;\; \delta g \;\; \text{on} \;\; \partial\Omega_{ell} \tag{89}$$

with

$$\varepsilon = \frac{E^2 \left(2bh + h^2\right) \cos^2\beta}{\left(a^2 \sin^2\beta + b^2 \cos^2\beta\right) \;\; \left[\,(b+h)^2 + E^2\right]} \tag{90}$$

that practically may be neglected, see Holota and Nesvadba (2016).

Hence, the linear gravimetric boundary value problem in terms of the curvilinear coordinates z, β, λ attains the form

$$\Delta_{ell} T = \;\; f \;\; \text{in} \;\; \Omega_{ell} \tag{91}$$

and

$$\frac{\partial T}{\partial n} = - \; \delta g \;\; \text{on} \;\; \partial\Omega_{ell}, \tag{92}$$

where $f = \delta(T, h)$.

Neglecting the fact that f depends on T, we can represent the solution of the problem formally by means of a classical apparatus of mathematical physics. Indeed, we can use Neumann's function N (Green's function of the second kind) constructed in the end of Sect. 3 which enables us to write

$$\begin{aligned} T\,(\boldsymbol{y}\,) = & \frac{1}{4\pi} \int\limits_{\partial\Omega_{ell}} N\,(\boldsymbol{x}, \boldsymbol{y})\;\; \delta g\,(\boldsymbol{x})\;\; d_x S \\ & - \;\; \frac{1}{4\pi} \int\limits_{\Omega_{ell}} N\,(\boldsymbol{x}, \boldsymbol{y})\;\; f\,(\boldsymbol{x})\;\; d_x V \end{aligned} \tag{93}$$

with $d_x S$ and $d_x V$ denoting the surface and the volume element, respectively, cf. Eq. (3) valid for spherical solution domain.

Nevertheless, Neumann's function N can also be used to solve the transformed linear gravimetric boundary value problem, where f depends on T. In this case the integral formula (93) represents an integro-differential equation for T and an iteration approach has to be applied. For this purpose we put

$$F\,(\boldsymbol{y}) = \frac{1}{4\pi} \int\limits_{\partial\Omega_{ell}} N\,(\boldsymbol{x}, \boldsymbol{y})\;\; \delta g\,(\boldsymbol{x})\;\; d_x S \tag{94}$$

and

$$K\,T\,(\boldsymbol{y}) = -\frac{1}{4\pi} \int\limits_{\Omega_{ell}} N\,(\boldsymbol{x}, \boldsymbol{y})\;\; \delta\,[T\,(\boldsymbol{x})\;\; h\,(\boldsymbol{x})]\;\; d_x V, \tag{95}$$

where $F(\boldsymbol{y}\,)$ is a harmonic function and $KT(\boldsymbol{y}\,)$ is an integro-differential operator applied on T, such that

$$\Delta_{ell} K T = \;\; \delta\,(T, h) \;\; \text{in} \;\; \Omega_{ell} \;\; \text{and} \;\; \frac{\partial K T}{\partial n} = 0 \;\; \text{on} \;\; \partial\Omega_{ell}. \tag{96}$$

Our aim is to find T from $T = F + KT$ by means of the method of successive approximations

$$T = \lim_n T_n, \;\; T_n = F + K\,T_{n-1}, \tag{97}$$

where T_0 is the starting approximation, e.g. $T_0 = F$.

The crucial point is to show that K is a contraction mapping which as a sufficient condition guarantees the convergence of the iteration process according to the famous Banach's fixed point theorem, see e.g. Rektorys (1974) or Gilbarg and Trudinger (1983). This is our next goal. As a guideline the contractivity proof for the simple gravimetric boundary value problem investigated in Sobolev's weight space $W_2^{(2)}\,(S_R)$ in Holota (1985, 1986, 1989, 1992a, b) will be followed. The most intricate step to estimate the second order derivatives of Ku has been done by means of a special case of the Calderon-Zygmund inequality. It belongs to the

so-called L_p estimates for Poisson's equation (analogous to Chauder's theory in Hölder's spaces), see Gilbarg and Trudinger (1983).

6 Conclusions

The boundary value problems considered in this paper are formulated for an unbounded solution domain that in some idealized and/or adopted sense reflects the exterior of the Earth. The solution meets Poisson's or Laplace's differential equation and its directional derivative has to satisfy a given condition on the boundary. For potential theory and the theory of partial differential equations the solution of these problems represents a field of advanced applications. In this contribution we tried to discuss some of these facts and also to contribute to methods and solution techniques which come into consideration.

In the introduction we limited our discussion to Neumann's problem formulated for the exterior of a sphere. We focused on the use of three important integral kernels within the classical and weak solution concept. Concerning the classical concept, we mentioned the solution of Neumann's problem by means of Green's function method. Neumann's function (Green's function of the second kind) $N(\boldsymbol{x},\boldsymbol{y})$ is of key importance in this approach. The problem appears in physical geodesy, but usually interpreted for Laplace's differential equation. Note that in consequence Neumann's function is standardly considered in a restricted form in this case, i.e., one or both the variable points $\boldsymbol{x}$ and $\boldsymbol{y}$ lie on the boundary ∂S_R. Nevertheless, in Sect. 2 we showed a close form representation of Neumann's function for $\boldsymbol{x}$ and $\boldsymbol{y}$ moving inside the closure of the solution domain, i.e. $\boldsymbol{x}$, $\boldsymbol{y} \subset \partial S_R \cup S_R$, which is a more general result.

Similarly, a closed form representation was shown for the reproducing kernel of Hilbert's space $H_2^{(1)}(S_R)$ and for Galerkin's elements in case that the solution of Neumann's problem is approximated by a linear combination of elementary potentials. It may be of interest that for the computation of Galerkin's elements it was necessary to use the Legendre (incomplete) elliptic integral of the first kind. In a sense the content of Sect. 2 represents a germ of the next discussion.

In Sect. 3 the construction of Neumann's function, the reproducing kernel and Galerkin's elements was approach again, but this time for the solution domain given by the exterior of the ellipsoid of revolution, i.e. S_R was substituted by Ω_{ell}. The results are represented by infinite series of ellipsoidal harmonics. They allow a direct numerical treatment (which we give attention to in parallel), but in this paper we tried to present an analytic way for their summation. This was achieved under some approximations. Neglecting terms multiplied by the third and higher powers of the numerical eccentricity $e=E/a$, we give closed form representation for the reproducing kernel, Galerkin's elements and subsequently also for Neumann's function. The results rest on the use of Legendre (incomplete) elliptic integrals of the first and the second kind. This is highlighted in Sect. 4.

The intention to approach reality motivated the last section. It is demonstrated for the weak as well as classical solution concept applied to the linear gravimetric boundary value problem, in particular for Galerkin's approximations of the solution and for the use of Green's function method. The Galerkin's elements are of a somewhat more complex structure and in the case of Green's function method in addition a modification of spatial coordinates was used to solve the problems associated with the construction of Neumann's function for the complicated boundary of the solution domain. Successive approximations are applied in both the cases. On the level of individual iteration steps the mathematical apparatus developed for the ellipsoidal solution domain is used.

Acknowledgements This work was supported by the Czech Science Foundation through Project No. 14-34595S and by the Ministry of Education, Youth and Sports of the Czech Republic through Project No. LO1506. This support is gratefully acknowledged. Sincere thanks go also to two anonymous reviewers for valuable comments.

References

Bjerhammar A, Svensson L (1983) On the geodetic boundary-value problem for a fixed boundary surface – satellite approach. Bull Geod 57:382–393

Garabedian PR (1964) Partial differential equations. Wiley, New York

Gilbarg D, Trudinger NS (1983) Elliptic partial differential equations of second order. Springer, Berlin

Grafarend EW (1989) The geoid and the gravimetric boundary-value problem. Rep 18 Dept Geod, The Royal Institute of Technology, Stockholm

Heiskanen WA, Moritz H (1967) Physical geodesy. W.H. Freeman and Company, San Francisco

Hobson EW (1931) The theory of spherical and ellipsoidal harmonics. University Press, Cambridge

Hofmann-Wellenhof B, Moritz H (2005) Physical geodesy. Springer, Wien

Holota P (1985) A new approach to iteration solutions in solving geodetic boundary value problems for real topography. In: Proc. 5th Int. Symp. Geod. and Phys. of the Earth, GDR, Magdeburg, Sept. 23rd-29th, 1984, Part II. Veroff. d. Zentr. Inst. f. Phys. d. Erde, Nr. 81, Teil II, pp 4–15

Holota P (1986) Boundary value problems in physical geodesy: present state, boundary perturbation and the Green-Stokes representation. In: Proc. 1st Hotine-Marussi Symp. on Math. Geodesy, Rome, 3-5 June 1985, vol 2. Politecnico di Milano, pp 529–558

Holota P (1989) Laplacian versus topography in the solution of the Molodensky problem by means of successive approximations. In: Kejlso E, Poder K, Tscherning CC (eds) Festschrift to Torben Krarup. Geodaetisk Inst., Meddelelse No. 58, Kobenhavn, pp 213–227

Holota P (1992a) On the iteration solution of the geodetic boundary-value problem and some model refinements. Contribution to Geodetic Theory and Methodology. In: XXth General Assembly of the

IUGG, IAG-Sect. IV, Vienna, 1991. Politecnico di Milano, 1991: pp 31-60; also in: Travaux de l'Association Internationale de Geodesie, Tome 29, Paris, pp 260–289

Holota P (1992b) Integral representation of the disturbing potential: effects involved, iteration technique and its convergence. In: Holota P, Vermeer M (eds) Proc. First continental workshop on the geoid in Europe, Prague, May 11-14, 1992. Research Inst. of Geod., Topog. and Cartog., Prague, in co-operation with IAG-Subcommis. for the Geoid in Europe, Prague, pp 402–419

Holota P (1997) Coerciveness of the linear gravimetric boundary value problem and geometrical interpretation. J Geod 71:640–651

Holota P (1999) Vartiational methods in geoid determination and function bases. Phys Chem Earth (A) 24(1):3–14

Holota P (2000) Direct method in physical geodesy. In: Schwarz KP (ed) Geodesy beyond 2000 – the challenges of the first decade. IAG General Assembly, Birmingham July 19-30, 1999. International Association of Geodesy Symposia, vol 121. Springer, Berlin, pp 163–170

Holota P (2003) Green's function and external masses in the solution of geodetic boundary-value problems. In: Tziavos IN (ed) Gravity and Geoid, 3rd Meeting of the Intl. Gravity and Geoid Commission, Thessaloniki, Greece, August 26-30, 2002. Ziti Editions, Thessaloniki, pp 108–113

Holota P (2004) Some topics related to the solution of boundary-value problems in geodesy. In: Sansò F (ed) V Hotine-Marussi Symposium on Mathematical Geodesy, Matera, Italy, June 17-21, 2002. International Association of Geodesy Symposia, vol 127. Springer, Berlin, pp 189–200

Holota P (2011) Reproducing kernel and Galerkin's matrix for the exterior of an ellipsoid: application in gravity field studies. Studia geophysica et geodaetica 55(3):397–413

Holota P (2016) Domain transformation and the iteration solution of the linear gravimetric boundary value problem. In: Freymueller J, Sánchez L (eds) International Symposium on Earth and Environmental Sciences for Future Generations. Proceedings of the IAG General Assembly, Prague, Czech Republic, June 22-July 2, 2015. International Association of Geodesy Symposia, vol 147. Springer, Cham, pp 47–52. https://doi.org/10.1007/1345_2016_236

Holota P, Nesvadba O (2012) Method of successive approximations in solving geodetic boundary value problems: analysis and numerical experiments. In: Sneeuw N, Novák P, Crespi M (eds) VII Hotine-Marussi Symposium on Mathematical Geodesy, Rome, Italy, 6-10 June, 2009. International Association of Geodesy Symposia, vol 137. Springer, Cham, pp 189–198

Holota P, Nesvadba O (2014) Reproducing kernel and Neumann's function for the exterior of an oblate ellipsoid of revolution: application in gravity field Studies. Studia geophysica et geodaetica 58(4): 505–535

Holota P, Nesvadba O (2016) Small modifications of curvilinear coordinates and successive approximations applied in geopotential determination. In: 2016 AGU Fall Meeting, Session G21B (Scientific and Practical Challenges of Replacing NAD 83, NAVD 88, and IGLD 85), San Fransico, USA, 12-16 December 2016, poster. https://agu.confex.com/agu/fm16/meetingapp.cgi/Paper/189936

Holota P, Nesvadba O (2017) Galerkin's matrix for Neumann's problem in the exterior of an oblate ellipsoid of revolution: approximation of the Earth's gravity potential by buried masses. Studia geophysica et geodaetica (submitted)

Hotine M (1969) Mathematical geodesy. ESSA Monographs, Washington, D.C.

Klees R (1997) Topics on boundary elements methods. In: Sansò F, Rummel R (eds) Geodetic boundary value problems in view of the one centimeter geoid. Lecture Notes in Earth Sciences, vol 65. Springer, Berlin, pp 482–531

Koch KR, Pope AJ (1972) Uniqueness and existence for the geodetic boundary-value problem using the known surface of the Earth. Bull Geod 106:467–476

Kufner A, John O, Fučík S (1977) Function spaces. Academia, Prague

Nečas J (1967) Les méthodes directes en théorie des équations elliptiques. Academia, Prague

Nesvadba O, Holota P, Klees R (2007) A direct method and its numerical interpretation in the determination of the Earth's gravity field from terrestrial data. In: Tregoning P, Rizos C (eds) Dynamic planet – monitoring and understanding a dynamic planet with geodetic and oceanographic tools. IAG Symposium, Cairns, Australia, 22-26 August 2005. International Association of Geodesy Symposia, vol 130. Springer, Berlin, pp 370–376

Neyman YM (1979) A variational method of physical geodesy. Nedra Publishers, Moscow. (in Russian)

Pick M, Pícha J, Vyskočil V (1973) Úvod ke studiu tíhového pole Země. Academia, Prague. 1973; also in English: Theory of the Earth's gravity field. Elsevier, Amsterdam, 1973

Rektorys K (1974) Variační metody v inženýrských problémech a v problémech matematické fyziky. SNTL Publishers of Technical Literature, Prague. 1974; also in English: Variational methods. Reidel, Dordrecht 1977

Roach GF (1982) Green's functions, 2nd edn. Cambridge University Press, Cambridge

Sokolnikoff IS (1971) Tensor analysis. Theory and applications to geometry and mechanics of continua. Nauka Publishers, Moscow. (in Russian)

Tscherning CC (1975) Application of collocation. Determination of a local approximation to the anomalous potential of the Earth using "exact" astro-gravimetric collocation. In: Brosowski B, Martensen E (eds) Methoden und Verfahren der Mathematischen Physik, vol 14, pp 83–110

GEOMED2: High-Resolution Geoid of the Mediterranean

R. Barzaghi, D. Carrion, G. S. Vergos, I. N. Tziavos, V. N. Grigoriadis, D. A. Natsiopoulos, S. Bruinsma, F. Reinquin, L. Seoane, S. Bonvalot, M. F. Lequentrec-Lalancette, C. Salaün, O. Andersen, P. Knudsen, A. Abulaitijiang, and M. H. Rio

Abstract

Geoid models for the Mediterranean were computed using the remove-compute-restore method and Stokes-FFT, using shipborne gravity or altimetry inferred gravity data over sea and land gravity data. The remove step over sea does not include residual terrain correction (bathymetry), which leads to slightly worse results. The models were compared to an independent geoid constructed by subtracting the Mean Dynamic Topography from the Mean Sea Surface, and secondly to drifter-observed current speeds. Results revealed significant errors in the gravimetric geoid at smallest scales, and analysis of the results of this intermediate model showed that improvement is required in the gravity data preprocessing, specifically the de-biasing of marine data, as well as the gridding (interpolation) procedure. These issues will be addressed before the release of the final geoid model early 2018. Based on the drifter comparisons, the geoid based on altimeter data is the most accurate, more accurate than EIGEN6C4, and notably so at scales less than 50 km.

Keywords

Altimetry · Geoid · Mean Dynamic Topography · Mediterranean Sea

1 Introduction

The objective of the GEOMED 2 project is the determination of a high-accuracy and high resolution marine geoid taking advantage of the improved global gravity field models, thanks to GRACE and GOCE in particular, and the compilation of a cleaned-up gravity database of the Mediterranean based on Bureau Gravimétrique International (BGI) and Service Hydrographique et Océanographique de la Marine (SHOM) data (Lequentrec-Lalancette et al. 2016). Computation of a gravimetric (i.e. using only surface data) geoid of the Mediterranean Sea is challenging due to:

- marine gravity data coverage is poor over several parts;
- quality of the marine gravity data is not homogeneous (bias, precision);
- data reduction is not at the level achieved over land.

A geoid computed with gravity inferred from altimetry data, or a mean sea surface corrected for mean dynamic

R. Barzaghi (✉) · D. Carrion
Politecnico di Milano, Milan, Italy
e-mail: riccardo.barzaghi@polimi.it

G. S. Vergos · I. N. Tziavos · V. N. Grigoriadis · D. A. Natsiopoulos
GravLab, Aristotle University, Thessaloniki, Greece

S. Bruinsma · F. Reinquin
CNES – Space Geodesy Office, Toulouse, France

L. Seoane · S. Bonvalot
OMP/GET, Toulouse, France

M. F. Lequentrec-Lalancette · C. Salaün
Shom – French Hydrographic Office, Brest, France

O. Andersen · P. Knudsen · A. Abulaitijiang
DTU Space, Copenhagen, Denmark

M. H. Rio
CLS, Ramonville Saint Agne, France

J. T. Freymueller, L. Sanchez (eds.), *International Symposium on Advancing Geodesy in a Changing World*,
International Association of Geodesy Symposia 149, https://doi.org/10.1007/1345_2018_33

topography (i.e., an 'oceanographic' geoid model), can be used as benchmarks. However, contamination by ocean dynamic signal is unavoidable, which is why a pure gravimetric solution is preferred.

An independent quality evaluation of the geoid models is done by comparison of calculated to drifter-observed current velocities. This type of evaluation allows a very detailed quality assessment as a function of region and spatial scale. This paper presents an intermediate model, which is based on most but not all available data, and computed with the Stokes FFT method.

2 Data

All available gravity data from BGI, SHOM, and national databases from Italy, Croatia and Greece were compiled in a 10W–40E longitude and 29N–48N latitude window. In particular, marine gravity data from the Morelli cruises (Allan and Morelli 1971), and the University of Cambridge cruises in the eastern basin (Report of the Dept. of Geodesy and Geophysics, Cambridge University 1974) were used. The marine data have been validated and preprocessed as described in a previous paper (Lequentrec-Lalancette et al. 2016). Two main marine gravity data sets have been used. First of all, data from the BGI database (i.e., data from different national agencies such as SHOM and NOAA/NGDC) and secondly, the compilation of all Morelli data. The more recent data available at BGI (SHOM survey data) have a mean error of 2 mGal, determined through cross over adjustment, whereas the Morelli data have a mean error of 3.6 mGal. In Lequentrec-Lalancette et al. (2016), the Morelli data and the SHOM survey data have been compared with the global gravity field model EIGEN6C4 (Förste et al. 2014) and the marine gravity model DTU13 (Andersen et al. 2010), and the results are listed in Table 1.

The offset between data and EIGEN6C4 is higher for Morelli data than with the more recent survey data. A simple method of de-biasing has been applied on each sub-cruise of the survey data and of Morelli data to reduce the mean bias between marine gravity data and the global gravity model chosen, in this case the EIGEN6C4 model (Förste et al. 2014). The adopted de-biasing method is a simple adjustment of the mean differences between the model and the data.

Table 1 Statistics of the differences between data and models, in mGal

Difference	Mean	StD	Min	Max
Survey – EIGEN6C4	−1.59	5.71	−53.24	48.94
Morelli – EIGEN6C4	4.07	5.71	−51.60	76.80
Survey – DTU13	−1.78	4.89	−52.08	46.85
Morelli – DTU13	4.25	5.00	−57.84	79.96

Table 2 Statistics of the differences between data and models, in mGal

Difference	Mean	StD	Min	Max
BGI data in East Med. – EIGEN6C4	−0.38	9.99	−116.24	72.91
BGI data in East Med. – DTU13	−0.55	9.62	−117.59	75.54

Furthermore, other marine gravity data from the BGI database were added, mainly to fill in some data gaps in the Eastern Mediterranean basin. The statistics of these data with respect to EIGEN6C4 (to d/o 2,190) and DTU13 are listed in Table 2.

The marine data were then sampled by selecting the points closest to the barycenter of a $7.5'' \times 7.5''$ regular grid.

Finally, the whole gravity dataset, i.e. marine and land data, has been reduced with the EIGEN6C4 model to degree and order (d/o) 1,000, and only the data over land were corrected for terrain effects with the DTM from Shuttle Radar Topography Mission (Farr et al. 2007). The marine data were not reduced using the bathymetry because residual gravities became slightly larger, which is in line with recent results of Hirt et al. (2017). Reductions to higher and lower d/o, as well as with a recent GOCE satellite-only model to d/o 230 (Bruinsma et al. 2014), were tested too but resulted in less accurate geoid models. The distribution of the marine data is shown in Fig. 1.

A second source of marine gravity anomalies is altimetry, which provides data on a regular $2.5'$ or $1'$ grid, without gaps and currently to within kilometers of the coast. The precision of the computed gravity anomalies is 2–3 mGal (one sigma), but locally larger errors are present due to significant ocean variability (i.e. contamination of the gravity signal), altimeter re-tracking (i.e. selected waveform), and in the coastal zones due to different processing methods (geoid vs geoid slope). In this study, the DTU15 (Andersen et al. 2017) and UCSD V24.1 (Sandwell et al. 2014) were used. These data grids also were only reduced with EIGEN6C4 to d/o 1,000. Differences between these two models are not negligible over the entire Mediterranean basin (0.5 and 3.7 mGal mean and sigma, respectively), but are larger for regions with important land contamination due to islands such as in the Aegean Sea, where the standard deviation is 6.2 mGal.

3 Method

After the remove step described in the previous section, a regular $2'$ grid was constructed with reduced gravity data using the kriging method with GRAVSOFT's (Forsberg and Tscherning 2008) GEOGRID program. The resulting reduced gravity map for the surface data (land and ship) is displayed in Fig. 2. A second $2'$ regular grid based on the altimetry-inferred gravity was constructed by replacing the data over sea.

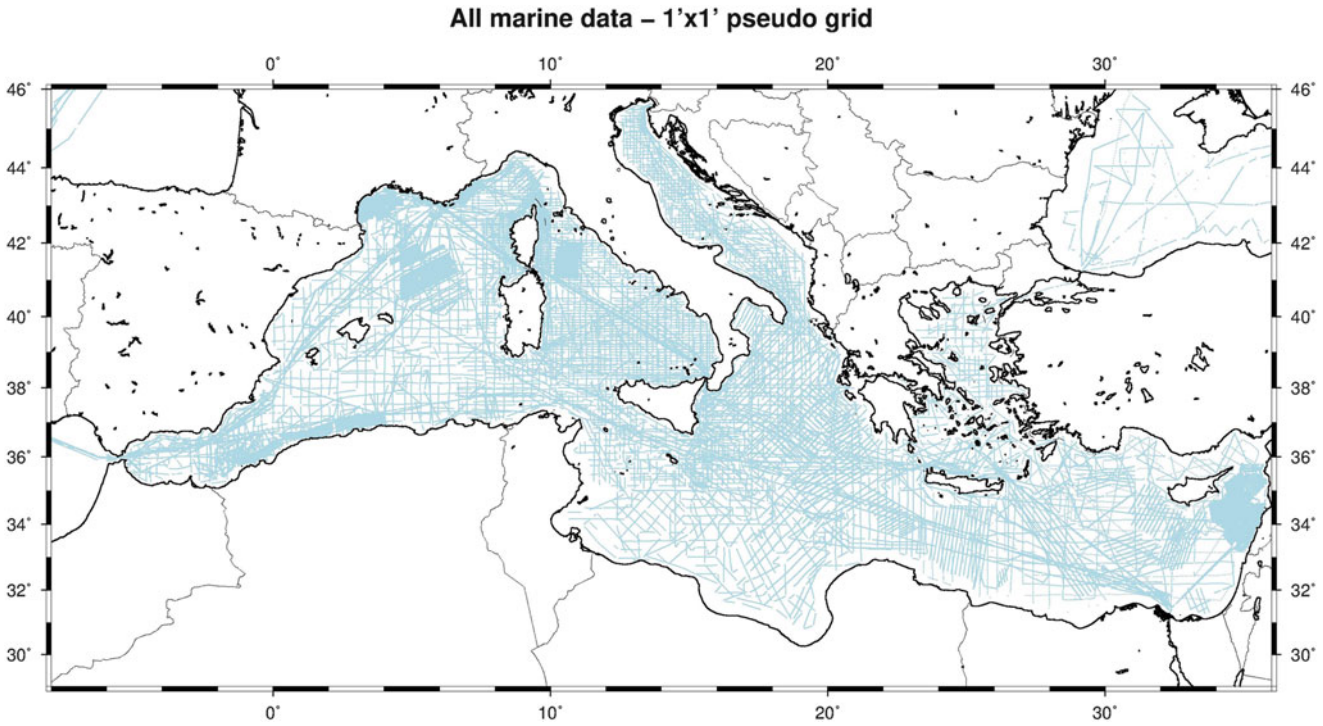

Fig. 1 The distribution of the shipborne marine gravity data

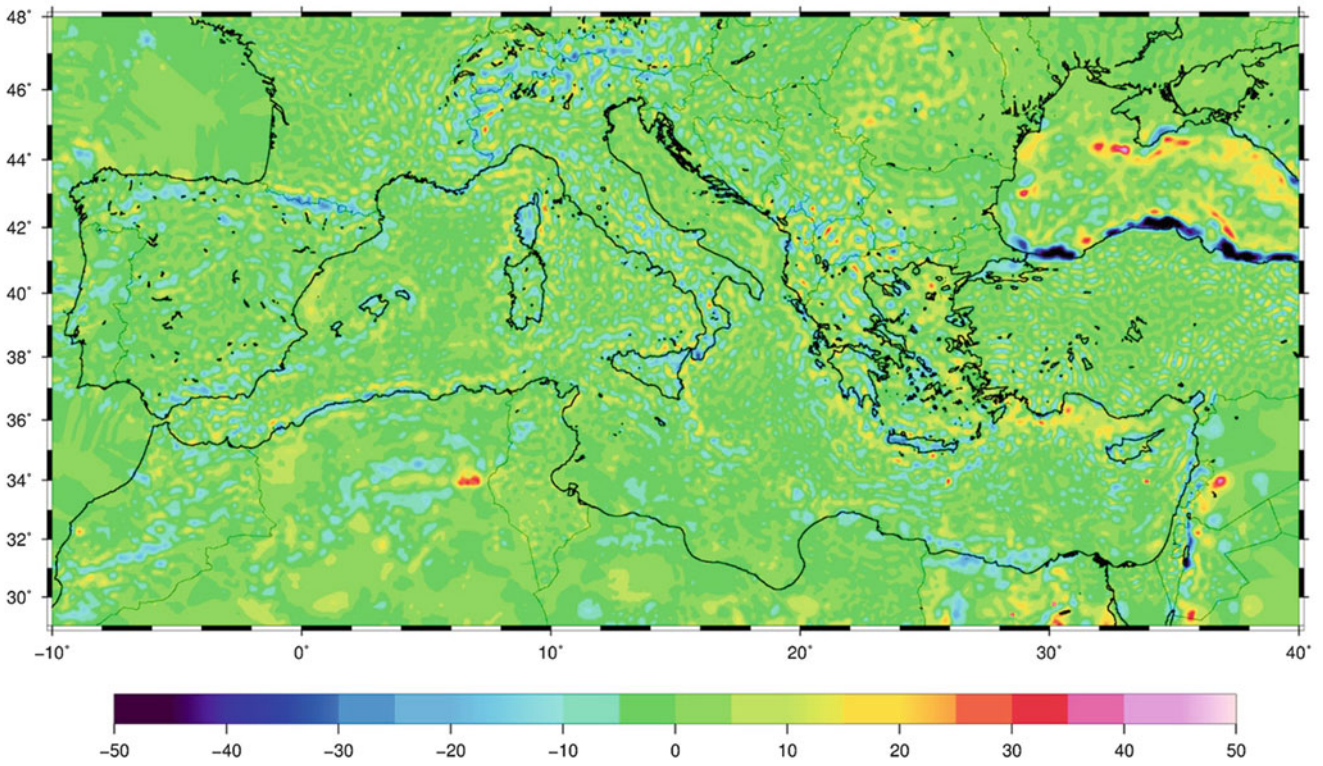

Fig. 2 The $2' \times 2'$ interpolated residual gravity grid (mGal)

The residual geoid estimates using the two aforementioned gravity grids were computed using 1D-FFT spherical Stokes convolution as (Haagmans et al. 1993)

$$N_{res}\left(\varphi_l,\lambda_k\right)=\frac{R}{4\pi\gamma}\sum_{j=0}^{N-1}\left[\sum_{i=0}^{M-1}\Delta g_{res}\left(\varphi_j,\lambda_i\right)\times cos\,\varphi_j\,S\left(\varphi_l,\varphi_j,\lambda_k-\lambda_i\right)\Delta\lambda\right]\Delta\varphi \quad (1)$$

where, the geoid prediction is carried out along a parallel at latitude φ_l based on gridded point gravity values along a parallel φ_j. In Eq. (1), N_{res} denotes residual geoid heights, Δg_{res} the available residual gravity anomalies, R is a mean Earth radius and $S(\bullet)$ Stokes's kernel function (Sideris 2013). Equation (1) is a 1D convolution with respect to longitude, so that after employing the addition theorem of the discrete Fourier transform, Stokes's integral can be evaluated for the specific parallel (Sideris 2013). Within the GEOMED2 project a tapered version of the Wong-Gore (Wong and Gore 1969) modification of Stokes's kernel function has been employed through the SPFOUR software of the GRAVSOFT package (Forsberg and Tscherning 2008). The tapering has been employed so as to remove the same wavelengths from Stokes' kernel, as was done with the input gravity data, while the upper bound was set being 10° higher than the lower one. The final geoid estimate was obtained through addition of the EIGEN6C4 geoid to d/o 1,000, i.e. the restore step. The resulting geoid models are called gravimetric (using surface data only) and altimetric geoid solution, respectively.

4 Results and Validation

Comparison of the estimated geoids with the 'oceanographic' geoid model (hereafter 'CLS geoid'), based on the Mean Sea Surface CNES-CLS 15 (https://www.aviso.altimetry.fr/en/data/products/auxiliary-products/mss.html) minus MDT SOCIB (Rio et al. 2014), constitutes an independent validation of our models. The results are listed in Table 3, which also gives results for EIGEN6C4, i.e. as the current reference.

Figure 3 shows the difference between the CLS and the gravimetric and altimetric (DTU15 data) geoids. As one can see, the gravimetric geoid has large differences with respect to the CLS estimate around the Balearic Islands, in the Alboran Sea, the Aegean Sea, south of Crete and south of Cyprus. The discrepancies in the Alboran Sea, south of Crete and Cyprus may be related to ocean dynamics (large Eddy Kinetic Energy), while the discrepancies in the Aegean Sea may be due to errors in the altimetric estimate (short arcs due to the large number of islands in this region). The large differences around the Balearic Islands are unexpected and are probably due to some wrong interpolation of the ground data or to high non corrected bathymetric effects which need to be carefully checked in future investigations.

On the other hand, and as expected, the discrepancies between the CLS and the altimetric (DTU15) geoids are smoother since the two estimates are based on more homogeneous and partly the same data.

Furthermore, the relative accuracy of the geoid models is evaluated through the computation of the ocean Mean Dynamic Topography (MDT; MSS minus geoid) and the inferred mean geostrophic currents using the method described in Mulet et al. (2012), and this is done as a function of spatial scale and region. Here, the CNES-CLS 15 MSS is used, and scales 10–200 km are analyzed. For this test, EIGEN6C4 has been considered as the benchmark. These computations showed that the altimetric geoid is more accurate than EIGEN6C4 at scales below 50 km, and equivalent from 50 to 200 km (see Fig. 4, top panels). On the other hand, the gravimetric geoid is equivalent to EIGEN6C4 to 100 km, and rapidly getting worse for smaller scales. Inspection of results for the gravimetric and altimetric geoids shown in Fig. 4 at the scale of 50 km, computed in 1° bins, reveal that the gravimetric geoid is more accurate in certain regions, indicated by the black dot, but that it suffers from noise at small spatial scales. Specifically, it is more accurate in the Alboran Sea, the Sicily channel, the Ionian Sea and the Levantine (zonal). The discrepancies observed in the gravimetric geoid are due to a combination of insufficient geographical coverage of the survey near the coasts and in some places between the cruises (Balearic islands), inhomogeneous precision, and remaining bias issues. The results confirm that altimetry derived gravity data such as DTU15 or UCSD V24.1 models have to be used to fill the gaps (Lequentrec-Lalancette and Rouxel 2010) if one requires ultimate precision. That will be done in a next step.

Table 3 Mean and standard deviation (StD) of the geoid height difference, in m

Geoid height difference between	Mean	StD
CLS & gravimetric geoid	0.048	0.083
CLS & altimetric geoid (DTU15 data)	0.054	0.050
CLS & EIGEN6C4 geoid	0.052	0.055
Gravimetric & altimetric geoid	0.010	0.063

5 Conclusions and Outlook

The intermediate gravimetric geoid presented in this paper is not competitive yet, since, as a whole, it is less accurate than EIGEN6C4 and less accurate than a geoid computed with altimeter-inferred gravity. Still, for certain parts of the Mediterranean the gravimetric geoid model is the most

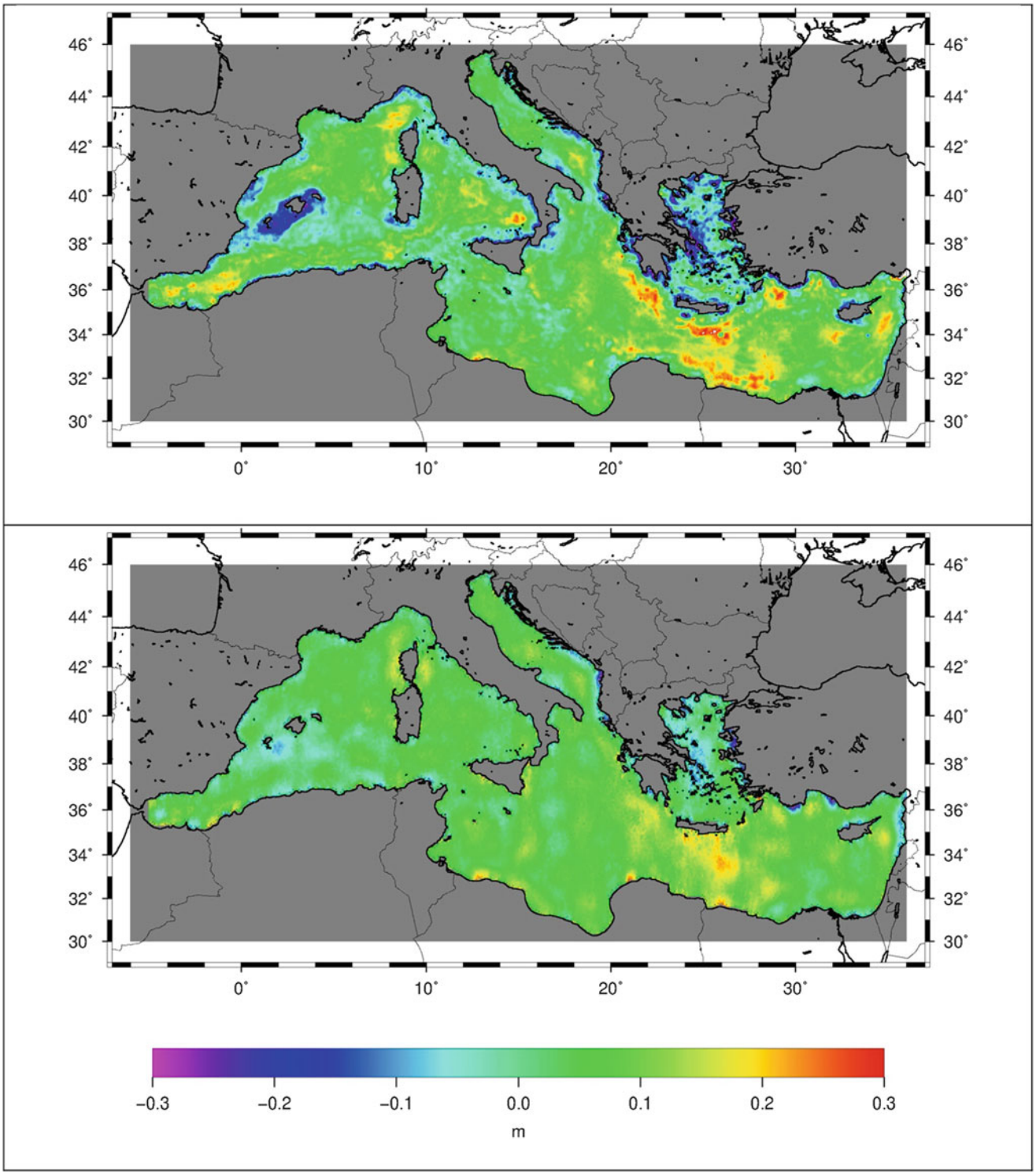

Fig. 3 The geoid height difference between the CLS and the gravimetric geoid estimate (top) and the altimetric geoid (bottom)

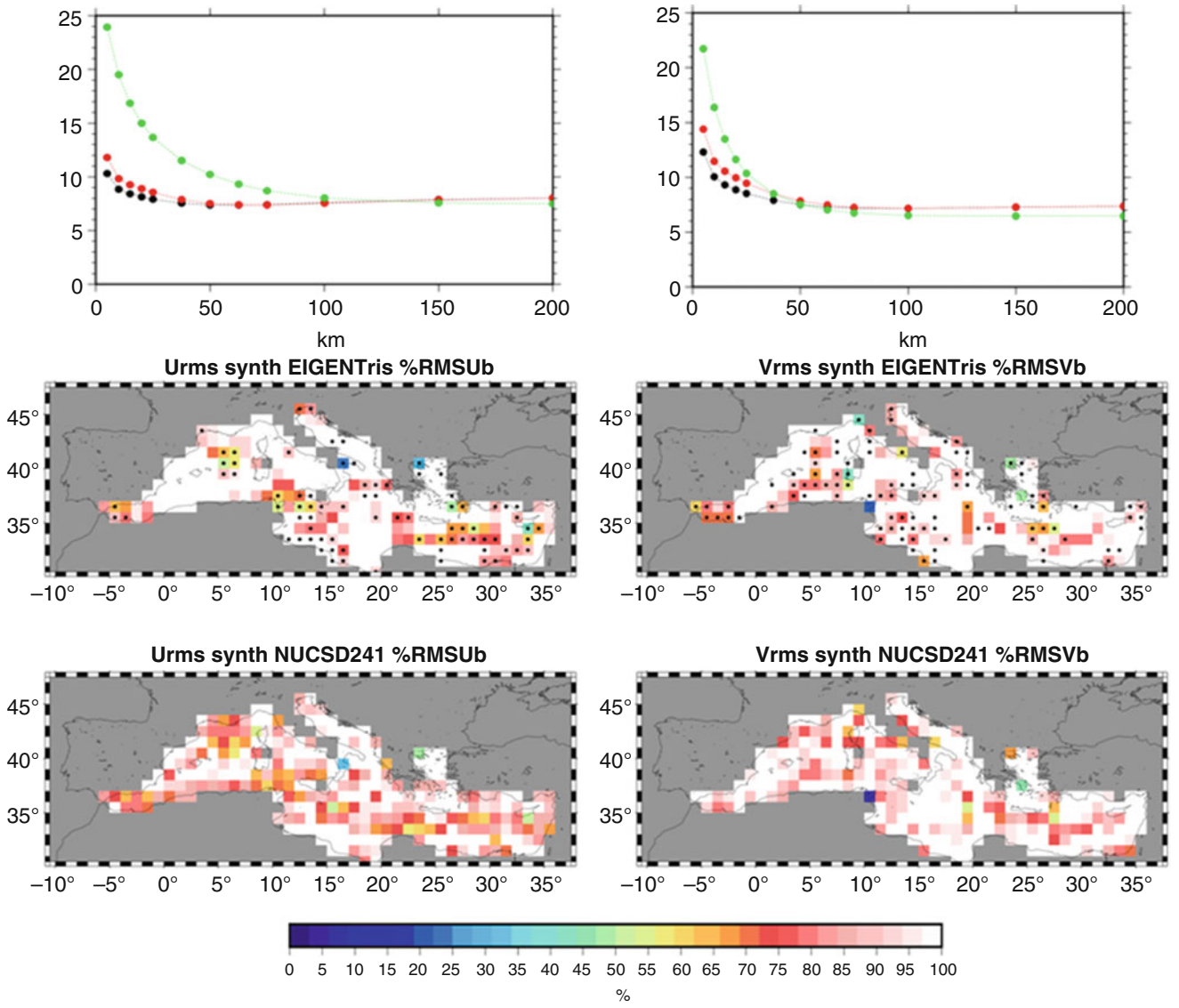

Fig. 4 The RMS, in cm/s, of the difference between drifter-observed geostrophic current speeds and geoid-model-inferred as a function of spatial scale (top) for zonal (left) and meridional (right) components. Black = altimetric geoid, red = EIGEN6C4 geoid, green = gravimetric geoid. 1° × 1° binned maps of the ratio between RMS of predicted minus drifter observed velocities and drifter velocity std. dev. at 50 km scale (middle panel = gravimetric geoid, bottom panel = altimetric geoid). Black dots indicate where the gravimetric geoid compares better

accurate in the comparisons between drifter-observed and geoid derived geostrophic current speeds. Thus, the altimetric geoid proved to be the most accurate at this point of the project, but improvements of the gravimetric solution are expected. Particularly, positive impacts are expected by debiasing of shipborne data per track, and by a more drastic exclusion of marine data, which can reduce the highest errors of the Morelli dataset (up to 26 mGal; Lequentrec-Lalancette et al. 2016). More marine data will be added in some areas like near the Balearic Islands. To obtain a full coverage over sea, altimetric and gravimetric data will be combined according to methods described in (Lequentrec-Lalancette et al. 2003, Lequentrec-Lalancette and Rouxel 2010). Over the land areas some gaps will be filled too. The methodology of gridding will be improved near the coasts and some tests with different computation methods will be performed (collocation, other Stokes modification kernel). The final geoid model for the Mediterranean, taking all of the above into account, is expected to be available in 2018.

References

Allan TD, Morelli C (1971) A geophysical study of the Mediterranean Sea. NATO Subcommittee on oceanographic Research, Technical reports n 55, 141 pp

Andersen OB, Knudsen P, Berry P (2010) The DNSC08GRA global marine gravity field from double retracked satellite altimetry. J Geod 84(3):191–199. https://doi.org/10.1007/s00190-009-0355-9

Andersen OB, Knudsen P, Kenyon S, Factor JK, Holmes S (2017) Global gravity field from recent satellites (DTU15) – Arctic improvements. EAGE First Break 35(11):37–40

Bruinsma SL, Förste C, Abrikosov O, Lemoine JM, Marty JC, Mulet S, Rio MH, Bonvalot S (2014) ESA's satellite-only gravity field model via the direct approach based on all GOCE data. Geophys Res Lett 41(21):7508–7514. https://doi.org/10.1002/2014GL062045

Farr TG et al (2007) The shuttle radar topography mission. Rev Geophys 45:RG2004. https://doi.org/10.1029/2005RG000183

Förste C, Bruinsma SL, Abrikosov O, Lemoine JM, Marty JC, Flechtner F, Balmino G, Barthelmes F, Biancale R (2014) EIGEN-6C4 The latest combined global gravity field model including GOCE data up to degree and order 2190 of GFZ Potsdam and GRGS Toulouse. GFZ Data Services. https://doi.org/10.5880/icgem.2015.1

Forsberg R, Tscherning CC (2008) Gravsoft manual

Geophysical data report of the Eastern Mediterranean Sea : RRS Shackleton cruises 3/72, 5/72, 1/74, July 28-Sept. 1, 1972, Oct. 4-Nov. 9,1972, May 9-June 29, 1974 (1974) University of Cambridge, Department of Geodesy and Geophysics, Cambridge, The University

Haagmans R, de Min E, Van Gelderen M (1993) Fast evaluation of convolution integrals on the sphere using 1D FFT, and a comparison with existing methods for stokes' integral. Man Geod 18:227–241

Hirt C, Rexer M, Claessens S, Rummel R (2017) The relation between degree-2160 spectral models of Earth's gravitational and topographic potential – a guide on global correlation measures and their dependency on approximation effects. J Geod 91(10):1179–1205. https://doi.org/10.1007/s00190-017-1016-z

Lequentrec-Lalancette MF, Rouxel D (2010) Comparison of a Marine Gravimetric Geoid and Global Satellite Model in the Atlantic Ocean. In: Lacoste-Francis H (ed) Proceedings of ESA living planet symposium, held on 28 June–2 July 2010 at Bergen in Norway. ISBN 978-92-9221-250-6. ESA SP-686, 2010, id.499

Lequentrec-Lalancette MF, Rouxel D, Hernandez F, Schaeffer P (2003) Mapping of the free air anomaly using altimetric and marine gravity data. In: Tziavos (ed) 3rd Meeting of the International Gravity and Geoid Commission (IGGC), Gravity and Geoid 2002–GG2002, pp 353–357

Lequentrec-Lalancette MF, Salaün C, Bonvalot S, Rouxel D, Bruinsma S (2016) Exploitation of marine gravity measurements of the mediterranean in the validation of global gravity field models. In: International Association of Geodesy Symposia, Springer, Berlin

Mulet S, Rio MH, Bruinsma S (2012) Assessment of the preliminary GOCE geoid models accuracy for estimating the ocean mean dynamic topography. Mar Geod 35:314–336. https://doi.org/10.1080/01490419.2012.718230

Rio MH, Pascual A, Poulain PM, Menna M, Barcelo B, Tintoré J (2014) Computation of a new mean dynamic topography for the Mediterranean Sea from model outputs, altimeter measurements and oceanographic in-situ data. Ocean Sci 10(4):731. https://doi.org/10.5194/osd-11-655-2014

Sandwell DT, Müller RD, Smith WHF, Garcia E, Francis R (2014) New global marine gravity model from CryoSat-2 and Jason-1 reveals buried tectonic structure. Science 346(6205):65–67. https://doi.org/10.1126/science.1258213

Sideris MG (2013) Geoid determination by FFT techniques. In: Sansò F, Sideris M (eds) Geoid determination. Lecture notes in earth system sciences, vol 110. Springer, Berlin

Wong L, Gore R (1969) Accuracy of geoid heights from modied stokes kernels. Geophys J R Astron Soc 18:81–91

Evaluation of Altimetry Data in the Baltic Sea Region for Computation of New Quasigeoid Models over Poland

Joanna Kuczynska-Siehien, Adam Lyszkowicz, and Michael G. Sideris

Abstract

The paper presents the comparison and validation of currently available gravity anomalies from the satellite altimetry models with the shipborne and airborne gravity anomalies along the Polish coast and in the Baltic Sea. The mean value of differences between the investigated DTU10 and GMG V24.1 altimetry-derived models is equal to 0.02 mGal. However, significant differences can be seen in the coastal areas. Shipborne and airborne marine gravity datasets, collected over the past 65 years by various institutions, were also compared.

Furthermore, the new gravimetric quasigeoid models for the territory of Poland were computed using the new gravity data from the satellite altimetry, the EIGEN-6C4 geopotential model, and the SRTM elevation model. The accuracy of these models, estimated using the ASG-EUPOS permanent GNSS stations, reaches 1.4 cm.

Keywords

Baltic Sea gravity data · Regional quasigeoid model · Satellite altimetry models

1 Introduction

Numerous gravimetric geoid/quasigeoid models in Poland were computed using the remove-compute-restore (RCR) method with Fast Fourier Technique (FFT) (e.g. Lyszkowicz and Denker 1994), the Least Squares Collocation (LSC) approach (e.g. Lyszkowicz 2010; Szelachowska and Krynski 2014) and the Royal Institute of Technology (KTH) method (Kuczynska-Siehien et al. 2016). In all cases the same set of mean gravity anomalies for the Baltic Sea, obtained based on the data from the geophysical marine missions (Lyszkowicz 1994), were used. These marine gravity anomalies cover the very limited southern part of the Baltic Sea. The currently available gravity data from the satellite altimetry, e.g. the DTU10 (Andersen 2010) and V24.1 (Sandwell et al. 2014) global marine gravity models, cover the whole Baltic Sea. Furthermore, the recent geoid/quasigeoid models involved Earth Geopotential Model 2008 (EGM2008) (Pavlis et al. 2012), and Shuttle Radar Topography Mission (SRTM) data as a digital elevation model (DEM). These data can be also replaced with the latest global geopotential models (GGM) and DEM.

Considering the above, the first aim of the study is to compare and validate the gravity anomalies from the DTU10 and V24.1 models with the shipborne gravity anomalies along the Polish coast and in the Baltic Sea. In the next step, the new gravimetric quasigeoid models for the territory of Poland are computed using the new gravity data from the satellite altimetry, the EIGEN-6C4 geopotential model (Förste et al. 2014), and the SRTM 1 Arc-Second Global (https://www2.jpl.nasa.gov/srtm/) elevation model.

J. Kuczynska-Siehien (✉) · M. G. Sideris
Department of Geomatics Engineering, University of Calgary, Calgary, AB, Canada

J. Kuczynska-Siehien (✉)
Faculty of Geodesy, Geospatial and Civil Engineering, University of Warmia and Mazury in Olsztyn, Olsztyn, Poland
e-mail: joanna.kuczynska@uwm.edu.pl

A. Lyszkowicz
Polish Air Force Academy, Deblin, Poland

J. T. Freymueller, L. Sanchez (eds.), *International Symposium on Advancing Geodesy in a Changing World*, International Association of Geodesy Symposia 149, https://doi.org/10.1007/1345_2018_35

The accuracy of the computed new models is estimated using the high precision ASG-EUPOS network of permanent Global Navigation Satellite System (GNSS) stations connected to the new Polish vertical datum PL-EVRF2007-NH.

2 Data

Both investigated satellite altimetry models, V24.1 and DTU10, have a spatial resolution of 1′ (1–2 km). Global Marine Gravity (GMG) V24.1 combines radar altimeter measurements from CryoSat-2 and Jason-1 satellites (Sandwell et al. 2014). The model is substantially improved in comparison to the previous versions based on retracked Geosat and ERS-1 satellites data (Sandwell and Smith 2009). The second GMG model used, DTU10, was developed based on ERS-2 and ENVISAT satellites data (Andersen 2010). The DTU10 model is an improved version of the DNSC08GRA model, which was derived using double retracking of ERS-1 geodetic mission waveform data (Andersen et al. 2010).

The Baltic Sea gravity data used in the study consists of five datasets (Table 1). The dataset #1 is the result of digitalization of 1:200,000 scale gravimetric maps and includes 1,293 Faye anomalies. The dataset #2 contains the ship-track gravity data from Zaria and Turlejski cruises along the Polish Coast of the Baltic Sea. Mean 5′ × 5′ free-air gravity anomalies for the northern part of the Baltic Sea, obtained from Finnish Geodetic Institute, comprise the dataset #3. The dataset #4 is a collection of mean 1′ × 1′ free-air gravity anomalies computed from the ship gravity measurements which were carried out by the research team from Riga in 1978 and 1980. Airborne gravity data are included in the dataset #5.

Terrestrial gravity data used in the study consists of nine sets of Faye gravity anomalies from Poland and the neighbouring countries (Krynski 2007). The gravity anomalies were interpolated on 1′ × 1′ grid nodes for the area 48°N < φ < 55°N and 12°E < λ < 26°E using GEOGRID program from the GRAVSOFT package (Forsberg and Tscherning 2008). The interpolation was performed using the least square collocation method with the correlation length 2.55 km and the standard uncertainties for the observations 1 mGal.

The Gravity Recovery and Climate Experiment (GRACE) and the Gravity field and steady-state Ocean Circulation Explorer (GOCE) missions' data brought an improvement in the determination of global geopotential models. The used EIGEN-6C4 model (Förste et al. 2014) is a global combined gravity field model up to degree and order 2190. It was elaborated jointly by GFZ Potsdam and GRGS Toulouse from the Laser Geodynamics Satellite (LAGEOS) data, 10 years of GRACE RL03 data, GOCE data, terrestrial data up to degree 370, DTU12 ocean geoid data and EGM2008 geoid heights for lands.

Chosen DEM, SRTM 1 Arc-Second Global, has a resolution of 30 m at the equator, and is provided e.g. by the U.S. Geological Survey (USGS) portal (https://earthexplorer.usgs.gov/). The data has a worldwide coverage with void filled using interpolation methods described in (Reuter et al. 2007).

The obtained geoid models were evaluated on 105 eccentric points of ASG-EUPOS network. It is a network of permanent GNSS stations fully operating since 2008 (Bosy et al. 2008). Normal heights of the eccentric points were determined in PL-EVRF2007-NH, whereas ellipsoidal ones in ETRF2000 e. 2011. The ellipsoidal heights of the GNSS network points were determined with an accuracy of 1 cm. The normal heights of these points were determined by connecting them to the national precise levelling network.

3 Comparison of Marine Gravity Data

Firstly, the DTU10 and GMG V24.1 altimetry-derived models were compared to one another to evaluate the differences between them. Both models were acquired on a regular latitude/longitude 1′ × 1′ grid nodes for the area 54°N < φ < 60°N and 10°E < λ < 27°E, i.e. for the Baltic Sea. The differences between gravity anomalies from these models are shown in Fig. 1 and their statistics in the first raw of Table 2. Their mean value is equal to 0.02 mGal. However, significant differences up to several dozens of mGals can be seen, mostly near the coast. The problem with the accuracy of satellite derived gravity data close to the coast is well-known (e.g. Deng et al. 2002; Amos et al. 2005; Claessens 2012). This is caused mainly by the poorer accuracy of applied corrections and losing track close to the coast.

Table 1 Statistics and origin of marine gravity datasets [mGal]

Dataset	Origin	Number of points	Min	Max	Mean	STD
#1	Institute of Geodesy and Cartography in Warsaw, Poland, 1972	1,293	−32.71	23.80	−0.85	11.36
#2	Institute of Geodesy and Cartography in Warsaw, Poland, 1971 and 1972	1,216	−31.90	16.70	−2.36	10.70
#3	Finnish Geodetic Institute, Finland, 1993	1,346	−83.46	18.17	−36.11	15.52
#4	Space Research Centre PAS, Poland, 1994	14,981	−29.74	22.37	−3.88	12.89
#5	Kort&Matrikelstyrelsen, Denmark, 1999	4,833	−80.60	29.70	−17.3	20.10

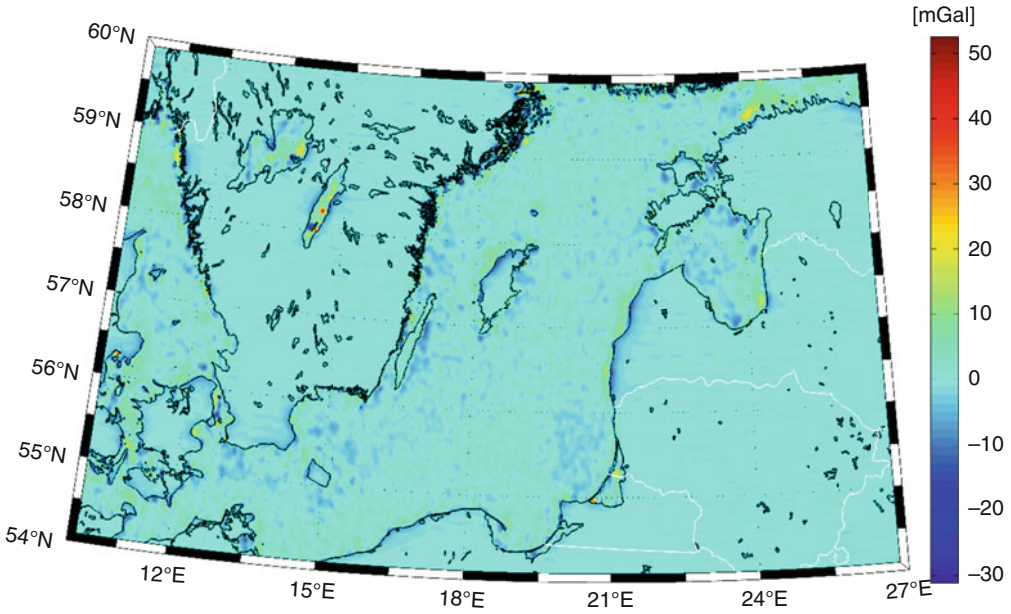

Fig. 1 Comparison of DTU10 with GMG V24.1

Table 2 Comparison of altimetric and marine gravity datasets with GMG V24.1 [mGal]

Dataset	Number of outliers	Min	Max	Mean	STD
DTU10	–	−31.15	52.61	0.02	2.40
#1	56	−7.31	5.79	−3.11	2.20
#2	59	−7.94	4.63	−2.94	2.29
#3	24	−9.28	8.59	−0.68	2.81
#4	304	−6.33	4.47	−0.88	1.30
#5	79	−9.60	9.40	0.60	2.70

Furthermore, all gravity datasets, containing shipborne and airborne gravity data, were compared to the GMG V24.1 model (Figs. 1, 2, 3, 4, 5, 6) as it is the newest one and the differences between this model and DTU10 are negligible out of coastal areas. Since marine gravity observations near the Polish coast and in the other areas of the Baltic Sea have been collected over the past 65 years by various institutions, they are stored in different formats and in different, not always known, datums. All datasets were analyzed and transformed, where necessary and possible, to ensure consistency between them. For the comparison, the original gridded anomalies from the GMG V24.1 model were interpolated, using bilinear interpolation, to the positions of the shipborne and airborne gravity data. The statistics of differences after removing 3σ outliers are shown in Table 2. Significant differences between datasets (exceeding the value of standard deviation) are not noticed. Dataset #1 and #2 have similar values of gravity anomalies. It can be explained by the fact that these datasets were created at the same time. Due to the largest number of points and the lowest standard deviation, the dataset #4 was chosen for further investigation.

4 Quasigeoid Computation and Results

In the next step, the three quasigeoid models were determined for the area of Poland and the southern part of the Baltic Sea, using the RCR method employing FFT. The differences between them result from the use of the three different marine gravity datasets, i.e. the shipborne gravity dataset #4, the DTU10 model and the GMG V24.1 model. As the RCR method is well-known, it will be only briefly described here. More details can be found in e.g. Sansò and Sideris (2013). The general concept of the RCR method consists of the following steps: (1) removing the effects of the Earth's gravity field and the topography from the data, (2) computing the residual geoid heights using FFT method, (3) restoring the effect of the Earth's gravity field and the topography in geoid heights. As the used Faye gravity anomalies Δg_F have already removed the terrain effect, the residual gravity anomalies Δg_{res} are obtained through removing from them the long wavelength component Δg_{GGM} of the Earth's gravity field, which is calculated from a GGM:

$$\Delta g_{res} = \Delta g_F - \Delta g_{GGM} \tag{1}$$

where

$$\Delta g_{GGM}(r,\varphi,\lambda) = \frac{GM}{r^2}\sum_{n=2}^{n_{max}}(n-1)\left(\frac{a}{r}\right)^n \sum_{m=0}^{n}(C_{nm}cosm\lambda + S_{nm}sinm\lambda)\,P_{nm}(sin\varphi) \tag{2}$$

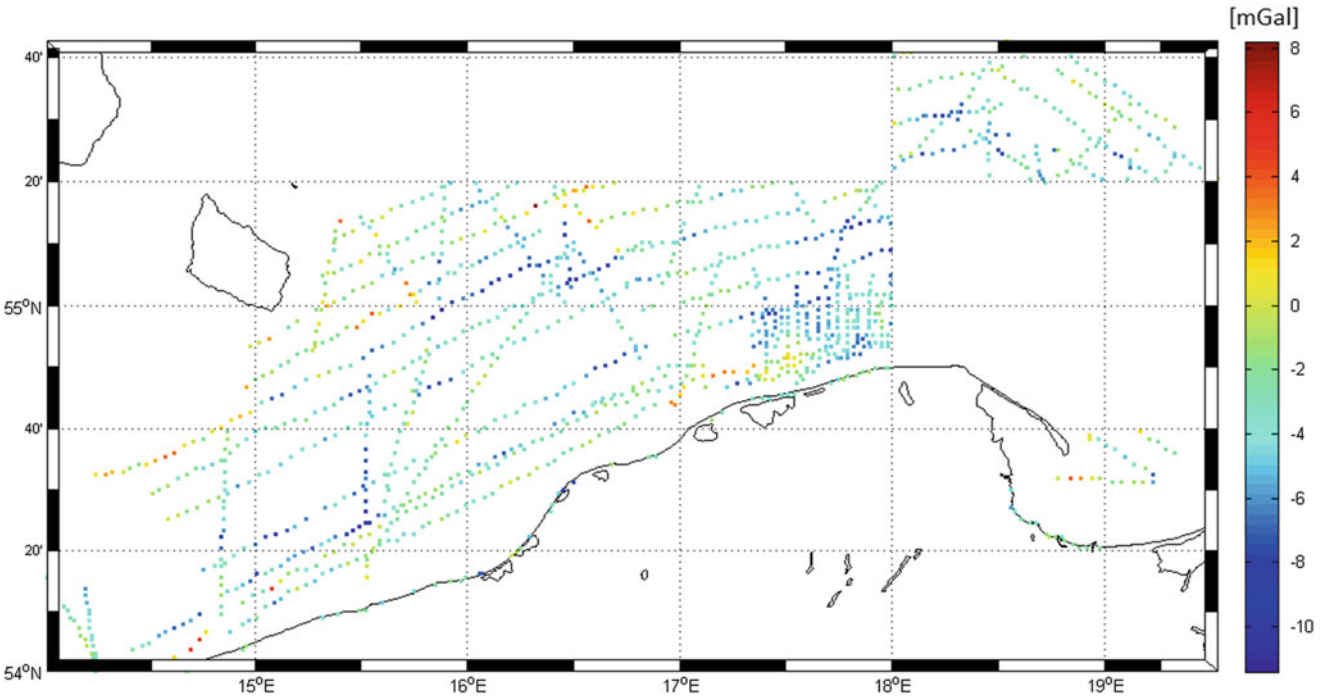

Fig. 2 Comparison of dataset #1 with GMG V24.1

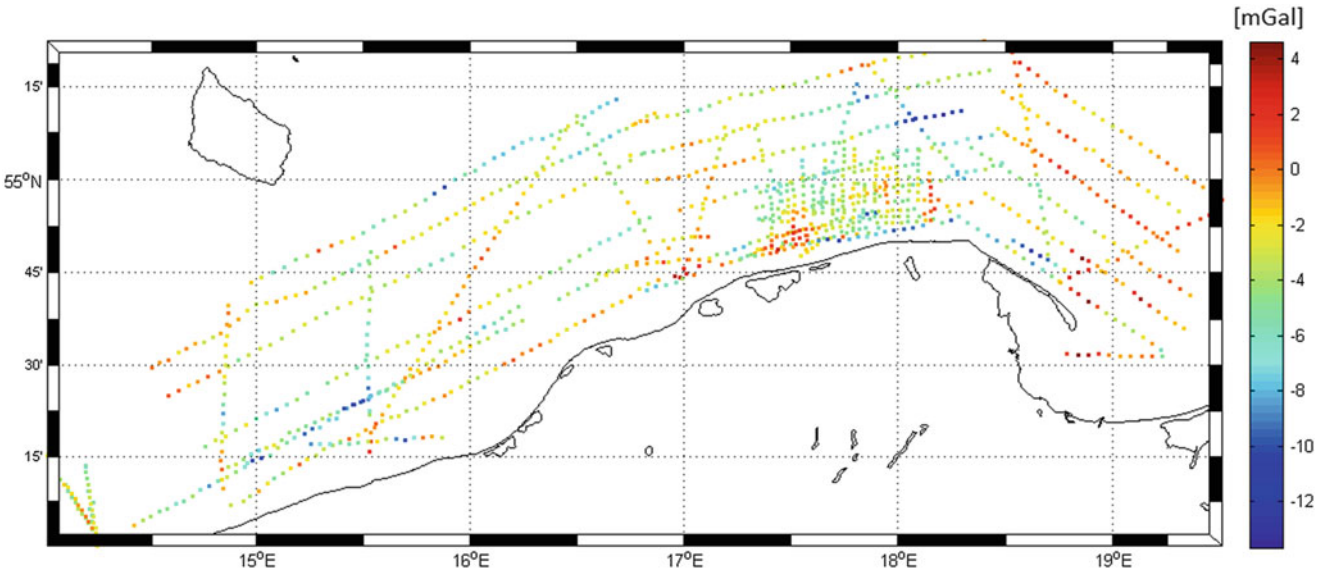

Fig. 3 Comparison of dataset #2 with GMG V24.1

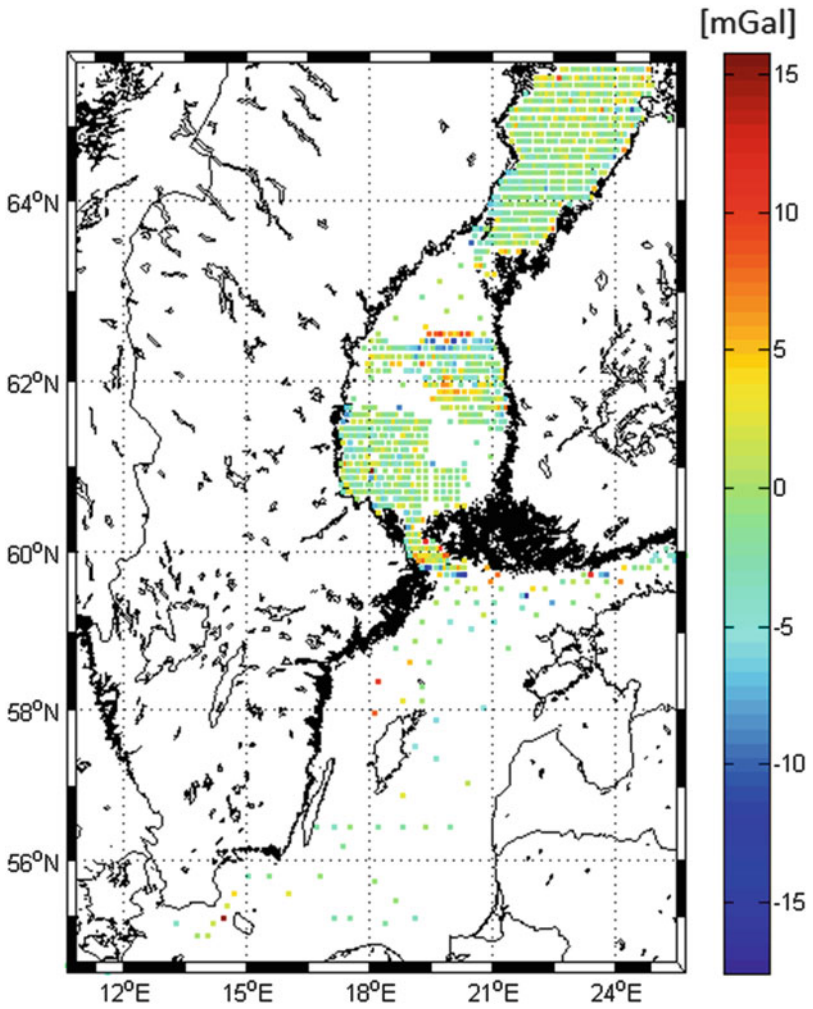

Fig. 4 Comparison of dataset #3 with GMG V24.1

where C_{nm}, S_{nm} are fully normalized spherical harmonic coefficients of degree n and order m, n_{max} is the maximum degree of GGM, GM is the product of the Newtonian gravitational constant and mass of the geopotential model, r, φ, λ are spherical polar coordinates, a is the equatorial radius of geopotential model and P_{nm} are the fully normalized associated Legendre'a functions (Torge 2001).

Residual geoid heights $N_{\Delta g_{res}}$ in the FFT method are computing from the Stokes formula in the planar approximation (Vaníček and Christou 1994):

$$N_{\Delta g_{res}} = \frac{1}{\gamma}\Delta g_{res}(x,y) * l_n(x,y) \tag{3}$$

where:

$$l_n(x,y) = \frac{1}{2\pi}\left(x^2+y^2\right)^{-\frac{1}{2}} \tag{4}$$

is planar form of Stokes' kernel function and * denotes convolution.

Gravimetric geoid heights are obtained according to the formula:

$$N = N_{GGM} + N_{\Delta g_{res}} + N_H \tag{5}$$

where N_{GGM} is determined from GGM:

$$N_{GGM}(r,\varphi,\lambda) = N_0 + \frac{GM}{r\gamma_0}\sum_{n=2}^{n_{max}}\left(\frac{a}{r}\right)^n \sum_{m=0}^{n}(C_{nm}cosm\lambda + S_{nm}sinm\lambda)\,P_{nm}(sin\varphi) \tag{6}$$

where γ_0 is the normal gravity on the ellipsoid and N_0 results from the difference in the mass of the Earth used in IERS Convention and GRS80 ellipsoid.

Due to the displacement of the topographic masses in gravity reductions, changing the gravitational potential (the indirect effect of the topographic reduction), the computed surface is not the geoid, but a slightly different surface called

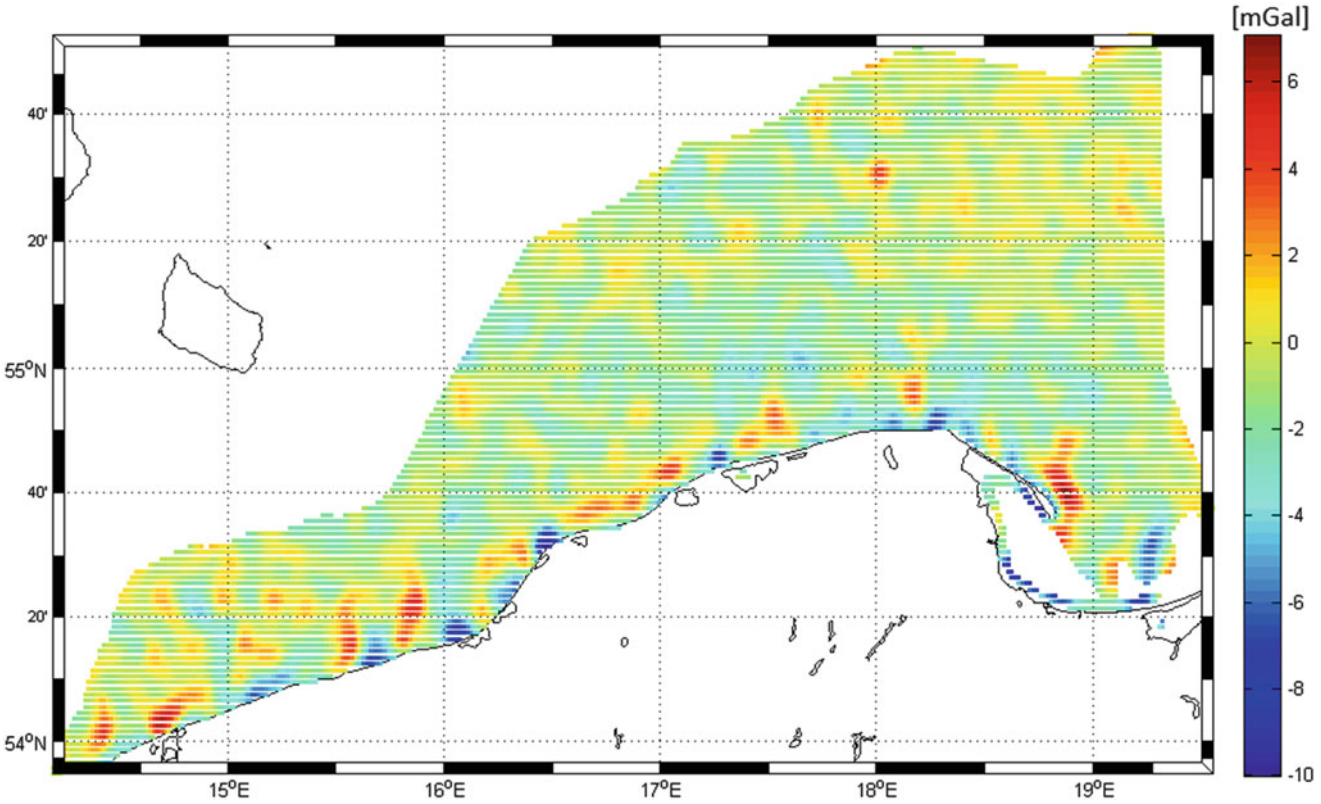

Fig. 5 Comparison of dataset #4 with GMG V24.1

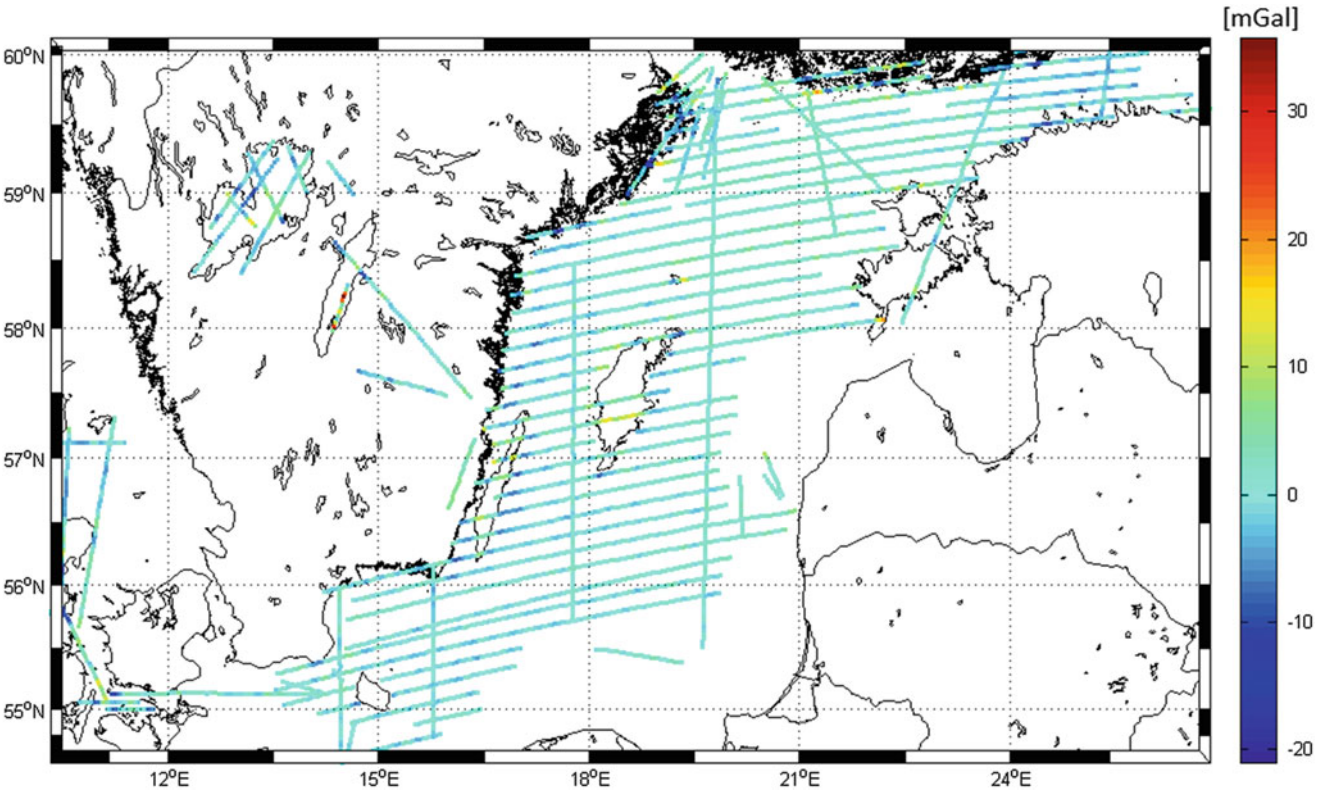

Fig. 6 Comparison of dataset #5 with GMG V24.1

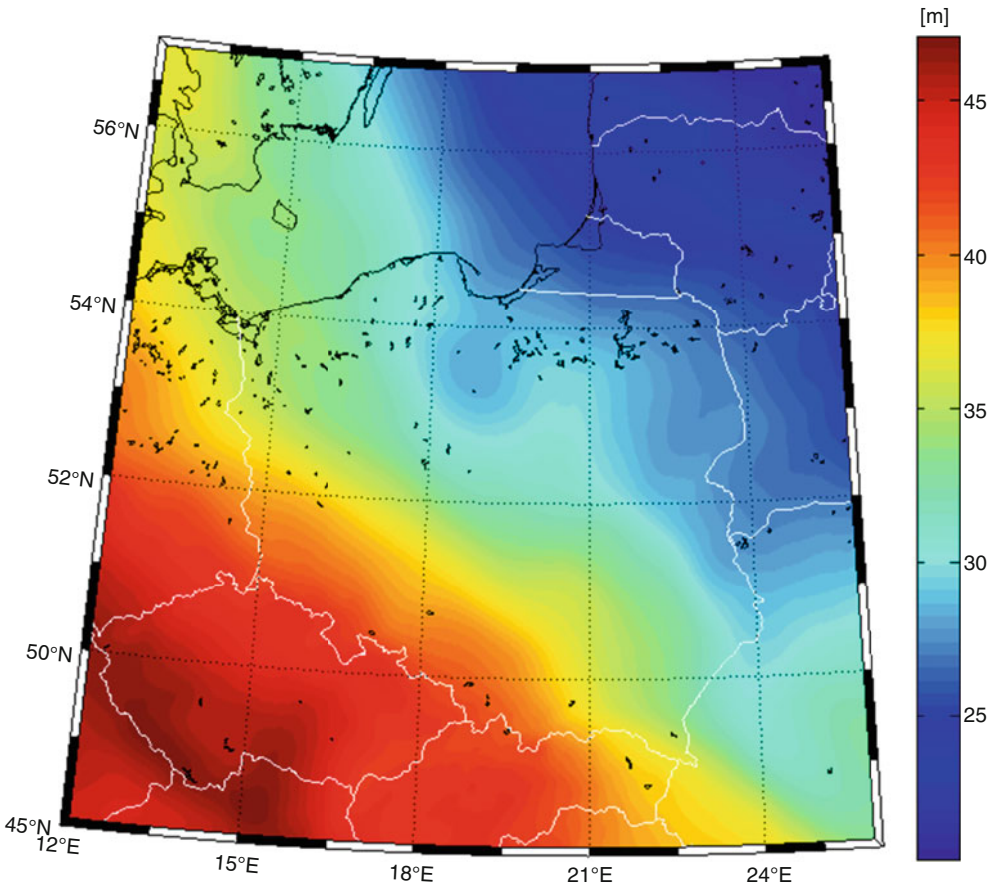

Fig. 7 Quasigeoid model from terrestrial gravity anomalies and gravity dataset #4

the co-geoid. The vertical distance between the geoid and the co-geoid can be computed from (Grushinsky 1976):

$$N_H = -\frac{\pi G \rho}{\gamma_m} H_P^2 \tag{7}$$

where ρ is mass density, H_P is topographic height of the point P and γ_m is the mean normal gravity on the reference ellipsoid.

The transformation of the geoid undulation N to the height anomaly ζ is realized, using the Bouguer anomaly Δg_B, according to the formula, e.g. (Torge and Müller 2012):

$$\zeta = N - \frac{\Delta g_B}{\gamma_m} H_P \tag{8}$$

The gravity anomalies, used for the quasigeoids determination, were prepared by merging the terrestrial gravity anomalies (described in Data) with the marine gravity anomalies (i.e. dataset #4, DTU10 and GMG V24.1). Moreover, the EIGEN-6C4 model was used for calculating the residual gravity anomalies and the geoid undulation N_{GGM}. The SRTM 1 Arc-Second Global DEM model was used to compute the indirect effect of topography. The GRAVSOFT package (Forsberg and Tscherning 2008) was applied for the computation of the quasigeoid models. The results are shown in Fig. 7 and in Table 3.

Table 3 Statistics of computed quasigeoid models and their differences [m]

Model	Min	Max	Mean	STD
quasi#1	20.31	47.06	33.55	6.92
quasi#2	20.32	47.33	33.59	6.91
quasi#3	20.30	47.33	33.58	6.92
quasi#1 – quasi#3	−0.70	0.70	−0.04	0.09
quasi#1 – quasi#2	−0.70	0.71	−0.04	0.10
quasi#2 – quasi#3	−0.11	0.09	−0.01	0.02

Marine gravity data included: quasi#1 – Dataset #4; quasi#2 – DTU10; quasi#3 – GMG V24.1

The computed quasigeoids were compared (Fig. 8, Table 3) and evaluated on 105 eccentric points of ASG-EUPOS permanent GNSS stations (Figs. 9, 10, Table 4). Theoretically, the calculated quasigeoid heights ζ should be equal to the difference between ellipsoidal heights h obtained by GNSS measurements and normal heights H^n. In practice, due to the occurrence of various random and systematic errors in

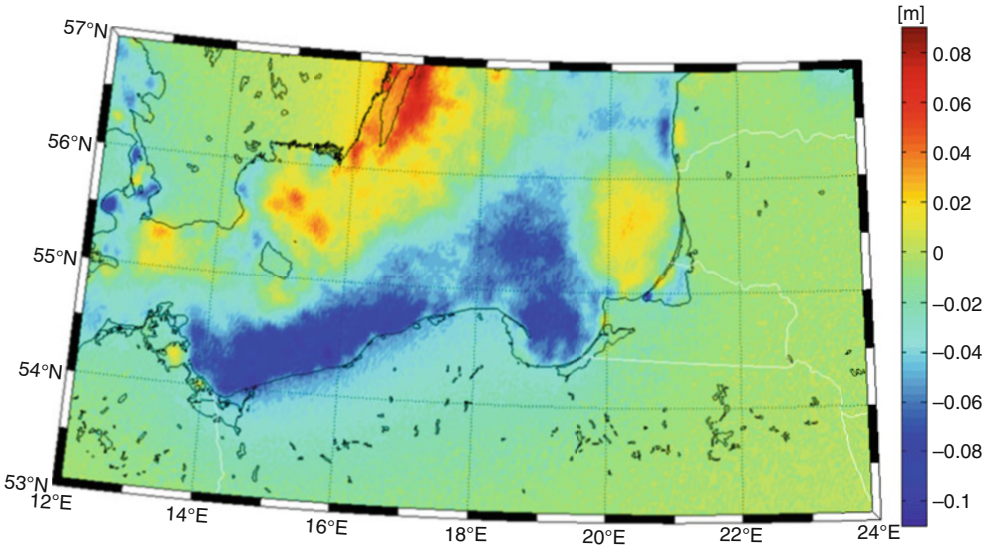

Fig. 8 Comparison of quasigeoid model from terrestrial gravity data combined with DTU10 and with GMG V24.1

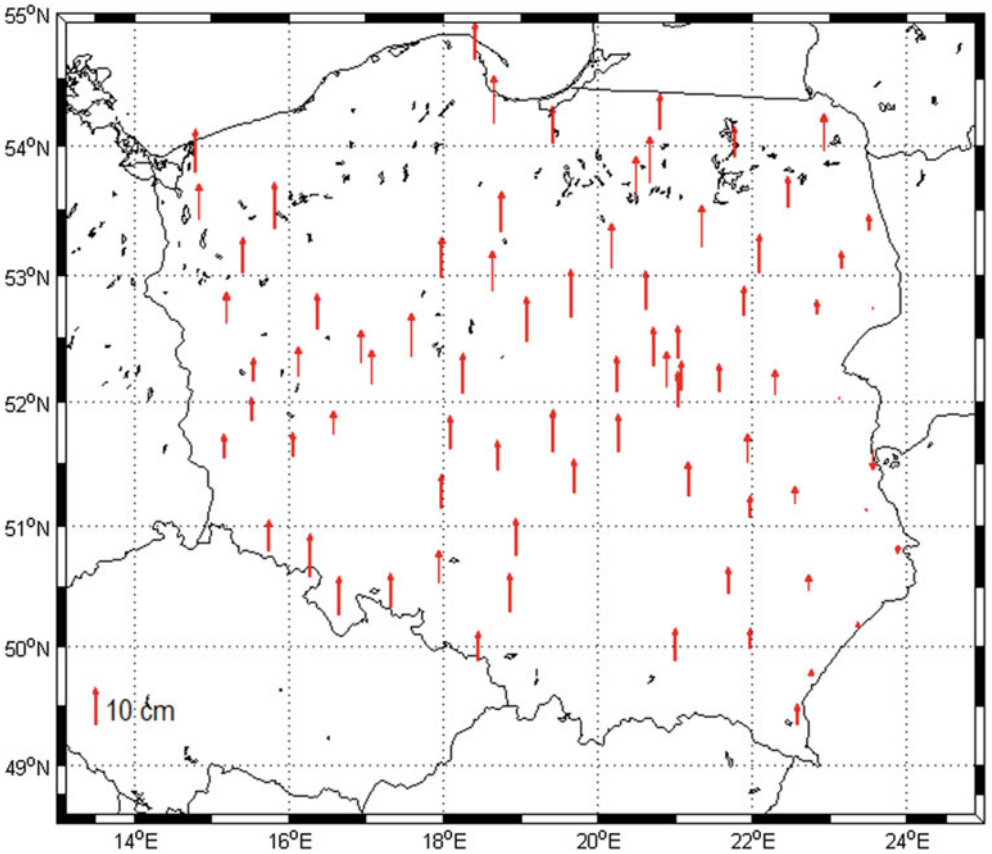

Fig. 9 Evaluation of the accuracy of quasigeoid model from terrestrial gravity anomalies and gravity dataset #4 on GNSS/levelling points of the Polish ASG-EUPOS network

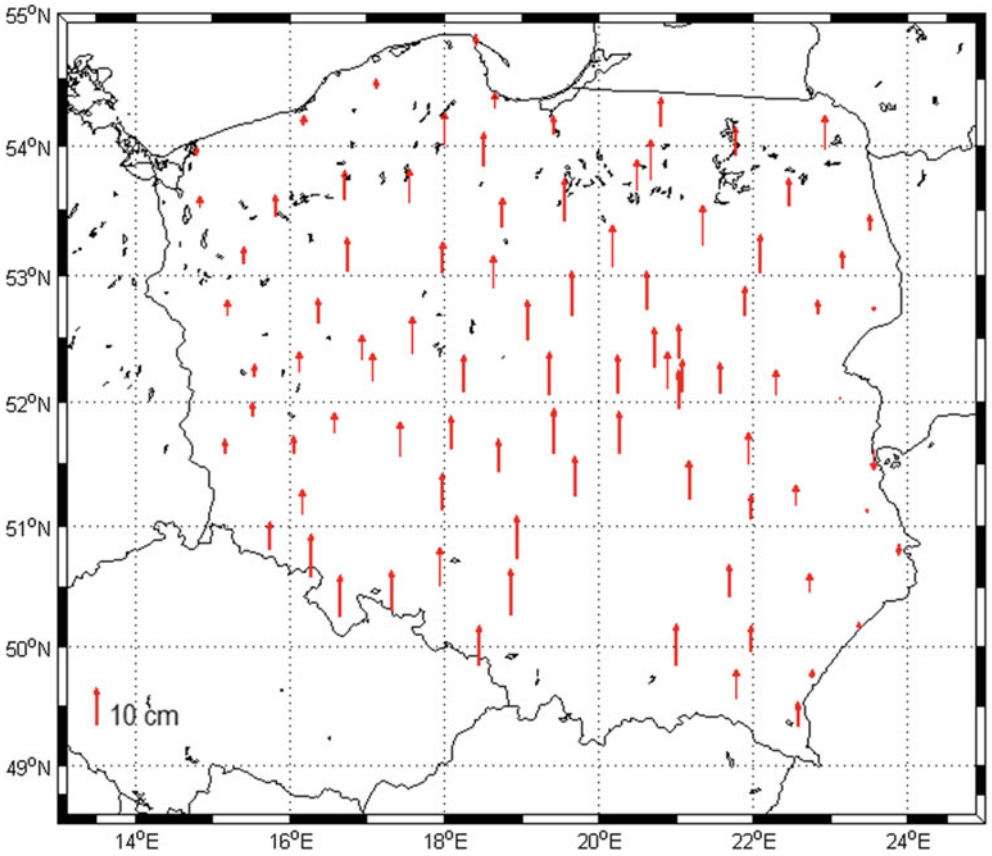

Fig. 10 Evaluation of quasigeoid model from terrestrial gravity anomalies and GMG V24.1 on GNSS/levelling points of the Polish ASG-EUPOS network

Table 4 Estimated accuracy of computed quasigeoid models [cm]

Quasigeoid model	Number of outliers	STD before fit	STD after fit
quasi#1	21	3.6	1.4
quasi#2	5	4.2	2.4
quasi#3	7	3.7	2.0

Marine gravity data included: quasi#1 – Dataset #4; quasi#2 – DTU10; quasi#3 – GMG V24.1

all components, the relationship for each i point is given by:

$$h_i - H_i^n - \zeta_i = \varepsilon_i \tag{9}$$

The elimination of systematic factors ε_i is necessary in order to properly assess the calculated quasigeoid models. After testing several parametric models, the 7-parameter model (Fotopoulos 2003) was used in the evaluation.

From the results in Table 3, the differences between the models are small, i.e. the mean value do not exceed four centimeters. Comparing the quasigeoid models obtained based on the altimetry data, the mean difference in their height anomalies equals 1 cm. As it is seen in Fig. 8, the biggest differences occur in the coastal areas of the Baltic Sea, but they do not exceed 11 cm.

The estimated accuracy, in terms of the standard deviation of differences of height anomalies obtained from the models and corresponding ones from the ASG-EUPOS sites, exceed three centimeters before fitting. After using the 7-parameter model, the minimum standard deviation of differences is 1.4 cm for the quasigeoid model obtained with the dataset #4 as a marine gravity data. However, it can be seen from Fig. 10 that the use of the altimetry data reduced the number of outliers in the northern part of Poland. Furthermore, the differences of height anomalies in that part of the country are much smaller than in the case of using the dataset #4 (Fig. 9).

5 Conclusions

Comparison, made on the Baltic Sea, between the DTU10 and GMG V24.1 satellite altimetry models shows small differences with the mean equals 0.02 mGal. Significant differences, up to several dozens of mGals, occur near the coast, which relates to a well-known problem with the accuracy of satellite derived gravity data. Regarding the investigated five datasets of airborne and shipborne marine gravity, the standard deviation of differences between all datasets and the GMG V24.1 model is 2 mGal and coincides with their

accuracy. Since these data have been collected in different formats and datums, their comparison and validation cannot be done with certainty.

The new quasigeoid models for Poland, through the use of the altimetry-derived gravity data, were extended for the Baltic Sea to 57°N. The accuracy achieved for the both quasigeoids, modelled using the DTU10 and GMG V24.1 data, as it was expected based on the altimetry models' comparison, is similar and equals 2 cm. The achieved accuracy is also comparable to the accuracy of the last quasigeoid models computed for Poland. Although the best accuracy, with the standard deviation 1.4 cm, was achieved for the quasigeoid model based on the marine gravity dataset #4, the number of outliers for this dataset is the most numerous. The use of altimetry data not only reduced the number of outliers, but also increased the accuracy of the quasigeoid model in the northern part of Poland.

Acknowledgements Land and marine gravity data were kindly released from Institute of Geodesy and Cartography in Warsaw, Finnish Geodetic Institute, Polish Space Research Centre PAS and Kort&Matrikelstyrelsen. All figures were prepared using MAP-LAB (Piretzidis and Sideris 2016).

References

Amos MJ, Featherstone WE, Brett J (2005) Crossover adjustment of New Zealand marine gravity data, and comparisons with satellite altimetry and global geopotential models. In: Jekeli C, Bastos L, Fernandes J (eds) Gravity, geoid and space missions. Springer, Berlin, pp 266–271. https://doi.org/10.1007/3-540-26932-0_46

Andersen OB (2010) The DTU10 gravity field and mean sea surface. In: Second international symposium of the gravity field of the Earth (IGFS2), Fairbanks, Alaska

Andersen OB, Knudsen P, Berry PAM (2010) The DNSC08GRA global marine gravity field from double retracked satellite altimetry. J Geod 84:191. https://doi.org/10.1007/s00190-009-0355-9

Bosy J, Oruba A, Graszka W, Leonczyk M, Ryczywolski M (2008) ASG-EUPOS densification of EUREF Permanent Network on the territory of Poland. Reports on Geodesy No 2(85): 105–112

Claessens SJ (2012) Evaluation of gravity and altimetry data in Australian coastal regions. In: Kenyon S, Pacino M, Uri M (eds) Geodesy for planet earth: proceedings of the 2009 IAG symposium, vol 136. Springer, Berlin, pp 435–442. https://doi.org/10.1007/978-3-642-20338-1_52

Deng XL, Featherstone WE, Hwang C, Berry PAM (2002) Estimation of contamination of ERS-2 and POSEIDON satellite radar altimetry close to the coasts of Australia. Mar Geod 25(4):249–271. https://doi.org/10.1080/01490410290051572

Forsberg R, Tscherning CC (2008) An overview manual for the GRAVSOFT geodetic gravity field modelling programs, 2nd edn. Technical University of Copenhagen

Fotopoulos G (2003) An analysis on the optimal combination of geoid, orthometric and ellipsoidal height data. PhD Thesis, University of Calgary

Förste Ch, Bruinsma SL, Abrikosov O, Lemoine JM, Schaller T, Götze HJ, Ebbing J, Marty JC, Flechtner F, Balmino G, Biancale R (2014) The latest combined global gravity field model including GOCE data up to degree and order 2190 of GFZ Potsdam and GRGS Toulouse

Grushinsky NP (1976) Theory of the earth figure. Nauka, Moscow

Krynski J (2007) Precise quasigeoid modelling in Poland—results and accuracy estimation (in Polish). Monographic series of the Institute of Geodesy and Cartography, No 13, Warsaw, Poland, p 266

Kuczynska-Siehien J, Lyszkowicz A, Birylo M (2016) Geoid determination for the area of Poland by the least squares modification of Stokes' formula. Acta Geodyn Geomater 13(1):181. https://doi.org/10.13168/AGG.2015.0041

Lyszkowicz A (1994) Gravity anomalies for the Southern Part of Baltic Sea and their statistics. In: Proceedings of the Joint Symposium of the International Gravity Commission and the International Geoid Commission, Graz, Austria, pp 102–107

Lyszkowicz A (2010) Quasigeoid for the area of Poland computed by least squares collocation. Technical Sciences, No 13, Y 2010

Lyszkowicz A, Denker H (1994) Computation of gravimetric geoid for Poland using FFT. Artificial satellites, planetary geodesy No 21, str.1-11

Pavlis NK, Holmes SA, Kenyon SC, Factor JK (2012) The development and evaluation of the earth gravitational model 2008 (EGM2008). J Geophys Res 117(B4). https://doi.org/10.1029/2011JB008916

Piretzidis D, Sideris MG (2016) MAP-LAB: A MATLAB graphical user interface for generating maps for geodetic and oceanographic applications. In: Poster presented at the international symposium on gravity, geoid and height systems 2016, 19–23 September 2016, Thessaloniki, Greece, https://doi.org/10.13140/RG.2.2.16099.76323

Reuter HI, Nelson A, Jarvis A (2007) An evaluation of void filling interpolation methods for SRTM data. Int J Geogr Inf Sci 21(9):983–1008. https://doi.org/10.1080/13658810601169899

Sandwell DT, Smith WHF (2009) Global marine gravity from retracked Geosat and ERS altimetry: ridge segmentation versus spreading rate. J Geophys Res 114:B01411. https://doi.org/10.1029/2008JB006008

Sandwell DT, Müller RD, Smith WHF, Garcia E, Francis R (2014) New global marine gravity model from CryoSat-2 and Jason-1 reveals buried tectonic structure. Science 346(6205):65–67. https://doi.org/10.1126/science.1258213

Sansò F, Sideris MG (2013) Geoid determination: theory and methods (lecture notes in earth sciences). Springer, Berlin

Szelachowska M, Krynski J (2014) GDQM-PL13 - the new gravimetric quasigeoid model for Poland. Geoinf Issues 1(6):5–19

Torge W (2001) Geodesy, 3rd edn. de Gruyter, Berlin

Torge W, Müller J (2012) Geodesy, 4th edn. Walter de Gruyter, Berlin. ISBN 978-3-25-020718-7

Vaníček P, Christou NT (eds) (1994) Geoid and its geophysical interpretations. CRS Press, Boca Raton

AFRGDB_V2.0: The Gravity Database for the Geoid Determination in Africa

Hussein A. Abd-Elmotaal, Kurt Seitz, Norbert Kühtreiber, and Bernhard Heck

Abstract

The available gravity data set for Africa consists of land point gravity data as well as shipborne and altimetry derived gravity anomalies data, but suffers from a lot of significant large gaps. The establishment of the AFRGDB_V2.0 gravity database for Africa has been carried out using a weighted least-squares prediction technique. The land gravity data got the highest precision, while the shipborne and altimetry gravity data got a moderate precision. The data gaps are filled by an underlying grid utilizing the GOCE Dir_R5 model, getting the lowest precision within the prediction technique. The window technique has been used to produce the best reduced anomalies before the interpolation process. The AFRGDB_V2.0 gravity database on a uniform $5' \times 5'$ grid has been established by the developed process and has been validated using real data. This validation proved that the established gravity database for Africa has an internal precision of about 5.5 mgal, and an external accuracy of about 7 mgal.

Keywords

Africa · Geoid determination · Gravity · Least-squares prediction · Window technique

1 Introduction

The African geoid, being the main product of the IAG Sub-Commission on the Gravity and Geoid in Africa, will be determined using Stokes' integral in the frequency domain. This requires gridded gravity data. The present investigation introduces the current status of the ongoing research to establish the gravity database for Africa.

H. A. Abd-Elmotaal (✉)
Civil Engineering Department, Faculty of Engineering, Minia University, Minia, Egypt
e-mail: abdelmotaal@lycos.com

K. Seitz · B. Heck
Geodetic Institute, Karlsruhe Institute of Technology, Karlsruhe, Germany
e-mail: kurt.seitz@kit.edu; bernhard.heck@kit.edu

N. Kühtreiber
Institute of Geodesy, Graz University of Technology, Graz, Austria
e-mail: norbert.kuehtreiber@tugraz.at

The available gravity data set has a lot of significant gaps, while in some areas the distribution is very dense, besides the fact that the shipborne and altimetry data have a line structure (along tracks). This leads to a problem in determining a reasonable empirical covariance function, and consequently reduces the capability of the used least-squares prediction technique. Filtering the available gravity data and degrading the ocean gravity data took place to overcome this problem.

The existing large data gaps are filled by an underlying grid employing the GOCE Dir_R5 model (Bruinsma et al. 2013), up to degree and order 300, to avoid the random freedom of the interpolation solution at the gap areas. The choice of the Dir_R5 model has been made because it has proved to give the closest values to the actual gravity field of Africa (Abd-Elmotaal 2015).

It is well known that the interpolation errors are directly proportional to the degree of smoothness of the interpolated field. Accordingly, the window technique (Abd-Elmotaal and Kühtreiber 2003) has been used to obtain the best reduced anomalies before the interpolation process. The weighted

J. T. Freymueller, L. Sánchez (eds.), *International Symposium on Advancing Geodesy in a Changing World*, International Association of Geodesy Symposia 149, https://doi.org/10.1007/1345_2018_29

least-squares prediction technique (Moritz 1980) is then used employing the reduced anomalies to estimate gridded gravity anomalies.

It should be mentioned that the $5' \times 5'$ gravity anomaly grid values developed at Leeds University which have been used to compute the first geoid model for Africa by Merry et al. (2005) have never become available again.

2 Available Data

2.1 Land Data

The available land gravity data set consists of 154,037 gravity data points. These gravity data have been collected over the past decade from different sources by the first author. The land data have been filtered on a $1' \times 1'$ grid (i.e., in each cell of $1' \times 1'$, only one data point, the closest to the cell-center, has been selected) to enhance the behaviour of the empirical covariance function by avoiding false empirically determined covariances larger than the variance near the origin (cf. Kraiger 1988). The number of land data after the grid filtering became 127,067 points.

The land data set passed through a smart gross-error detection scheme developed by Abd-Elmotaal and Kühtreiber (2014) using the least-squares prediction technique (Moritz 1980). The gross-error detection technique estimates the gravity anomaly value at the computational point employing the surrounding stations. Comparing the estimated and data values defines a possible gross-error. Then, the effect of the computational point on the surrounding stations is examined by comparing the estimation of their values including and excluding the computational point. Data points which show a real gross-error behaviour are removed from the database. The number of land data after the gross-error removal became 126,202 points.

Figure 1a shows the distribution of the land data set (after grid filtering and gross-error removal). It illustrates that the land data contain very large data gaps. The free-air gravity anomalies on land range between −163.2 and 465.5 mgal with an average of about 9.8 mgal and a standard deviation of 40.9 mgal.

2.2 Shipborne Data

The available shipborne gravity data set, after a preliminary gross-error detection scheme developed by Abd-Elmotaal and Makhloof (2013), consists of 971,945 gravity data points. The applied preliminary gross-error detection approach is based on the least-squares prediction technique. It estimates the gravity anomaly value at the computational point utilizing the surrounding stations. Hence, a comparison between the estimated and data values is used to define a possible blunder. The gross-error technique works in an iterative scheme till the standard deviation of the discrepancy between the data and estimated values becomes less than 1.5 mgal.

The shipborne data have been filtered on a $3' \times 3'$ grid to enhance the behaviour of the empirical covariance function as well as to decrease the dominant effect of the ocean data. The number of shipborne data after the grid filtering became 148,858 points. A smart gross-error detection scheme, similar to that applied on the land data (Abd-Elmotaal and Kühtreiber 2014), has been performed on the shipborne data set. The number of shipborne data after the smart gross-error removal became 148,674 points.

Figure 1b shows the distribution of the shipborne gravity data (after grid filtering and gross-error removal). It illus-

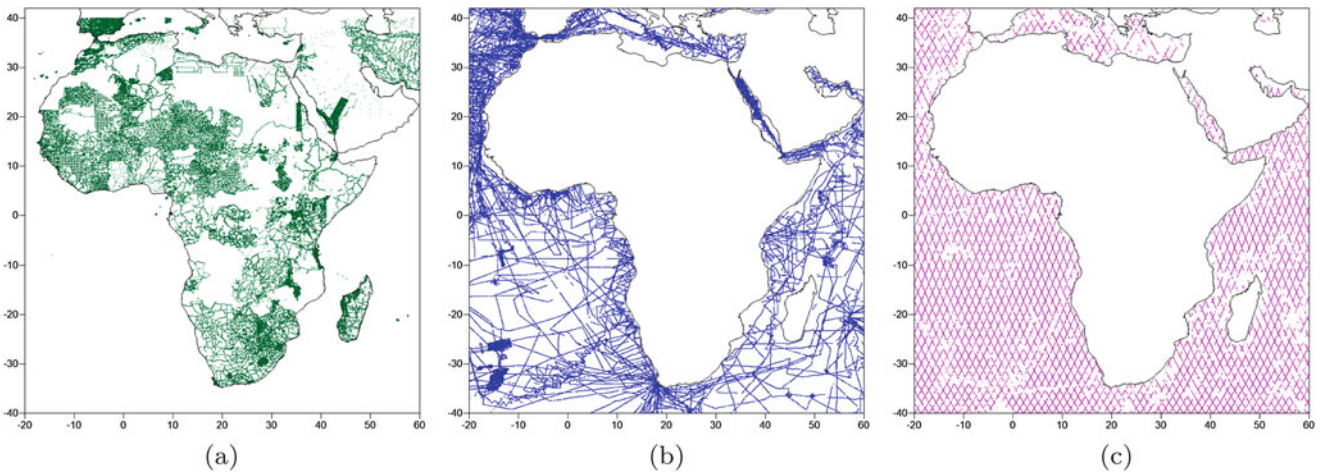

Fig. 1 Distribution of the (**a**) land, (**b**) shipborne and (**c**) altimetry African free-air gravity anomalies

trates a better distribution than that of the land data. The remaining gaps of the shipborne data are partially filled with the altimetry-derived gravity anomalies. The shipborne free-air gravity anomalies range between −238.3 and 354.4 mgal with an average of about −6.2 mgal and a standard deviation of 34.9 mgal.

2.3 Altimetry Data

The available altimetry-derived gravity anomaly data set, which was constructed from the average of 44 repeated cycles of GEOSAT by the National Geophysical Data Center NGDC (www.ngdc.noaa.gov), after applying a preliminary gross-error detection technique similar to that applied on the shipborne data, consists of 119,249 gravity data points. A combination between the shipborne and altimetry data took place (Abd-Elmotaal and Makhloof 2014). This combination causes some gaps along altimetry tracks when the altimetry data don't match with the shipborne data (cf. Fig. 1c).

The altimetry-derived data have been filtered on a $3' \times 3'$ grid to enhance the behaviour of the empirical covariance function as well as to decrease the dominant effect of the ocean data. The number of altimetry-derived data after the grid filtering became 70,732 points. A smart gross-error detection scheme, similar to that applied on the land data, has been carried out on the altimetry-derived data set. The number of altimetry-derived data after the smart gross-error removal became 70,589 points.

Figure 1c shows the distribution of the available altimetry data (after grid filtering and gross-error removal). It illustrates, more or less, a regular distribution. The altimetry free-air gravity anomalies range between −172.2 and 156.6 mgal with an average of 4.1 mgal and a standard deviation of 18.2 mgal.

2.4 Digital Height Models

The remove-restore technique requires a set of Digital Terrain Models (DTMs). A set of DTMs for Africa covering the window $(-42° \le \phi \le 44°; -22° \le \lambda \le 62°)$ are available for the current investigation. The AFH16S30 $30'' \times 30''$ model has been chosen to represent the fine DTM, and the AFH16M03 $3' \times 3'$ model has been chosen to represent the coarse DTM (Abd-Elmotaal et al. 2017). Figure 2 shows the AFH16S30 $30'' \times 30''$ fine DTM for Africa. The heights range between −8,291 and 5,777 m with an average of −1,623 m and a standard deviation of about 2,407 m.

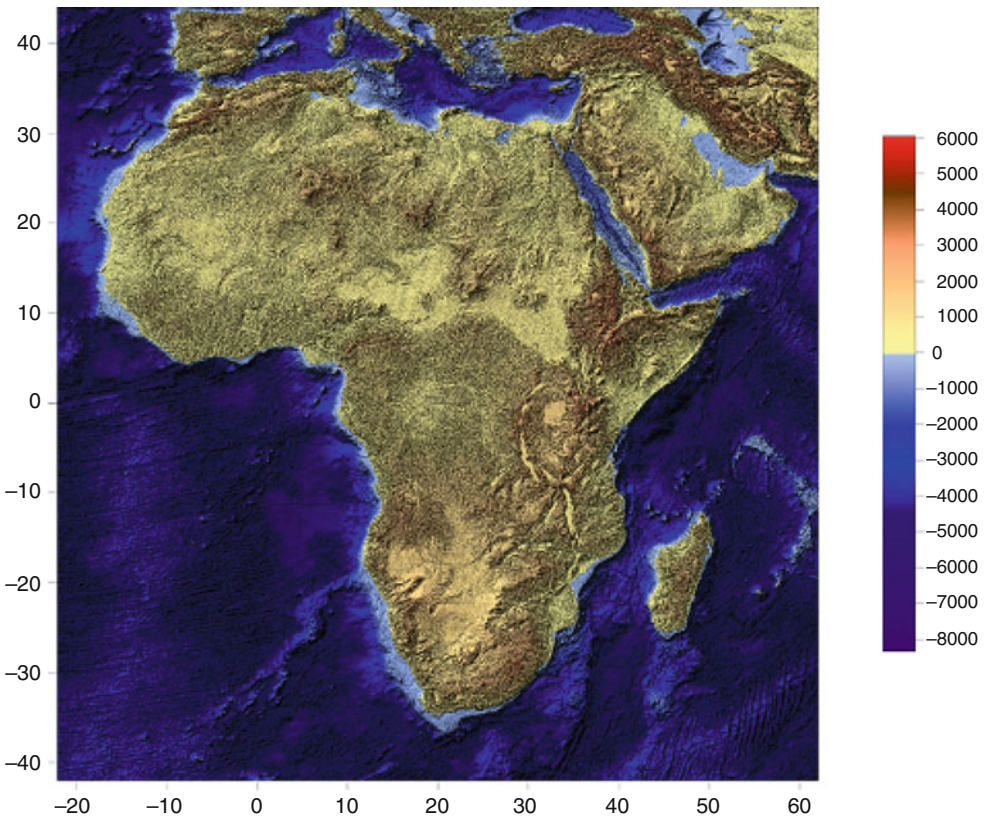

Fig. 2 The $30'' \times 30''$ AFH16S30 DTM for Africa (after Abd-Elmotaal et al. 2017). Units in m

3 Methodology

As stated earlier, the AFRGDB_V2.0 gravity database is created by interpolating the best reduced anomalies using the weighted least-squares interpolation technique, and hence a restore step took place as the final step of the gravity database establishment. In the following subsections, the used steps will be described in detail.

3.1 Window Remove-Restore Technique

The gravity reduction is performed using the window remove-restore technique. The remove step of the window remove-restore technique is described by (Abd-Elmotaal and Kühtreiber 1999, 2003) (cf. Fig. 3)

$$\begin{aligned}\Delta g_{red} &= \Delta g_F - \Delta g_{TI\,win} - \Delta g_{GM\,Adapt}\Big|_{n=2}^{N_{max}} \\ &= \Delta g_F - \Delta g_{TI\,win} - \\ &\quad - \left(\Delta g_{GM}\Big|_{n=2}^{N_{max}} - \Delta g_{wincof}\Big|_{n=2}^{N_{max}}\right), \end{aligned} \tag{1}$$

where Δg_F stands for the measured free-air gravity anomalies, $\Delta g_{GM\,Adapt}$ is the contribution of the adapted reference field, $\Delta g_{TI\,win}$ is the contribution of the topographic-isostatic masses for a fixed data window, Δg_{GM} is the contribution of the used reference field, Δg_{wincof} is the contribution of the dimensionless harmonic coefficients of the topographic-isostatic masses of the data window and N_{max} is the used maximum degree. A value of $N_{max} = 1{,}800$ and the EGM2008 (Pavlis et al. 2012) have been used as reference field in the current investigation.

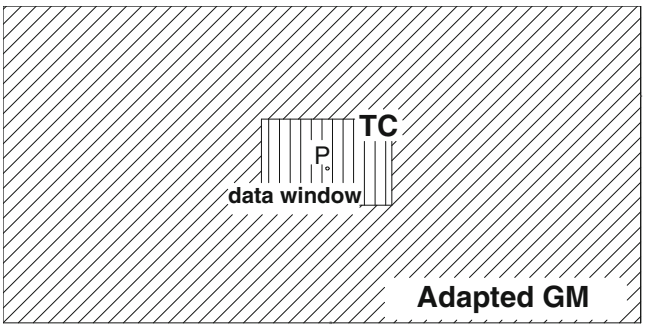

Fig. 3 The window remove-restore technique

For the underlying grid, the free-air gravity anomalies are computed by

$$\Delta g_F = \Delta g_{Dir\_R5}\Big|_{n=2}^{300}, \tag{2}$$

where Δg_{Dir_R5} stands for the gravity anomalies computed by using the GOCE DIR_R5 reference model (Bruinsma et al. 2013). The underlying grid is computed using Eq. (2) on a $15' \times 15'$ unregistered grid with the final output grid for the data gaps *only* (i.e., the underlying grid is shifted by half of the grid cell of the output grid). The window-reduced anomalies for the underlying grid are then computed by Eq. (1).

3.2 Gravity Reduction

Table 1 illustrates the statistics of the free-air and the reduced anomalies for each data category. It shows that the window remove-restore anomalies are much better (centered with smaller standard deviation) than the free-air anomalies. For the total data set (land + shipborne + altimetry), the standard deviation has dropped to its one third, while for the land data only, the standard deviation has dropped to its one fourth. Table 1 also shows that the statistics of the window-reduced anomalies for the underlying grid match, to some extent, those of the window-reduced anomalies for the total data, which is considered as a good sign.

Table 1 Statistics of the free-air and reduced gravity anomalies

			Statistical parameters			
Type	Category	# pts	Min	Max	Mean	Std
Free-air	Land	126,202	−163.2	465.5	9.8	40.9
	Shipborne	148,674	−238.3	354.4	−6.2	34.9
	Altimetry	70,589	−172.2	156.6	4.1	18.2
	Total	345,465	−238.3	465.5	1.8	35.4
	Underlying	48,497	−90.7	127.3	2.5	15.9
Window reduced	Land	126,202	−230.6	318.8	−1.0	10.4
	Shipborne	148,674	−96.2	58.7	−0.7	11.4
	Altimetry	70,589	−85.6	98.6	7.1	12.3
	Total	345,465	−230.6	318.8	0.8	11.7
	Underlying	48,497	−245.5	198.5	0.2	19.3

Units in mgal

3.3 Interpolation

The used least-squares interpolation technique employs the generalized covariance model of Hirvonen (Moritz 1980)

$$C(s) = \frac{C_\circ}{(1 + A^2 s^2)^p} \tag{3}$$

with

$$A = \frac{1}{\xi}\left(2^{\frac{1}{p}} - 1\right)^{\frac{1}{2}}, \tag{4}$$

where $C_\circ$ and ξ are the empirically determined variance and correlation length, respectively, and s is the spherical distance between the pair of points under consideration. The dimensionless curvature parameter χ is related to the curvature κ of the covariance function at $s = 0$ by (Kraiger 1988)

$$\chi = \frac{\kappa\, \xi^2}{C_\circ}. \tag{5}$$

Therefore, it affects the values of the covariances near the origin. The curvature parameter χ is related to the parameter p as (Moritz 1976; Abd-Elmotaal 1992)

$$\chi = 2p\left(2^{\frac{1}{p}} - 1\right). \tag{6}$$

The estimation of the parameter p has been made through the fitting of the empirically determined covariance function by employing a least-squares regression algorithm developed by Abd-Elmotaal and Kühtreiber (2016). A value of $p = 0.472$ has been estimated. The values of the empirically determined variance $C_\circ$ and correlation length ξ for the empirical covariance function are as follows:

$$\begin{aligned} C_\circ &= 165.41\,\text{mgal}^2, \\ \xi &= 8.13\,\text{km}. \end{aligned} \tag{7}$$

Figure 4 illustrates the fitting of the empirically determined covariance function performed by least-squares regression algorithm (Abd-Elmotaal and Kühtreiber 2016). The very good fitting of the empirically determined covariance function is evident.

An unequal weight least-squares interpolation process was applied for the African result window ($-40° \le \phi \le 42°; -20° \le \lambda \le 60°$) on a $5' \times 5'$ grid yielding the interpolated gridded reduced anomalies Δg^G_{red}. The used standard deviations for the four gravity anomaly types are as follows: $\sigma_{land} = 1$ mgal, $\sigma_{shipborne} = 3$ mgal, $\sigma_{altimetry} = 5$ mgal, $\sigma_{underlying\,grid} = 20$ mgal.

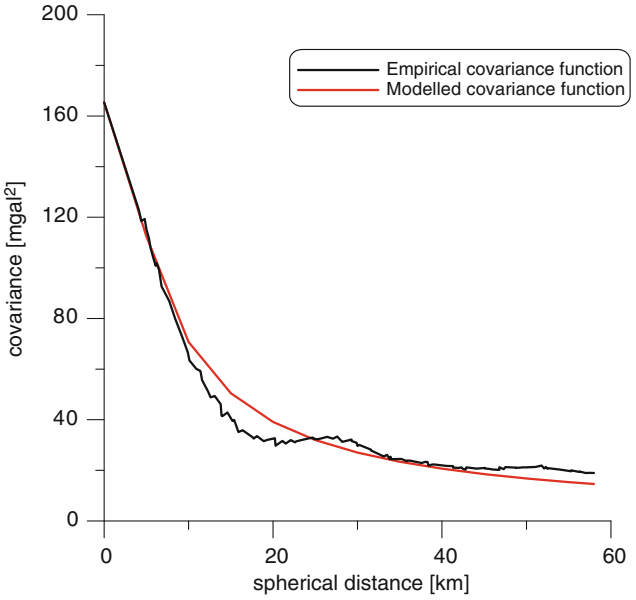

Fig. 4 Fitting of the empirically determined covariance function using least-squares regression algorithm (Abd-Elmotaal and Kühtreiber 2016)

3.4 Restore Step

The restore step of the window remove-restore technique, which took place on the $5' \times 5'$ grid points, is described by (Abd-Elmotaal and Kühtreiber 1999, 2003)

$$\Delta g^G_F = \Delta g^G_{red} + \Delta g^G_{TI\,win} + \Delta g^G_{GM}\Big|_{n=2}^{Nmax} - \\ - \Delta g^G_{wincof}\Big|_{n=2}^{Nmax}, \tag{8}$$

where the superscript G stands for values computed at the grid points. Δg^G_F computed by (8) represent the values for the AFRGDB_V2.0 gravity database for Africa.

Figure 5 illustrates the $5' \times 5'$ African free-air gravity anomaly database AFRGDB_V2.0. These free-air anomalies range between -243.04 and 468.00 mgal with an average of about 3.04 mgal and a standard deviation of 31.94 mgal.

It is worth mentioning that the false significantly large anomalies at the high mountainous area of Morocco for the previous AFRGDB_V1.0 gravity database (Abd-Elmotaal et al. 2015) have been eliminated for the current AFRGDB_V2.0 gravity database.

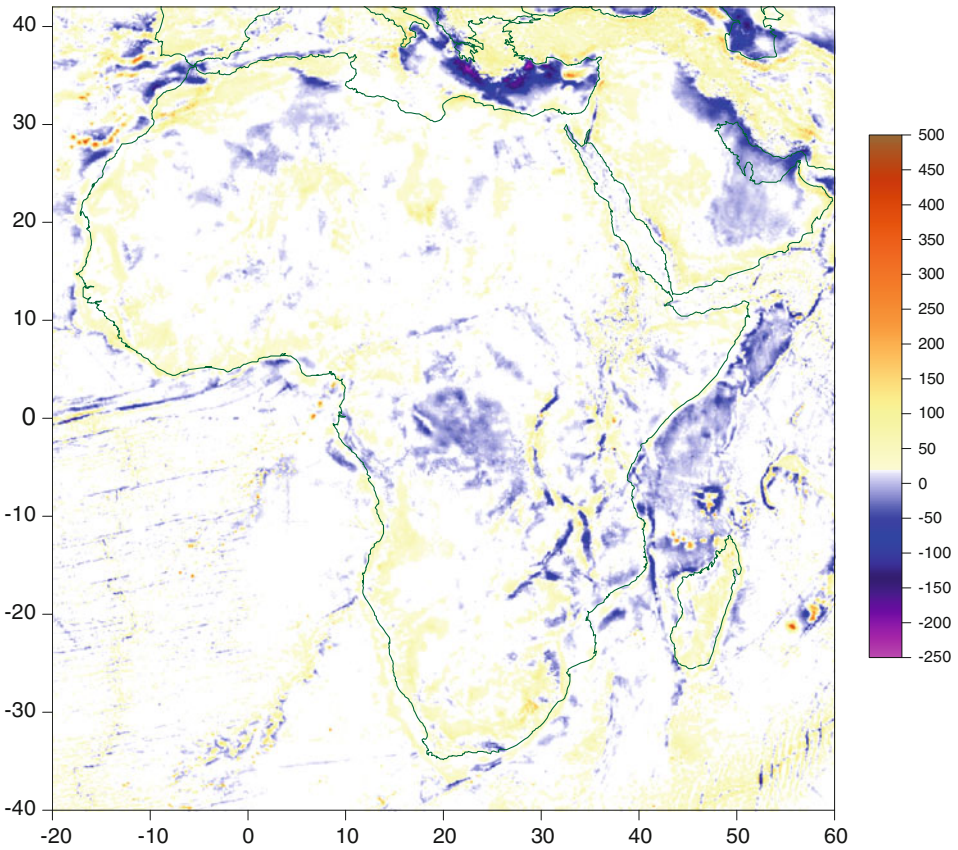

Fig. 5 The $5' \times 5'$ African free-air gravity anomaly database AFRGDB_V2.0. Units in mgal

4 Validation

The created AFRGDB_V2.0 gravity database for Africa has been validated both internally (at the used data points) and externally (at the non-used data points). The internal and external validations will be discussed in the following sections.

4.1 Internal Validation

The created AFRGDB_V2.0 gravity database has been validated internally at the used data points. Figure 6 illustrates the internal validation of the AFRGDB_V2.0 gravity database. The residuals between the data and the values of the AFRGDB_V2.0 range between −50.80 and 55.71 mgal with an average of about −0.37 mgal and a standard deviation of 5.56 mgal. 81.9% of the points have residuals below 5 mgal in magnitude (the white pattern in Fig. 6).

Figure 7 illustrates a histogram of the internal validation for the AFRGDB_V2.0 gravity database. The residuals (data minus database values) show a Gaussian normal distribution with high precision index, which indicates a high precision of the established gravity database. 84.4% of the data points have residuals less than 5.56 mgal (the standard deviation).

4.2 External Validation

Figure 8 illustrates the distribution of the external validation points of the AFRGDB_V2.0 gravity database. These points are those which were not used in the creation of the AFRGDB_V2.0 gravity database. The number of the external validation points excluding blunders on land is around 27 thousand points, while the number of the external validation points on sea is around 871 thousand points.

The created AFRGDB_V2.0 gravity database has been validated externally at the non-used data points of Fig. 8. Figure 9 illustrates the external validation of the AFRGDB_V2.0

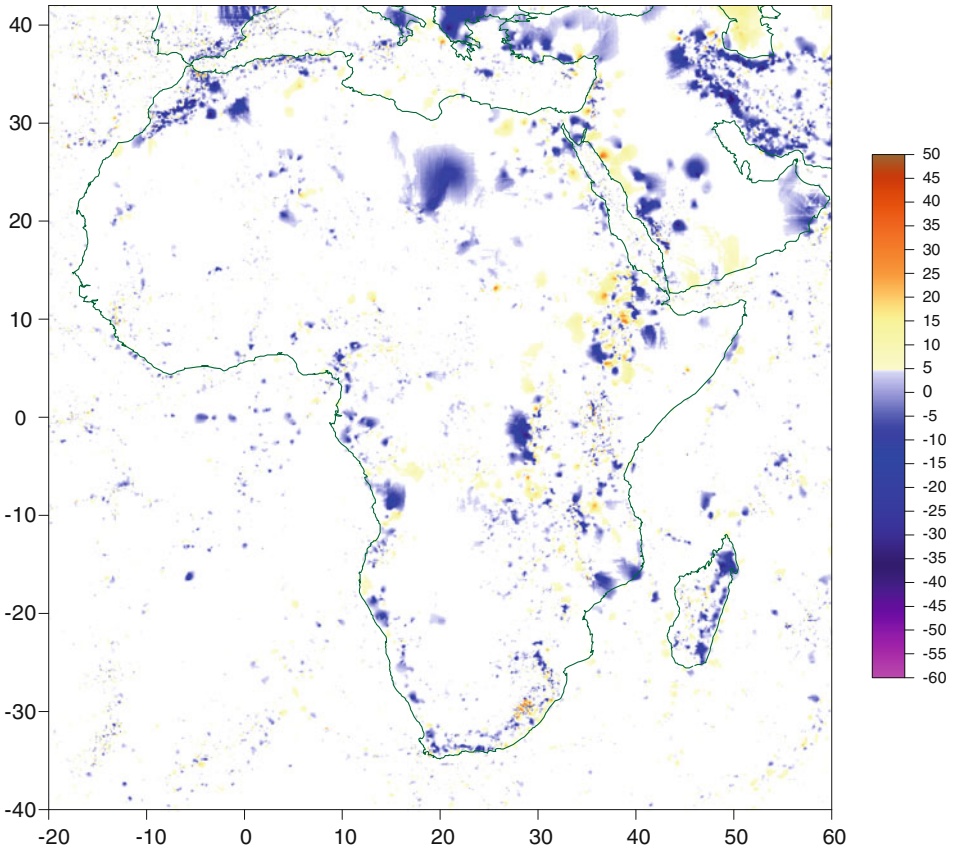

Fig. 6 Internal validation of the AFRGDB_V2.0 gravity database. Units in mgal

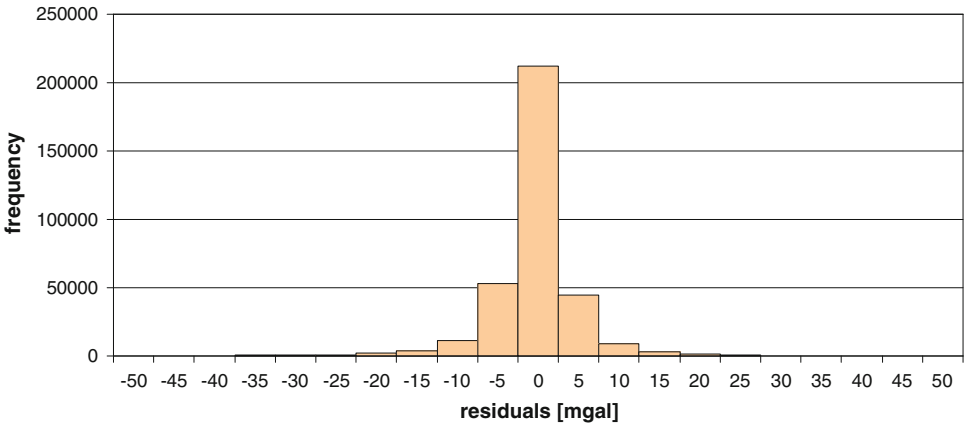

Fig. 7 Histogram of the internal validation for the AFRGDB_V2.0 gravity database

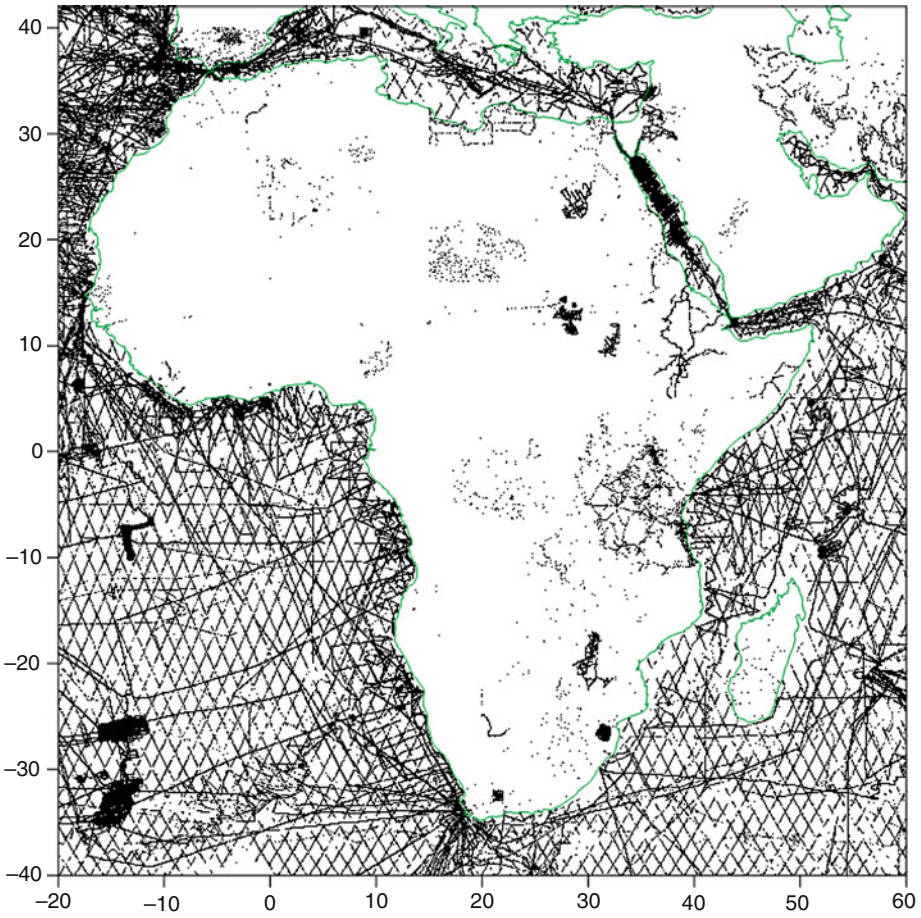

Fig. 8 Distribution of the external validation points of the AFRGDB_V2.0 gravity database

gravity database. The residuals between the data and the values of the AFRGDB_V2.0 range between −66.97 and 67.25 mgal with an average of about −0.59 mgal and a standard deviation of 6.99 mgal. 71.9% of the points have residuals below 5 mgal in magnitude (the white pattern in Fig. 9).

It should be pointed out that the distribution of the available external checking data points on land is too sparse (cf. Fig. 8). This leads to very large gaps, on which an artificial pattern of larger residuals are created from the interpolation method used to plot Fig. 9.

Figure 10 illustrates a histogram of the external validation for the AFRGDB_V2.0 gravity database. The residuals (data minus database values) show a Gaussian normal distribution with high precision index, which indicates a high accuracy of the established gravity database. 81.4% of the data points have residuals less than 6.99 mgal (the standard deviation).

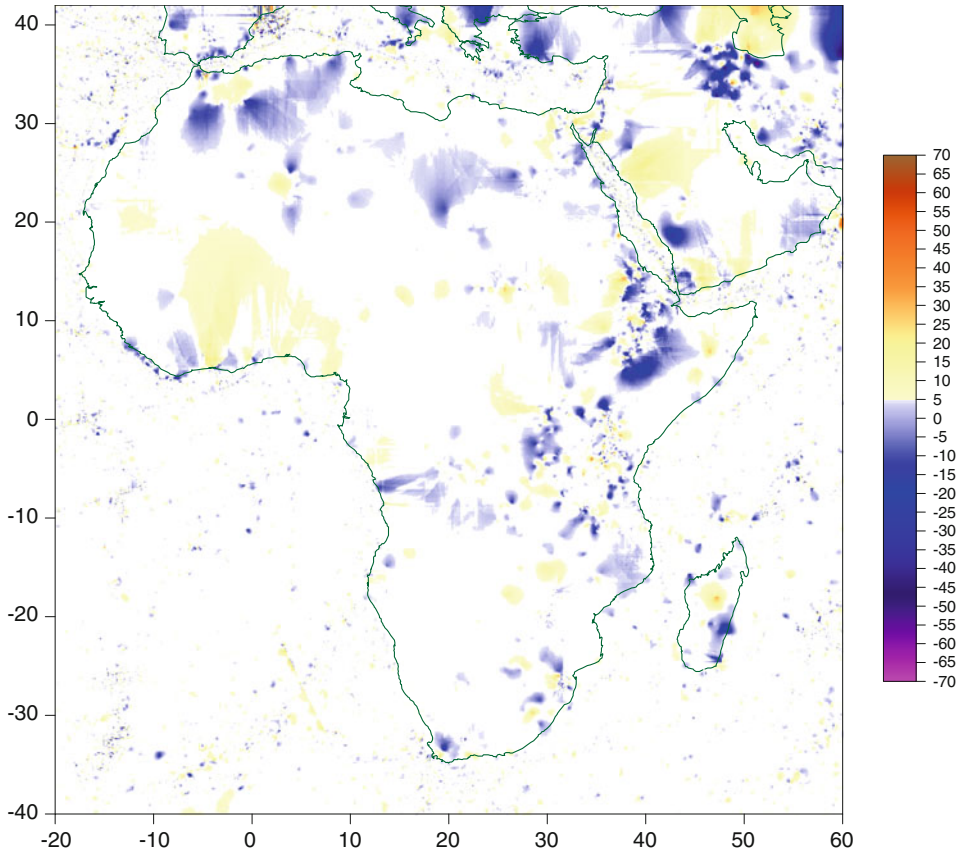

Fig. 9 External validation of the AFRGDB_V2.0 gravity database. Units in mgal

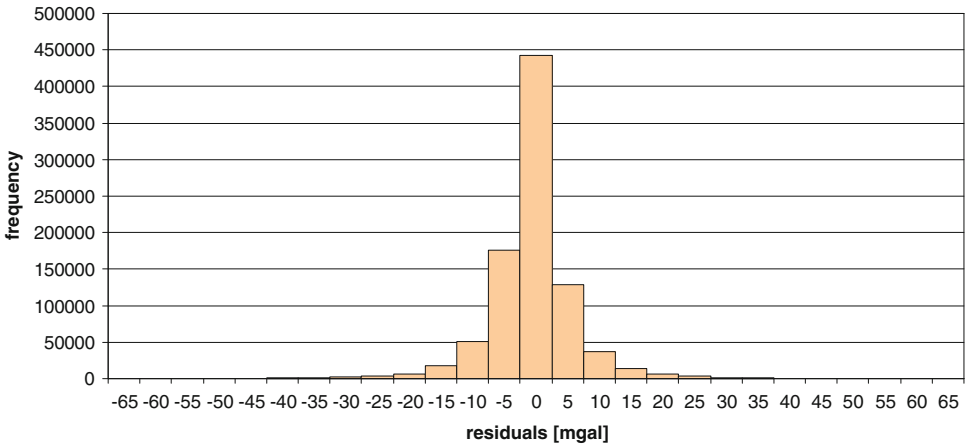

Fig. 10 Histogram of the external validation for the AFRGDB_V2.0 gravity database

5 Conclusion

An updated version of the African gravity database has been successfully established in the current investigation using a combination of real data on land and sea and an underlying grid filling the large data gaps. This underlying grid has been created using the GOCE Dir_R5 model up to degree and order 300. A grid filtering of $3' \times 3'$ resolution has been applied to the sea data to decrease their dominant effect on the solution. A grid filtering of $1' \times 1'$ resolution has been applied to the land data to enhance the behaviour of the empirically determined covariance function, especially near the origin.

The window remove-restore technique has been used to get the best smoothed reduced anomalies. An unequal weight least-squares prediction technique has been carried out to interpolate the reduced anomalies on a grid of $5' \times 5'$ resolution. The established AFRGDB_V2.0 gravity database for Africa has an internal precision of about 5.5 mgal, and an external accuracy of about 7 mgal, which is considered as a great achievement so far.

Acknowledgements This project was supported financially by the Science and Technology Fund (STDF), Egypt, Grant No. 7944. The authors would like to thank Dr. Sylvain Bonvalot, Director of the Bureau Gravimétrique International (BGI), for providing part of the used data set for Africa. The support by the International Association of Geodesy (IAG) and the International Union of Geodesy and Geophysics (IUGG) is kindly acknowledged. The authors would like to thank the editor of the current paper and two anonymous reviewers for their useful comments.

References

Abd-Elmotaal HA (1992) Statistical behaviour of the free-air, Bouguer and isostatic anomalies in Austria. Bull Geod 66(4):325–335. https://doi.org/10.1007/BF00807417

Abd-Elmotaal HA (2015) Validation of GOCE models in Africa. Newton's Bull 5:149–162

Abd-Elmotaal HA, Kühtreiber N (1999) Improving the geoid accuracy by adapting the reference field. Phys Chem Earth Part A 24(1):53–59

Abd-Elmotaal HA, Kühtreiber N (2003) Geoid determination using adapted reference field, seismic Moho depths and variable density contrast. J Geod 77(1–2):77–85

Abd-Elmotaal HA, Kühtreiber N (2014) Automated gross error detection technique applied to the gravity database of Africa. In: General Assembly of the European Geosciences Union, Vienna, 27 April–2 May 2014

Abd-Elmotaal HA, Kühtreiber N (2016) Effect of the curvature parameter on least-squares prediction within poor data coverage: case study for Africa. In: General Assembly of the European Geosciences Union, Vienna, April 17–22, 2016

Abd-Elmotaal HA, Makhloof A (2013) Gross-errors detection in the shipborne gravity data set for Africa. Geodetic Week, Essen, 8–10 October 2013. www.uni-stuttgart.de/gi/research/Geodaetische_Woche/2013/session02/Abd-Elmotaal-Makhloof.pdf

Abd-Elmotaal HA, Makhloof A (2014) Combination between altimetry and shipborne gravity data for Africa. In: 3rd International Gravity Field Service (IGFS) General Assembly, Shanghai, 30 June–6 July 2014

Abd-Elmotaal HA, Seitz K, Kühtreiber N, Heck B (2015) Establishment of the gravity database AFRGDB_V1.0 for the African geoid. In: International association of geodesy symposia, vol 144, pp 131–138. https://doi.org/10.1007/1345_2015_51

Abd-Elmotaal HA, Makhloof A, Abd-Elbaky M, Ashry M (2017) The African $3'' \times 3''$ DTM and its validation. In: International association of geodesy symposia. https://doi.org/10.1007/1345_2017_19

Bruinsma S, Förste C, Abrikosov O, Marty JC, Rio MH, Mulet S, Bonvalot S (2013) The new ESA satellite-only gravity field model via the direct approach. Geophys Res Lett 40(14):3607–3612. https://doi.org/10.1002/grl.50716

Kraiger G (1988) Influence of the curvature parameter on least-squares prediction. Manuscr Geodaet 13(3):164–171

Merry C, Blitzkow D, Abd-Elmotaal HA, Fashir H, John S, Podmore F, Fairhead J (2005) A preliminary geoid model for Africa. In: A window on the future of geodesy. Springer, Berlin, pp 374–379

Moritz H (1976) Covariance functions in least-squares collocation. Ohio State University, Department of Geodetic Science and Surveying, Rep 240

Moritz H (1980) Advanced physical geodesy. Wichmann, Karlsruhe

Pavlis N, Holmes S, Kenyon S, Factor J (2012) The development and evaluation of the earth gravitational model 2008 (EGM2008). J Geophys Res 117(B04406). https://doi.org/10.1029/2011JB008916

Combined Use of a Superconducting Gravimeter and Scintrex Gravimeters for Hydrological Correction of Precise Gravity Measurements: A Superhybrid Gravimetry

Yuichi Imanishi, Kazunari Nawa, Yoshiaki Tamura, Hiroshi Ikeda, Ryo Honda, Takashi Okuda, and Makoto Okubo

Abstract

A variant of hybrid gravimetry using both a superconducting gravimeter and Scintrex gravimeters is proposed. One of the main factors limiting the accuracy of time lapse gravity measurements is the instrumental drift of spring-type gravimeters. Running the Scintrex CG-5 gravimeter in the nighttime on the same pier as the superconducting gravimeter allows us to model the long-term behavior of the former and to remove efficiently the effect of irregular drift on measured gravity. Initial tests performed at Ishigakijima, Japan, proved that accuracy of a few μGal level can be achieved with this method. This will help us precisely correct for the effect of underground water on superconducting gravimeters with 2-dimensional local gravity survey.

Keywords

Hybrid gravimetry · Scintrex gravimeter · Superconducting gravimeter

Abbreviation

SG Superconducting gravimeter

1 Introduction

Microgravity measurement is a powerful tool for investigating underground structure and dynamics in terms of density distribution and its temporal changes. Traditionally, portable spring-type gravimeters were used in survey works for obtaining spatial distribution of gravity acceleration (e.g. Furuya et al. 2003). One of the problems in this kind of study is the effect of instrumental drift of relative gravimeters which makes it difficult to track long term changes in gravity. As a solution to this problem, use of an absolute gravimeter as the base of relative gravity measurements was proposed (Okubo 2001), and was termed "hybrid gravimetry" because

Y. Imanishi (✉)
Earthquake Research Institute, The University of Tokyo, Bunkyo, Tokyo, Japan
e-mail: imanishi@eri.u-tokyo.ac.jp

K. Nawa
Geological Survey of Japan, National Institute of Advanced Industrial Science and Technology, AIST Tsukuba Central 7, Tsukuba, Ibaraki, Japan
e-mail: k.nawa@aist.go.jp

Y. Tamura
Mizusawa VLBI Observatory, National Astronomical Observatory of Japan, Oshu, Iwate, Japan
e-mail: yoshiaki.tamura@nao.ac.jp

H. Ikeda
Research Facility Center for Science and Technology, University of Tsukuba, Tsukuba, Ibaraki, Japan
e-mail: ikeda@bk.tsukuba.ac.jp

R. Honda
Mount Fuji Research Institute, Yamanashi Prefectural Government, Fujiyoshida, Yamanashi, Japan
e-mail: honda@mfri.pref.yamanashi.jp

T. Okuda
Earthquake and Volcano Research Center, Graduate School of Environmental Studies, Nagoya University, Nagoya, Aichi, Japan
e-mail: okuda@seis.nagoya-u.ac.jp

M. Okubo
Natural Science Cluster, Kochi University, Kochi, Kochi, Japan
e-mail: okubo@kochi-u.ac.jp

J. T. Freymueller, L. Sanchez (eds.), *International Symposium on Advancing Geodesy in a Changing World*, International Association of Geodesy Symposia 149, https://doi.org/10.1007/1345_2018_31

it is a combination of absolute and relative gravity measurements. With this method, all relative measurements can be referred to gravity acceleration in the absolute sense, allowing us to investigate long term changes of gravity in the survey area by compiling results from different campaigns. Practically, accuracy of hybrid gravimetry is limited by the accuracy of relative gravity measurements, which ranges typically on the order of 10 μGal (1 μGal = 10^{-8} ms^{-2}), even if the absolute gravity acceleration at the base station can be determined more accurately. This is again due to the instrumental drift of relative gravimeters during the survey which one can not control. Many researchers have extensively investigated how to mitigate the influence of drift in order to improve the accuracy (e.g. Reudink et al. 2014; Fores et al. 2017).

In this paper, we propose a variant of the hybrid gravimetry using both a GWR superconducting gravimeter and Scintrex gravimeters, which may be classified as "super-hybrid gravimetry" (Sugihara 2009; Hinderer et al. 2015). The superconducting gravimeter (SG) (Goodkind 1999) is an extremely stable and precise gravimeter. Basically, it is installed at a particular site for continuously monitoring temporal changes in gravity, and it is not regarded as a portable instrument. Also, the SG has finite instrumental drift. The drift mostly follows a linear or exponential function of time (Van Camp and Francis 2007), with typical magnitude ranging from a few μGal to some tens of μGal per year. Since it is a relative gravimeter in the sense that it solely does not provide information on absolute gravity acceleration, calibration of its absolute scale as well as the instrumental drift must be done by parallel registration with an absolute gravimeter at least twice. Once it is calibrated against absolute gravity measurements, the SG may be regarded as a pseudo absolute gravimeter generating continuous gravity recordings at a much higher rate. Then, an obvious advantage of using an SG as the base of hybrid gravity survey is that one can make measurements as often as desired, to reduce the sampling interval. In addition to this, use of a Scintrex CG-3 or CG-5 gravimeter in relative measurements provides another important improvement. The Scintrex gravimeters, unlike traditional LaCoste G-type gravimeters, can be operated in an automatic acquisition mode without human attendance, allowing us to obtain continuous recordings which can be directly compared with those from the SG. As shown later, this proves to be very useful for modeling long-term instrumental drift of Scintrex gravimeters and therefore for significantly improving the accuracy of relative measurements in gravity survey.

In the following, we will show initial results of a super-hybrid gravity experiment performed at Ishigakijima, Japan, obtained with a superconducting gravimeter and two CG-5's.

2 Gravity Measurements and Data Processing

In February 2012, continuous gravity monitoring with the superconducting gravimeter CT #036 was started at the VERA Ishigakijima station, Okinawa, Japan (Ikeda et al. 2013). The station is one of the four VLBI stations which belong to the VERA project (e.g. Honma et al. 2000) of the National Astronomical Observatory of Japan. The main purpose of this gravity experiment is detection of possible gravity signals associated with the long-term slow slip events occurring beneath the Yaeyama Islands (Heki and Kataoka 2008). Such gravity signals, if they exist at all, are expected to be small, not exceeding a few μGal. Therefore, gravity signals from other sources must be modeled and corrected precisely so that they do not mask slow slip signals. In particular, hydrological effects on gravity seem to pose serious problems at the Ishigakijima station, as in many other gravity sites employing SGs (Imanishi et al. 2006; Van Camp et al. 2006; Kroner and Jahr 2006; Meurers et al. 2007). Some evidences acquired up to now show that the underground water beneath the gravity station is likely to be interacting with the atmosphere and the ocean, thus affecting observed gravity in a complicated manner. One of the difficulties in gravity correction for the underground water lies in the fact that it requires knowledge of the hydrological nature of the underground which varies from place to place in general. Given the geographical location and geological settings of the Ishigakijima station, a practical strategy for addressing this problem would be to repeat gravity surveys around the station (e.g. Hector et al. 2015). This is the motivation of our gravity survey around the SG station using Scintrex gravimeter(s) as mobile instruments.

Figure 1 shows the topography of the survey area around the VERA Ishigakijima station. The SG station is located near the foot of Mt. Omoto (526 m), and to the southwest there is a low land expanding toward the sea coast. From the viewpoint of precise gravimetry, it is of interest to see how the variable underground water in this area can be detected with surface gravity measurements. Figure 1 also shows the local gravity network in Ishigakijima consisting of about 30 stations established for repeated gravity survey (Miyakawa et al., in preparation). The SG is located at the station named "09".

The SG CT #036 had been operated until 2011 at the Inuyama Observatory of Nagoya University (Nawa et al. 2009). Analysis of the data acquired at Inuyama indicates that the drift rate of this SG is extremely small, very likely to be less than 1 μGal/year (Ikeda et al. 2013). After it was moved to Ishigakijima in 2012, absolute gravity measurements have been made only once (in 2015) at the VERA Ishigakijima station. Therefore, the instrumental drift of the

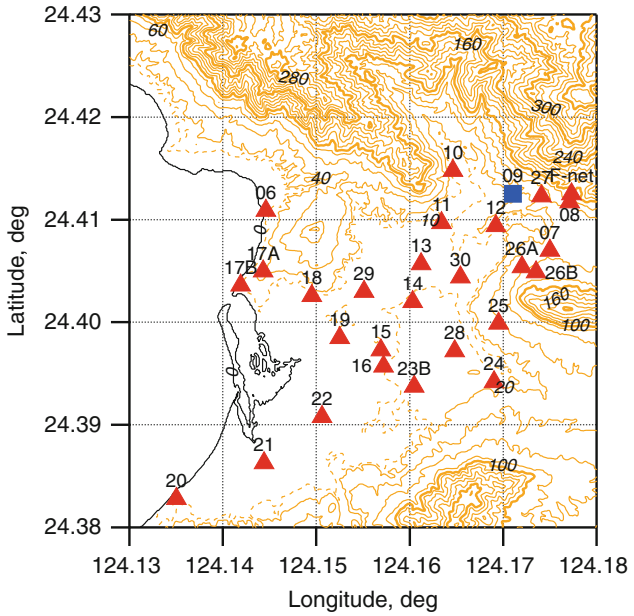

Fig. 1 Topography of the survey area of this study. Contour interval is 20 m, except for the dashed contour for 10 m height. Blue square is the VERA Ishigakijima station where SG (CT #036) is installed. Red triangles are gravity stations for relative measurements, each of which is given a temporary two-digit code (not all stations are shown here). "09" is the SG station

CT #036 has not been calibrated on the basis of absolute gravity. Analysis of 6 years' worth of data suggests that the drift rate of the CT #036 at Ishigakijima is also very small, not exceeding a few μGal/year. So, in the analysis below, we assume that the drift of the CT #036 is negligibly small within the five-day period of our gravity survey.

Our experiment of superhybrid gravity measurements took place from January 30 to February 3, 2017. Two Scintrex CG-5 gravimeters (serial number 120340890 and 140,141,153, hereafter abbreviated as #0890 and #1153) were used for relative measurements. Figure 2 shows the processing of the data from CG-5 #0890. At night, the CG-5's were operated in the "auto-repeat mode" on the same pier as the SG at the VERA station. Then, we may assume that the SG and the CG-5's sense the same temporal changes in gravity. The sampling interval of the CG-5's was either 1 min or 2 min. Considering that the SG data have much lower noise floor than the CG-5's, it will be justified to simply subtract the SG data from the CG-5 data in order to make correction for gravity signals of natural origin, in other words, tides, atmosphere, ocean, and so on, as shown in Fig. 2b. This may be regarded as a way of simple separation of real gravity signals from instrumental drift. The almost linear trend shown in Fig. 2b consists mostly of instrumental drift of the CG-5. Fitting a linear function of time to this gives a residual series shown in Fig. 2c. The gaps in this curve correspond to the intervals when the meter was employed in survey outside the VERA station. Here we can see rapid changes in the data after transportation of the meter. This is the well-known effect of tilting of the meter (Gettings et al. 2008; Reudink et al. 2014), with typical time scales shorter than 1 day. Reudink et al. (2014) elaborates on this effect and presents possible guidelines for mitigating it. Aside from these, we can also see a large irregular trend having a much longer time scale. This is surely another issue of instrumental drift, and can have a serious impact on the accuracy of gravity survey because it is both large and unpredictable.

Our proposal of addressing this problem is to represent this trend by some numerical model and to apply it to all the data acquired in gravity survey. This is made possible thanks to the side-by-side comparison with the SG in the nighttime. Here we have used cubic spline functions to represent the slowly changing drift, as shown in Fig. 2c. The data are preaveraged so that there are 24 nodes in the 6-day period. Those portions affected by transportation are not used. By subtracting the modeled drift, we have the final estimate of residual series for the base station, as shown in Fig. 2d. Notice that after removing the modeled drift, the instrumental drift (except the transportation effect) is suppressed to 1 μGal level.

The data from CG-5 #1153 are processed with the same method. Figure 3 shows the result. The linear drift rate of #1153 is 0.17 mGal/day, smaller than that of #0890 (0.49 mGal/day).

Under the assumption that the long-term irregular drift of the CG-5 is independent of the transportation effect, the numerical models can be applied also to the data acquired at all stations in the gravity survey. Among the stations employed in our study, let us focus on the station named "30" (see Fig. 1). This site was measured four times (twice by #0890 and twice by #1153) in total during the experiment. Figure 4 and Table 1 show the relative gravity with respect to the base station for the four measurements. In processing the gravity data for this station, we have subtracted the SG data from CG-5 data. In other words, we have assumed that temporally variable components of gravity are common to the base station and the station "30" within the period of the experiment. From the data shown in Fig. 4b, d, #1153 appears to be more susceptible to the effect of transportation than #0890. Due to the limitation in available time, each measurement in the survey lasted no longer than 1 h. The relative gravity values and their errors listed in Table 1 are the simple averages and their standard deviations of 16 data points in the latter part for each measurement. It is noted that these results, obtained on different days and by different gravimeters, agree with each other within a few μGal. The weighted average of these four results is $(+5.7388 \pm 0.0010)$ mGal.

Table 1 also lists the results for the station "23B" where gravity measurements were made twice using the gravimeter

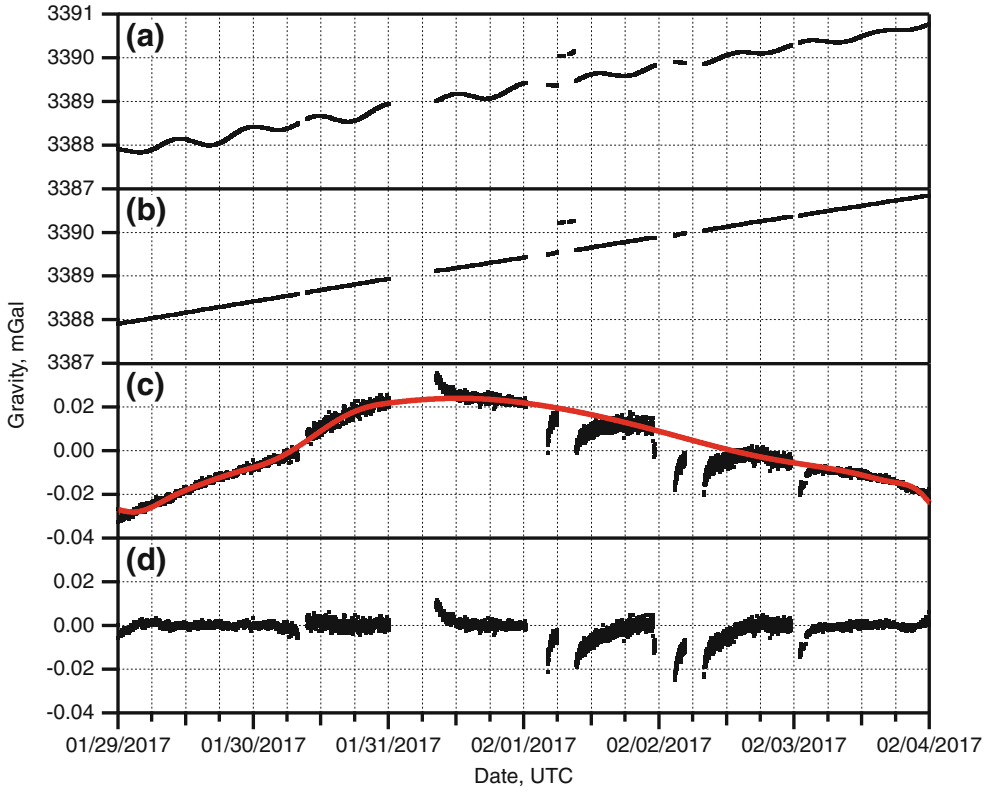

Fig. 2 Data from the Scintrex CG-5 gravimeter (#0890). (**a**) Raw readings. Spikes and outliers have been removed. Correction for tides is not applied. (**b**) Subtracting the SG data from CG-5 data, the instrumental drift looks almost like a linear function of time. (**c**) After removing the linear trend (black), the long-term drift is modeled by cubic spline functions (red). (**d**) With the modeled drift removed, the instrumental drift is reduced to 1 μGal level

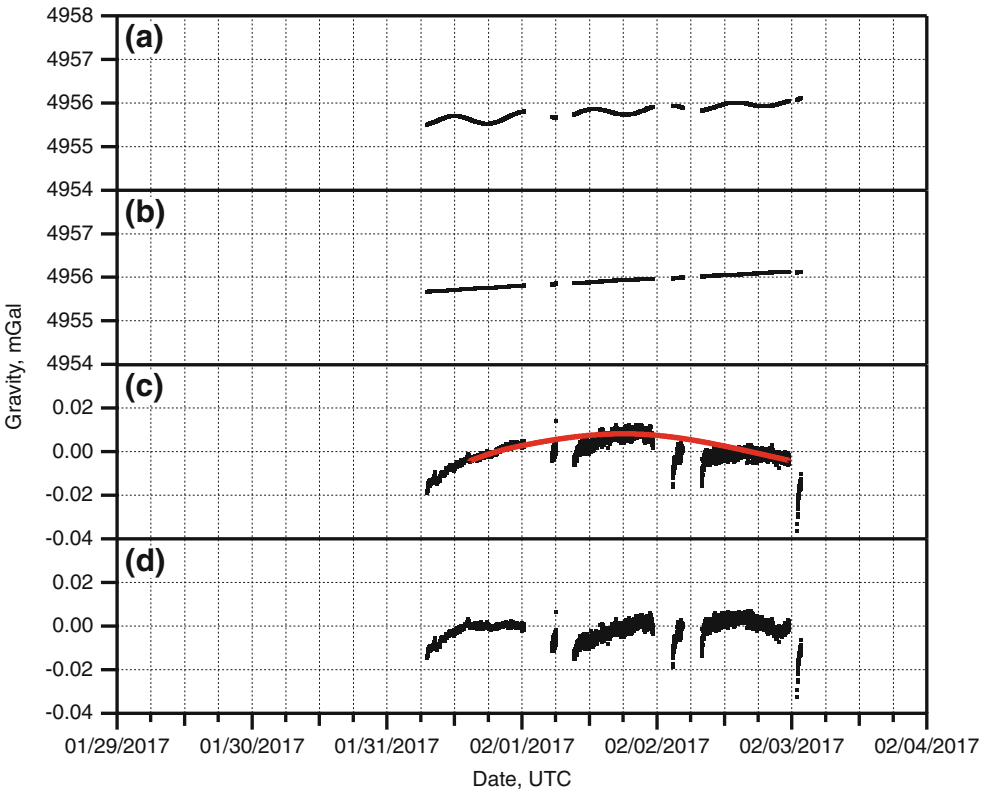

Fig. 3 Same as Fig. 2 but for CG-5 #1153. No data are available before January 31 and after February 3

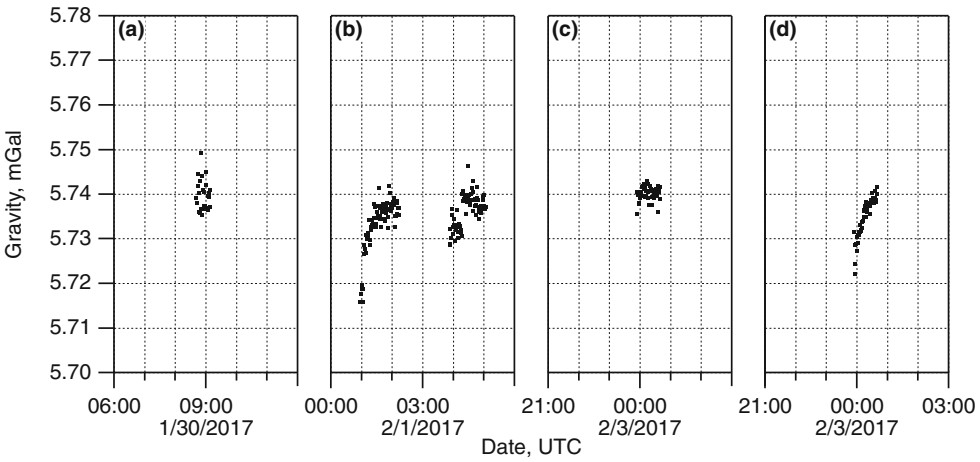

Fig. 4 Corrected gravity values at the station "30" by two CG-5's. Gravity is the difference with respect to the value at the base station. (**a**) CG-5 #0890. The wind was very strong then. (**b**) CG-5 #1153. There are two measurements. (**c**) CG-5 #0890 (**d**) CG-5 #1153

Table 1 Relative gravity acceleration at two stations with respect to the base station (VERA)

Station ID	Date	Instrument	Relative gravity (mGal)
13	Jan 31, 2017	#0890	$+5.7393 \pm 0.0029$
	Feb 1, 2017	#1153	$+5.7375 \pm 0.0021$
	Feb 3, 2017	#0890	$+5.7397 \pm 0.0017$
	Feb 3, 2017	#1153	$+5.7387 \pm 0.0019$
23B	Feb 1, 2017	#1153	$+5.7976 \pm 0.0017$
	Feb 2, 2017	#1153	$+5.7948 \pm 0.0021$

#1153 in the experiment. The weighted average of the two measurements at "23B" is $(+5.7965 \pm 0.0013)$ mGal. These results indicate that our strategy has been successful in retrieving gravity to the accuracy better than a few μGal.

3 Conclusions

In this paper, we have proposed combined use of the superconducting gravimeter and the Scintrex gravimeters for time lapse gravity measurements. Although both types of gravimeters are relative instruments, the SG, once calibrated against the absolute scale, can serve as an absolute standard for hybrid gravimetry. Repeated measurements by means of Scintrex CG-5 gravimeters at the stations near the SG site at Ishigakijima proved that use of the SG data as a reference can help addressing the problem of irregular instrumental drift of spring-type gravimeters, and therefore improving the accuracy of the local gravity survey. We plan to repeat similar experiments at Ishigakijima in order to see if there are long-term changes in spatial gravity distribution possibly associated with underground water.

Acknowledgements We thank the VERA Project of National Astronomical Observatory of Japan for supporting our superconducting gravimeter observations at the VERA Ishigakijima station. Comments by two anonymous reviewers were helpful for improving the paper. This work was financially supported by JSPS KAKENHI Grant Numbers JP23340125, JP26289350 and JP26610139, and by the Cooperative Research Program of Earthquake Research Institute, The University of Tokyo.

References

Fores B, Champollion C, Le Moigne N, Chery J (2017) Impact of ambient temperature on spring-based relative gravimeter measurements. J Geod 91:269–277

Furuya M, Okubo S, Sun W, Tanaka Y, Oikawa J, Watanabe H, Maekawa T (2003) Spatiotemporal gravity changes at Miyakejima volcano, Japan: caldera collapse, explosive eruptions and magma movement. J Geophys Res 108:2219–2235

Gettings P, Chapman DS, Allis R (2008) Techniques, analysis, and noise in a salt Lake Valley 4D gravity experiment. Geophysics 73(6):WA71–WA82

Goodkind JM (1999) The superconducting gravimeter. Rev Sci Instrum 70:4131–4152

Hector B, Séguis L, Hinderer J, Cohard JM, Wubda M, Descloitres M, Benarrosh N, Boy JP (2015) Water storage changes as a marker for base flow generation processes in a tropical humid basement catchment (Benin): insights from hybrid gravimetry. Water Resour Res 51:8331–8361

Heki K, Kataoka T (2008) On the biannualy repeating slow slip events at the Ryukyu trench, Southwest Japan. J Geophys Res 113:B11402. https://doi.org/10.1029/2008JB005739

Hinderer J, Calvo M, Abdelfettah Y, Hector B, Riccardi U, Ferhat G, Bernard JD (2015) Monitoring of a geothermal reservoir by hybrid gravimetry; feasibility study applied to the Soultz-sous-Forêts and Rittershoffen sites in the Rhine graben. Geotherm Energy 3:16

Honma M, Oyama T, Hachikusa K, Sawada-Satoh S, Sebata K, Miyoshi M, Kameya O, Manabe S, Kawaguchi N, Sasao T, Kameno S, Fujisawa K, Shibata KM, Bushimata T, Miyaji T, Kobayashi H, Inoue M, Imai H, Araki H, Hanada H, Iwadate K, Kaneko Y, Kuji S, Sato K, Tsuruta S, Sakai S, Tamura Y, Horiai K, Hara T, Yokoyama K, Nakajima J, Kawai E, Okubo H, Osaki H, Koyama Y, Sekido M, Suzuyama T, Ichikawa R, Kondo T, Sakai K, Wada K, Harada N, Tougou N, Fujishita M, Shimizu R, Kawaguchi S, Yoshimura A, Nakamura M, Hasegawa W, Morisaki S, Kamohara R, Funaki T, Yamashita N, Watanabe T, Shimoikura T, Nishio M, Omodaka T, Okudaira A (2000) J-net galactic-plane survey of VLBI radio sources for VLBI exploration of radio astrometry (VERA). Publ Astron Soc Jpn 52:631–643

Ikeda H, Nawa K, Imanishi Y (2013) Refurbishment and performance of the superconducting gravimeter CT-36. J Geod Soc Jpn 59:25–36
Imanishi Y, Kokubo K, Tatehata H (2006) Effect of underground water on gravity observation at Matsushiro, Japan. J Geodyn 41:221–226
Kroner C, Jahr T (2006) Hydrological experiments around the superconducting gravimeter at Moxa observatory. J Geodyn 41:268–275
Meurers B, Van Camp M, Petermans T (2007) Correcting superconducting gravity time-series using rainfall modelling at the Vienna and Membach stations and application to earth tide analysis. J Geod 81:703–712
Nawa K, Suda N, Yamada I, Miyajima R, Okubo S (2009) Coseismic change and precipitation effect in temporal gravity variation at Inuyama, Japan: a case of the 2004 off the Kii peninsula earthquakes observed with a superconducting gravimeter. J Geodyn 48:1–5
Okubo S (2001) Investigating earthquakes and volcanic activities with hybrid gravimetry. Jishin J 31:47–58
Reudink R, Klees R, Francis O, Kusche J, Schlesinger R, Shabanloui A, Sneeuw N, Timmen L (2014) High tilt susceptibility of the Scintrex CG-5 relative gravimeters. J Geod 88:617–622
Sugihara M (2009) Continuous gravity measurements for geothermal reservoir monitoring: –present status and a future scenario–. In: New Zealand Geothermal Workshop 2009 Proceedings, pp 14–19
Van Camp M, Francis O (2007) Is the instrumental drift of superconducting gravimeters a linear or exponential function of time? J Geod 81:337–344
Van Camp M, Vanclooster M, Crommen O, Petermans T, Verbeeck K, Meurers B, van Dam T, Dassargues A (2006) Hydrogeological investigations at the Membach station, Belgium, and application to correct long periodic gravity variations. J Geophys Res 111:B10403. https://doi.org/10.1029/2006JB004405

Evaluation of the Global Altimetric Marine Gravity Field DTU15: Using Marine Gravity and GOCE Satellite Gravity

O. B. Andersen, P. Knudsen, S. Kenyon, S. Holmes, and John K. Factor

Abstract

Global marine gravity field modelling using satellite altimetry has been undergoing constant improvement since the launch of Cryosat-2 mission in 2010. With its 369 day-repeat Cryosat-2 provides one repeat of geodetic mission data with 8 km global resolution each year. Together with the completion of the Jason-1 end-of-life geodetic mission in 2011 and 2012, these new satellites has provided more than 4 times three times as much geodetic missions altimetric sea surface height observations than ever before. The higher precision of these new sea surface height observations compared with observations from ERS-1 and Geosat results in a dramatic improvement of the shorter wavelength of the gravity field (12–20 km) resulting in much favorable comparison with marine gravity. The pan-Arctic altimetric gravity field now surpassing 2008 Arctic Gravity Field project derived from multiple gravity field sources. A direct comparison between Arctic marine gravity fields and independent gravity field from the Gravity Field and Steady-State Ocean Circulation Explorer to degree and order 280 confirms this.

Keywords

GOCE · Marine gravity · Satellite altimetry

1 Introduction

Since the release of the DTU10 global marine gravity field in 2010, the amount of geodetic mission altimetry has nearly tripled revolutionizing our ability to derive marine gravity from satellite data (Andersen et al. 2010a). Cryosat-2 has provided new data along its 369 day near repeat since 2010 (Wingham et al., 2006). Between May 2012 and June 2013 the Jason-1 satellite provided a 406 days geodetic mission as part its end of life mission providing data of high spatial density.

Cryosat-2 and Jason-1 are new generations of satellite altimeters offering increased range precision compared with the older ERS-1 and Geosat generation satellites flown more than 20 years ago. Both satellites offer an improvement in range precision between 20–50% compared with conventional altimetry. Range precision directly maps into gravity field accuracy this should also significantly improve global marine gravity field mapping. The Jason-1 is extremely valuable for both global high resolution gravity field modelling at low to mid latitude (Sandwell et al. 2014). However, north of 66° degree and throughout the Arctic Ocean only satellites with a higher inclination like Cryosat-2, ERS-1, ENVISAT and SARAL/AltiKA provides data.

In this article we try to quantify the accuracy improvement these new satellites gives to global altimetric gravity field modeling. We use comparisons with highly accurate marine

O. B. Andersen (✉) · P. Knudsen
DTU Space, Kongens Lyngby, Denmark
e-mail: oa@space.dtu.dk

S. Kenyon
S2 Analytics, Arnold, MO, USA

S. Holmes
SGT-inc, Greenbelt, MD, USA

J. K. Factor
NGA, Arnold, MO, USA

J. T. Freymueller, L. Sanchez (eds.), *International Symposium on Advancing Geodesy in a Changing World*,
International Association of Geodesy Symposia 149, https://doi.org/10.1007/1345_2018_52

airborne gravity observations. In the Arctic Ocean, where marine gravity is sparse, we perform a comparison with a satellite only gravity field from the Gravity Field and Steady-State Ocean Circulation Explorer (GOCE) to degree and order 280.

2 Cryosat-2 and Jason-1 Geodetic Mission Altimetry

Cryosat-2 provides data to 200 km from the North Pole due to its inclination of 88°. The limit of former geodetic satellites was 86°N for ICESat; 82°N for ERS-1; 72°N for GEOSAT and 66°N for the Jason satellites.

The availability of the new altimetric data is a quantum leap forward for altimetric gravity field modeling in Polar region now covered with altimetry data to 200 km from the North Pole. The ice-covered part of the Arctic Ocean the high-resolution Synthetic Aperture Radar Altimetry (SAR) is used (i.e., Raney 1998). SAR is particularly important in ice-covered regions, as it decrease the footprint of the radar beam by a factor of 100 and increases the ability of sea surface height mapping in leads within the ice.

In order to derive sea surface height in ice-covered Arctic Ocean we have retracked the Cryosat-2 Level 1B SAR waveform data over the Arctic Ocean using an empirical narrow peak retracker (Jain et al. 2015). This retracker is an in-house developed empirical SAR retracker developed for the Arctic. Figure 1 shows the number of validated 1-Hz Sea surface height observations per 10 × 10 km (or 100 km^2) cells in the Arctic Ocean, that can be used to predict gravity altimetric gravity. The figure shows data from all geodetic missions including: ERS-1, Geosat, Jason-1 and Cryosat-2.

The 1-Hz altimetric observations are derived by averaging all 20 Hz individual sea surface height observations within one-second bins and the associated range error is computed as the standard deviation of the 20 observations. Typically, seventeen sea surface height is the lower limit for estimating 1 Hz values in the open ocean. Within the ice-covered regions (leads) we lowered the limit of 20 Hz observations to four within each one second bin. Consequently, these data will have range precision than normal open ocean 1 Hz averaged sea surface height observations. Details can be found in Stenseng and Andersen (2012).

3 Updated Methodology

After retracking, all available sea-surface heights are corrected for various range corrections (Andersen and Scharroo 2011) and processed to extract the residual geoid information following the methods described in Andersen et al. (2010b). A remove-restore technique relative to EGM2008 (Pavlis et al. 2012) was applied, and the data are processed in global mesh of tiles of 1° by 3° latitude by longitude. North of 88°N and on land we augmented DTU15 with EGM2008 free-air gravity to ensure global coverage.

For the development of DTU15 the methodology was updated in two ways:

Firstly, the Mean dynamic topography (MDT) associated with EGM2008 was updated and extended beyond degree and order 180 as an evaluation with Exact Repeat mission (ENVISAT and Jason-1) sea surface height data revealed

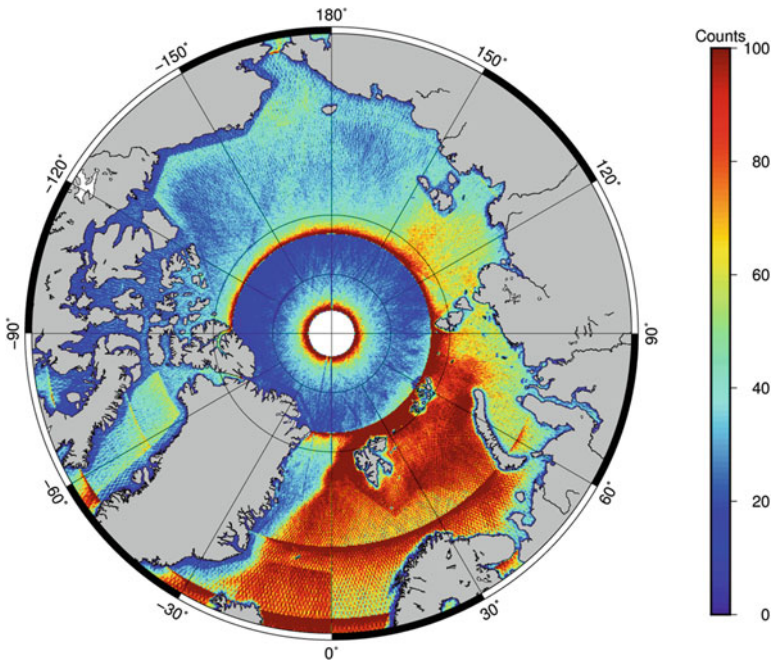

Fig. 1 Number of sea level observations per 10 × 10 km block for the Arctic Ocean available for the derivation of the DTU15 global marine gravity field. Close to the inclination of the individual satellites (88° for Cryosat-2; 82° for ERS+ENVISAT+SARAL; 72° for GEOSAT and 66° for Jason-1) higher density of observations will be available

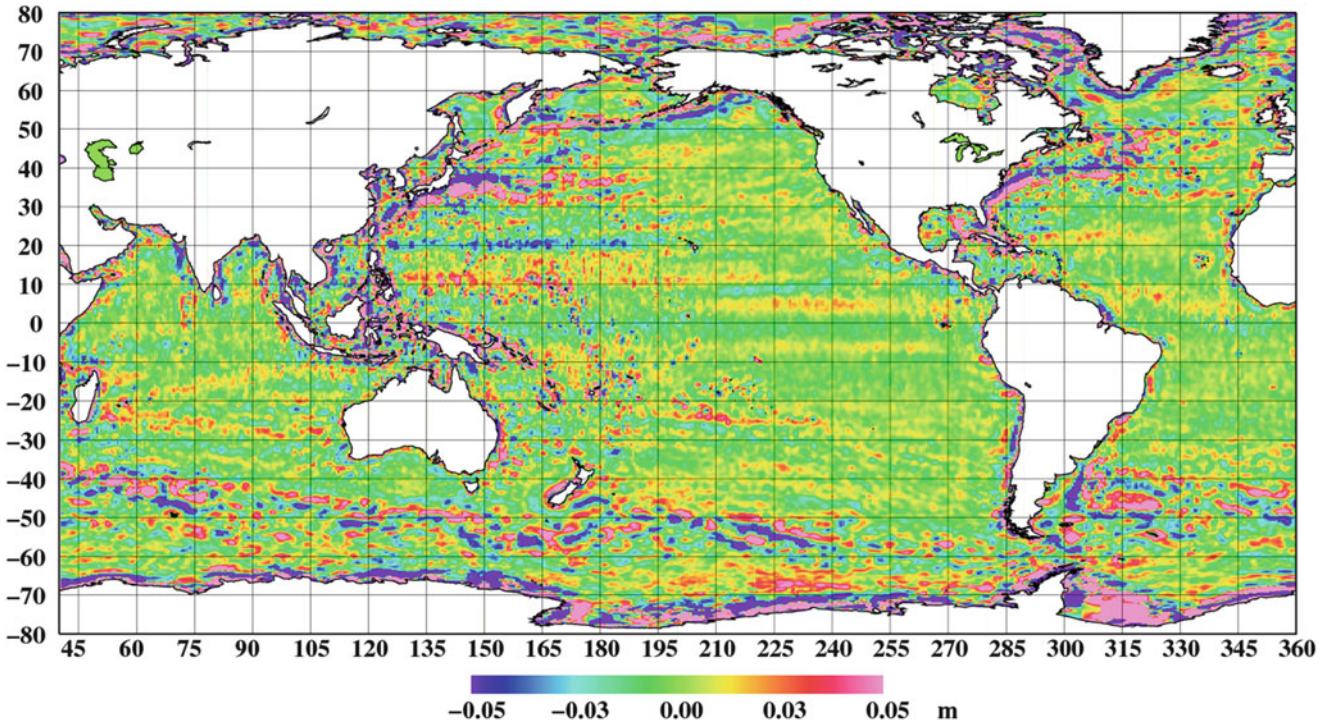

Fig. 2 The short wavelength residual Mean Dynamic Topography signal in the MDT associated with EGM2008 as computed from repeated satellite altimetry from Jason-1 and ENVISAT

that this MDT exhibits short wavelength residual signal on the few cm scale associated with inadequate mapping of the topography associated with particularly current systems. We computed a residual MDT, shown in Fig. 2 from altimetry and removed this along with the EGM08 MDT when calculating DTU15. This significantly stabilizes the crossover adjustment applied to reduce oceanographic noise in the sea surface height observations (Andersen et al. 2010a).

Secondly, the spatial filtering in the interpolation of the residual geoid height was relaxed compared with previous DTU gravity fields. In the interpolation of residual geoid heights onto a 1-min grid the correlation length in the second order Markov covariance function was decreased from 6.5 to 5.5 km half wavelength. In the Fast Fourier Transformation used to convert gridded residual geoid heights to gravity the filtering could also be relaxed from 6.5 to 6 km to maintain wavelength longer than 12 km in the global marine gravity field.

4 Evaluation with Marine Gravity Observations

An evaluation with more than 1.4 million high quality edited un-classified marine gravity observations from the National Geospatial-intelligence Agency was used to evaluate the various available global marine gravity fields in the northwest part of the Atlantic Ocean between 20°N and 45°N and 270°E and 330°E. The Sandwell and Smith marine gravity field release 23.1 and 24.1 (Sandwell et al. 2013) are available from http://topex.ucsd.edu/marine_grav/mar_grav.html were also included in the comparison with marine observations.

Table 1 Comparison with more than 1.4 mission quality controlled marine gravity field observations in the northwest Atlantic Ocean

	Std (mGal)	Mean (mGal)	Max (mGal)
DTU15	2.51	0.5	32.3
DTU13	2.83	0.5	32.2
DTU10	3.16	0.5	44.1
SS 23.1	3.13	0.7	43.4
SS 24.1	3.11	0.7	41.9

The evaluation shown in Table 1 has marine gravity field observations all the way from the coast until the deepest part of the Atlantic Ocean and all across the Gulf Stream.

Compared with former DTU gravity fields DTU10 and DTU13 as well as the Sandwell and Smith gravity field, DTU15 shows an improvement in standard deviation with marine gravity observations of around 12–23%.

The comparison between altimetry and marine gravity will also include errors in the marine gravity observations. The accuracy of the marine gravity field observations is quoted at 1.5 mGal. With an standard deviation of 2.5 mGal

between DTU15 and the marine gravity field observations, this means that the accuracy of the DTU15 altimetric gravity field must be around 2 mGal. A significant part of the marine gravity observations used in Table 1 is measured in a region of high sea surface variability (Gulf Stream region). In regions of high sea surface variability, the accuracy of altimetric derived marine gravity field is decreased. This means that for regions of lower sea surface variability the accuracy of the DTU15 is likely better than 2 mGal.

5 Evaluation in the Arctic Using GOCE

In the Arctic Ocean an evaluation of available marine gravity field were performed using an independent source of information. Here the gravity observations comparison (GOCO) satellite only geoid model called GOCO05S was used for the evaluation.

For the comparison we also included the 2008 version of the Arctic Gravity field (ArcGP) from http://earth-info.nga.mil/GandG/wgs84/agp/index.html which is based on compilation of available gravity field observations in the Arctic.

Free air gravity field at 5 min spatial resolution was derived from the GOCO05S geoid to degree and order 280. Subsequently all land cells within the DTU15 & SS23.1 & ArcGP gravity field were substituted with these GOCO05S gravity field values. Hence, all discrepancies with GOCO05S reflect only differences within the Arctic Ocean. The global marine gravity fields by Sandwell and Smith are limited to 80°N leaving a Polar Gap of 10°. Subsequently we used DTU15 to augment SS23.1 north of 80°N.

The comparison in Fig. 3 illustrates the accuracy of recent altimetric gravity field in the Arctic Ocean. The comparison with the GOCO05S is limited to degree and order 280 corresponding to wavelength longer than roughly 150 km. The standard deviation of the differences are 1.097 mGal for the ArcGP dataset and around 0.8 mGal for both DTU15 and SS23.1 gravity fields. The upper right panel of Fig. 3 illustrate the different gravity sources used to compute ArcGP. By correlating the ArcGP and GOCO05S it is evident that the errors in ArcGP is associated with the potential offsets within the various data compilations in ArcGP. In the Canadian Basin a tilt in the NRL data seems to degrade the comparison. Similarly, the KMS-Norway data used around Svalbard seems to have a bias. North of 80°N the error in GOCO05S increases towards the North Pole and we limited the comparison to 82°N. The GOCO05S error north of 80 is visible in the lower panels for the comparison for SS 23.1 and DTU15 (SS 23.1 is identical to DTU15 north of 80°N).

There are visible differences in the comparison between GOCO05S and SS v23.1 and between GOCO05S and DTU15. Within the Canadian Arctic Archipelago region SS 23.1 shows visible differences pointing towards an offset in SS23.1. In the Baffin Bay between Canada and Greenland, DTU15 clearly shows the largest discrepancies. This might indicate problems with the short wavelength correction shown in Fig. 2, which has the same north-south direction as the differences with GOCO05S.

6 Conclusion

With the completion of the Jason-1 end-of-life geodetic mission, and the ongoing Cryosat-2 mission three times as many sea surface height observations have become available compared with the old ERS-1 and Geosat geodetic mission data.

These new data have initiated new era in satellite derived marine gravity as these second-generation altimetric data have higher range precision. Particularly the mapping of gravity field wavelength within the 13–18 km range have increased dramatically revealing both new gravity field structures (Stenseng and Andersen 2012) and related bathymetric signals (Sandwell et al. 2014).

In the Arctic Ocean comparison with marine gravity from the satellite only geoid model called GOCO05S to degree and order 280 indicate that particularly the long wavelength of recent altimetric gravity fields surpasses the 2008 ArcGP gravity field compilation. A comparison with a huge compilation of more than 1.4 million quality controlled marine gravity field observations revealed an accuracy of around 2 mGal in the Gulf Stream region for DTU15.

Several interesting developments from these new data are still to come in the near future. One is the use of the Synthetic Aperture Radar Altimeter data from other Cryosat-2 regions. As of 2016 a new unforeseen geodetic mission has become available with the SARAL/AltiKa which is put into an uncontrolled geodetic mission due to a problem with the reaction wheel which is important to maintain the exact repeat mission. Further to this, Jason-2 entered a 3-year geodetic end-of-life mission in 2017. This will provide a novel geodetic mission data with uniform cross-track spacing of 4 km upon completion in 2019.

Data Availability

The DTU15 global high-resolution marine gravity field along with the DTU suite of related geophysical products like bathymetry is available from ftp.space.dtu.dk/pub/DTU15 or by email request to the author at oa@space.dtu.dk.

In Memoriam

Simon Holmes, co-author on this article passed away too soon in 2017. Simon will be missed as an outstanding scientist and, most profoundly, as a great friend.

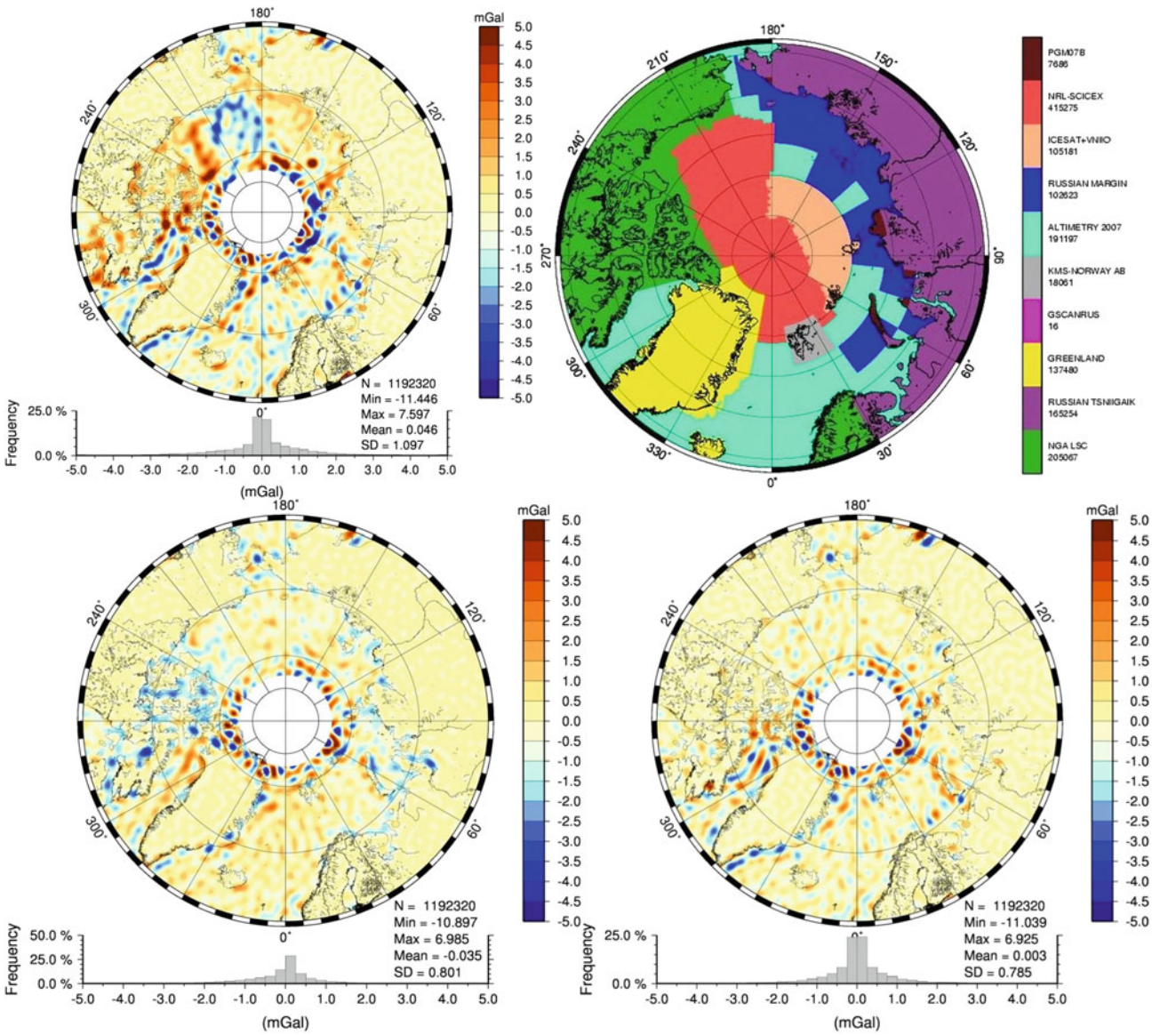

Fig. 3 Comparison between the GOCO05S gravity field and the ArcGP (upper left), the SS 23.1 (lower left) and DTU15 (lower right). The sources for the ArcGP are shown in the upper right panel

References

Andersen OB, Scharroo R (2011) Range and geophysical corrections in coastal regions: and implications for mean sea surface determination. In: Vignudelli S et al (eds) Coastal altimetry. Springer, New York, pp 103–145. https://doi.org/10.1007/978-3-642-12796-0_5

Andersen OB, Knudsen P, Berry P (2010a) Recent development in high resolution global altimetric gravity field modeling. Lead Edge 29(5):540–545, ISSN: 1070-485X

Andersen OB, Knudsen P, Berry PAM (2010b) The DNSC08GRA global marine gravity field from double retracked satellite altimetry. J Geod 84:191–199. https://doi.org/10.1007/s00190-009-0355-9

Jain M, Andersen OB, Dall J, Stenseng L (2015) Sea surface height determination in the Arctic using Cryosat-2 SAR data from primary peak empirical retrackers. Adv Space Res 55(1):40–50. https://doi.org/10.1016/j.asr.2014.09.006. ISSN: 0273-1177

Pavlis NK, Holmes S, Kenyon S, Factor JK (2012) The development and evaluation of the Earth Gravitational Model 2008 (EGM2008). J Geophys Res. https://doi.org/10.1029/2011JB00891

Raney RK (1998) The delay Doppler radar altimeter. IEEE Trans Geosci Remote Sens 36:1578–1588

Sandwell DT, Garcia E, Soofi K, Wessel P, Chandler M, Smith WHF (2013) Towards 1-mGal accuracy in global marine gravity from Cryosat-2, Envisat and Jason-1. Lead Edge 2013:892–898

Sandwell DT, Müller RD, Smith WH, Garcia E, Francis R (2014) New global marine gravity model from CryoSat-2 and Jason-1 reveals buried tectonic structure. Science 346(6205):65–67. https://doi.org/10.1126/science.1258213

Stenseng L, Andersen OB (2012) Preliminary gravity recovery from CryoSat-2 data in the Baffin Bay. Adv Space Res 50(8):1158–1163

Wingham D, Francis CR, Baker S, Bouzinac C, Brockley D, Cullen R, de Chateau-Thierry P, Laxon SW, Mallow U, Mavrocordatos C, Phalippou L, Ratier G, Rey L, Rostan F, Viau P, Wallis DW (2006) CryoSat-2: a mission to determine the fluctuations in Earths land and marine ice fields. Adv Space Res 37(4)

Part III

Time Variable Gravity Field

Status of Development of the Future Accelerometers for Next Generation Gravity Missions

B. Christophe, B. Foulon, F. Liorzou, V. Lebat, D. Boulanger, P.-A. Huynh, N. Zahzam, Y. Bidel, and A. Bresson

Abstract

The GRACE FO mission, led by the JPL (Jet Propulsion Laboratory) and GFZ (GeoForschungsZentrum), is an Earth-orbiting gravity mission, continuation of the GRACE mission, which will produce an accurate model of the Earth's gravity field variation providing global climatic data during 5 years at least. Europe and US propose new gravity missions beyond GRACE-FO, with improved performance thanks to laser interferometry and better accelerometers. ONERA has procured the accelerometers for the previous geodetic mission (CHAMP, GRACE, GOCE and now GRACE-FO) and continues to improve the instruments to answer to the challenge of the future missions according to two main domains: Firstly, a new design of electrostatic accelerometer is proposed, based on MicroSTAR configuration, a 3-axes ultra-sensitive accelerometer, with a cubic proof-mass. Secondly, ONERA studies the hybridization of such electrostatic accelerometer with cold atom interferometer technology in order to take advantage of each instrument (high sensitivity for electrostatic accelerometer in short term, and absolute measurement for atom interferometer). A first result of the hybrid instrument, obtained on ground, is presented.

Keywords

Atom interferometer · Electrostatic accelerometer · Gravity

1 Introduction

The knowledge of the Earth gravity field has been deeply improved since 17 years, thanks to new gravity satellite missions: the German CHAMP satellite launched in 2000 (Reigber et al. 1999), the twin satellites of the German-US project GRACE launched in 2002 (Tapley et al. 2004), then the ESA's GOCE mission launched in 2009 (Allasio et al. 2009; Drinkwater et al. 2007). These three missions have in common to carry ONERA electrostatic accelerometers for measuring the surface forces.

CHAMP and GOCE satellites end in September 2010 and November 2013 respectively, and GRACE satellites will be decommissioned at the end of 2017 due to battery cell problems on one satellite (after more than 15 years in orbit for an initial mission lifetime of 5 years). The German-US GRACE Follow-On (GRACE-FO) mission will continue the GRACE mission objectives with a launch scheduled on March 21st, 2018 (Flechtner et al. 2014).

Beyond GRACE-FO, European (Panet et al. 2012; Cesare and Sechi 2013; Elsaka et al. 2014) and US (Wiese et al. 2009, 2012) scientists study future gravity missions, based on GRACE measurement principle, but with improved instruments. For the accelerometer, the requirements are:

– a noise level between $1.5 \times 10^{-12}\,\mathrm{m/s^2/\sqrt{Hz}}$ (Cesare and Sechi 2013) and $4 \times 10^{-11}\,\mathrm{m/s^2/\sqrt{Hz}}$ over 1–10 mHz (Gruber et al. 2014);

B. Christophe (✉) · B. Foulon · F. Liorzou · V. Lebat · D. Boulanger · P.-A. Huynh
DPHY, ONERA, Université Paris Saclay, Chatillon, France
e-mail: Bruno.Christophe@onera.fr

N. Zahzam · Y. Bidel · A. Bresson
DPHY, ONERA, Université Paris Saclay, Palaiseau, France

J. T. Freymueller, L. Sánchez (eds.), *International Symposium on Advancing Geodesy in a Changing World*,
International Association of Geodesy Symposia 149, https://doi.org/10.1007/1345_2018_42

– an improvement of the low-frequency noise of the accelerometer (below 1 mHz) with respect to GOCE;
– an identical performance along the three directions;
– the capability to use the accelerometer in the attitude control, by providing accurate angular acceleration in complement of the star trackers;

With respect to these requirements, ONERA works into two complementary directions:

1. an electrostatic accelerometer with a cubic proof-mass, MicroSTAR, providing three sensitive axes and angular accelerations;
2. the hybridization of electrostatic accelerometer with atom interferometer in order to improve the low-frequency noise.

2 Electrostatic Accelerometer MicroSTAR

2.1 Description

Up to now, ONERA accelerometers have a less-sensitive axis in order to levitate the proof-mass on ground under 1 g. This behavior allows a verification of the accelerometers on an anti-seismic pendulum. With the experience on the accelerometer design and the new catapult drop tower (von Kampen et al. 2006), it is possible to envisage ground verification only through free fall drop, without levitation under 1 g. It was applied with success with Microscope mission (Touboul et al. 2011).

The accelerometer MicroSTAR is a three axes sensitive accelerometer, initially imagined for interplanetary missions with a bias rejection system (Lenoir et al. 2011). But its configuration with a cubic proof-mass is also interesting for future gravity mission as it provides the same performance along the three axes but also angular accelerations for attitude control or recovery (Christophe et al. 2015). The proof-mass is surrounded by three pairs of identical electrode plates in Ultra Low Expansion material (ULE), each pair controlling two degrees of freedom. The accelerometer electronic architecture is composed of six control loops, one for each degree of freedom of the proof-mass. Along each of the three axes, one translation and one rotation are controlled by similar schemes.

2.2 Performance

The performance of the MicroSTAR accelerometer can be adapted with respect to each mission and spacecraft, as the acceleration is dependent on the trajectory and on the mass and surface of the spacecraft. The range and the noise of the instrument are adjusted during the definition by tuning the size of the proof-mass in order to modify the gap between proof-mass and electrodes. The choice of proof-mass material gives also opportunity of performance improvement.

For achieving the noise requirement for future gravity mission, the mechanical core of the accelerometer is composed of an Arcap cubic proof-mass of 30 × 30 × 30 mm and 218 g, surrounded by three pairs of identical electrode plates, at a distance of 400 µm. This configuration provides a measurement range of $\pm 6.4 \times 10^{-6}$ m/s^2. Figure 1a presents the noise figure leading to a RMS accuracy as low as $\pm 6.6 \times 10^{-12}$ m/s^2 inside the measurement bandwidth from 0.2 mHz to 0.1 Hz. The main contributors of the noise are the capacitive detector noise at high frequency, the Analog to Digital converter (ADC) in the measurement bandwidth and the thin wire damping (wire for polarizing the proof-mass), the contact potential noise (CPD) and the bias thermal fluctuation at low frequency.

With this configuration, the accelerometer provides also the angular acceleration with a RMS accuracy of as low as $\pm 2.2 \times 10^{-10}$ rad/s^2 inside the measurement bandwidth from 0.2 mHz to 0.1 Hz (see the noise in Fig. 1b)

2.3 Status of Development

A reduced prototype of MicroSTAR, with a cubic proof-mass of 20 × 20 × 20 mm in ULE, was built in order to

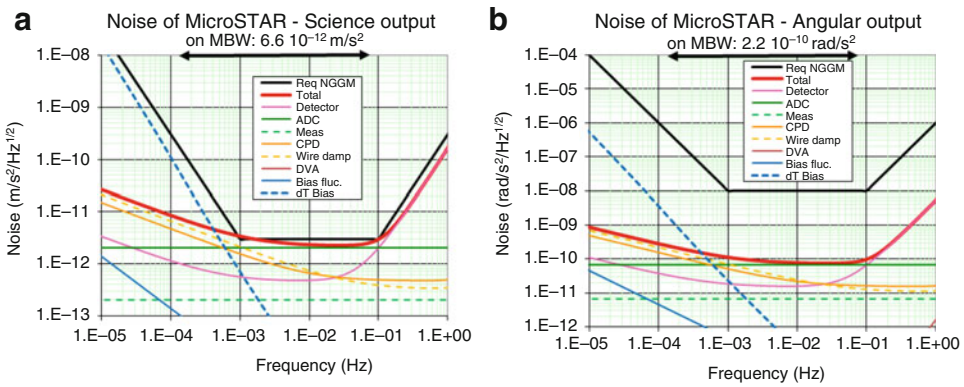

Fig. 1 Noise error budget of the MicroSTAR accelerometer with a gap of 400 µm and a proof-mass of 218 g for future gravity mission. (**a**) Linear output, (**b**) angular output

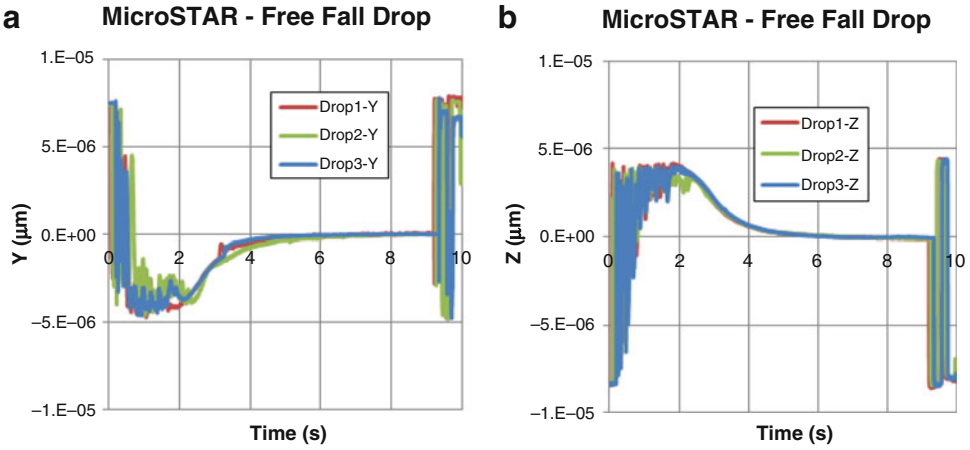

Fig. 2 MicroSTAR prototype proof-mass decentering along Y (**a**) and Z (**b**) during three free fall drops (red, green and blue)

verify the concept and optimize the accelerometer control loop. The gap between proof-mass and electrode is adapted to allow ground levitation along one direction. The front-end electronic unit is implemented around the mechanical sensor.

In December 2016, three first drops have been done at Zarm to verify the accelerometer control loop. Figure 2 shows the proof-mass acquisition along Y and Z axis. The curves show the decentering of the proof-mass with respect to the cage during each drop. The drop capsule is released in free fall at 0 s and finishes its fall at 9.4 s. After 2 s, the control loop of the accelerometer stabilizes the proof-mass at the center of the cage. The three drops provide the same figure of acquisition of the proof-mass.

3 Hybridization of Electrostatic Accelerometer and Atom Interferometer

3.1 Principle

A new generation of sensors based on cold atom interferometry is emerging and seems very promising. These atomic instruments have already demonstrated on ground impressive results, especially with the development of state-of-the-art gravimeters (Hu et al. 2013; Gillot et al. 2014; Freier et al. 2016), and should reach their full potential only in space, where the microgravity environment allows long interaction times and providing absolute measurement (Carraz et al. 2015). It is so natural to think to hybridize this instrument with electrostatic accelerometer, which has higher short term sensitivity, but suffers from bias evolution. An hybrid instrument could be the opportunity to make a big step in this context for gravity space missions. Following this idea, this study aims to demonstrate the first colocation of an electrostatic accelerometer and an atom interferometer.

3.2 Description of Ground Prototype

The hybrid prototype is obtained by mounting an electrostatic accelerometer just below a cold atom gravimeter (Bidel et al. 2013), the electrostatic accelerometer proof-mass acting as the Raman mirror for the atom interferometer.

In order to perform an efficient hybridization between the atom accelerometer and the electrostatic one, both measuring points should be as close as possible allowing both sensors to measure exactly the same acceleration. In practice, in all the experiments having demonstrated the coupling of an atomic sensor with a mechanical one, the Raman mirror, acting as the reference for the atomic measurement, is fixed rigidly to the mechanical accelerometer housing, reducing the separation between the two measuring points. To our knowledge, no experiment has reported hybridization by directly linking the atoms and the proof mass through the Raman laser.

3.3 Results

One strong feature of a hybrid architecture is to benefit from the intrinsic long term stability of an atom interferometer to correct the electrostatic accelerometer drift. To illustrate this scheme and highlight all its potential, we have implemented experimentally a hybridization algorithm combining both ES and atomic outputs. In this Kalman like algorithm, the output of the hybrid sensor is given at 4 Hz and the electrostatic accelerometer (the continuous output of the electrostatic accelerometer is nevertheless still available) is used to determine the atom interferometer fringe index for each cycle. Also for each cycle, the electrostatic accelerometer bias is evaluated thanks to the atom interferometer (Geiger et al. 2011).

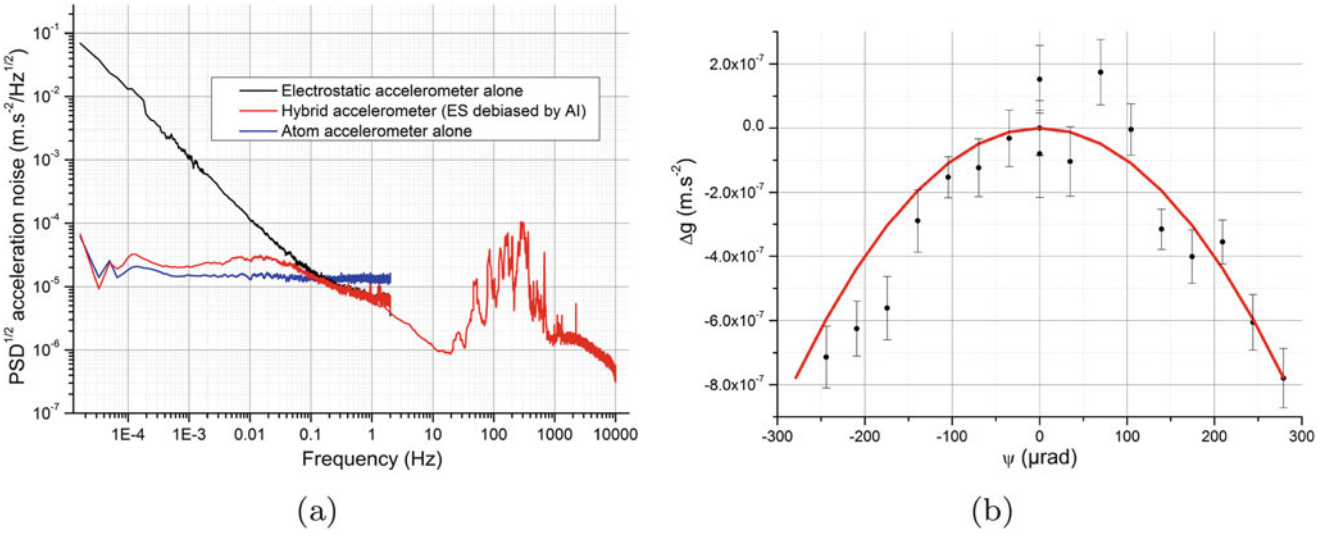

Fig. 3 (**a**) Root square of Power Spectral Density acceleration noise for the electrostatic accelerometer (ES), the atom interferometer (AI), and the hybrid accelerometer. The interrogation time of the atom interferometer is T = 20 ms. (**b**) Gravity measurement variation according to the angular orientation ψ of the electrostatic accelerometer proof-mass. The measurements are given by the atom interferometer for T = 46 ms. Each point results from around 2 min averaging

Concretely, the bias is calculated by subtracting the values of both sensors according to the following equation:

$$bias_i = bias_{i-1} + G_b.\left(acc_i^{ES} - bias_{i-1} - acc_i^{AI}\right) \quad (1)$$

where

- $bias_i$ is the bias estimated after cycle i,
- G_b is the gain of the bias correction loop,
- acc_i^{ES} is the non-corrected ES output after cycle i,
- acc_i^{AI} is the AI output after cycle i.

We can see on Fig. 3a such experimental results of this hybridization algorithm for an interrogation time, T = 20 ms, of the atom interferometer that illustrates qualitatively in a clear way the gain that could be reached in a future space mission.

Of course, this first experimental result obtained on ground under 1 g constraint does not allow to reach the performance expected from an electrostatic accelerometer, an atom interferometer or a hybrid instrument in a future space mission: due to the presence of 1 g the free fall time of the atoms is reduced at T = 20 ms and the electrostatic accelerometer proof-mass is levitated with high voltage (about 1,000 V). In space, the performance will be improved by increasing the free fall of the atoms and with a different geometric and electronic configurations for the electrostatic accelerometer in order to have the performance announced in Fig. 1.

Other advantage of the hybridization concept is the fact that the control of the electrostatic accelerometer proof-mass could be a way to mitigate satellite rotation impact on atom interferometer signals. In this study, a first step has been made towards proof-mass control of the electrostatic accelerometer to ultimately compensate parasitic rotations. The experiment consists in demonstrating the ability to control in a precise way the rotation of the proof-mass around the two horizontal axis θ and ψ. The proof-mass was thus rotated to retrieve the square dependency of the measured gravity with misalignment θ and ψ (see Fig. 3b).

4 Conclusions

ONERA has designed a new electrostatic accelerometer, MicroSTAR, with the same high performance along the three-axis. This accelerometer provides also, thanks to a cubic proof-mass, true angular accelerations. A ground prototype of MicroSTAR has been built and tested through drop tower tests with good acquisition of the proof-mass along two axes. In parallel, ONERA studies hybridization of MicroSTAR with atomic interferometer. A ground prototype has been built and tested under 1 g. The principle of the hybridization has been demonstrated with the low-frequency noise improvement. The use the electrostatic accelerometer proof-mass as the mirror for the atomic interferometer will also allow to counteract the attitude motion of the satellite during the atom free fall.

Acknowledgements The study on hybridized instrument was funded by ESA.

References

Allasio A, Muzi D, Vinai B, Cesare S, Catastini G, Bard M, Marque J (2009) GOCE: space technology for the reference earth gravity field determination. In: EUCASS 2009, Versailles

Bidel Y, Carraz O, Charrière R, Cadoret M, Zahzam N, Bresson A (2013) Compact cold atom gravimeter for field applications. Appl Phys Lett 102:144107

Carraz O, Siemes C, Massotti L, Haagmans R, Silvestrin P (12 June 2015) Measuring the Earth's gravity field with cold atom interferometers. arXiv:1506.03989 [physics, physics:quant-ph]. http://arxiv.org/abs/1506.03989

Cesare S, Sechi G (2013) Next generation gravity mission. In: D'Errico M (ed) Distributed space missions for earth system monitoring. Space technology library, vol 31. Springer, New York, pp 575–598

Christophe B, Boulanger D, Foulon B, Huynh P-A, Lebat V, Liorzou F, Perrot E (2015) A new generation of ultra-sensitive electrostatic accelerometers for GRACE Follow-on and towards the next generation gravity missions. Acta Astronaut 117:1–7

Drinkwater M, Haagmans R, Muzi D, Popescu A, Floberghagen R, Kern M, Fehringer M (2007) The GOCE gravity mission: ESA's first core Earth explorer. In: ESA Special Publication SP-627

Elsaka B, Raimondo J-C, Brieden P, Reubelt T, Kusche J, Flechtner F, Iran Pour S, Sneeuw N, Müller J (2014) Comparing seven candidate mission configurations for temporal gravity field retrieval through full-scale numerical simulation. J Geod 88(1):31–43

Flechtner F, Morton P, Watkins M, Webb F, Status of the grace follow-on mission (2014). In: Marti U (ed) Gravity, geoid and height systems. International association of geodesy symposia, vol 141. Springer, Cham, pp 117–121

Freier C, Hauth M, Schkolnik V, Leykauf B, Schilling M, Wziontek H, Scherneck H-G, Müller J, Peters A (2016) Mobile quantum gravity sensor with unprecedented stability. J Phys 723:012050

Geiger R, Menoret V, Stern G, Zahzam N, Cheinet P, Battelier B, Villing A, Moron F, Lours M, Bidel Y, Bresson A, Landragin A, Bouyer P (2011) Detecting inertial effects with airborne matter-wave interferometry. Nat Commun 2(474). https://doi.org/10.1038/ncomms1479

Gillot P, Francis O, Landragin A, Pereira Dos Santos F, Merlet S (2014) Stability comparison of two absolute gravimeters: optical versus atomic interferometers Metrologia 51:L15

Gruber T, Murböck M et al (2014) e2.motion - concept for a next generation gravity field mission, vol B318. Tech. rep., Deutche Geodätische Kommission der Bayerischen Akademie der Wissenschaften. ISBN: 978-3-7696-8597-8

Hu Z-K, Sun B-L, Duan X-C, Zhou M-K, Chen L-L, Zhan S, Zhang Q-Z, Luo J (2013) Demonstration of an ultrahigh-sensitivity atom-interferometry absolute gravimeter. Phys Rev A 88:043610

Lenoir B, Lévy A, Foulon B, Lamine B, Christophe B, Reynaud S (2011) Electrostatic accelerometer with bias rejection for gravitation and solar system physics. Adv Space Res 48(7):1248–1257

Panet I, Flury J, Biancale R, Gruber Th, Johannessen J, van den Broeke MR, van Dam T et al (2012) Earth system mass transport mission (e.motion): a concept for future earth gravity field measurements from space. Surv Geophys 34:141–163. https://doi.org/10.1007/s10712-012-9209-8

Reigber C, Schwintzer P, Lühr P (1999) The CHAMP geopotential mission. Boll Geofis Teor Appl 40:285-289

Tapley BD, Bettadpur S, Watkins M, Reigber C (2004) The gravity recovery and climate experiment: mission overview and early results. Geophys Res Lett 31(9):L09607

Touboul P, Métris G, Rodrigues M et al (2017) MICROSCOPE mission: first results of a space test of the equivalence principle. Phys Rev Lett 119:231101. https://doi.org/10.1103/PhysRevLett.119.231101

von Kampen P, Kaczmarczik U, Rath HJ (2006) The new drop tower catapult system. Acta Astronaut 59(1):278–283. https://doi.org/10.1016/j.actaastro.2006.02.041

Wiese DN, Folkner WM, Nerem RS (2009) Alternative mission architectures for a gravity recovery satellite mission. J Geod 83(1):569–581. https://doi.org/10.1007/s00190-008-0274-1

Wiese DN, Nerem RS, Lemoine FG (2012) Design considerations for a dedicated gravity recovery satellite mission consisting of two pairs of satellites. J Geod 86(1):81–98. https://doi.org/10.1007/s00190-011-0493-8

On Computation of Potential, Gravity and Gravity Gradient from GRACE Inter-Satellite Ranging Data: A Systematic Study

K. Ghobadi-Far, S.-C. Han, B. D. Loomis, and S. B. Luthcke

Abstract

In situ gravimetric observables are computed from GRACE inter-satellite K-band ranging (KBR) and GPS measurements, along with non-gravitational accelerations. For time-variable gravity field analysis, residual KBR data could be directly used to approximate gravimetric observables. We study the systematic errors in approximating potential difference, line-of-sight (LOS) gravity difference and LOS gravity gradient with residual KBR data. Based on a simulation study, we show that the approximation errors are significant at the low frequency part of the gravity spectrum for all three observable types. The approximation errors remain below 10% of the signal for the potential difference, LOS gravity difference, and LOS gravity gradient, at frequencies >1 cycle-per-revolution (CPR), >7 CPR, and 7–40 CPR, respectively. Considering the actual error of residual KBR data, it is feasible to accurately compute the gravimetric observables directly from band-pass filtered residual range-rate and range-acceleration data, and employ them for analyses concerning the regional time-variable gravity field of the Earth such as continental hydrology.

Keywords

GRACE · KBR · LOS gravity gradient · LOS gravity difference · Potential difference

1 Introduction

The GRACE mission monitored the time-variable gravity field of the Earth for more than 15 years. The ability of GRACE to model the temporal variations of the Earth's gravity field with an unprecedented accuracy is primarily due to its ultra-precise inter-satellite K-band ranging (KBR) measurements (Tapley et al. 2004).

The conventional approach for analysis of GRACE data is based on the dynamic orbit integration, which directly deals with the geometric KBR data. Alternatively, based on a combination of the GRACE GPS and KBR data, together with orientation information and measurements of non-gravitational accelerations, in situ gravimetric observables are computed along the satellite orbit. Potential difference, line-of-sight (LOS) gravity difference and LOS gravity gradient are the three GRACE-related gravimetric observables. For time-variable gravity analysis, a reference field including static gravity and some other signals like ocean tide is reduced from GRACE data to form the residual observations. The (geometric) residual KBR data can be used to approximate residual gravimetric observables suitable for studying time-variable gravity signals. The approach based on gravimetric observables is simpler than the conventional approach based on orbit integration, but it suffers from

K. Ghobadi-Far (✉) · S.-C. Han
School of Engineering, University of Newcastle, Callaghan, NSW, Australia
e-mail: khosro.ghobadifar@uon.edu.au

B. D. Loomis · S. B. Luthcke
Geodesy and Geophysics Laboratory, NASA Goddard Space Flight Center, Greenbelt, MD, USA

J. T. Freymueller, L. Sanchez (eds.), *International Symposium on Advancing Geodesy in a Changing World*, International Association of Geodesy Symposia 149, https://doi.org/10.1007/1345_2018_39

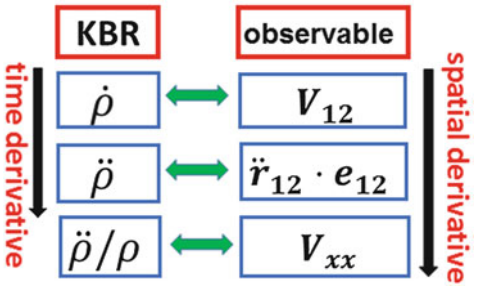

Fig. 1 Flowchart representing the approximate relations between gravimetric observables (potential difference V_{12}, LOS gravity difference $\ddot{r}_{12} \cdot e_{12}$ and LOS gravity gradient V_{xx}) and KBR data (inter-satellite range ρ, range-rate $\dot{\rho}$ and range-acceleration $\ddot{\rho}$)

systematic errors due to approximations. Studying these systematic errors is the topic of this paper.

In this paper, we briefly review the computation of gravimetric observables from GRACE data; for potential difference, see e.g. Bjerhammar (1967), Jekeli (2017), Guo et al. (2015), and Han et al. (2005), for LOS gravity difference, see e.g. Ditmar et al. (2012), Weigelt (2017), Chen et al. (2008), and Killett et al. (2011), and for LOS gravity gradient, see Keller and Sharifi (2005). We provide analytical expressions for approximation errors in terms of state vectors of satellites. In particular, based on a simulation analysis, we aim to quantify the systematic errors introduced by approximating potential difference, LOS gravity difference and LOS gravity gradient by residual range-rate, range-acceleration and range-acceleration divided by range, respectively. The relations between (geometric) KBR observations and computed gravimetric quantities is shown in Fig. 1. In general, it is known that the errors of such approximations are significant only at the low frequency part of gravity spectrum (e.g. Ditmar et al. 2012; Jekeli 2017). The computed in situ gravimetric observables are directly applicable for studying various time-variable gravity signals due to hydrology, tides, earthquakes, etc.

2 Mathematical Formulation

In this section, analytical expressions for approximation errors, which are defined as the difference between residual KBR data and gravimetric observables, are provided.

2.1 Potential Difference

The energy integral equation for a satellite pair in the inertial frame is given by (Jekeli 1999)

$$V_{12} = \frac{1}{2}\left(|\dot{\boldsymbol{r}}_2|^2 - |\dot{\boldsymbol{r}}_1|^2\right) + V_{12}^{\mathrm{R}} + E_{0,12}, \tag{1}$$

where V, $\dot{\boldsymbol{r}}$, V^{R} and E_0 are potential, velocity vector, rotation potential and constant of the integration, respectively. In order to incorporate the range-rate, inter-satellite velocity vector $\dot{\boldsymbol{r}}_{12}$ is decomposed into its along-track (or LOS), cross-track and radial components (Jekeli 2017)

$$\dot{\boldsymbol{r}}_{12} = (\dot{\boldsymbol{r}}_{12}\cdot \boldsymbol{e}_{12})\,\boldsymbol{e}_{12} + (\dot{\boldsymbol{r}}_{12}\cdot \boldsymbol{e}_n)\,\boldsymbol{e}_n + (\dot{\boldsymbol{r}}_{12}\cdot \boldsymbol{e}_r)\,\boldsymbol{e}_r, \tag{2}$$

where $\boldsymbol{e}_{12}$, $\boldsymbol{e}_n$ and $\boldsymbol{e}_r$ are unit vectors along the LOS, cross-track and radial directions, respectively. Rewriting $\left(|\dot{\boldsymbol{r}}_2|^2 - |\dot{\boldsymbol{r}}_1|^2\right)$ as $\dot{\boldsymbol{r}}_{12}\cdot(\dot{\boldsymbol{r}}_2 + \dot{\boldsymbol{r}}_1)$ and inserting (2) in (1) results in (Jekeli 2017)

$$\begin{aligned} V_{12} = {} & \frac{1}{2}\dot{\rho}\,(\dot{\boldsymbol{r}}_1 + \dot{\boldsymbol{r}}_2)\cdot \boldsymbol{e}_{12} + \frac{1}{2}\left(|\dot{\boldsymbol{r}}_2\cdot \boldsymbol{e}_n|^2 - |\dot{\boldsymbol{r}}_1\cdot \boldsymbol{e}_n|^2\right) \\ & + \frac{1}{2}\left(|\dot{\boldsymbol{r}}_2\cdot \boldsymbol{e}_r|^2 - |\dot{\boldsymbol{r}}_1\cdot \boldsymbol{e}_r|^2\right) + V_{12}^{\mathrm{R}} + E_{0,12}, \end{aligned} \tag{3}$$

Finally, since we are interested in time-variable gravity, the approximation error in terms of residual quantities is formulated as

$$\begin{aligned} \Delta_{\dot{\rho}} = {} & \delta\dot{\rho} - s\delta V_{12} = s^{\circ} \\ & \times \Big\{ -\frac{1}{2}\left[\left(|\dot{\boldsymbol{r}}_2\cdot \boldsymbol{e}_n|^2 - |\dot{\boldsymbol{r}}_1\cdot \boldsymbol{e}_n|^2\right) - \left(|\dot{\boldsymbol{r}}^{\circ}_2\cdot \boldsymbol{e}^{\circ}_n|^2 - |\dot{\boldsymbol{r}}^{\circ}_1\cdot \boldsymbol{e}^{\circ}_n|^2\right)\right] \\ & -\frac{1}{2}\left[\left(|\dot{\boldsymbol{r}}_2\cdot \boldsymbol{e}_r|^2 - |\dot{\boldsymbol{r}}_1\cdot \boldsymbol{e}_r|^2\right) - \left(|\dot{\boldsymbol{r}}^{\circ}_2\cdot \boldsymbol{e}^{\circ}_r|^2 - |\dot{\boldsymbol{r}}^{\circ}_1\cdot \boldsymbol{e}^{\circ}_r|^2\right)\right] \\ & -\delta V_{12}^{\mathrm{R}} - \delta E_{0,12} \Big\}. \end{aligned} \tag{4}$$

where $s = 2/(\dot{\boldsymbol{r}}_1 + \dot{\boldsymbol{r}}_2)\cdot \boldsymbol{e}_{12}$ and quantities with superscript $\circ$ indicate those computed from reference orbits.

It is noted that throughout the paper we assume that additional terms responsible for non-gravitational accelerations, tides, etc. are taken into account in the reference orbits computed using dynamic orbit integration.

2.2 LOS Gravity Difference

Differentiating both sides of $\dot{\rho} = \dot{\boldsymbol{r}}_{12}\cdot \boldsymbol{e}_{12}$ with respect to time results in

$$\ddot{\rho} = \ddot{\boldsymbol{r}}_{12}\cdot \boldsymbol{e}_{12} + \dot{\boldsymbol{r}}_{12}\cdot \dot{\boldsymbol{e}}_{12}, \tag{5}$$

which can be reformulated into (Ditmar et al. 2012; Rummel 1979)

$$\ddot{\rho} = \ddot{\boldsymbol{r}}_{12}\cdot \boldsymbol{e}_{12} + \frac{1}{\rho}|(\dot{\boldsymbol{r}}_{12}\cdot \boldsymbol{e}_n)\,\boldsymbol{e}_n + (\dot{\boldsymbol{r}}_{12}\cdot \boldsymbol{e}_r)\,\boldsymbol{e}_r|^2, \tag{6}$$

For residual quantities, the approximation error is given by

$$\Delta_{\ddot{\rho}} = \delta\ddot{\rho} - \delta\ddot{\boldsymbol{r}}_{12}\cdot\boldsymbol{e}_{12} = \frac{1}{\rho^{\circ}} \times \Big(\big|(\dot{\boldsymbol{r}}_{12}\cdot\boldsymbol{e}_n)\,\boldsymbol{e}_n + (\dot{\boldsymbol{r}}_{12}\cdot\boldsymbol{e}_r)\,\boldsymbol{e}_r\big|^2 - \big|\big(\dot{\boldsymbol{r}}^{\circ}_{12}\cdot\boldsymbol{e}^{\circ}_n\big)\,\boldsymbol{e}^{\circ}_n + \big(\dot{\boldsymbol{r}}^{\circ}_{12}\cdot\boldsymbol{e}^{\circ}_r\big)\,\boldsymbol{e}^{\circ}_r\big|^2\Big). \tag{7}$$

It is worth mentioning that the approximation error $\Delta_{\ddot{\rho}}$ is the residual centrifugal acceleration in this case.

2.3 LOS Gravity Gradient

LOS gravity gradient, which is evaluated at the barycentre of twin satellites, can also be computed from GRACE data. This is due to the fact that GRACE can be seen as a gradiometer with arm length ρ in the LOS direction.

The gradiometric observable (i.e. LOS gravity difference divided by inter-satellite range) is formulated as (Keller and Sharifi 2005)

$$\frac{\ddot{\boldsymbol{r}}_{12}\cdot\boldsymbol{e}}{\rho} = \frac{\ddot{\rho}}{\rho} - \frac{1}{\rho^2}\big|(\dot{\boldsymbol{r}}_{12}\cdot\boldsymbol{e}_n)\,\boldsymbol{e}_n + (\dot{\boldsymbol{r}}_{12}\cdot\boldsymbol{e}_r)\,\boldsymbol{e}_r\big|^2 = \boldsymbol{e}_{12}^{\mathrm{T}}\boldsymbol{G}\,\boldsymbol{e}_{12} + \Delta_{\mathrm{grad}}, \tag{8}$$

where $\boldsymbol{G}$ is the 3×3 gravity gradient tensor and Δ_{grad} represents truncation error due to neglecting higher order terms in the series. Expressing the right hand side of Eq. (8) in the Local Orbital Reference Frame (LORF), for which the x-axis coincides with the LOS direction, provides the relation between gradiometric observable and LOS gravity gradient

$$\frac{\ddot{\boldsymbol{r}}_{12}\cdot\boldsymbol{e}}{\rho} = V_{xx}^{\mathrm{LORF}} + \Delta_{\mathrm{grad}}, \tag{9}$$

note that this is because $\boldsymbol{e}_{12}^{\mathrm{LORF}} = [1\ 0\ 0]^T$.

The LOS gravity gradient can be approximated by $\ddot{\rho}/\rho$. Combining Eqs. (8) and (9), the approximation error is derived as

$$\Delta_{\ddot{\rho}/\rho} = \frac{\delta\ddot{\rho}}{\rho} - \delta V_{xx}^{\mathrm{LORF}} = \frac{\Delta_{\ddot{\rho}}}{\rho^0} + \Delta_{\mathrm{grad}}. \tag{10}$$

which is the sum of residual centrifugal acceleration divided by ρ (see Eq. 7) and the truncation error of gradiometric observable (Eq. 9).

3 Quantification of Approximation Errors

In this section, the approximation errors are quantified using a simulation analysis. To that end, we simulated reference orbits of GRACE satellites using the GEODYN software for March 2004 on the basis of reference force models and non-gravitational accelerations reported in Luthcke et al. (2013). The *true* orbits are simulated by adding the time-variable gravity model of NASA GSFC mascon of March 2004 to the reference models. The residual KBR data is computed as the difference between reference and *true* dynamic orbits. We also computed potential difference, LOS gravity difference and LOS gravity gradient along the reference orbits using spherical harmonic coefficients of the time-variable gravity field of the same month. Using the in-orbit comparison between residual KBR data and gravimetric observables, we evaluate the approximation errors in time, frequency and space.

Figure 2 shows a term-by-term analysis of the approximation errors for the first four orbital revolutions. Figure 2a shows the case for potential difference as in Eq. (4). It is seen that the residual range-rate follows the (scaled) potential difference very closely. Please note that $\Delta_{\dot{\rho}}$ is the sum of the last three panels in Fig. 2a (see Eq. 4). The radial component of inter-satellite velocity vector is the primary contributor to the approximation error. Although its contribution is relatively high, it is composed of low frequency signals (Jekeli 2017). Employing the analysis in the spectral domain (see Fig. 3a) shows that the $\Delta_{\dot{\rho}}$ signal power is concentrated at the 1 cycle-per-revolution (CPR) frequency. The post-fit KBR residuals, which are obtained after subtracting the time-variable gravity solution from $\delta\dot{\rho}$, represent the actual error of GRACE KBR data. Comparing $\Delta_{\dot{\rho}}$ with the post-fit range-rate residuals in Fig. 3a shows that, except for the very low frequency part of the spectrum, the approximation error is at least one order of magnitude smaller than the actual error of the KBR data. The KBR thermal noise is also shown for comparison in Fig. 3.

Figure 2b shows a term-by-term quantification of Eq. (7). The patterns of $\delta\ddot{\rho}$ and $\delta\ddot{\boldsymbol{r}}_{12}\cdot\boldsymbol{e}_{12}$ are very similar. Moreover, the approximation error $\Delta_{\ddot{\rho}}$ is one order of magnitude smaller than the signal. Similar to the case of range-rate, the term with the radial component of the inter-satellite velocity vector is the main contributor to the approximation error (Weigelt 2017). However, Fig. 3b shows that unlike $\Delta_{\dot{\rho}}$, the approximation error of the LOS gravity difference $\Delta_{\ddot{\rho}}$ is significant at frequencies up to 7 CPR ($\sim$1.3 mHz).

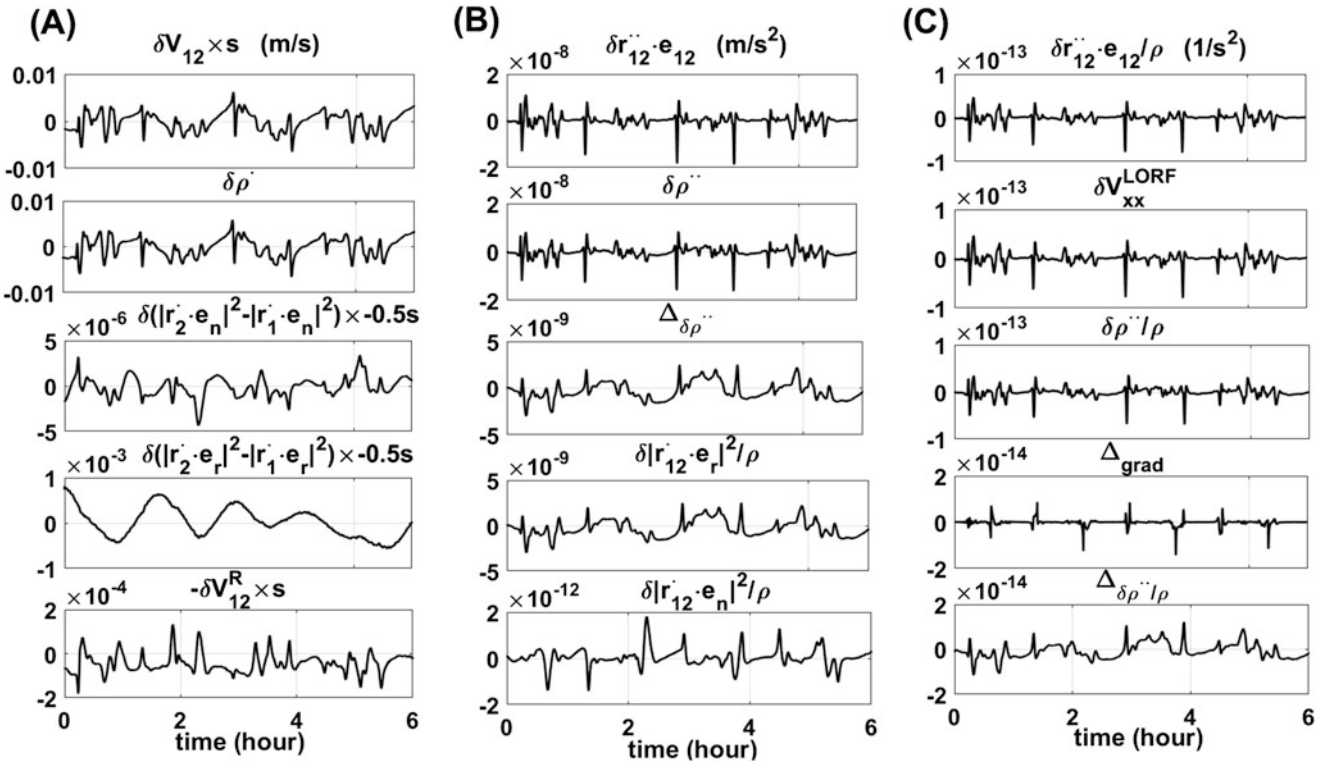

Fig. 2 Term-by-term analysis of the equation of (**a**) potential difference (Eq. 4), (**b**) LOS gravity difference (Eq. 7), and (**c**) LOS gravity gradient (Eq. 10). See text for description

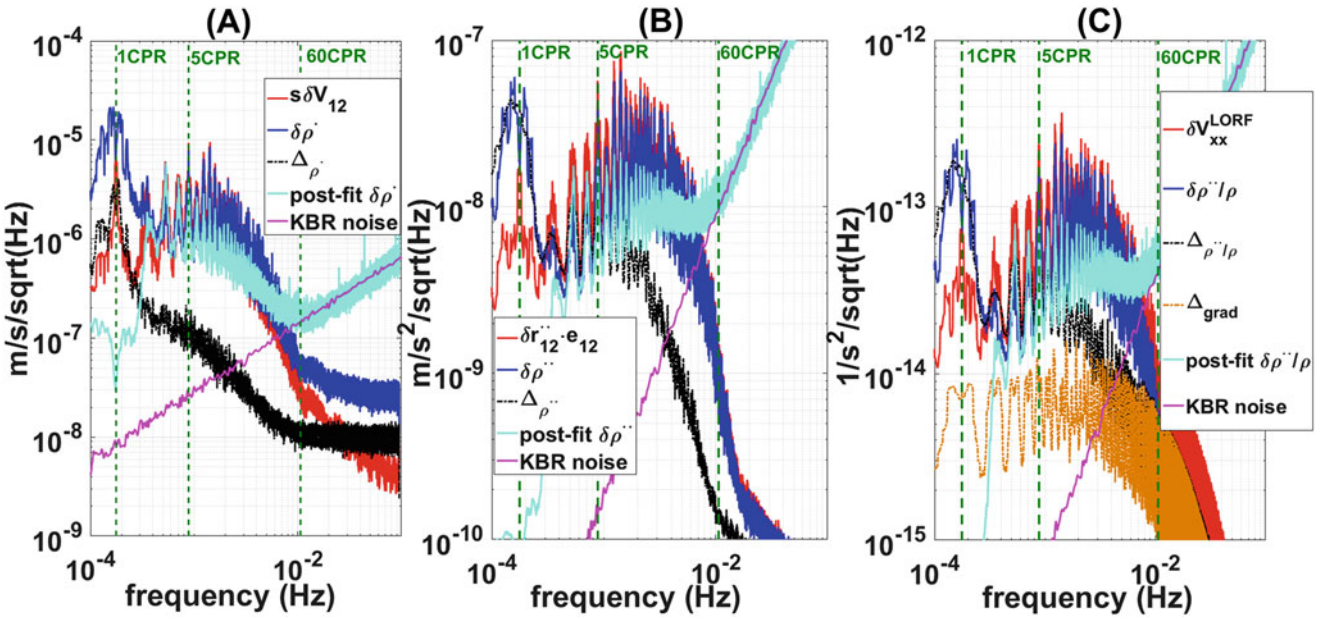

Fig. 3 PSD of signal and approximation error in the case of (**a**) potential difference, (**b**) LOS gravity difference, and (**c**) LOS gravity gradient. Red, blue and black lines show the gravimetric observables, residual KBR and approximation errors, respectively. Purple and Cyan lines show the KBR thermal noise and KBR post-fit residuals, respectively. Dashed vertical green lines indicate 1, 5 and 60 CPR frequencies ($1\ \mathrm{CPR} = 1.8 \times 10^{-4}$ Hz)

In the case of LOS gravity gradient, the approximation error has two components. Figures 2c and 3c show that the truncation error Δ_{grad} (the difference between $\ddot{\boldsymbol{r}}_{12} \cdot \boldsymbol{e}/\rho$ and V_{xx}^{LORF} as in Eq. 9) is a high frequency signal (see brown curve in Fig. 3c) that dominates the approximation error at

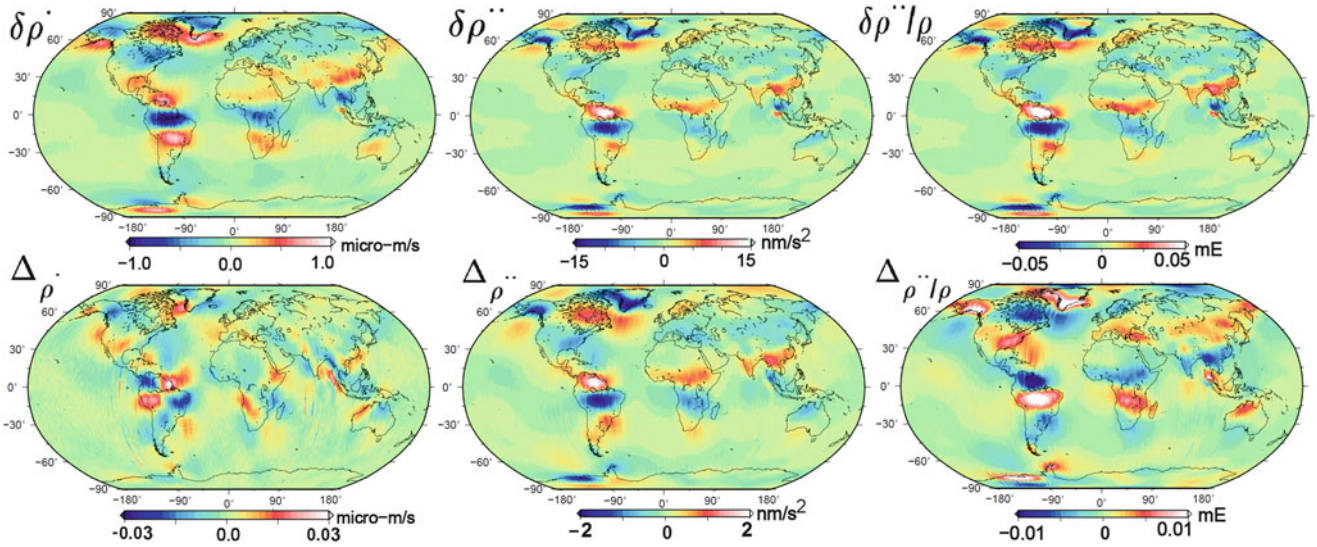

Fig. 4 Spatial maps of $\delta\dot{\rho}$ (top-left), $\delta\ddot{\rho}$ (top-middle) and $\delta\ddot{\rho}/\rho$ (top-right), together with the approximation errors, band-pass filtered between 0.9 and 10.6 mHz (i.e. 5–60 CPR). Note that 1 $mE = 10^{-12}1/S^2$

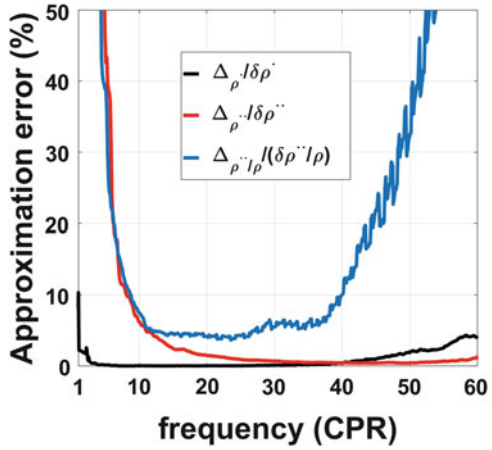

Fig. 5 Percentage of signal power of approximation errors relative to their associated KBR signals in the frequency band 1–60 CPR

frequencies above 40 CPR (7.1 mHz). At lower frequencies, similar to the case of LOS gravity difference, the radial component of the inter-satellite velocity vector dominates the error.

In order to assess the problem in the spatial domain, Fig. 4 shows the band-pass filtered (between 5 and 60 CPR; i.e. 0.9–10.6 mHz) residual KBR signals and the approximation errors. It can be seen that in this frequency band, $\Delta_{\dot{\rho}}$ is the smallest one among all three cases. The signal size of band-pass filtered $\Delta_{\dot{\rho}}$ is about 3% of $\delta\dot{\rho}$. The approximation error of $\delta\ddot{\rho}/\rho$ is the largest one, reaching as high as 20% of the signal itself. In the case of range-acceleration, the approximation error is about 15% of the signal in this frequency band.

Finally, we compare the three cases by evaluating the signal power of each approximation error relative to its corresponding KBR signal in the frequency domain in Fig. 5. In the case of potential difference, except at 1 CPR, $\Delta_{\dot{\rho}}$ remains below 5% of $\delta\dot{\rho}$ over the full spectrum. $\Delta_{\ddot{\rho}}$ and $\Delta_{\ddot{\rho}/\rho}$ exhibit similar behaviour at frequencies below 13 CPR, while at higher frequencies (>40 CPR) the signal power of $\Delta_{\ddot{\rho}/\rho}$ increases rapidly. This result is due to the truncation error of the gradiometric observable (Δ_{grad} in Eq. 9).

It should be noted that the approximation errors in this paper were formulated and quantified in terms of KBR data (e.g. range-rate) instead of gravimetric observables (e.g. potential difference), but quantifying the errors in terms of gravimetric observables would not change the conclusions of this paper.

4 Conclusions

Inter-satellite ranging residuals, such as from GRACE KBR system, can be used to approximate in situ potential difference, LOS gravity difference and LOS gravity gradient. In this systematic study, we formulated the approximation errors in terms of state vectors of the satellites and quantified them with a simulation analysis. Numerical results showed that in all three cases, the radial component of the inter-satellite velocity vector causes a long-wavelength error. The approximation error remains less than 5% of the residual KBR signal in the 10–60 CPR frequency band for potential difference and LOS gravity difference (computed from residual range-rate and range-acceleration, respectively), while the LOS gravity gradient approximation

error becomes larger than 10% of the signal for frequencies >40 CPR.

Altogether, this implies that one can treat band-pass filtered GRACE residual KBR data as an accurate representation of gravimetric observables. Therefore, it is advantageous to analyse the band-pass filtered range-rate and range-acceleration residuals in the recovery of various regional time-variable gravity signals.

Acknowledgments This work is funded by The University of Newcastle to support NASA's GRACE and GRACE Follow-On projects as an international science team member to the missions.

References

Bjerhammar A (1967) On the energy integral for satellites. Report of the Royal Institute of Technology (KTH). Division of Geodesy, Stockholm

Chen Y, Schaffrin B, Shum CK (2008) Continental water storage changes from GRACE line-of-sight range acceleration measurements. In: VI Hotine-Marussi symposium on theoretical and computational geodesy. Springer, Heidelberg, pp 62–66

Ditmar P, Da Encarnação JT, Farahani HH (2012) Understanding data noise in gravity field recovery on the basis of inter-satellite ranging measurements acquired by the satellite gravimetry mission GRACE. J Geod 86(6):441–465. https://doi.org/10.1007/s00190-011-0531-6

Guo JY, Shang K, Jekeli C, Shum CK (2015) On the energy integral formulation of gravitational potential differences from satellite-to-satellite tracking. Celest Mech Dyn Astron 121(4):415–429. https://doi.org/10.1007/s10569-015-9610-y

Han SC, Shum CK, Jekeli C, Alsdorf D (2005) Improved estimation of terrestrial water storage changes from GRACE. Geophys Res Lett 32(7). https://doi.org/10.1029/2005GL022382

Jekeli C (1999) The determination of gravitational potential differences from satellite-to-satellite tracking. Celest Mech Dyn Astron 75(2):85–101. https://doi.org/10.1023/A:1008313405488

Jekeli C (2017) The energy balance approach. In: Naeimi M, Flury J (eds) Global gravity field modeling from satellite-to-satellite tracking data, Lecture notes in earth system sciences. Springer, Heidelberg, pp 127–160. https://doi.org/10.1007/978-3-319-49941-3_5

Keller W, Sharifi MA (2005) Satellite gradiometry using a satellite pair. J Geod 78(9):544–557. https://doi.org/10.1007/s00190-004-0426-x

Killett B, Wahr J, Desai S, Yuan D, Watkins M (2011) Arctic Ocean tides from GRACE satellite accelerations. J Geophys Res Oceans 116(C11). https://doi.org/10.1029/2011JC007111

Luthcke SB, Sabaka TJ, Loomis BD, Arendt AA, McCarthy JJ, Camp J (2013) Antarctica, Greenland and Gulf of Alaska land-ice evolution from an iterated GRACE global mascon solution. J Glaciol 59(216):613–631

Rummel R (1979) Determination of short-wavelength components of the gravity field from satellite-to-satellite tracking or satellite gradiometry. Manuscr Geodaet 4(2):107–148

Tapley BD, Bettadpur S, Ries JC, Thompson PF, Watkins MM (2004) GRACE measurements of mass variability in the earth system. Science 305(5683):503–505. https://doi.org/10.1126/science.1099192

Weigelt M (2017) The acceleration approach. In: Naeimi M, Flury J (eds) Global gravity field modeling from satellite-to-satellite tracking data, Lecture notes in earth system sciences. Springer, Heidelberg, pp 97–126. https://doi.org/10.1007/978-3-319-49941-3_4

Calibration of GRACE Accelerometers Using Two Types of Reference Accelerations

Igor Koch, Akbar Shabanloui, and Jakob Flury

Abstract

Two approaches for the calibration of GRACE (Gravity Recovery And Climate Experiment) accelerometers are revisited. In the first approach, surface forces acting on the satellite are considered to derive the reference acceleration. In the second approach, the total acceleration consisting of a gravitational and a non-gravitational contribution is first determined from the reduced-dynamic orbits. The approximation of discrete satellite positions by a polynomial function allows the total acceleration to be obtained by a twofold derivative w.r.t. time. Calibration parameters (scale factor and bias) and statistical values are estimated for periods with a low and high solar activity. The quality of these two approaches shows dependencies on solar activity and consequent variations in the magnitude of the non-gravitational reference acceleration. Besides, the quality of the presented results is affected by the orientation of the orbital plane w.r.t. the Sun. The second approach is vitiated by a periodic disturbing signal on cross-track axis. This signal has been pointed out in earlier studies (Calabia et al., Aerosp Sci Technol 45, 2015; Calabia and Jin, Aerosp Sci Technol 49, 2016). We apply a moving window median filter to recover the underlying non-gravitational signal for accelerometer calibration. The calibration is accomplished by a direct comparison of reference accelerations and observed accelerometer measurements without introducing any a priori values or constraints. The focus of this work is more sensor oriented than gravity field recovery (GFR) related. Nevertheless, the results can be used as initial values for precise orbit determination (POD) or for pre-processing of accelerometer measurements in a multi step gravity field recovery approach (Klinger and Mayer-Gürr, Adv Space Res 58(9), 2016).

Keywords

Accelerometry · GRACE · Satellite accelerometer calibration

1 Introduction

The GRACE mission has been in orbit since 2002 and is based on two twin satellites, GRACE A and B, that observe static and temporal changes of Earth's gravity field (Tapley et al. 2004). For this purpose, the knowledge of the non-gravitational forces acting on the satellites is of major importance, since for the recovery of Earth's gravity field parameters, acceleration effects of gravitational and non-gravitational nature have to be separated. Therefore, an accelerometer that measures the total non-gravitational acceleration experienced by the satellite is located in the center of mass of each satellite (Flury et al. 2008). However, these measurements are not absolute values, but rather have to be corrected in their magnitude and variational amplitude

I. Koch (✉) · A. Shabanloui · J. Flury
Institut für Erdmessung, Leibniz Universität Hannover, Hannover, Germany
e-mail: koch@ife.uni-hannover.de

J. T. Freymueller, L. Sánchez (eds.), *International Symposium on Advancing Geodesy in a Changing World*,
International Association of Geodesy Symposia 149, https://doi.org/10.1007/1345_2018_46

by a calibration in the post-processing. In the scope of gravity field estimation several methods to calibrate accelerometer measurements are applied. Usually, calibration parameters are estimated directly within precise orbit determination or gravity field recovery procedures, e.g. Van Helleputte et al. (2009), Dahle et al. (2013), Watkins and Yuan (2014), Bettadpur (2018). There exist a priori calibration parameters based on GRACE data between the start of the mission and end of March 2009, but because of possible variations due to the specific analysis of the data, these parameters should only be regarded as recommendations (Bettadpur 2009).

It should be noted that a calibration parameter estimation within POD or GFR is not part of this work. Here the focus is laid on constraint-free estimation of non-gravitational acceleration that is used as reference for the calibration of accelerometer data. Two approaches for the computation of the non-gravitational reference acceleration are realized. In the first approach, further denoted as NGM (non-gravitational modeling), surface accelerations acting on a spacecraft composed of atmospheric drag and direct solar radiation pressure are taken into account. This approach can be regarded as a basic method for the estimation of non-gravitational reference acceleration. For instance, a two-step calibration process carried out in Klinger and Mayer-Gürr (2016) uses approach NGM for initial accelerometer calibration. The modeled reference acceleration enables a threshold-based screening of the accelerometer data, while in a second step the pre-screened accelerometer data is used within GFR, where the calibration parameters are re-estimated.

In the second approach, the total acceleration consisting of a gravitational and non-gravitational contribution is first determined from the GNSS-based reduced-dynamic orbits. The approximation of discrete satellite positions by a polynomial function allows the total acceleration to be obtained by a twofold derivative w.r.t. time. Subtraction of the gravitational part provides a further reference, onwards referred as NGO (Non-Gravitational acceleration based on Orbit derivatives), for accelerometer calibration. By applying different strategies for numerical differentiation of geometric and reduced-dynamic orbit products, this approach has been presented in previous studies, e.g. Bezděk (2010) and Calabia et al. (2015).

The main focus of this work is the comparison of these two approaches w.r.t. different strengths of solar activity. Therefore, accelerometer calibration parameters, i.e. scale factor and bias, and corresponding statistical values for two periods, one with a high solar activity as P_{max} covering from 2002/11/01 to 2003/01/31 and the other with a low solar activity P_{min} covering from 2008/06/01 to 2008/08/31 (cf. Fig. 1), are estimated and investigated.

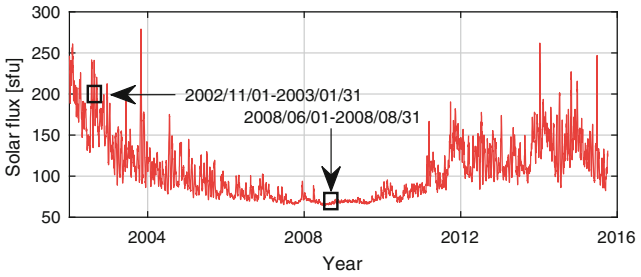

Fig. 1 Solar activity during the period 2002–2016. The two periods studied in this work are highlighted

Table 1 GRACE Level-1B products used in this study

Product	Data
GNV1B	Reduced-dynamic position, velocity
ACC1B	Linear acceleration
SCA1B	Satellite attitude (quaternions)
MAS1B	Satellite mass
THR1B	Thruster events

2 GRACE Data

In this study several GRACE Level-1B (L1B) data products are used (Case et al. 2010). An overview is given in Table 1. GNV1B products contain satellite positions and velocities at 5s interval obtained from reduced-dynamic POD. Linear accelerations in the GRACE science reference frame (SRF) are part of ACC1B data products. These measurements are given every second. Quaternions from SCA1B are utilized to transform between inertial and orbital frame. Furthermore, the mass of the satellite from MAS1B data products is essential for the calculation of the non-gravitational acceleration effects. Here the daily mean mass is utilized. Thruster firing events from THR1B are used to filter thruster affected accelerometer measurements.

3 Methods

3.1 NGM Approach

In the approach NGM, the reference acceleration $\mathbf{a}_{\mathrm{ref,NGM}}$ is computed as the sum of modeled non-gravitational effects $\mathbf{a}_{\mathrm{ngr},i}$:

$$\mathbf{a}_{\mathrm{ref,NGM}} = \sum_{i=1}^{2} \mathbf{a}_{\mathrm{ngr},i}\,. \tag{1}$$

Non-gravitational acceleration models and parameters that are used to determine the sum of separate acceleration effects $\mathbf{a}_{\mathrm{ngr},i}$ are summarized in the upper part of Table 2. Compared to atmospheric drag and solar radiation pressure, the

Table 2 Overview of the used non-gravitational and gravitational models and parameters

	i	Acceleration	Model: Parameters	Reference
non-gravitational	1	Atmospheric drag	Atmospheric density model: NRLMSISE-00	Picone et al. (2002)
			Wind: Earth's atmosphere co-rotation	Montenbruck and Gill (2005)
			Drag coefficient: $C_D = 3.5$ (P_{max}), $C_D = 2.3$ (P_{min})	
			Satellite macro model	Bettadpur (2012)
	2	Solar radiation pressure	Shadow model: conic	Montenbruck and Gill (2005)
			Solar flux at 1 AU: $W = 1367$ Watt/m^2	Montenbruck and Gill (2005)
			Solar ephemerides: DE430	Folkner et al. (2014)
			Solar radiation pressure coefficient: $C_R = 1.1$ (P_{max}), $C_R = 1.0$ (P_{min})	
			Satellite macro model	Bettadpur (2012)
gravitational	1	Static gravity	EIGEN-6S4, C_{20}: tide free, $n_{max} = 180$	Förste et al. (2015)
	2	Temporal gravity	Long wavelength: EIGEN-6S4, drift, annual and semi-annual variations	Förste et al. (2015)
			Short wavelength: AOD1B RL06	Dobslaw et al. (2017)
	3	Third bodies	Ephemerides: DE430 including Sun and Moon	Folkner et al. (2014)
	4	Solid Earth tides	Ephemerides: DE430 including Sun and Moon	Folkner et al. (2014)
	5	Ocean tides	EOT11a, $n_{max} = 120$, admittance theory for minor waves	Rieser et al. (2012)
	6	Relativistic effects	Schwarzschild effect	Petit and Luzum (2010)
	7	Pole tides	IERS Conventions 2010	Petit and Luzum (2010)
	8	Ocean pole tides	IERS Conventions 2010	Petit and Luzum (2010), Desai (2002)
	9	Atmospheric tides	N1 model, seasonal means	Biancale and Bode (2006)

corresponding magnitude of these effects is usually several orders smaller. Therefore, the acceleration caused by albedo and thermal infrared is not taken into account in this study. Nevertheless, the influence of these effects will be studied in future articles.

As a common inertial reference system the Geocentric Celestial Reference System (GCRS) is used. The transformation of satellite GNV1B positions that are provided in the International Terrestrial Reference System (ITRS) is done according to Petit and Luzum (2010).

3.2 NGO Approach

In the approach NGO, the non-gravitational reference acceleration $\mathbf{a}_{\mathrm{ref,NGO}}$ is determined by the difference of the total acceleration $\mathbf{a}$ and the sum of gravitational acceleration effects $\mathbf{a}_{\mathrm{gr},i}$:

$$\mathbf{a}_{\mathrm{ref,NGO}} = \mathbf{a} - \sum_{i=1}^{9} \mathbf{a}_{\mathrm{gr},i}\,. \tag{2}$$

Gravitational background models and parameters used for predicting the sum of acceleration effects $\mathbf{a}_{\mathrm{gr},i}$ can be found in the bottom part of Table 2. The total acceleration of a satellite $\mathbf{a}$ is obtained by taking the second derivative of the GNV1B positions w.r.t. time. In this scheme, after transformation of the positions to GCRS, the smoothing polynomial approach is used to calculate piece-wise polynomial coefficients based on least squares adjustment (Luers and Wenning 1971). In its general form, a polynomial function of degree n can be described by Eq. (3):

$$f(\tau) = \sum_{i=0}^{n} a_i \tau^i\,. \tag{3}$$

In this equation a_i denote polynomial coefficients and the argument τ corresponds to the time of the sample points. The parameter vector $\mathbf{x}$ containing the piece-wise polynomial coefficients is estimated by least squares adjustment:

$$\mathbf{x} = \left(\mathbf{A}^{\mathrm{T}}\mathbf{A}\right)^{-1}\mathbf{A}^{\mathrm{T}}\mathbf{l}. \tag{4}$$

Here, **l** denotes the observation vector which includes the x-, y- or z-components of satellite's inertial positions and **A** is the corresponding design matrix. For the computation of the polynomial coefficients a unit weight matrix is employed. In this work, a polynomial of degree $n = 7$ has been fitted to $m = 21$ position components. Note that the time arguments $\tau_1 \ldots \tau_m$ of the regarded position components were normalized to $[-1, 1]$ in order to make the estimation of the polynomial coefficients numerically stable. This method takes advantage of the equidistant 5s GNV1B positions, so $\tau = 0$, assumed that m is uneven, always corresponds to the sample point in the middle of the interval $[-1, 1]$ and that is also the sample point whose acceleration is evaluated.

3.3 Accelerometer Calibration

The magnitude of the ACC1B measurements $\mathbf{a}_{\text{uncal}}$ is corrected by the introduction of a bias vector **b**. The amplitude is adjusted by a diagonal scale matrix **S** containing a scale factor for each axis:

$$\mathbf{a}_{\text{cal}} = \mathbf{S}\,\mathbf{a}_{\text{uncal}} + \mathbf{b}. \tag{5}$$

The unknown scale matrices and bias vectors are determined on a daily basis using least squares adjustment. Note that all the terms in Eq. (5) refer to the GRACE science reference frame. In order to use the computed reference accelerations (cf. Eqs. (1) and (2)) as observations in least squares adjustment, the computed reference accelerations have to be transformed from GCRS to SRF. For this purpose, SCA1B quaternions are used to form the corresponding rotation matrices as described in Sutton (2008). Accelerometer measurements that are affected by thruster firings are removed before adjustment. In order to exclude spike affected accelerometer measurements from the adjustment, values outside the 3-sigma distribution are not considered. Although the reduced-dynamic approach acts as a low-pass filter during orbit determination, generated positions contain noise that is amplified during differentiation considerably. In order to decrease the noisy characteristic of the accelerations obtained with approach NGO before calibration parameter estimation, a moving window median filter with a size of 30 acceleration measurements is applied.

4 Results and Discussion

In general, different parameters, variables and assumptions affect the quality of the reference accelerations. Particularly, the approach NGM is based on numerous parameters and models that are often inaccurate and biased. Some of these parameters are for example the atmospheric density and wind model, solar flux and geomagnetic proxies, eclipse modeling, the macro model and variables such as the drag and solar radiation pressure coefficients (Doornbos 2011). In POD, the unknown parameters are estimated in order to absorb biases in the models and noise in the measurements. Besides, general quality of approach NGO is primary affected by choice and actuality of employed models (Bezděk 2010). In this study, extreme solar condition periods are regarded. The quality of the results is clearly dependent on the magnitude of the non-gravitational acceleration that is affected by solar activity. The F10.7 solar radio flux during period P_{max} fluctuates between 114 and 213 solar flux units (sfu) (cf. Fig. 1) which corresponds to a rather high solar activity. The solar activity during period P_{min} varies between 64 and 68 sfu, so this period can be regarded as the least sun-disturbed period during GRACE operating time. These variations in solar activity lead to differences in the magnitude of the total non-gravitational reference accelerations.

To get an impression how the ACC1B measurements and the computed reference accelerations using the two approaches fit together, some calibrated datasets are illustrated in Fig. 2. The similarity of the calibrated ACC1B acceleration with the respective reference acceleration has been quantified by means of the correlation coefficient. The monthly mean correlation coefficients are shown in Table 3. It is striking that the variability of NGM related to the investigated periods is, in contrast to approach NGO, minimal. The correlation coefficients for NGM range from 0.91 to 0.95, while for approach NGO, a strong variance can be observed that is dependent on the magnitude of the computed reference accelerations. Note that the presented correlation coefficients are not the best quality indicators for the calibration parameters, especially the biases, but good indicators to assess the quality of the recovered non-gravitational signal using approach NGO.

An aspect that determines the quality of the constraint-free and daily calibration parameter estimation, is the orientation of the satellite's orbital plane w.r.t. the Sun, often referred to as β' angle. β' equals 0° when the satellite's orbital plane coincidences with the Earth-Sun line of sight. If the orbital plane is perpendicular w.r.t. the Earth-Sun line of sight, β' equals ±90°. The drift of the GRACE orbit's ascending node prevents β' to reach ±90°. In this work, β' reaches +71° and −73° for periods P_{max} and P_{min} respectively. It was decided to exclude the epochs with aforementioned maximum/minimum β' ±7°, since during this periods unrealistic calibration parameters and small correlation coefficients were obtained. This period was neither considered for the calculation of the correlation coefficients that are shown in Table 3, nor for the mean calibration parameters that will be presented later in this chapter. The two excluded periods are highlighted in Fig. 3.

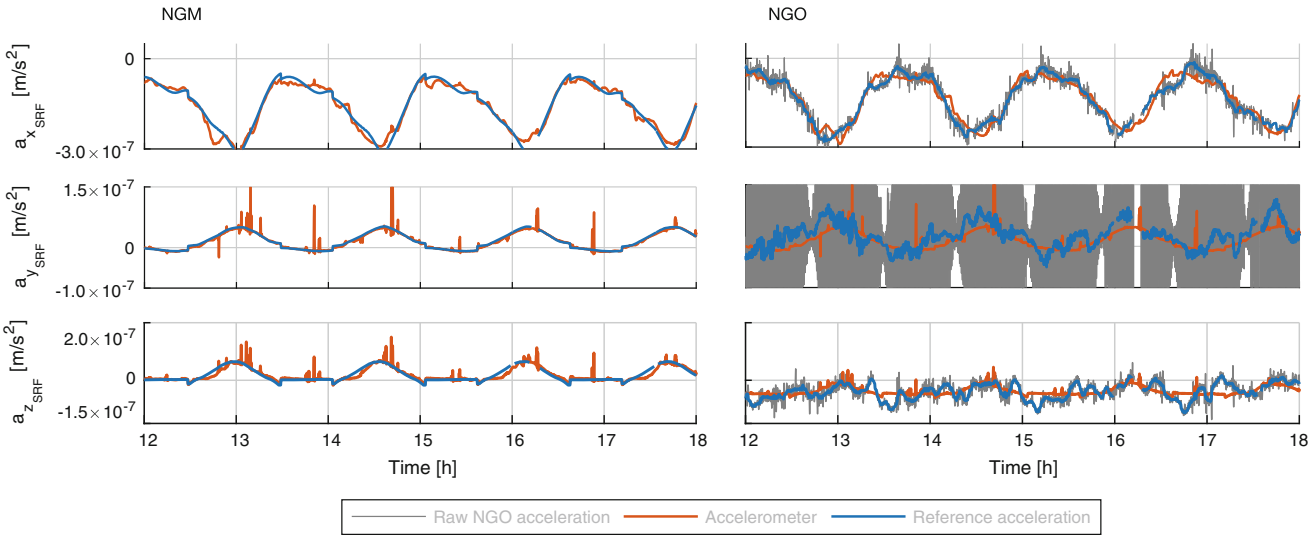

Fig. 2 Exemplary calibrated GRACE B ACC1B accelerometer measurements (red) using approaches NGM (left) and NGO (right) for the epoch 2003/01/01. Upper panel: x_{SRF}, middle panel: y_{SRF} and bottom panel: z_{SRF}

Table 3 Mean correlation coefficient of calibrated ACC1B data and modeled reference acceleration

	P_{max}		P_{min}	
	NGM	NGO	NGM	NGO
x_{SRF}	0.93	0.96	0.93	0.77
y_{SRF}	0.95	0.68	0.91	0.52
z_{SRF}	0.91	0.51	0.93	0.11

An aspect important to consider when applying approach NGO to the GNV1B reduced-dynamic orbit data, is a disturbing signal of unknown origin in y_{SRF} direction, with an absolute amplitude of about 1×10^{-6} m/s^2 and a dominant period of half a revolution. This kind of disturbing signal has already been pointed out in Calabia et al. (2015) and Calabia and Jin (2016) for different periods of time. In Calabia and Jin (2016) the authors indicate a maximum amplitude of 6×10^{-6} m/s^2 for y_{SRF} and 1.5×10^{-6} m/s^2 for z_{SRF} direction. In Calabia et al. (2015) the authors refer to Bezděk (2010), where the y_{SRF} axis seems to be affected by a similar periodic disturbing signal. By using the aforementioned moving window median filter an underlying signal that is suitable for calibration can be retrieved for period P_{max} (cf. Fig. 2). The recovered signal is in good agreement with the accelerometer measurements. The corresponding mean correlation coefficient is 0.68 (cf. Table 3). In contrast, during weak solar activity the correlation coefficient of the recovered reference acceleration w.r.t. the calibrated accelerometer measurements is only 0.52.

A time series of estimated daily calibration parameters for the two investigated periods can be seen in Fig. 3. In addition, long term fits to estimated biases from POD are plotted as a reference (Bettadpur 2009). Mean estimated calibration parameters and corresponding standard deviations are reported in Table 4. A comparison of the reference values with the obtained daily calibration parameters should be treated warily because different types of approaches are compared. In this study, assumptions, i.e. that the scale factors are approximately one over the whole period, are not introduced. Although, for x_{SRF} often realistic values can be obtained, daily scales for y_{SRF} and z_{SRF} usually vary a lot, i.e. Klinger and Mayer-Gürr (2016) and Bruinsma et al. (2007). Using the two presented approaches, the daily scale factors and biases are optimal in a least squares sense w.r.t. the modeled reference accelerations and are not affected by any constraints. Despite the mentioned variance of the calibration parameters, the presented calibration procedure may lead to highly correlated calibration parameters (Bruinsma et al. 2007; Van Helleputte et al. 2009). Although out of the scope of this study and objective of further investigations, constraints can be applied to de-correlate scale factors and biases, i.e. Bruinsma et al. (2007), Van Helleputte et al. (2009). The long term fits from Bettadpur (2009) are a generalized form of calibration parameters obtained in POD. In POD and GFR these values can be treated as initial values and corrections to these values have to be estimated iteratively.

In Fig. 3 and Table 4 it can be seen that approach NGO differs from NGM when estimating parameters for the x_{SRF} component for period P_{max}. The NGO bias time series shows a stable behavior over the time span of three months and is in good agreement with the long term biases. Similar aspects can be observed for the x_{SRF} scale. Although realistic values are obtained for both approaches (NGM: 0.91, NGO: 0.93), the standard deviation of approach NGO is more than three times smaller. To obtain a mean scale value comparable to

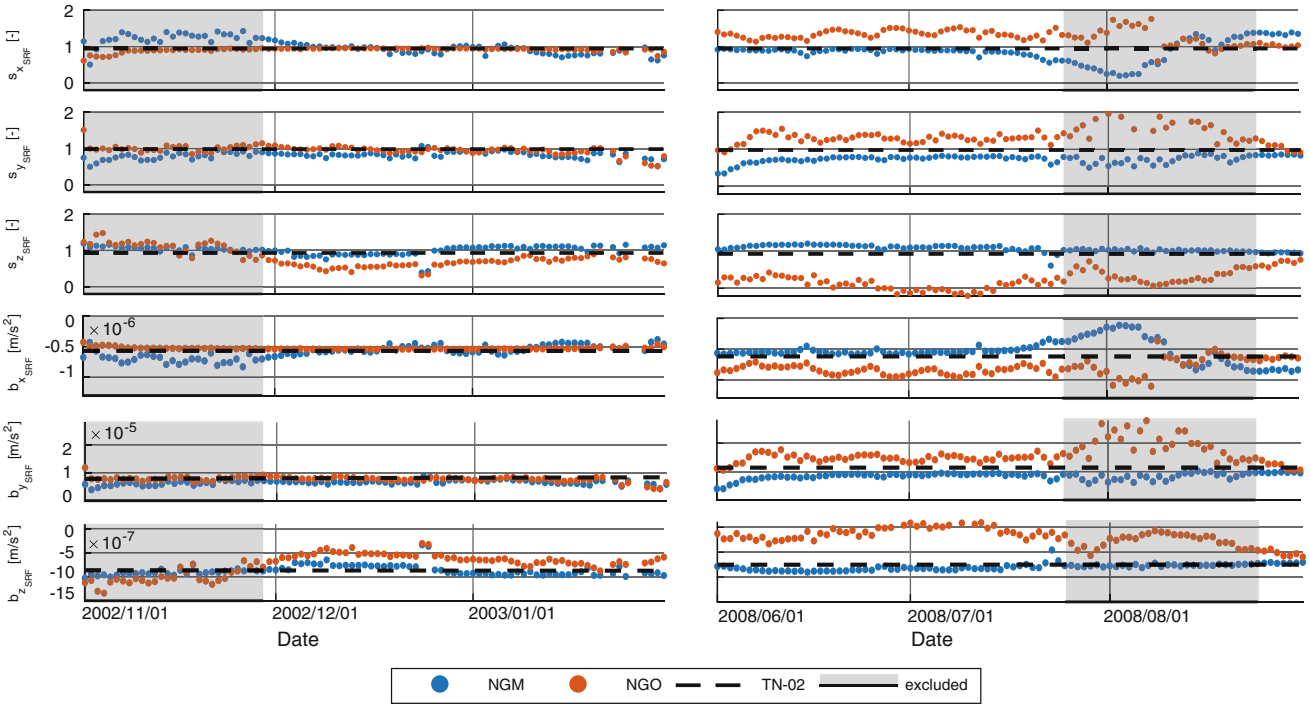

Fig. 3 Daily estimated accelerometer calibration parameters: Left (P_{max}: 2002/11/01−2003/01/31); Right (P_{min}: 2008/06/01−2008/08/31). First three upper rows represent scale parameters and the last three rows show bias parameters

Table 4 Mean accelerometer calibration parameters for the period with a strong solar activity (P_{max}: 2002/11/01−2003/01/31) and weak solar activity (P_{min}: 2008/06/01−2008/08/31) using approaches NGM and NGO

		P_{max}				P_{min}			
		Scale [−]		Bias [m/s^2]		Scale [−]		Bias [m/s^2]	
		NGM	NGO	NGM	NGO	NGM	NGO	NGM	NGO
x_{SRF}	Mean	0.91	0.93	-5.38×10^{-7}	-5.35×10^{-7}	0.92	1.31	-5.69×10^{-7}	-8.22×10^{-7}
	Std	0.13	0.04	6.79×10^{-8}	1.42×10^{-8}	0.18	0.14	1.12×10^{-7}	9.04×10^{-8}
y_{SRF}	Mean	0.83	0.93	6.72×10^{-6}	7.57×10^{-6}	0.74	1.26	8.45×10^{-6}	1.44×10^{-5}
	Std	0.09	0.12	7.30×10^{-7}	9.18×10^{-7}	0.11	0.15	1.22×10^{-6}	1.67×10^{-6}
z_{SRF}	Mean	0.98	0.66	-8.46×10^{-7}	-6.15×10^{-7}	1.09	0.18	-8.14×10^{-7}	-1.45×10^{-7}
	Std	0.15	0.13	1.29×10^{-7}	1.13×10^{-7}	0.11	0.24	7.30×10^{-8}	1.82×10^{-7}

the value derived from approach NGO, the drag coefficient during period P_{max} has to be set rather large (cf. Table 2). It is important to note that the strong variability of the solar flux during period P_{max} demands the employment of a variable drag coefficient for approach NGM instead of a constant coefficient. This means that external information from POD could help to decrease the standard deviation of the calibration parameters obtained with approach NGM. For y_{SRF} and especially z_{SRF} directions, bigger disagreements between the two approaches can be seen. In comparison to the constant scale and long term bias, there is a better agreement for y_{SRF} when using approach NGO. In contrast, for z_{SRF} more realistic values are obtained using approach NGM. Because of the weak signal in z_{SRF} and the amplification of noise, it is more difficult to obtain appropriate scale factors and biases with approach NGO.

Daily calibration parameters for period P_{min} are shown on the right side of Fig. 3. During small solar activity approach NGM differs from approach NGO considerably. Compared to approach NGO, obtained calibration parameters using approach NGM are closer to the constant scale factors and long term biases. Especially calibration parameters of the x_{SRF} and z_{SRF} components fit very well with the reference values reported in Bettadpur (2009). In comparison to period P_{max}, no meaningful calibration parameters were obtained using approach NGO. The small magnitude of the non-gravitational acceleration decreases the signal-to-noise ratio (SNR) of the non-gravitational accelerations extracted from the reduced-dynamic orbits and makes it impossible to obtain adequate calibration parameters without any constraints. Most notable deviations from the constant scales and long term biases around the β' turning point can be seen

for x_{SRF} during period $\mathrm{P}_{\mathrm{min}}$. As the orbital plane reaches this orientation w.r.t. the Sun, the satellite spends minimal time in the Earth's shadow region. This mentioned aspect in combination with a very small solar activity leads to measured and modeled non-gravitational accelerations with minimal variation of the signal amplitude. This small signal variation causes highly correlated calibration parameters.

5 Conclusions

In this work we studied if two types of modeled accelerations can serve as a good reference for the calibration of accelerometer measurements. We solved for daily scale factors and biases without the introduction of any a priori values and constraints for two 90 day periods during strong and weak solar activities. The approach NGM is first of all dependent on a reasonable choice of the drag coefficient that suits the specific activity of the sun. In contrast, approach NGO needs the employment of accurate time-variable gravity models.

This study showed that the quality of approach NGM is not as much affected by the solar activity (and therefore the absolute magnitude of the modeled reference acceleration) as approach NGO. For approach NGO, realistic scales and biases only could be obtained for the x_{SRF} and y_{SRF} directions during the period with strong solar activity. The quality of the obtained daily calibration parameters for the period with low solar activity using approach NGO is highly affected by the decreased signal-to-noise ratio of the non-gravitational acceleration extracted from the reduced dynamic orbits. This makes it impossible to estimate adequate scale factors and biases at the same time. Nevertheless, we think that if we would only solve for the biases, better results would always be obtained with approach NGO which employs GNSS measurements and accurate time-variable gravity models. To solely solve for the biases guarantees that the results are not distorted by unrealistic scale factors.

Furthermore, we confirm that when applying approach NGO to the GNV1B orbits, a disturbing signal on y_{SRF} axis is present. We used a moving median filter to successfully recover the underlying signal. Although further investigations are needed, our first experiments using our own computed reduced-dynamic orbits for approach NGO, show that the disturbing signal is highly likely caused by the characteristics of the provided GNV1B orbit data.

Acknowledgements We are thankful for the valuable comments of the three anonymous reviewers who helped to improve this article considerably. JPL is acknowledged for providing GRACE Level 1B data. Collaborative Research Centre 1128 "Relativistic Geodesy and Gravimetry with Quantum Sensors (geo-Q)" is acknowledged for financial support.

References

Bettadpur S (2009) Recommendation for a-priori bias & scale parameters for Level-1B ACC data (version 2). Tech. note, Center for Space Research

Bettadpur S (2012) Product specification document GRACE 327–720. Tech. rep., Center for Space Research

Bettadpur S (2018) UTCSR Level-2 processing standards document for Level-2 product release 0006. Tech. rep., Center for Space Research

Bezděk A (2010) Calibration of accelerometers aboard GRACE satellites by comparison with POD-based nongravitational accelerations. J Geodyn 50

Biancale R, Bode A (2006) Mean annual and seasonal atmospheric tide models based on 3-hourly and 6-hourly ECMWF surface pressure data. Scientific Technical Report STR06/01, GeoForschungsZentrum Potsdam

Bruinsma S, Biancale R, Perosanz F (2007) Calibration parameters of the CHAMP and GRACE accelerometers. Poster, CNES, department of Terrestrial and Planetary Geodesy, GeoForschungsZentrum Potsdam

Calabia A, Jin S (2016) Assessment of conservative force models from GRACE accelerometers and precise orbit determination. Aerosp Sci Technol 49

Calabia A, Jin S, Tenzer R (2015) A new GPS-based calibration of GRACE accelerometers using the arc-to-chord threshold uncovered sinusoidal disturbing signal. Aerosp Sci Technol 45

Case K, Kruizinga G, Wu SC (2010) GRACE Level 1B data product user handbook. Tech. rep., Jet Propulsion Laboratory

Dahle C, Flechtner F, Gruber C, König D, König R, Michalak G, Neumayer K-H (2012) GFZ GRACE Level-2 processing standards document for Level-2 product release 0005. Tech. rep., GeoForschungsZentrum

Desai S (2002) Observing the pole tide with satellite altimetry. J Geophys 1078(C11)

Dobslaw H, Bergmann-Wolf I, Dill R, Poropat L, Thomas M, Dahle C, Esselborn S, König R, Flechtner F (2017) A new high-resolution model of non-tidal atmosphere and ocean mass variability for de-aliasing of satellite gravity observations: AOD1B RL06, 2017. Geophys J Int 211(1):263–269

Doornbos E (2011) Thermospheric density and wind determination from satellite dynamics. Ph.D thesis, Delft University of Technology

Flury J, Bettadpur S, Tapley BD (2008) Precise accelerometry onboard the GRACE gravity field satellite mission. Adv Space Res 42(8):1414–1423

Folkner WM, Williams JG, Boggs, DH, Park RS, Kuchynka P (2014) The planetary and lunar ephemerides DE430 and DE431. IPN Progress Report

Förste C, Bruinsma S, Rudenko S, Abrikosov O, Lemoine JM, Marty JC, Neumayer KH, Biancale R (2015) EIGEN-6S4: A time-variable satellite-only gravity field model to d/o 300 based on LAGEOS, GRACE and GOCE data from the collaboration of GFZ Potsdam and GRGS Toulouse. European Geosciences Union, General Assembly 2015 Vienna (Austria) 12–17 April 2015

Van Helleputte T, Doornbos E, Visser P (2009) CHAMP and GRACE accelerometer calibration by GPS-based orbit determination. Adv Space Res 43:1890–1896

Klinger B, Mayer-Gürr T (2016) The role of accelerometer data calibration within GRACE gravity field recovery: Results from ITSG-Grace2016. Adv Space Res 58(9)

Luers JK, Wenning RH (1971) Polynomial smoothing: linear vs cubic. Technometrics 13(3):589–600

Montenbruck O, Gill E (2005) Satellite orbits - models, methods and applications. Springer, Berlin, Heidelberg

Petit G, Luzum B (eds) (2010) IERS Conventions 2010. Verlag des Bundesamts für Kartographie und Geodäsie, Frankfurt am Main

Picone JM, Hedin AE, Drob DP (2002) NRLMSISE-00 empirical model of the atmosphere: Statistical comparisons and scientific issues. J Geophys Res 107

Rieser D, Mayer-Gürr T, Savcenko R, Bosch W, Wünsch J, Dahle C, Flechtner F (2012) The ocean tide model EOT11a in spherical harmonics representation. Tech. note

Sutton E (2008) Effects of solar disturbances on the thermosphere densities and winds from CHAMP and GRACE satellite accelerometer data. University of Colorado at Boulder

Tapley BD, Bettadpur S, Watkins M, Reigber C (2004) The gravity recovery and climate experiment: Mission overview and early results. Geophys Res Lett 31(9)

Watkins MM, Yuan D-N (2014) JPL Level-2 processing standards document, for Level-2 product release 05.1. Tech. rep., Jet Propulsion Laboratory

Part IV

Geodetic Remote Sensing

PPP Without Troposphere Estimation: Impact Assessment of Regional Versus Global Numerical Weather Models and Delay Parametrization

Thalia Nikolaidou, Felipe Nievinski, Kyriakos Balidakis, Harald Schuh, and Marcelo Santos

Abstract

Mapping functions based on global Numerical Weather Models (NWM) have been developed in recent years to model the tropospheric delay in space geodetic techniques such as the Global Navigation Satellite Systems (GNSS). However, the estimation of residual tropospheric delay is still a necessity when high accuracy is required. Additionally, correlation between the estimated tropospheric delay, the receiver clock offset and the station height component, prolongs the time required for the solution to converge and impacts directly the accuracy of the results. In this study, we applied tropospheric corrections from high resolution NWM in GPS processing, in an attempt to acquire rapid and accurate positioning results, waiving the need to estimate residual tropospheric delay. Although high resolution NWM have outperformed standard atmosphere parameters and global models, it is the first time they have been compared against NWM-derived corrections, such as the operational Vienna Mapping Function 1 (VMF1) parameters. The processing strategy employed utilizes different scenarios characterized by their (a) NWM temporal and spatial resolution (b) grid or site-specific domain and (c) delay parametrization. The results were assessed in terms of height components bias, convergence frequency and time as well as residuals of the GPS analysis. Results showed an overall scenarios agreement of about 20 cm for the height component. However, the site-specific domain and high resolution NWM scenarios outperformed the grid-based ones in most of the cases; centimeter compared to decimeter daily height time series bias along faster convergence time constituted their performance. The final height offset with respect to their ITRF14 values was almost three times larger for the grid-based scenarios compared to the site-specific ones. The iono-free least squares adjustment residuals analysis revealed similar patterns for all the scenarios while the estimated heights experienced a reduction on the days of heavy precipitation under most of the scenarios; for some of the stations the advantage of using direct ray-tracing became obvious during those days.

T. Nikolaidou (✉) · M. Santos
Department of Geodesy and Geomatics Engineering, University of New Brunswick, Fredericton, NB, Canada
e-mail: Thalia.Nikolaidou@unb.ca; msantos@unb.ca

F. Nievinski
Department of Geodesy, Federal University of Rio Grande do Sul, Porto Alegre, Brazil
e-mail: felipe.nievinski@ufrgs.br

K. Balidakis
GFZ German Research Centre for Geosciences, Space Geodetic Techniques, Potsdam, Germany
e-mail: balidak@gfz-potsdam.de

H. Schuh
GFZ German Research Centre for Geosciences, Space Geodetic Techniques, Potsdam, Germany

Technische Universität Berlin, Institute of Geodesy and Geoinformation Science, Berlin, Germany
e-mail: schuh@gfz-potsdam.de

J. T. Freymueller, L. Sanchez (eds.), *International Symposium on Advancing Geodesy in a Changing World*, International Association of Geodesy Symposia 149, https://doi.org/10.1007/1345_2018_44

Keywords
GPS · High-resolution NWM · Mapping function · Numerical weather model · Precise point positioning · Troposphere modeling · VMF1

Abbreviations

CMC	Canadian Meteorological Centre
ECMWF	European Centre for Medium-Range Weather Forecasts
GAPS	Global Navigation Satellite System Analysis and Positioning Software
GNSS	Global Navigation Satellite Systems
GPS	Global Positioning System
HRDPS	High Resolution Deterministic Prediction System
IERS	International Earth Rotation and Reference Systems Service
IGS	International GNSS Service
MF	Mapping function
NWM	Numerical Weather Model
PP	Point Positioning
PPP	Precise Point Positioning
SD	Slant delay
TUW	Technische Universität Wien
UNB	University of New Brunswick
VMF1	Vienna Mapping Functions 1
ZD	Zenith delay

1 Introduction

In the analysis of Global Navigation Satellite Systems (GNSSS) observations, precise knowledge of the status of the neutral atmosphere (troposphere) is essential. On the one hand, for high-accuracy applications, where estimation of residual zenith tropospheric delay is necessary, existing correlations between the estimated parameters degrade the accuracy of the estimated position, prolong the convergence time and can even lead to faulty parameter estimation when lacking an adequate number of observations. Specifically, correlation between the estimated zenith tropospheric delay, station height and receiver clock offset peaks for observations at high elevation angles (Nilsson et al. 2013) and precise modelling of the troposphere is required to achieve geodetic accuracy. Several methods aiming to decorrelate the estimated parameters and improve the modelling for high-accurate GNSS applications have been developed in past years (e.g., Shi and Gao 2014; Ahn 2016; Yao et al. 2017; Douša et al. 2018). However, the need of supplementary data and/or algorithm adjustment as well as possible shortcomings for real-time applications impede their general implementation.

On the other hand, for navigation or positioning applications where the level of absolute accuracy is not demanding, such as autonomous positioning, i.e., use of single Global Positioning System (GPS) engine or high-rate relative movement tracking, one may omit estimating the tropospheric delay especially when few observations are expected. In such cases, whether single or dual frequency Point Positioning (PP) is utilized, an external input is required for the elimination of the tropospheric delay or as it is commonly called, error. The quality of the external input is critical as any possible error will affect the estimated station height.

Evidently, whether or not the troposphere is estimated, precise modelling of it aids positioning accuracy. Several options exist for the mitigation of the tropospheric error. The most popular of these are "blind" models, which use empirical meteorological parameters or "grid-based" ones, computed via ray-tracing in a Numerical Weather Model (NWM). The parametrization of the tropospheric error at an arbitrary elevation angle, referred to as the slant delay (SD), is performed by means of a mapping function (MF) applied to the zenith delay (ZD) at the site. The current state-of-art and recommended by the latest International Earth Rotation and Reference Systems Service (IERS) conventions MFs (Petit and Luzum 2010), are the Vienna Mapping Functions 1 (VMF1), (Boehm and Schuh 2004) that utilize the European Centre for Medium-Range Weather Forecasts (ECMWF) operational NWM to model the atmosphere.

Although results of such a parametrization can be of sufficient precision, ± 3 mm of station height (Böhm 2007) and serve the needs of specific applications, under the presence of atypical atmospheric conditions (e.g., heavy precipitation, severe weather phenomena) the actual meteorological parameters can be far from the model prediction resulting in a computed delay bias that can reach up to 2 m for low elevation angles.

Moreover, when large azimuth asymmetry is present, especially in mountainous or coastal areas, VMF-type MFs are unable to capture the azimuth asymmetry due to their mathematical structure. Existing gradients can reach up to a few decimeters for low elevation angles (Masoumi et al. 2017) introducing a centimeter bias to the height component of the station according to the rule of thumb by Niell and Petrov (2003) and as refined by Boehm and Schuh (2004).

Modelling of such gradients is required (Boehm and Schuh 2013) and an effort was made to generate azimuth dependent MF (Boehm et al. 2005) but its inability to supersede the VMF1 rendered it non-operational (Landskron 2017). Currently, the asymmetric delay component is treated separately by employing linear and nonlinear gradient components (Landskron 2017; Masoumi et al. 2017; Balidakis et al. 2018).

Ray-tracing is able to simulate the delay at each satellite, with or without the need to map the zenith delay. Additionally, the NWM provides the atmospheric 3D information from which one is able to compute or estimate the azimuthal asymmetry.

Recently, NWM with increased spatial and temporal resolution have been made available e.g., by the Canadian Meteorological Centre (CMC), ECMWF and National Center for Environmental Prediction. The scope of this study is to evaluate the improvement in position when 3D ray-tracing (Nievinski and Santos 2010) is utilized, compared to the VMF-parametrization, when alternating the employed NWMs. The presented results demonstrate the impact a GPS Precise Point Positioning analysis (PPP) (Zumberge et al. 1997) when no residual tropospheric delay is estimated.

In the next sections, the research methodology is developed through five adopted scenarios used to retrieve the tropospheric delay. Two scenarios make use of ray-traced delays while the rest use the ZD-MF approach, alternating the employed NWM. More details on the scenarios are provided in Sect. 2. In the sequel, the retrieved delays are employed in PPP and the obtained height position is evaluated against its reference value. The residuals of the PPP analysis are discussed in Sect. 3, and a summary of the outcomes of the study is given in Sect. 4.

2 Data and Methodology

From 6th to 8th June, 2017 a severe precipitation event took place in Victoria Island, BC (Canada), totaling from 24 to 31 mm of rain, depending on the location, the second largest for that month (Fig. 1). Thus, the considered time duration to be examined was chosen from 1st to 10th of June 2017. The research was conducted based on data collected by eight

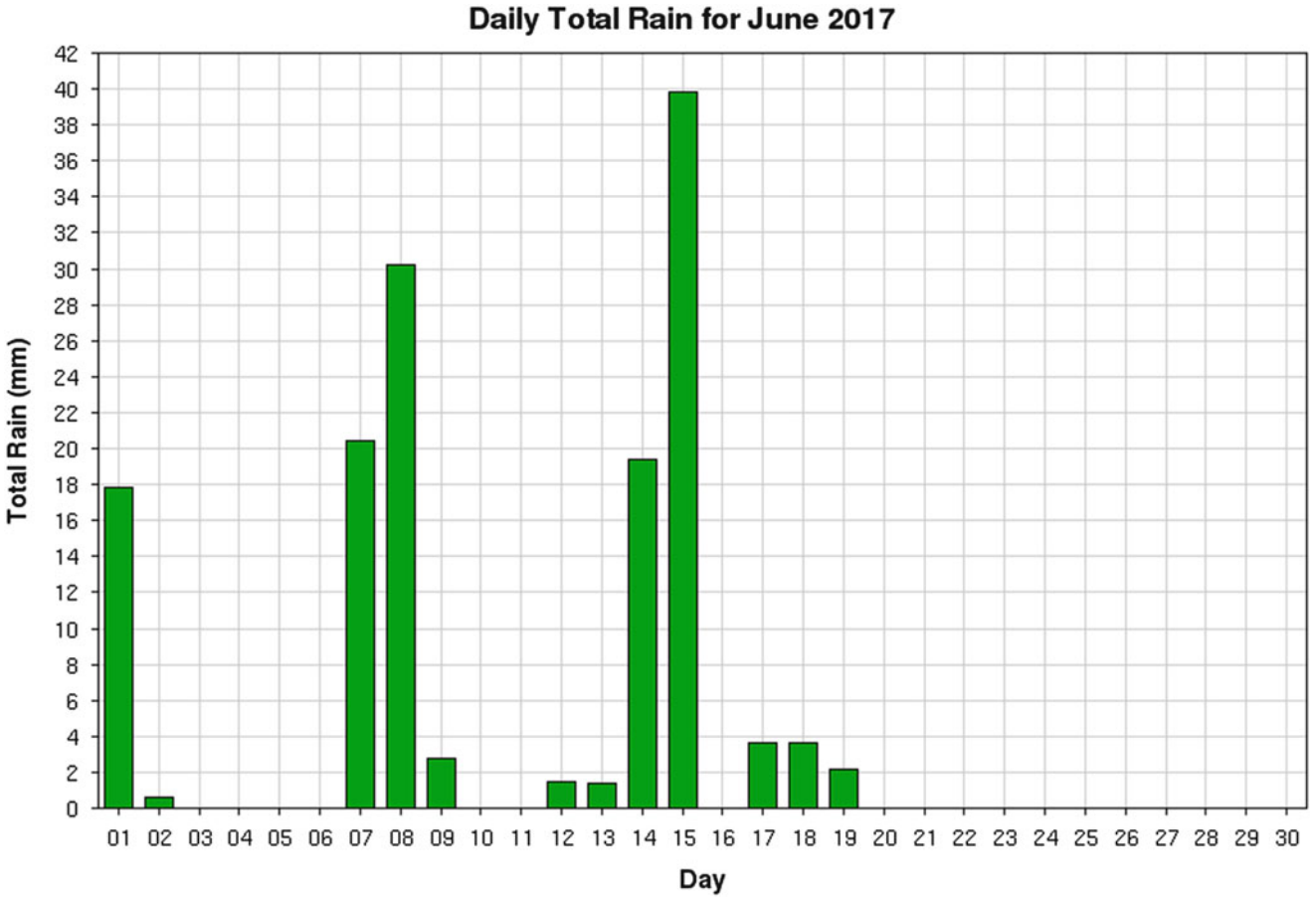

Fig. 1 Total rain records at meteorological station UCLUELET KENNEDY CAMP. Source: Meteorological Service of Canada, Environment and Climate Change Canada

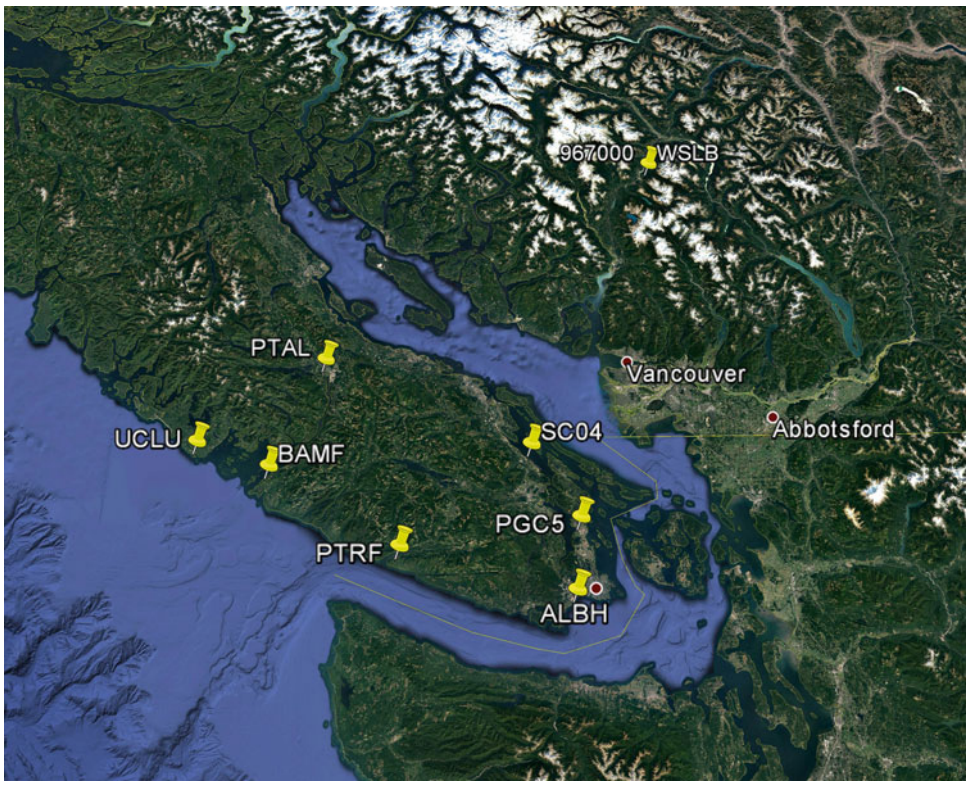

Fig. 2 Location of selected GNSS stations in British Colombia, Canada

GNSS stations (Fig. 2). Seven of those stations are located in the island near the ocean and their proximity allows the study of local meteorological phenomena. The last station, WSLB was chosen for its special location in Whistler, BC, at a height of more than 924 m.

In order to address the scope of this study we define three approaches to retrieve the tropospheric delay and the spatial resolution of the NWM: (a) mapping function along with the zenith delay (ZD-MF) on a geo-grid, (b) ZD-MF specific to each site, (c) direct ray-tracing for all recorded ranges. We also alternated the source used to model the atmosphere: global or regional high resolution (Hi-Res) NWM. In total we had five scenarios: M1, M2, M3, D1 and D2 (Table 1).

Scenario M1 utilizes the VMF1 in the standard way for GNSS analysis i.e., SDs are expressed as the product of the ZDs and MF; the ZD values and MF "a" coefficients are retrieved from the Technische Universität Wien (TUW) on-line repository.[1] The TUW products are interpolated in space (bilinear) and time (cubic) to match the observations' processing interval. We shall call this scenario "*ZD-MF VMF1 – grid*".

Scenario M2 differentiates with respect to M1 only due to the choice of the NWM: M2 uses the Global Deterministic Forecast System (GDPS) from the Canadian Meteorological Center (CMC). Although in a previous study (Nikolaidou et al. 2018) the equality of the products resulted from the ECMWF and CMC NWM has been demonstrated in terms of station position repeatability, under the presence of large azimuthal tropospheric asymmetry, the use of the latter is potentially advantageous due to its increased spatial resolution i.e. CMC has a horizontal resolution of approximately 66 km. Still, the current scenario products were generated at the same resolution as M1's to facilitate the comparison. This scenario is called "*ZD-MF CMC-Glb - grid*".

In scenario M3, although still using the ZD-MF approach, the computation is performed at each site, without grid interpolation, using the High Resolution Deterministic Prediction System (HRDPS), from the CMC. HRDPS has a horizontal resolution of about 2.5 km and a temporal resolution of 1 h. For this scenario, 2D ray-tracing (Nievinski and Santos 2010) – was performed, for the zenith delays and the mapping functions' "a" coefficients, at each site location and at the GPS data interval (5 min). The motivation for the creation of this scenario, is the assessment of the ZD-MF approach with respect to the direct approaches and particularly scenario D2 (explained below). It is referred to as "*ZD-MF CMC-Reg - site*".

Scenario D1 makes use of direct 3D ray-tracing performed for every station-satellite link, at the data interval of 5 min. The CMC GDPS was used to model the atmosphere which has median, with respect to ECMWF and HRDPS, spatial resolution (66 km) and a temporal resolution of 6 h. We shall refer to this scenario as "*SD CMC-Glb - site*".

[1] http://ggosatm.hg.tuwien.ac.at/delay.html.

Table 1 Generated scenarios and their characteristics

Scenario	Approach	NWM	Product spatial resolution	Product temporal resolution	Name
M1	ZD-MF	ECMWF operational	On grid ($2 \times 2.5°$)	Every 6 h	ZD-MF VMF1 – grid
M2	ZD-MF	CMC GLB	On grid ($2 \times 2.5°$)	Every 6 h	ZD-MF CMC-Glb – grid
M3	ZD-MF	CMC HRDPS	At the site	Every 1 h	ZD-MF CMC-Reg – site
D1	SD	CMC GLB	At the site	At observation level	SD CMC-Glb – site
D2	SD	CMC HRDPS	At the site	At observation level	SD CMC-Reg – site

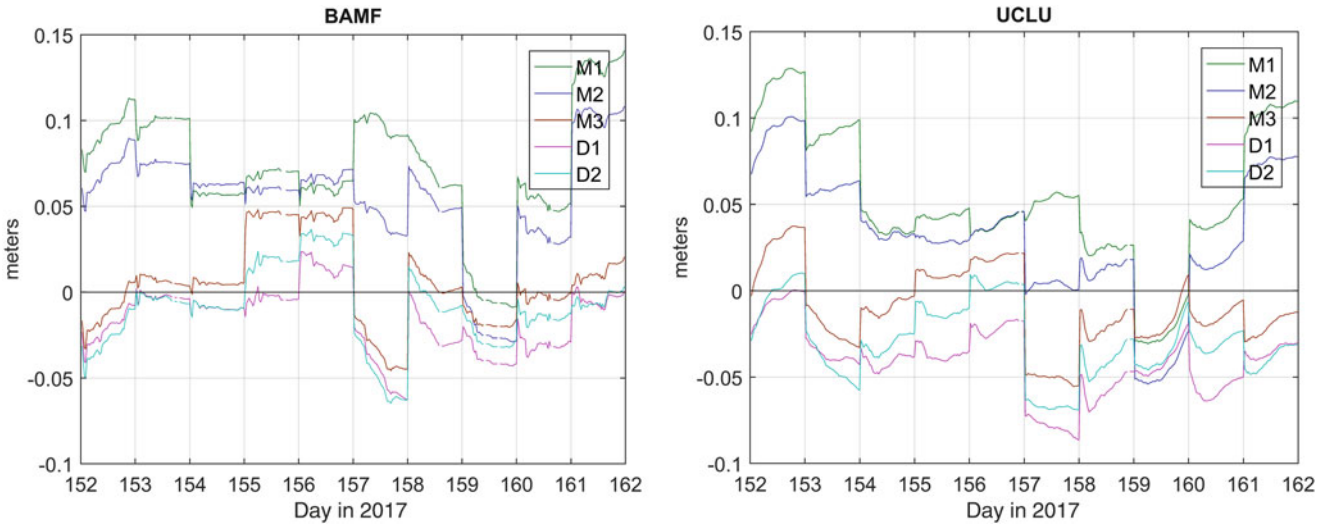

Fig. 3 Height time series (6 h processing) of every scenario: left BAMF and right UCLU station

Finally, scenario D2 represents again direct 3D ray-tracing but using the CMC HRDPS, with its high spatial-temporal resolution. One may suggest this scenario as the most promising one, in matters of predicting accurately the state of the atmosphere and thus the tropospheric delay. We will refer to this scenario as "*SD CMC-Reg - site*".

After acquiring the zenith delays along with the mapping functions and the slant delays for the direction of all recorded ranges, for all the stations and days, each approach was evaluated in GPS Precise Point Positioning (PPP) analysis. The University of New Brunswick's (UNB), available online, GNSS Analysis and Positioning Software[2] (GAPS) was employed (Leandro et al. 2007). Precise satellite orbits and clocks were utilized in a GPS-only processing mode and the default options for GAPS processing.[3] Each day was processed individually. It is important to be noted that throughout the analysis no additional tropospheric delay was estimated. In other words, the tropospheric error was left to be mitigated solely by the employed scenario. The results of PPP were analyzed focusing on the height component of each station. To make absolute comparisons, the ITRF14 position of the stations, was considered to be the reference value. For the International GNSS Service (IGS) station ALBH the IGS weekly position was available and thus was used instead. In the following sections, the height bias, the convergence time and the root mean square error of the residuals are examined for each station separately and then the performance for each scenario is summarized.

3 Analysis

3.1 Height Time Series Bias, RMSE and 95% Percentile, with Respect to the Reference Value

The scope of this section is to evaluate the height variation within each scenario, with respect to the reference value (ITRF14 or IGS weekly solution), throughout a 6-h worth processing period and for every station. Consequently, each scenario performance is accessed over all stations throughout the processing period of the 10 days.

In the beginning, the estimated height time series, discerned by scenario (choice), were compared with the reference value for all the days and each station. In general, and with the exceptions of few epochs, all scenarios have a maximum disagreement of 20 cm. Although the scenarios seem to

[2] http://gaps.gge.unb.ca.

[3] http://gaps.gge.unb.ca/strategy.html.

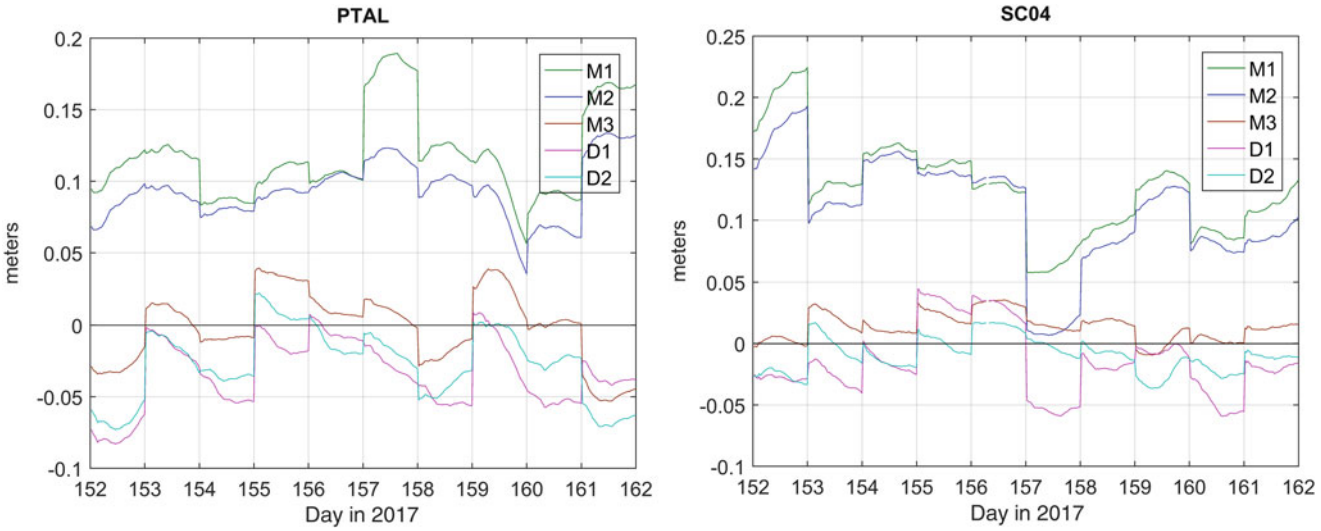

Fig. 4 Height time series (6 h of processing) of every scenario: left PTAL and right SCO4 station

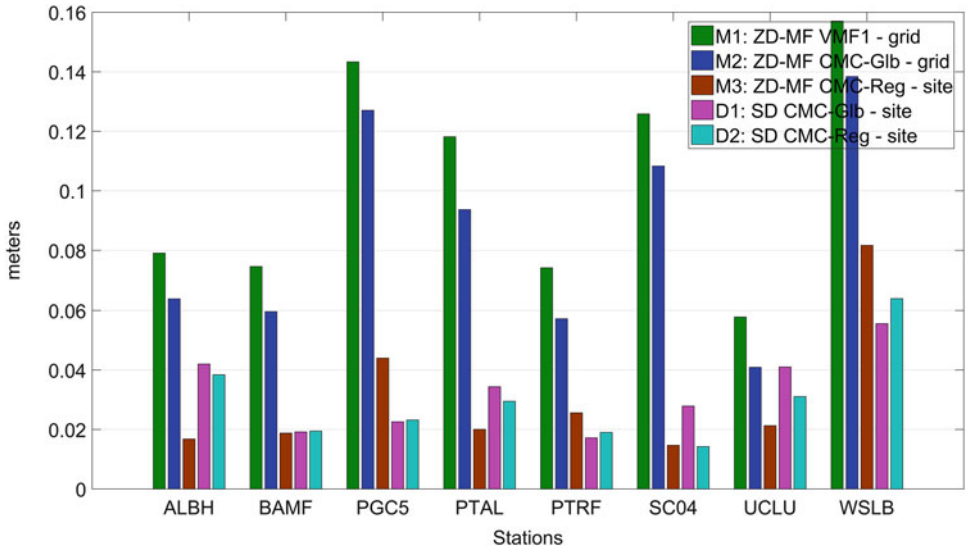

Fig. 5 Height time series bias, averaged over all days, for each scenario and station, when excluding initial convergence time

follow each other (Fig. 3),[4] one can easily separate between the grid-based (M1 and M2) and site-specific approaches (Fig. 4). It is noticeable, and further discussed below, that for the latter, the time series bias is smaller. Furthermore, the weather patterns are characteristically portrayed in the figures by the sudden height reduction on the 6th (day of year 157) of June for the stations BAMF, UCLU and SCO4 and then again on the 8th (day of year 159) for all the stations except SC04. These patterns agree well with the total rain records of the nearby meteorological stations.

Examining the total performance of each approach among all stations, although station-based variations exist, the grid scenarios M1 and M2 have overall the largest unsigned biases: 7–19 cm (7–15 cm excluding station WSLB). The (unsigned) biases for M3, D1 and D2 ranging from 4 to 11 cm (4–8 cm excluding WSLB) are the smallest at station PTRF and largest in all scenarios for station WSLB, which is located at an altitude of about 910 m in Whistler. Comparing the grid-based with the site-based scenarios the latter show an improvement ranging from 22% (at UCLU) to 67% (at PGC5) with a mean improvement over all stations of 49%.

Considering that the PPP technique is subject to a convergence time necessary for the parameters to reach their final value, a respective comparison was conducted excluding a mean convergence time of 2 h from every processing (Fig. 5). In this case, the site-based scenarios perform even better with a minimum improvement of 37% (UCLU) and maximum 78% (PGC5). An overall improvement of 65% is achieved. To be noted that at station UCLU, the site-based scenario using the global NWM provides slightly worse or equal, for

[4] An initial window of 2 h, allowed for convergence, has been excluded from the plot.

Table 2 Mean height time series bias for every scenario

Scenario	M1	M2	M3	D1	D2
Bias (m)	0.128	0.110	0.057	0.059	0.057
Bias (m) excl. conv.	0.104	0.086	0.030	0.033	0.030

the two comparisons respectively, results to the grid ZD-MF scenario that uses the same NWM.

The mean unsigned bias (with respect to the reference value) for each scenario is displayed in Table 2. With respect to the whole time series comparison, the grid approaches (M1 and M2) have a mean bias of more than 10 cm while the direct approaches (D1 and D2) and the ZD-MF approach using the Hi-Res NWM (M3) have a mean bias of about 6 cm. On the other hand, excluding convergence period, reduces all the biases by approximately 3 cm, allowing for about 50% improvement for all the site-based scenarios. It is hard to distinguish between the last three scenarios considering the small sample (8 stations) and their millimeter level differences.

The root mean square error (RMSE) of the height time series with respect to the reference value, when considering the full time series, is similar for all approaches and varies only by station; smallest at PTRF and largest at WSLB. Nonetheless, a slightly larger RMSE is noticed for the two grid approaches among all stations with the exception at UCLU. However, excluding the initial convergence period, besides the resulted scale difference, reveals a more spread behavior of each scenario (Fig. 6). Specifically, M1 and M2 have a similar (RMSE) standard deviation (STD), over all stations, of 3.4 cm; M3 has a STD of 2.2 cm followed by D1 and D2 scenarios with 2.3 cm and 1.5 cm respectively. Their respective RMSE mean values are: 11 and 9.2 cm for the M1 and M2 respectively and 3.5 cm on average for all the site-based scenarios (M3, D1 and D2). One may notice the resemblance between the STD and the presumed accuracy of each scenario in view of their parametrization and data source.

Lastly, as another means of assessing the precision of the scenarios employed, the 95% percentile of the height residuals (retrieved height time series – reference value) was calculated for every station and scenario (Fig. 7). As it can be observed, M1 and M2 scenarios have systematically the largest residuals; between the site-based scenarios, none has a systematic behavior over all stations; however, the following can be concluded: for M1 and M2, with a similar behavior, 95% of the residuals are below 18 and 15 cm respectively. This could indicate a slightly smaller frequency of the extreme-outlier retrieved values. The respective number for M3 is 7.7 cm while the two direct ray-tracing scenarios (D1 and D2), have the majority of their residuals below 8.4 cm and 8 cm respectively. Regardless the slightly higher values of the direct scenarios compared to the ZD-MF M3 scenario, which will be discussed later, the results show a potential superiority of the regional NWM handling extreme observations. The mean values of the 95% percentiles are shown in Table 3.

3.2 Convergence to the Reference Value (ITRF14)

Next, the convergence time of each approach was examined. Convergence hereafter is defined with respect to the reference value indicating the confluence of the time series to the latter: the height parameter is considered as "converged" if is within 1 cm deviation from the reference value for at least 20 consecutive minutes. With the above definition for

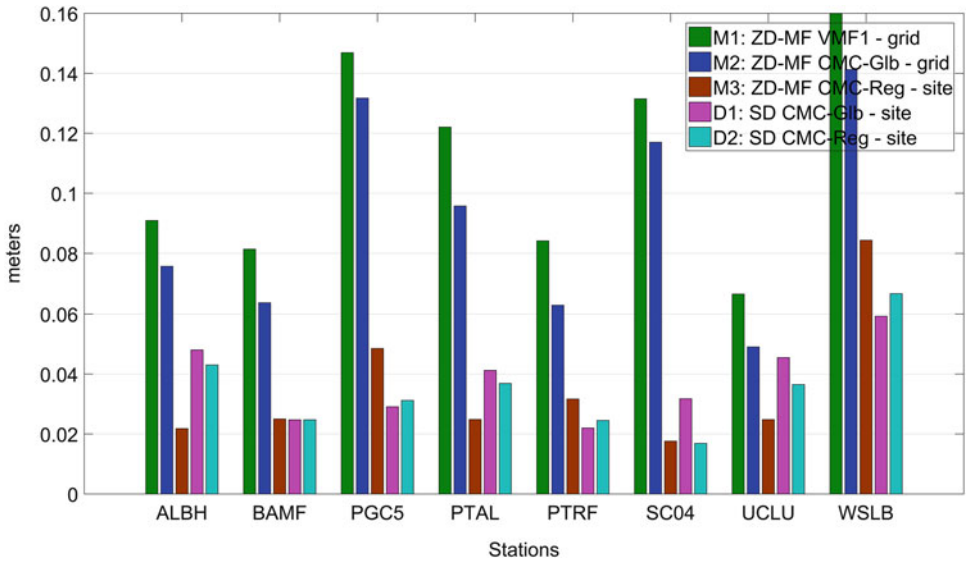

Fig. 6 Height time series RMSE for each scenario and station, when excluding initial convergence time

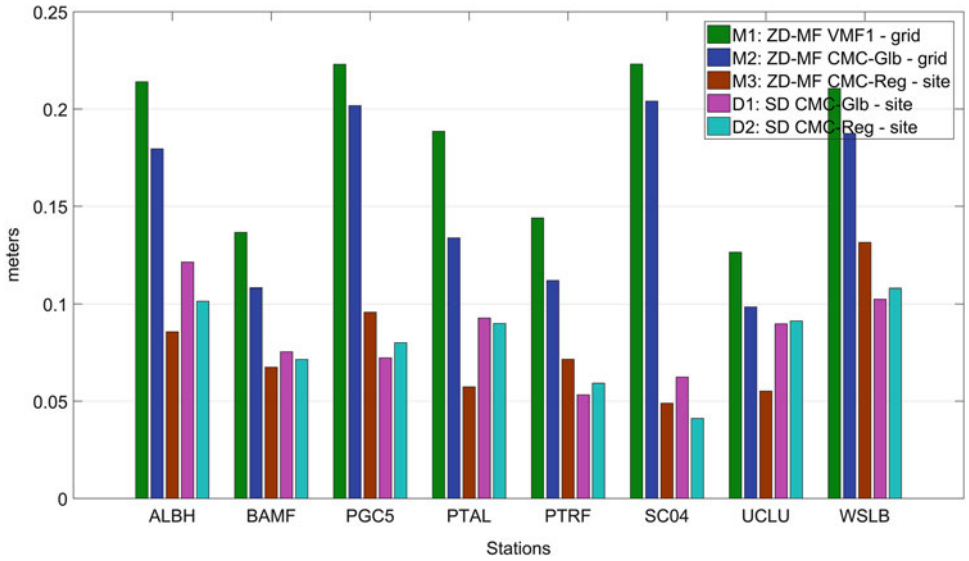

Fig. 7 95% percentile of the height time series residuals for each scenario and station

Table 3 95% percentile of the height time series residuals for each scenario

Scenario	M1	M2	M3	D1	D2
95% percentile (m)	0.183	0.153	0.077	0.084	0.080

convergence, Fig. 8 shows the mean number of times, over the 10 days, an approach has converged for every station. It is noticed that the grid approaches achieve convergence only for half of the stations (M1 and M2 did not converge for stations PGC5, PTAL and WSLB – M1 did not converge also for SC04). The approaches M3, D1 and D2 achieve convergence, at least once, for all stations but WSLB. The meteorological values retrieved from ray-tracing are the result of interpolation in the NWM grid datapoints. Thus, the delay at an arbitrary point (which does not coincide with a NWM datapoint) depicts an average delay of its neighboring NWM datapoints. The inability of the models to reach convergence at WSLB station can be attributed to a poor interpolation due to the ridged topography at the site. In other words, the poor prediction about the slant delay presumably resulted to a biased estimation of the station height.

Considering all the times each approach converged throughout the days and for all stations, M1 and M2, grid approaches, converged only 9% of the times (i.e. 7 times out of all possible 80) (Table 4). The approaches that utilize the Hi-Res NWM (M3 and D2) converged for about half of the times. The approach which utilize the global NWM converged 41% of the times.

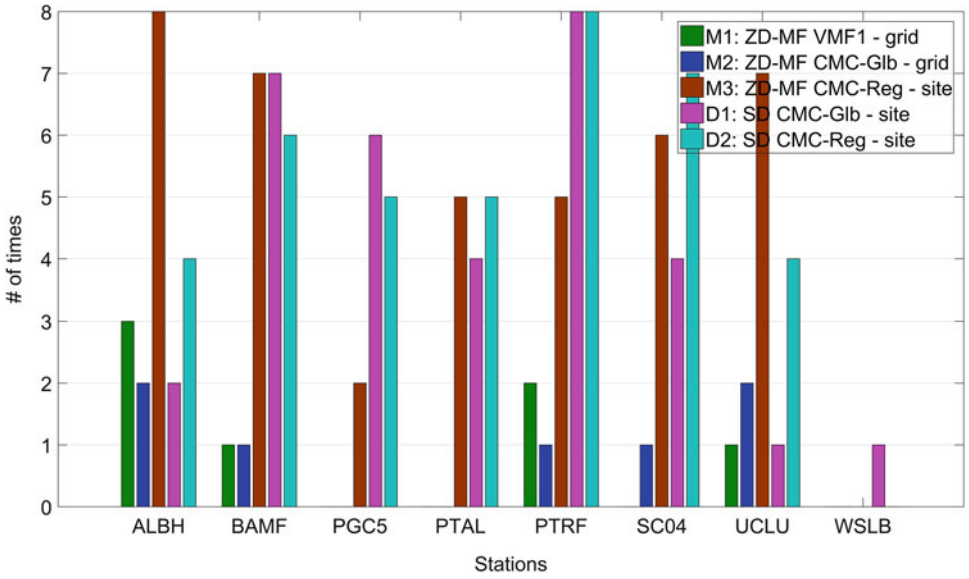

Fig. 8 Mean number of times each scenario converged, to the reference value, for each scenario and station

Table 4 Mean number of times each scenario converged to the reference value for each scenario

Scenario	M1	M2	M3	D1	D2
Total # of times it converged	7	7	40	33	39
% of times it converged	9	9	50	41	49

Table 5 Mean time (in hours) to converge to the reference value for each scenario

Scenario	M1	M2	M3	D1	D2
Mean time (h)	5.33	5.28	3.8	3.95	3.53

3.3 Time Required to Converge to the Reference Value (ITRF14)

Figure 9 shows the mean time taken by each approach to converge to the reference value. It can be seen that for station WSLB all the approaches took longer to converge (except D1 which was longer at UCLU). For station ALBH, in Albert Head, both the grid (M1 and M2) and the D1 and D2 direct approaches required comparable time to converge. The direct approaches showed the best results at station PTRF (again).

Considering all the stations, the direct approach on the Hi-Res NWM (D2) precedes, reaching convergence after about 3.5 h (212 min) followed by the ZD-MF approach (M3) on the same NWM (3.8 h) and the other direct approach on the global NWM (D1) (almost 4 h). About 5.3 h are needed for the VMF1 and UNB-VMF1 approaches (Table 5).

3.4 Final Height Value Bias with Respect to the Reference Value

Continuing the analysis, this section deals with the final value of the height, resulting from 6 h of processing when all estimated parameters are considered to have stabilized and their values attained their maximum precision (in terms of reaching their smallest standard deviation). In Fig. 10, the final height bias with respect to the reference height value is displayed, daily, for every approach and station. Although the height bias differs by day and station among each approach, it is noted that for two stations (BAMF and WSLB) all the approaches are characterized by a positive bias. It can be also seen that for Days Of Year (DOY) 152, 157 and 161 (June 1st, 6th and 10th respectively), three stations (PGC5, PTAL and PTRF) experience unusual lager biases (up to 8 cm) for the grid approaches.

Considering the mean final height bias for every approach per station (Fig. 11), the superior performance of both the direct approaches (D1, D2) is evident as well as the ZD-MF approach but utilizing the Hi-Res NWM at the site (M3). Despite the biases of the grid approaches (M1, M2), which vary based on the station, the UNBVMF1 grid (M2) has consistently smaller mean height bias than M1. The largest height biases in all approaches appear again for station WSLB for the aforementioned reason.

The mean final height bias for each approach is shown in Table 6. The approaches that make use of the Hi-Res NWM have almost equivalent mean final height bias of about 3 cm, with respect to the reference value. The direct approach on the global NWM follows with comparable bias (3.4 cm). As already pointed out the grid approach, that utilizes the CMC-Glb NWM, follows with a mean bias of almost 9 cm whereas the maximum value is at 10 cm for the VMF1 scenario which utilizes the ECMWF's operational model operational NWM.

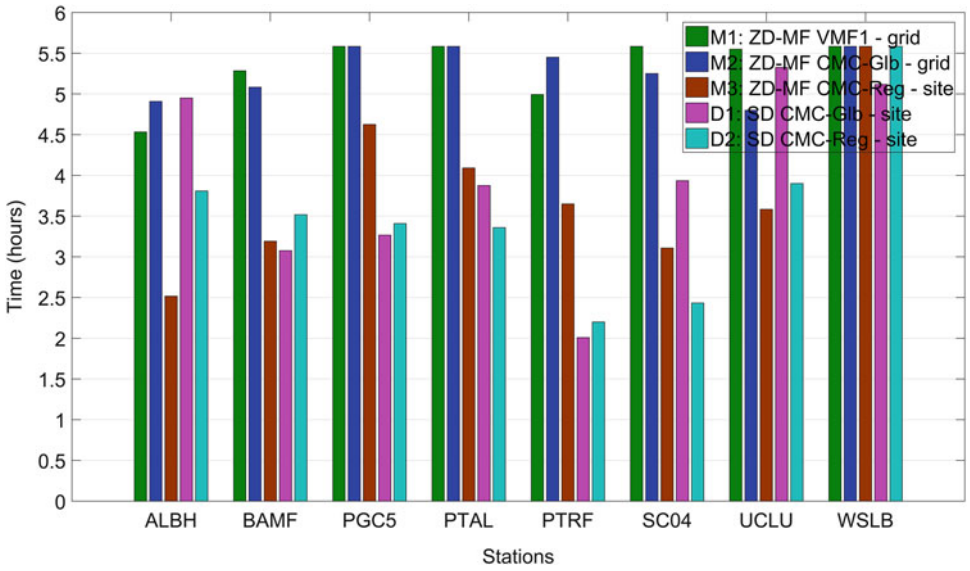

Fig. 9 Mean time (in hours) for each scenario to converge, to the reference value, for each station

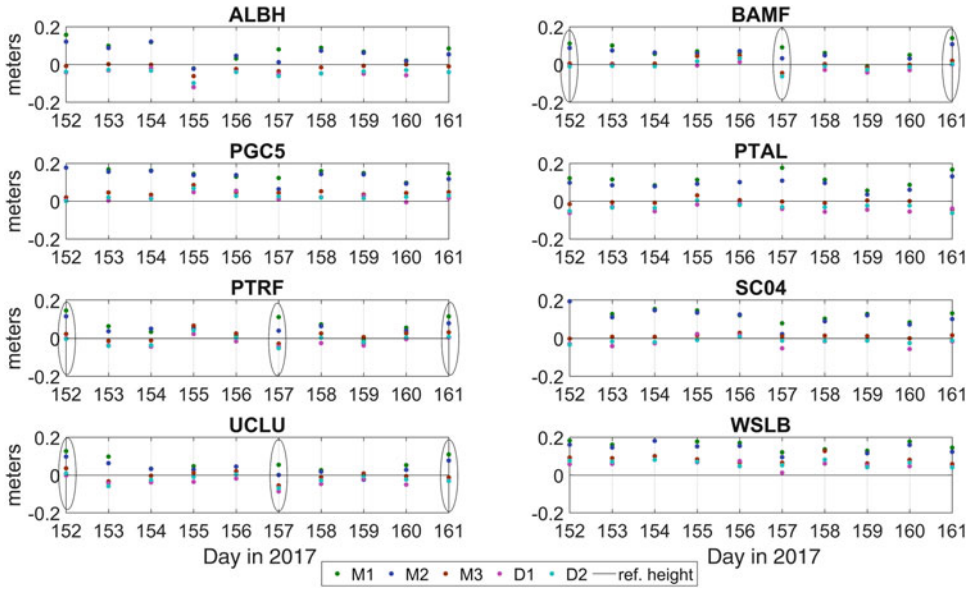

Fig. 10 Final height offset for every scenario, station and day of the study. From top left to bottom right the stations are: ALBH, BAMF, PGC5, PTAL, PTRF, SC04, UCLU and WSLB

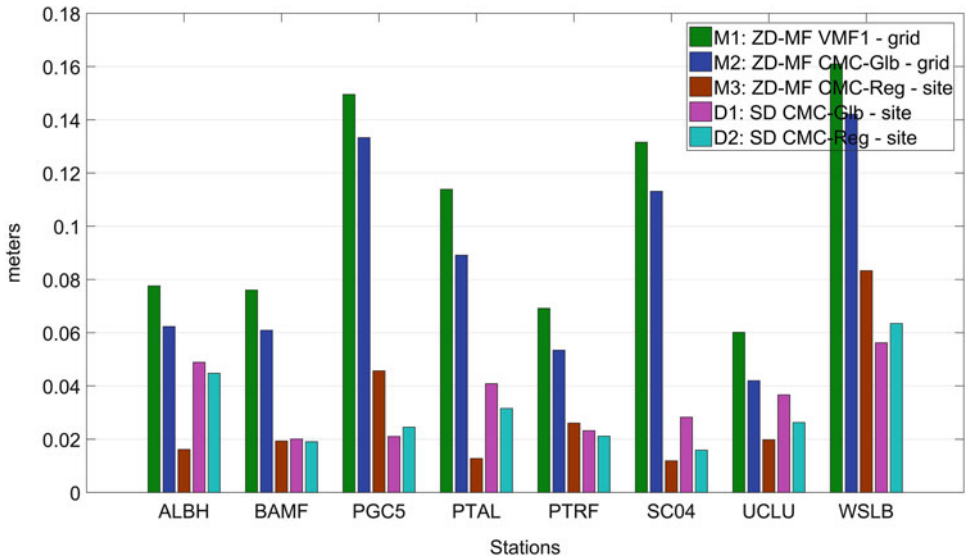

Fig. 11 Mean final height bias for each scenario and station

Table 6 Mean final height bias for each scenario

Scenario	M1	M2	M3	D1	D2
Final bias (cm)	10.9	8.7	2.9	3.4	3.1

Special care should be given to the fact that these results represent a view of the performance of the approaches at the selected sites and it would be ill advised to draw global or even long-term conclusions.

3.5 PPP Analysis Phase Residuals

To complete the analysis, it would be an oversight not to inspect the residuals of the PPP least squares adjustment filter. We examined the phase residuals as the code ones showed only small variations. The RMSE of the phase residuals for every approach and station are displayed in Fig. 12. Contrary to what was expected the direct approaches (D1, D2) have larger mean residuals compared to the ZD-MF approach which uses the Hi-Res NWM (M3); the M3 approach, has consistently the smallest RMSE. In general, the residuals of the direct approaches are comparable with the grid ones.

Table 7 presents the overview for each approach. In spite of the fact that M3 keeps the lead, the RMSE value of the residuals, among the approaches, excluding M3, is 1 cm. Therefore, one may presume that the variations of the residuals are on the noise level and are based on the current conditions, environment and location of the station. Approaches D1 and D2 unexpected large values could be attributed to the proximity of the station to the horizontal

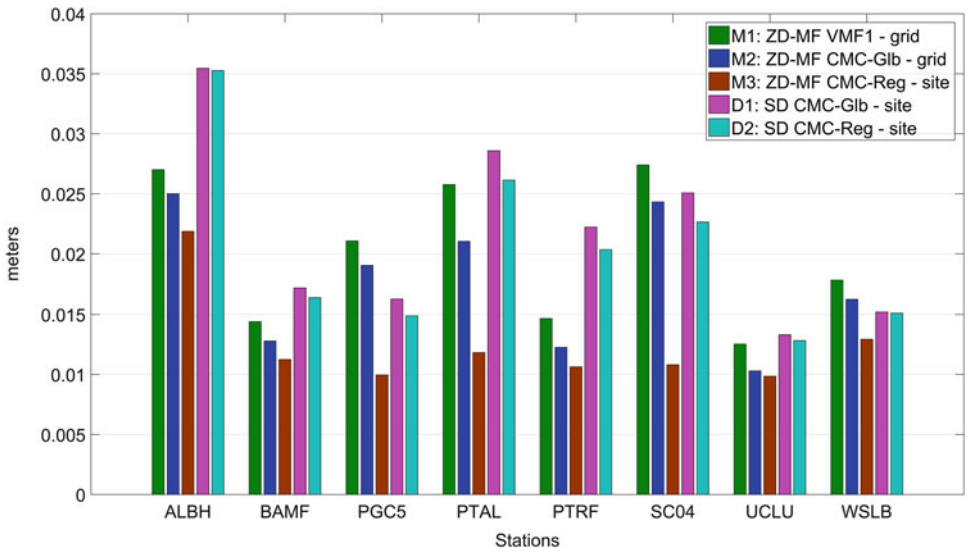

Fig. 12 RMSE phase residuals for each scenario and every station

Table 7 Mean phase residuals for each scenario

Approach	M1	M2	M3	D1	D2
RMSE of phase residuals (m)	0.010	0.009	0.007	0.010	0.010

spatial boundaries of the NWM; for low elevation angles part of the computed delay results outside the NWM limits where a surrogate modeling using climatology is employed. Notwithstanding, it would be considered doubtful to derive conclusions upon the residuals due to their small magnitude which is at the PPP noise level.

4 Conclusion

This study explored two ways of tropospheric delay parametrization in point positioning under using different NWM data sources and parameter resolutions. The delay parametrization using zenith delays and mapping functions was compared against direct ray-tracing at the observation level; three distinct NWM were employed namely the ECMWF, the CMC GLB and HRDPS, and the delay parameters were either interpolated from the nearby grid data points or computed directly at the site. With respect to the NWM employed the case study constitutes the first evaluation of the CMC HRDPS for positioning.

For the zenith delays and mapping functions approach, two grid scenarios using global NWM (ZD-MF VMF1/CMC-Glb) and one site scenario (ZD-MF CMC-Reg) using the regional high-resolution NWM were established, whereas for the direct ray-tracing, two scenarios at the observation level, one for each NWM category: global or regional high resolution, (SD CMC-Glb/Reg) were established.

All the scenarios were evaluated in PPP analysis using the GAPS software, while no tropospheric delay was estimated. Five criteria were used to characterize each scenario's performance: (a) the height time series bias, RMSE and 95% percentile (b) the final height offset, (c) the times each scenario converged, (d) the convergence time itself and (e) the residuals of the ionosphere-free PPP adjustment. In general, all the scenarios agreed within 20 cm, with regard to the height time series bias. However, the grid and non-grid (at the site) approaches could be easily grouped by their cm offset. The mean bias from the reference value was more than 1 decimeter for both grid scenarios and about half for the other ones. Using the site-based scenarios resulted in average 49% improvement in the height time series offset. When excluding an initial convergence period, the improvement rose to 65%. The RMSE of the time series, when considering the full height time series, varied mostly station-wise and was less due to the choice of the scenario. However, excluding the initial convergence period, the average RMSE of the site-based scenarios was 3.5 cm compared to 10 cm of the grid-based scenarios. A 95% percentile analysis of the height residuals showed a potential superiority of the regional NWM compared to the global one when the direct ray-tracing approach was utilized.

With regard to the times each scenario reached the reference value successfully (converged), the ZD-MF CMC-Reg-Site performed the best, achieving convergence for at least 20 consecutive minutes for half of the 10 days of processing. The direct ray-tracing scenarios, SD CMC-Glb-Site/Reg-Site followed closely but both the grid based global ZD-MF ones achieved convergence only 9% of the time. Time-wise, the site scenarios converged about 1.6 h faster compared to the grid ones. The final height offset was about 3 cm for the site scenarios and reached a minimum for the ZD-MF CMC-

Reg-Site. The SD CMC-Glb-Site and Reg-Site scenarios had approximately 10 cm offset from the reference value. Finally, the residuals of all the approaches had a RMSE value of about 10 cm with the exception of the ZD-MF CMC-Reg-Site that had 7 cm. In essence, one may point out that the site scenarios have a clear advantage whether they are employing the ZD-MF or the direct ray-tracing approach. However, the latter has systematically improved results even when compared to the ZD-MF approach at the site, using the same Reg-Site NWM. Lastly, a reduction in the estimated heights was noticed for the heavy precipitation days under most of the scenarios and for some stations the advantage of using direct ray-tracing became obvious.

Acknowledgements The authors would like to thank: the Natural Resources Canada for the GPS data used in this study, belonging to the Canadian Active Control System; the Canadian Meteorological Centre, Environment and Climate Change Canada for providing the data necessary for the creation of the tropospheric parameters and specifically Dr. Edouard Sandrine for her valuable assistance retrieving the data; the Technische Universität Wien (TUW) for providing the VMF1 tropospheric parameters; last but not least, the editor and the two unknown reviewers for their constructive comments and helping to improve the manuscript.

References

Ahn Y-W (2016) De-correlation of tropospheric error and height component on GNSS using combined Zenith-dependent parameter. University of New Brunswick, New Brunswick. http://www2.unb.ca/gge/Pubs/TR306.pdf. Accessed 13 Jul 2018

Balidakis K et al (2018) Estimating integrated water vapor trends from VLBI, GPS, and numerical weather models: sensitivity to tropospheric parameterization. J Geophys Res Atmos 123(12):6356–6372. https://doi.org/10.1029/2017JD028049. Accessed 17 Jul 2018

Boehm J, Schuh H (2004) Vienna mapping functions in VLBI analyses. Geophys Res Lett 31(1):L01603. https://doi.org/10.1029/2003GL018984. Accessed 9 Oct 2017

Boehm J, Ess M, Schuh H (2005) Asymmetric mapping functions for CONT02 from ECMWF. EVGA Work Meet No. 17:64–68

Böhm J (2007) Tropospheric delay modelling at radio wavelengths for space geodetic techniques. 80. https://publik.tuwien.ac.at/files/PubDat_121080.pdf. Accessed 20 Sept 2017

Böhm J, Schuh H (2007) Troposphere gradients from the ECMWF in VLBI analysis. J Geod 81(6):409–421.http://ggosatm.hg.tuwien.ac.at/DELAY/DOC/2007Boehm_etal_LHG.pdf. Accessed 20 Sept 2017

Boehm J, Schuh H (2013) Atmospheric effects in space geodesy. In: Boehm J, Schuh H (eds) Springer atmospheric sciences. Springer, Berlin. https://doi.org/10.1007/978-3-642-36932-2

Douša J et al (2018) A two-stage tropospheric correction model combining data from GNSS and numerical weather model. GPS Solutions 22(3):77. http://link.springer.com/10.1007/s10291-018-0742-x. Accessed 13 Jul 2018

Landskron D (2017) Modeling tropospheric delays for space geodetic techniques. Technischen Universität Wien, Wien. https://resolver.obvsg.at/urn:nbn:at:at-ubtuw:1-100249

Leandro RF, Santos MC, Langley RB (2007) GAPS: the GPS analysis and positioning software – a brief overview. http://gaps.gge.unb.ca/publications/iongnss2007.leandro.gaps.pdf. Accessed 20 Sept 2017

Masoumi S et al (2017) A directional model of tropospheric horizontal gradients in Global Positioning System and its application for particular weather scenarios. J Geophys Res Atmos 122(8):4401–4425. https://doi.org/10.1002/2016JD026184. Accessed 19 Nov 2017

Niell A, Petrov L (2003) Using a numerical weather model to improve Geodesy. In: Proceedings of 'The State of GPS Vertical Positioning Precision: Separation of Earth Processes by Space Geodesy' meeting held in April 2003 in Luxemburg. http://arXiv.org/physics/0401118

Nievinski FG, Santos MC (2010) Ray-tracing options to mitigate the neutral atmosphere delay in GPS. Geomatica 64(2):191–207

Nikolaidou T et al (2018) Impact of different NWM-derived mapping functions on VLBI and GPS analysis introduction and background. Earth Planets Space 70:95. https://doi.org/10.1186/s40623-018-0865-x. Accessed 18 Jul 2018

Nilsson T et al (2013) Path delays in the neutral atmosphere. Springer, Berlin, pp 73–136. https://doi.org/10.1007/978-3-642-36932-2_3. Accessed 22 Sept 2017

Petit G, Luzum B (2010) International Earth rotation and reference systems service (IERS) service international de la rotation terrestre et desSys emes de Référence IERS conventions (2010), Frankfurt am Main. https://www.iers.org/SharedDocs/Publikationen/EN/IERS/Publications/tn/TechnNote36/tn36.pdf;jsessionid=835D089F780AD79FEC5C1A69FD434DB5.live2?__blob=publicationFile&v=1. Accessed 6 Feb 2018

Shi J, Gao Y (2014) A troposphere constraint method to improve PPP ambiguity-resolved height solution. J Navig 67:249–262

Yao Y et al (2017) Enhancing real-time precise point positioning with zenith troposphere delay products and the determination of corresponding tropospheric stochastic models. Geophys J Int 208(2):1217–1230. https://academic.oup.com/gji/article-lookup/doi/10.1093/gji/ggw451. Accessed 20 Mar 2017

Zumberge JF, Heflin MB, Jefferson DC et al (1997) Precise point positioning for the efficient and robust analysis of GPS data from large networks. J Geophys Res Solid Earth 102:5005–5017. https://doi.org/10.1029/96JB03860

Calibration of Empirical Models of Thermospheric Density Using Satellite Laser Ranging Observations to Near-Earth Orbiting Spherical Satellites

Sergei Rudenko, Michael Schmidt, Mathis Bloßfeld, Chao Xiong, and Hermann Lühr

Abstract

The thermosphere causes by far the largest non-gravitational perturbing acceleration of near-Earth orbiting satellites. Especially between 80 km and 1,000 km, the thermospheric density distribution and variations are required to model accurately this acceleration for precise orbit determination (POD), ephemeris computation and re-entry prediction of the Low-Earth Orbiting (LEO) satellites. So far, mostly on-board accelerometers are used to measure the thermospheric density. However, such type of satellite is usually of complex shape and any error or mismodelling in the satellite drag coefficient and satellite effective cross-sectional area will directly propagate into the derived thermospheric density values. At GFZ, an empirical model of the thermospheric mass density denoted as "CH-Therm-2018" has been developed by using 9 years (2001–2009) of CHAMP observations.

A completely different approach for thermospheric density determination is based on using satellite laser ranging (SLR) measurements to LEO satellites equipped with retro-reflectors to determine an accurate satellite orbit. These measurements are sensitive to small perturbations acting on the satellite. In order to minimize the error induced by imprecise satellite macro-models, we use in our investigation SLR observations to satellites with a simple spherical shape and thus, relate estimated scaling factors to the thermospheric density.

In this paper, we use SLR observations to two ANDE-2 satellites – ANDE-Castor and ANDE-Pollux – as well as SpinSat with altitudes between 248 km and 425 km to calibrate the CH-Therm-2018 model, as well as four other empirical models of thermospheric density, namely CIRA86, NRLMSISE00, JB2008 and DTM2013. For our tests, we chose a period from 16 August 2009 to 26 March 2010 of low solar activity and a period from 29 December 2014 to 29 March 2015 of high solar activity. Using data of a few geodetic satellites obtained at the same and different time intervals allows us to investigate the reliability of the scaling factors of the thermospheric densities provided by the models.

S. Rudenko (✉) · M. Schmidt · M. Bloßfeld
Deutsches Geodätisches Forschungsinstitut at the Technische Universität München (DGFI-TUM), Munich, Germany
e-mail: sergei.rudenko@tum.de; mg.schmidt@tum.de; mathis.blossfeld@tum.de; http://dgfi.tum.de

C. Xiong · H. Lühr
Deutsches GeoForschungsZentrum (GFZ) Potsdam, Potsdam, Germany
e-mail: Chao.xiong@gfz-potsdam.de; hluehr@gfz-potsdam.de; http://www.gfz-potsdam.de/en/section/earths-magnetic-field

J. T. Freymueller, L. Sánchez (eds.), *International Symposium on Advancing Geodesy in a Changing World*, International Association of Geodesy Symposia 149, https://doi.org/10.1007/1345_2018_40

We have found that CIRA86 and NRLMSISE00 most significantly overestimate the thermospheric density at the period of low solar activity among the models tested. The JB2008 model is the least scaled model and provides reliable values of the thermospheric density for the periods of both low and high solar activity. The GFZ CH-Therm-2018 model, on the contrary, underestimates the thermospheric density at the time interval of low solar activity. Using SLR observations at longer time intervals should allow to investigate temporal evolution of the scaling factors of these models more precisely.

Keywords
ANDE-2 · Empirical thermosphere models · Precise orbit determination · Satellite Laser Ranging (SLR) · SpinSat · Thermospheric drag

1 Introduction

The non-gravitational acceleration within the equation of motion of a satellite comprises the direct solar radiation pressure, the pressure due to Earth's albedo and infrared radiation pressure, drag-like parts due to the thermospheric drag and the solar wind pressure and other terms, e.g., related to the Earth's magnetic field (Milani et al. 1987) as well as thermal effects related to different temperature values of the satellite surface, such as the Yarkovsky-Rubincam (Rubincam 1987) and the Yarkovsky-Schach (Afonso et al. 1989) effects.

For near-Earth or Low-Earth Orbiting (LEO) satellites – especially between altitudes of 80 km and 1,000 km – the atmospheric drag is the largest non-gravitational perturbation acceleration (Milani et al. 1987) and, thus, the main error source in Precise Orbit Determination (POD) of these satellites. The drag mainly depends on the thermospheric density, which is closely related to the electron density of the ionosphere and, thus, also to space weather activity (Emmert 2015). In the LEO satellite POD, the thermospheric density is presently described by empirical models such as the Jacchia-Bowman 2008 (JB2008) model (Bowman 2008) or the COSPAR International Reference Atmosphere 1986 (CIRA86) model (Hedin et al. 1988), which use globally defined space weather parameters such as the solar radio flux at a wavelength of 10.7 cm (F10.7) and some other parameters. The other two models widely used are NRLMSISE00 (Naval Research Laboratory Mass Spectrometer Incoherent Scatter Radar Extended, Picone 2002) and DTM2013 (Drag Temperature Model, Bruinsma 2015).

In the last two decades, accelerometer instruments and star trackers onboard such LEO satellites like the CHAllenging Minisatellite Payload (CHAMP, Reigber et al. 2002), the Gravity Recovery and Climate Experiment (GRACE, Tapley et al. 2004) and Gravity field and Ocean Circulation Explorer (GOCE, Floberghagen et al. 2011) provided thermospheric density data with a high accuracy and resolution. A review of thermospheric density models can be found in Emmert (2015). Based on 9 years (from August 2000 to July 2009) of CHAMP acceleration measurements covering periods of both high and low solar activities, a new empirical thermospheric mass density model "CH-Therm-2018" (Xiong et al. 2018) has been developed at GFZ.

Satellite data can be used not only to derive models of thermospheric density, but also to validate them. Thus, Doornbos et al. (2005) studied feasibility of using satellite orbit and tracking data for calibration of atmospheric density provided by CIRA-72 model. A detailed analysis of input parameters used by various atmospheric drag models was performed by Vallado and Finkleman (2014). The impact of atmospheric drag on some geodetic spherical satellites at the altitudes of 800–1500 km was discussed by Sośnica (2015). Recently, Bruinsma (2017) found that the DTM2013 model fits best to the thermospheric neutral density derived from GOCE observations from November 2009 to October 2013 at the satellite altitude of 170–275 km.

2 SLR Measurements to LEO Satellites

Satellite Laser Ranging (SLR) is a geodetic tracking technique which can be used for a POD of LEO satellites. SLR provides highly accurate travel time measurements of laser pulses reflected at Retro-Reflector Arrays (RRA) mounted on the satellite surface which have been emitted from telescopes on the Earth's surface. Due to the high precision [1–3 mm for a normal point for a geodetic satellite (Combrinck 2010)] SLR observations are highly sensitive to any perturbing acceleration acting on the satellite and, thus, to the atmospheric drag. An analysis of SLR observations to spherical (cannon-ball) satellites can be used to calibrate thermospheric density computed using various thermospheric density models and, therefore, to validate respective models (Panzetta et al. 2018). In order to increase the accuracy of estimated thermospheric density, we use in this investigation SLR observations to LEO satellites again

Table 1 The main parameters of the three applied satellites: COSPAR ID, diameter (D), mass (m), the ratio of the cross-sectional area of the satellite to its mass (A_{ref}/m), center-of-mass correction (CoM), drag coefficient (C_D) computed using the JB2008 model, initial altitude (h), orbit inclination (i) and the period of the SLR data availability

Satellite name	COSPAR ID	D (m)	m (kg)	A_{ref}/m (m^2/kg)	CoM (m)	C_D (–)	h (km)	i (°)	SLR data availability Start	End
ANDE-P	0903805	0.4826	27.442	0.006666	0.224	2.1149±0.0015	350	51.6	4 Aug. 2009	16 Mar. 2010
ANDE-C	0903806	0.4826	47.450	0.003855	0.225	2.1145±0.0016	350	51.6	4 Aug. 2009	1 Aug. 2010
SpinSat	9806714	0.5580	52.650	0.004645	0.264	2.1261±0.0023	425	51.6	12 Dec. 2014	31 Jan. 2017

of spherical shape, since the computation of air drag of such satellites is easier and more accurately than that one of satellites of complex form requiring precise information on the satellite macro-model and satellite orientation in space (Rudenko et al. 2017).

We use in our study the two satellites "Atmospheric Neutral Density Experiment-2" (ANDE-2) "Pollux" (P) and "Castor" (C) (Nicholas et al. 2009), as well as the "Special Purpose Inexpensive Satellite" (SpinSat, Nicholas et al. 2013). The ANDE-P and ANDE-C satellites were launched on 30 July 2009 from the Space Shuttle at the altitude of 350 km.[1] The SpinSat was deployed from the International Space Station (ISS) on 28 November 2014 at the altitude of 425 km.[2] All three satellites were sponsored by the Naval Research Laboratory and launched in near-circular orbits with an inclination of about 51.6° to the Earth's equator with the purpose to determine total thermospheric neutral density. SpinSat was used also for tests of spin control of the spacecraft using dedicated thrusters. The main parameters of these satellites are given in Table 1. Due to high air drag at these relatively low attitudes the duration of these missions was relatively short: about 8, 12 and 25 months of ANDE-P, ANDE-C and SpinSat, respectively. Thus, the ANDE-P spacecraft re-entered the Earth's atmosphere end of March 2010. The ANDE-C mission ended in August 2010, and SpinSat re-entered the Earth's atmosphere on 11 March, 2017.

Our approach is based on a fully dynamic POD of the selected spherical satellites using the DGFI Orbit and Geodetic parameter estimation Software (DOGS) (Gerstl 1997; Bloßfeld 2015). All a priori models used in the POD are based on the recommendations of the IERS Conventions 2010 (Petit and Luzum 2010). Based on the results obtained by Rudenko et al. (2018), DTRF2014 (Seitz et al. 2016) has been selected as a realization of the Terrestrial Reference System. More details on the applied POD approach and dynamical models used are given in Panzetta et al. (2018).

[1] https://ilrs.cddis.eosdis.nasa.gov/missions/satellite_missions/past_missions/anda_general.html.

[2] https://ilrs.cddis.eosdis.nasa.gov/missions/satellite_missions/past_missions/spin_general.html.

For the LEO POD, we model in our approach the thermospheric drag $\boldsymbol{a}_{\text{drag}}$ as

$$\boldsymbol{a}_{\text{drag}} = -\frac{1}{2}\, f_s\, \frac{A_{\text{ref}}}{m}\, C_D\, \rho_M\, v_{\text{rel}}^2\, \boldsymbol{u}_D, \tag{1}$$

where $\boldsymbol{u}_D$ is the drag unit vector, v_{rel} is the satellite velocity with respect to the atmosphere, A_{ref} is the effective cross-sectional area of the satellite, m is the satellite mass, C_D is the dimensionless drag coefficient, f_s is the scaling factor and ρ_M is the thermospheric neutral density provided by a model. The A_{ref}/m ratio is constant for a spherical passive satellite. The $\boldsymbol{a}_{\text{drag}}$, v_{rel} values and $\boldsymbol{u}_D$ are determined from satellite POD. C_D is computed using a Gas-Surface Interaction model taking into account constituents of thermosphere at a satellite position (Panzetta et al. 2018). Therefore, a scaling factor f_s can be derived from Eq. (1).

We apply in this study five empirical models of the thermospheric density (CIRA86, NRLMSISE00, JB2008, DTM2013 and CH-Therm-2018) for the POD of three LEO satellites (ANDE-P, ANDE-C and SpinSat) – different models for different satellites. The Horizontal Wind Model 2014 (Drob et al. 2015) is included for all five models. The scaling factor f_s in Eq. (1) accounts for the different magnitude of the density values computed from different models of thermospheric density. We estimate the scaling factor f_s according to Eq. (1) with a temporal resolution of 6–12 h depending on the amount of SLR observations available at the periods, when the number of observations exceeds the number of estimated parameters. The list of the parameters estimated at each orbital arc additionally includes six Keplerian elements. Since no precise information on the optical properties of the satellite surface is available, we put the satellite reflectivity coefficient to 1.0 for all satellites and estimate additionally one solar radiation pressure coefficient, one Earth's albedo and infrared radiation pressure coefficient, and transversal and normal once-per-revolution cosine and sine empirical accelerations at each arc.

3 Empirical Models of Thermospheric Density

The empirical model of thermospheric mass density, named "CH-Therm-2018", is derived using 9-year (2001–2009) data

from the CHAMP mission. Seven "key" parameters, height (h), solar flux ($P10.7$), season (DoY, day of year), magnetic local time (mlt), geographic latitude (θ) and longitude (ϕ), and magnetic activity represented by the solar wind merging electric field (E_m), have been taken into account for constructing the model. An exponential function with a constant scale height has been used for describing the height variation of the thermospheric mass density, and the solar flux and magnetic activity dependences have been described by using quadratic functions. The dependencies on DoY, mlt, θ and ϕ are described by using trigonometric functions (Xiong et al. 2018). Similar to Liu et al. (2013), a multi-variable least-squares fit has been used for deriving the coefficients from the CHAMP measurements.

The Mass-Spectrometer-Incoherent-Scatter (MSIS) model describes the neutral temperature and density in the upper atmosphere. In the thermosphere, i.e. above about 100 km, the COSPAR International Reference Atmosphere model CIRA86 is identical with MSIS86 (Fleming 1988). NRLMSISE00 (Picone 2002) is another empirical, global model of the Earth's atmosphere based on the earlier models MSIS86 and MSISE90, but updated with actual satellite drag information. The primary use of NRLMSISE00 is to compute predictions of the satellite orbital decay due to atmospheric drag.

The empirical atmospheric density Jacchia-Bowman 2008 (JB2008) model was developed as an improved version of the Jacchia-Bowman 2006 model which is based on Jacchia's diffusion equations (Bowman 2008). JB2008 is based on orbit-derived density data collected within the years 1997–2007 in the altitude range of 175–1,000 km. The model is valid for altitudes larger than 90 km and years starting from 1997.

The DTM2013 model is based on orbit- and accelerometer-derived data as well as optical spectrometer measurements from the years 1961 to 2012. It is valid for altitudes larger than 120 km.

All the four empirical models introduced before are amongst other quantities, driven by globally defined space weather parameters such as the F10.7 (reflecting solar activity) and the K_p (reflecting magnetic activity) indexes as well as other parameters such as local time and position; for more details on the models see e.g. Emmert (2015).

4 Results

We have processed SLR observations to the ANDE-C satellite at a 220-day time interval from 16 August 2009 to 26 March 2010 (satellite altitude range of 297–350 km) using four empirical models of thermospheric density: CIRA86, NRLMSISE00, DTM2013 and JB2008. We have chosen this time interval of the ANDE-C mission, since it contains more SLR observations than the remaining part. Figure 1 shows the estimates of the scaling factor f_s from ANDE-C SLR measurements using these models. A few gaps in the estimated scaling factors in Figs. 1, 2, 3, and 4 are caused by the gaps in the SLR observations for the respective satellites not allowing estimation of these parameters at such periods of time. The JB2008 model shows the median (mean) value of 0.980 (0.974) of f_s that is most close to 1 indicating that this model is the least scaled model among the four thermospheric models tested for this satellite (Table 2). The smallest standard deviation (0.159) of the estimated scaling factors is obtained for DTM2013 and the largest one (0.213) is computed for JB2008. The two MSIS models CIRA86 and NRLMSISE00 give very similar results for the mean (0.678), median (0.652, 0.657), RMS (0.706, 0.707) and standard deviations (0.195, 0.200) of the estimated scaling factors. The mean values of the scaling factors of the four thermospheric models obtained by us using SLR observations to the ANDE-C satellite at the time interval from 16 August 2009 to 26 March 2010 agree very well (within 8.8% for JB2008 and 4.0–4.7% for three other models and well within the standard deviations) with those obtained for the same models using SLR measurements to the ANDE-P satellite at an overlapping 49-day time interval from 16 August 2009 to 3 October 2009 (satellite altitude range of 248–369 km, Fig. 2). In fact, both satellites were flying at the same time at a similar altitude in close parts of the space. The scaling factors obtained from the ANDE-C satellite (Table 2) indicate smaller standard deviations than those obtained from the ANDE-P satellite (Table 3). This is, most probably, due to a doubled step size for the f_s estimation (12 h instead of 6 h) for ANDE-C at the major part of the time interval. Using the 0.6-year time interval from 2009.63 to 2010.23 we have estimated a linear trend of the scaling factors for each model that ranges from 0.360/year for DTM2013 up to 0.762/year for JB2008 (Table 2).

Figure 3 shows the estimated scaling factors f_s for the CH-Therm-2018 model applied in the ANDE-P POD at a 46-day time interval from 16 August to 30 September 2009, as compared to those obtained using the JB2008 model at the same time interval. Whereas the estimated scaling factor values for the JB2008 model are mostly less than 1 (median of 0.874, mean of 0.861 with a standard deviation of 0.261), the corresponding scaling factor values for the CH-Therm-2018 model are larger than 1 (median of 1.267, mean of 1.401, with a standard deviation of 0.597). The larger variability of the CH-Therm-2018 model is probably due to the parameterization with E_m for the magnetic activity, which is more variable than K_p used for other models.

We have processed additionally SLR observations to SpinSat at a 91-day time interval from 29 December 2014 to 29 March 2015 and altitude range of 393–425 km by using CIRA86, NRLMSISE00 and JB2008 thermospheric density

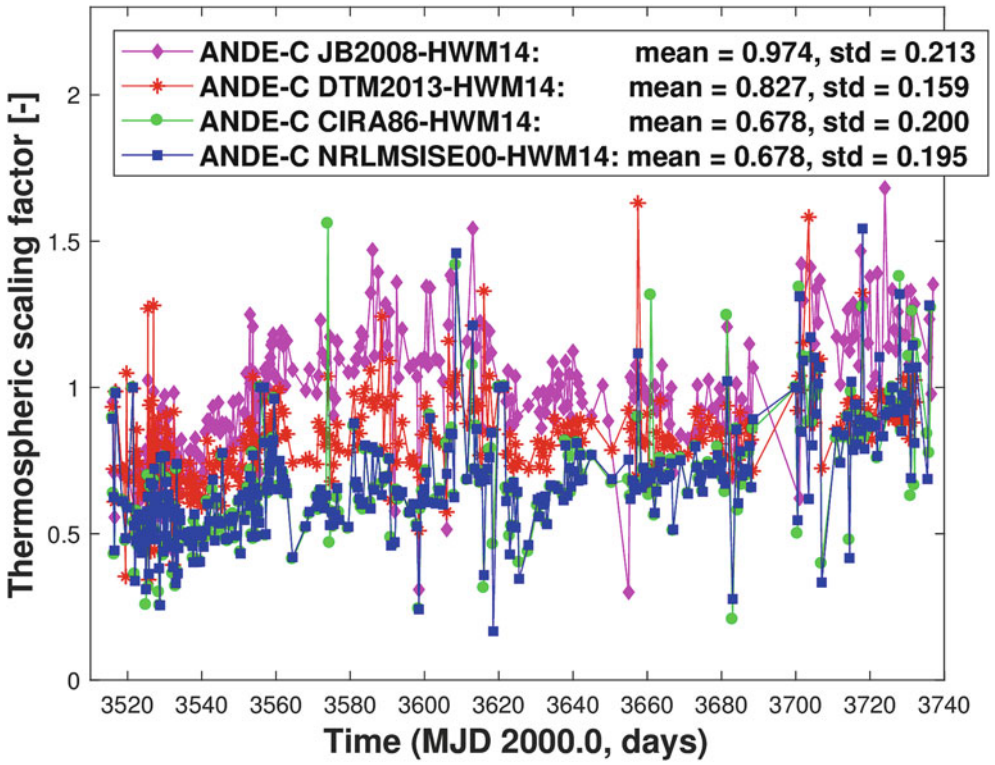

Fig. 1 Scaling factors f_s for CIRA86, NRLMSISE00, DTM2013 and JB2008 models estimated from ANDE-C SLR measurements from 16 August 2009 to 26 March 2010

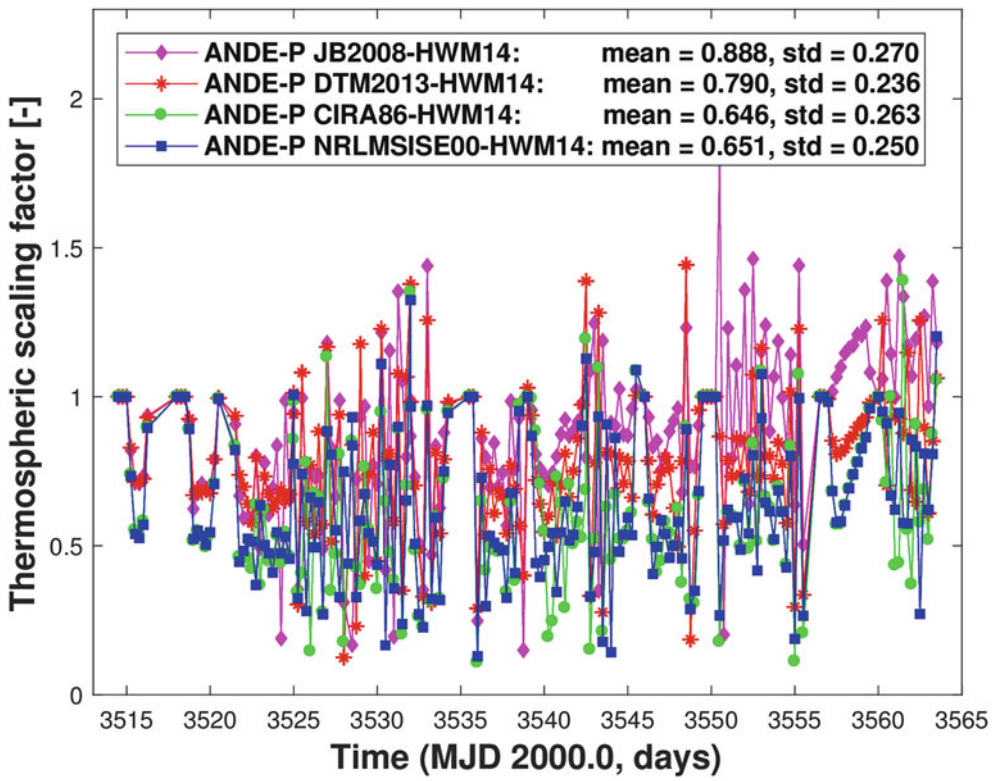

Fig. 2 Scaling factors f_s for CIRA86, NRLMSISE00, DTM2013 and JB2008 models estimated from ANDE-P SLR measurements from 16 August 2009 to 3 October 2009

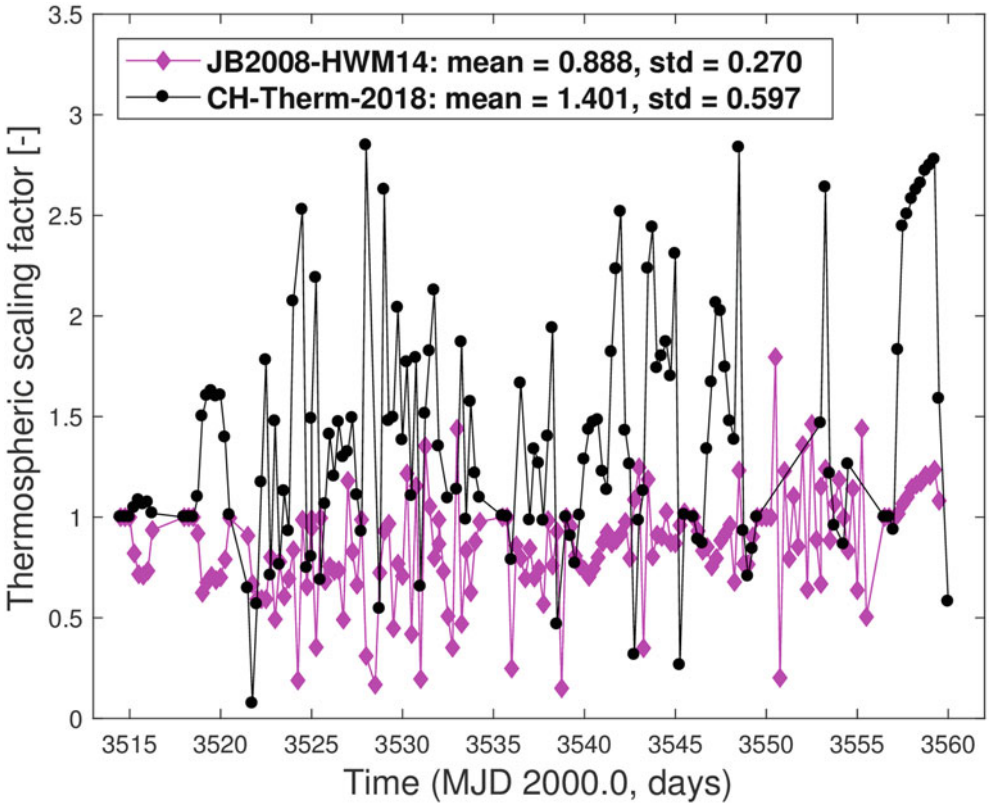

Fig. 3 Scaling factors f_s according to Eq. (1) estimated from ANDE-P POD using the JB2008 (blue) and CH-Therm-2018 (red) models for the 46 days from 16 August to 30 September 2009

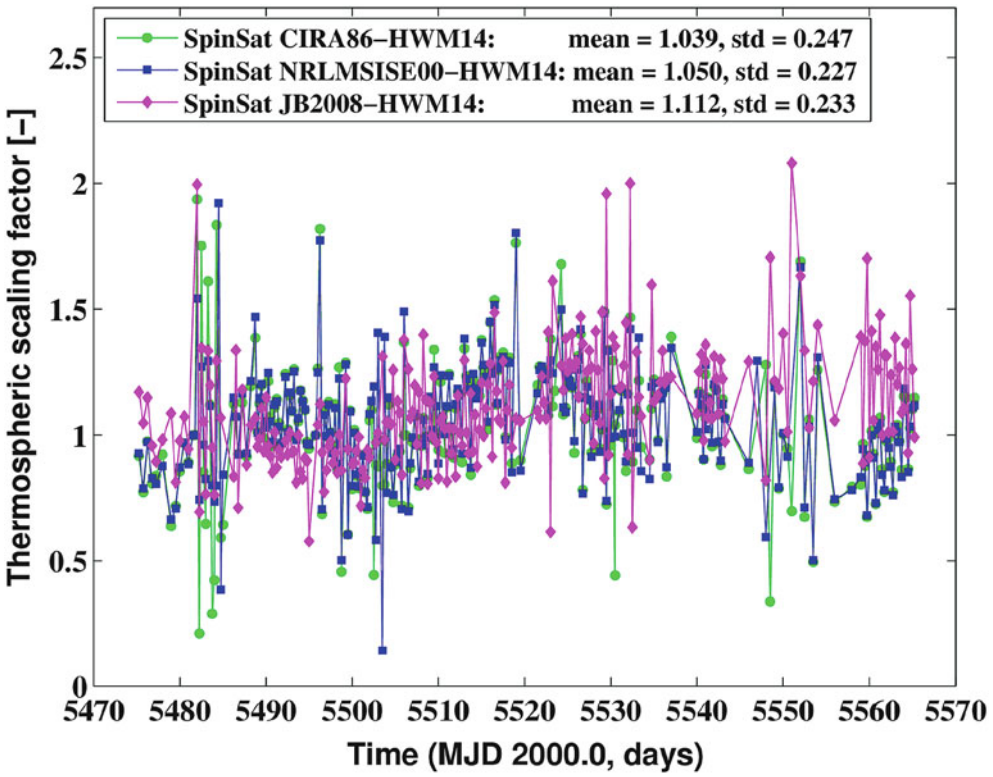

Fig. 4 Scaling factors f_s for CIRA86, NRLMSISE00 and JB2008 models estimated from SpinSat SLR measurements from 29 December 2014 to 29 March 2015

Table 2 Mean, median, RMS, standard deviation (STD) and trend of the scaling factors f_s for each thermospheric model (the wind model HWM14 is included) estimated using SLR observations to ANDE-C from 16 August 2009 to 26 March 2010

Thermospheric model	Mean (f_s)	Median (f_s)	RMS (f_s)	STD (f_s)	Trend (year^{-1})
CIRA86	0.678	0.652	0.707	0.200	0.560
NRLMSISE00	0.678	0.657	0.706	0.195	0.570
DTM2013	0.827	0.825	0.842	0.159	0.360
JB2008	0.974	0.980	0.997	0.213	0.762

Table 3 Mean, median, RMS and standard deviations (STD) of the scaling factors f_s for each thermospheric model (the wind model HWM14 is included) estimated using SLR observations to ANDE-P from 16 August to 3 October 2009

Thermospheric model	Mean (f_s)	Median (f_s)	RMS (f_s)	STD (f_s)
CIRA86	0.646	0.610	0.697	0.263
NRLMSISE00	0.651	0.595	0.697	0.250
DTM2013	0.790	0.790	0.825	0.236
JB2008	0.888	0.908	0.928	0.270
CH-Therm-2018	1.401	1.267	1.523	0.597

Table 4 Mean, median, RMS and standard deviations (STD) of the scaling factors f_s for each thermospheric model (the wind model HWM14 is included) estimated using SLR observations to SpinSat from 29 December 2014 to 29 March 2015

Thermospheric model	Mean (f_s)	Median (f_s)	RMS (f_s)	STD (f_s)
CIRA86	1.039	1.024	1.068	0.247
NRLMSISE00	1.050	1.038	1.074	0.227
JB2008	1.112	1.070	1.136	0.233

models. The scaling factors f_s computed by processing these data are shown in Fig. 4 indicating some periodical variations. The median (mean) values of the scaling factors range from 1.024 (1.039) for CIRA86 to 1.070 (1.112) for JB2008 (Table 4). Similar to the scaling factors derived from the ANDE-C data, the mean, median, RMS and standard deviation of the scaling factors of the CIRA86 and NRLMSISE00 models derived from SpinSat data are close to each other. At the same time, the mean, median, RMS and standard deviation of the scaling factors for CIRA86, NRLMSISE00 and JB2008 derived from SpinSat data for January to March 2015 are larger than those obtained using ANDE-C data for August 2009 to March 2010 (Table 2). This is in a good agreement with the results of Emmert et al. (2010) who found that during 2007–2009 the thermospheric densities at an altitude of 400 km were about 10–30% lower, compared with the values given by thermospheric models. With the increase of solar activity in 2010 (Fig. 5) the deficits of the models become smaller again. The increased standard deviations of the scaling factors obtained from SpinSat for December 2014 to March 2015, as compared to those obtained from ANDE-C for August 2009 to March 2010 are, most probably, due to the higher level of solar activity in the former time interval, as compared to that one in the later one. At the same time, the NRLMSISE00 model provides smaller scatter and therefore a smaller standard deviation of the estimated scaling factor for both time intervals (Tables 2 and 4), as compared to the CIRA86 model, indicating an improved quality of the NRLMSISE00 model.

5 Discussion, Summary and Outlook

From the analysis of SLR observations to the three spherical satellites ANDE-C, ANDE-P and SpinSat, we have computed the median and mean values of the estimated scaling factors of thermospheric density of five empirical models. We have found the following median (mean) values of the scaling factor of the CIRA86 model: 0.65 (0.68)±0.20 with a trend of 0.56/year from the analysis of ANDE-C observations from 16 August 2009 to 26 March 2010 and 1.02 (1.04)±0.25 by analyzing SpinSat observations from 29 December 2014 to 29 March 2015. The median (mean) value of the scaling factor for the NRLMSISE00 model is 0.66 (0.68)±0.20 with a trend of 0.57/year from the analysis of ANDE-C data from 16 August 2009 to 26 March 2010 and 1.04 (1.05)±0.23 from the analysis of SpinSat data from 29 December 2014 to 29 March 2015. The median (mean) value of the scaling factor for the JB2008 model is 0.98 (0.97)±0.21 with a trend of 0.76/year from the ANDE-C data from 16 August 2009 to 26 March 2010 and 1.07 (1.11)±0.23 from the SpinSat data from 29 December 2014 to 29 March 2015. The lower values of the thermospheric scaling factors obtained for CIRA86, NRLMSISE00 and JB2008 for August 2009 to March 2010 as compared to those ones derived for January to March 2015 indicate lower thermospheric density obtained from the observations as compared to that one computed using the models at the former period of low solar activity, as compared to that one in the later period. One should also keep in mind the different altitude of the satellites (about 297–350 km for ANDE-C and 393–425 km for SpinSat) used to derive the thermospheric scaling factors for these models. So, this indicates that the scaling factors of various thermospheric models can differ for different heights and levels of solar activity. The median and mean values of the scaling factor for DTM2013 is 0.83±0.16 with a trend of 0.36/year from the ANDE-C data from 16 August 2009 to 26 March 2010. The analysis of ANDE-P data from 16 August 2009 to 30 September 2009 reveals the following median (mean) values of the scaling factors of the JB2008 and CH-Therm-2018 models: 0.87 (0.86)±0.26 and 1.27 (1.40)±0.60, respectively.

The results obtained indicate that analysis of SLR observations to spherical satellites at the altitude of 297–425 km

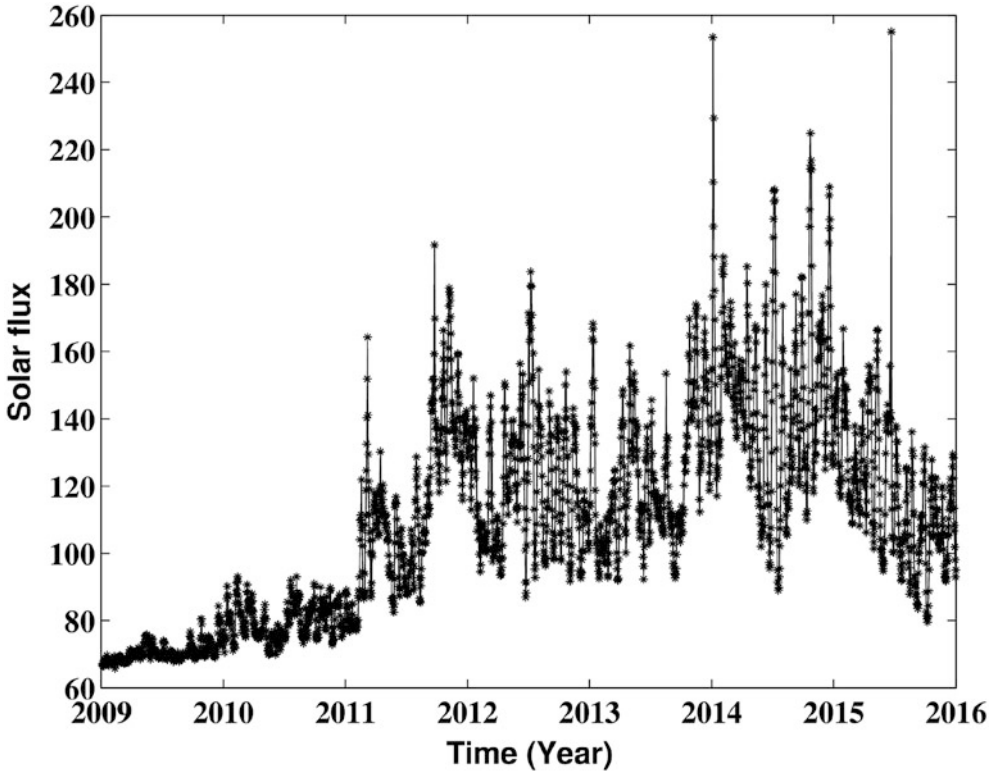

Fig. 5 Daily mean of the solar radio flux (in solar flux units) at 10.7 cm (2800 MHz)

can be used to calibrate thermospheric density provided by empirical models. The scaling factor of each model changes depending on the level of solar activity and satellite altitude. Moreover, the trend values obtained reflect just the time interval analyzed. Therefore, extending the time intervals of the analysis for these satellites for the thermospheric density models of our interest and using additionally SLR measurements to, e.g., the "Atmospheric Neutral Density Experiment Risk Reduction" (ANDE-RR) satellites that were in orbit in 2007–2008 at the altitude of 400 km downwards can provide more knowledge on the mean and median values of scaling factors and their temporal evolution.

Acknowledgements This study was performed within the project "Interactions of Low-orbiting Satellites with the Surrounding Ionosphere and Thermosphere (INSIGHT)" funded by the German Research Foundation (DFG) in the framework of the Special Priority Programme 1788 "Dynamic Earth". We are grateful to two anonymous reviewers and Editor-in-Chief for their comments that allowed us to improve this paper.

References

Afonso G, Barlier F, Mignard F, Carpino M, Farinella P (1989) Orbital effects of LAGEOS seasons and eclipses. Ann Geophys 7:501–514

Bloßfeld M (2015) The key role of Satellite Laser Ranging towards the integrated estimation of geometry, rotation and gravitational field of the Earth. PhD Dissertation, Technische Universität München (TUM), Munich

Bowman BR, Tobiska WK, Marcos FA, Huang CY, Lin CS, Burke WJ (2008) A new empirical thermospheric density model JB2008 using new solar and geomagnetic indices. In: AIAA/AAS astrodynamics specialist conference and exhibit, AIAA 2008-6438

Bruinsma SL (2015) The DTM-2013 thermosphere model. J Space Weather Space Clim 5(A1). https://doi.org/10.1051/swsc/2015001

Bruinsma S, Arnold D, Jäggi A, Sánchez-Ortiz N (2017) Semi-empirical thermosphere model evaluation at low altitude with GOCE densities. J Space Weather Space Clim 7(A4). https://doi.org/10.1051/swsc/2017003

Combrinck L (2010) Satellite laser ranging. In: Xu G (ed) Sciences of geodesy - I. Springer, Berlin/Heidelberg. https://doi.org/10.1007/978-3-642-11741-1_9

Doornbos E, Klinkrad H, Visser P (2005) Atmospheric density calibration using satellite drag observations. Adv Space Res 36(3):515–521. https://doi.org/10.1016/j.asr.2005.02.009

Drob DP, Emmert JT, Meriwether JW, Makela JJ, Doornbos E, Conde M, Hernandez G, Noto J, Zawdie KA, McDonald SE, Huba JD, Klenzing JH (2015) An update to the Horizontal Wind Model (HWM): the quiet time thermosphere. Earth Space Sci 2(7):301–319. https://doi.org/10.1002/2014EA000089

Emmert JT (2015) Thermospheric mass density: a review. Adv Space Res 56:773–824. https://doi.org/10.1016/j.asr.2015.05.038

Emmert JT, Lean JL, Picone JM (2010) Record-low thermospheric density during the 2008 solar minimum. Geophys Res Lett 37:L12102. https://doi.org/10.1029/2010GL043671

Fleming EL, Chandra S, Shoeberl M-R, Barnett JJ (1988) Monthly mean global climatology of temperature, wind, geopotential height and pressure for 0–120 km. National Aeronautics and Space Administration, Technical Memorandum 100697, Washington, DC

Floberghagen, R, Fehringer, M, Lamarre, D, et al (2011) Mission design, operation and exploitation of the gravity field and steady-state ocean circulation explorer mission. J Geod 85:749–758. https://doi.org/10.1007/s00190-011-0498-3

Gerstl M (1997) Parameterschätzung in DOGS-OC. In: DGFI Interner Bericht, MG/01/1996/DGFI, 2nd edn (in German)

Hedin AE, Spencer NW, Killeen TL (1988) Empirical global model of upper thermosphere winds based on Atmosphere and Dynamics Explorer satellite data. J Geophys Res 93:9959–9978. https://doi.org/10.1029/JA093iA09p09959

Liu H, Hirano T, Watanabe S (2013) Empirical model of the thermosphereic mass density based on CHAMP satellite observation. J Geophys Res Space Phys 118:843–848. https://doi.org/10.1002/jgra.50144

Milani A, Nobili AM, Farinella P (1987) Non-gravitational perturbations and satellite geodesy. Adam Hilger, Bristol, 125 pages

Nicholas AC, Finne T, Davis MA, Kessel R (2009) Atmospheric Neutral density Experiment (ANDE-2) flight hardware details, 26 May 2009. http://ilrs.gsfc.nasa.gov/docs/andehw.pdf

Nicholas A, Finne T, Galysh I, Mai A, Yen J, Sawka W, Ransdell J, Williams S (2013) SpinSat mission overview. In: Proceedings of the 27th AIAA/USU conference, small satellite constellations, Logan, UT, 10–15 Aug 2013, paper: SSC13-I-3. http://digitalcommons.usu.edu/cgi/viewcontent.cgi?article=2911&context=smallsat

Panzetta F, Bloßfeld M, Erdogan E, Rudenko S, Schmidt M, Müller H (2018) Towards thermospheric density estimation from SLR observations of LEO satellites - a case study with ANDE-Pollux satellite. J Geod, https://doi.org/10.1007/s00190-018-1165-8

Petit G, Luzum B (2010) IERS conventions (2010), Technical note 36. Verlag des Bundesamts für Kartographie und Geodäsie, Frankfurt. ISBN 3-89888-884-3

Picone JM, Hedin AE, Drob DP, Aikin AC (2002) NRLMSISE-00 empirical model of the atmosphere: statistical comparisons and scientific issues. J Geophys Res Space. https://doi.org/10.1029/2002JA009430

Reigber C, Lühr H, Schwintzer P (2002) CHAMP mission status. Adv Space Res 30:129–134. https://doi.org/10.1016/S0273-1177(02)00276-4

Rubincam D (1987) LAGEOS orbit decay due to Infrared radiation from Earth. J Geophys Res Solid Earth 92(B2):1287–1294. https://doi.org/10.1029/JB092iB02p01287

Rudenko S, Neumayer K-H, Dettmering D, Esselborn S, Schöne T, Raimondo J-C (2017) Improvements in precise orbits of altimetry satellites and their impact on mean sea level monitoring. IEEE Trans Geosci Remote Sens 55(6):3382–3395. https://doi.org/10.1109/TGRS.2017.2670061

Rudenko S, Bloßfeld M, Müller H, Dettmering D, Angermann D, Seitz M (2018) Evaluation of DTRF2014, ITRF2014 and JTRF2014 by precise orbit determination of SLR satellites. IEEE Trans Geosci Remote 56(6):3148–3158. https://doi.org/10.1109/TGRS.2018.2793358

Seitz M, Bloßfeld M, Angermann D, Schmid R, Gerstl M, Seitz F (2016) The new DGFI-TUM realization of the ITRS: DTRF2014 (data). Deutsches Geodätisches Forschungsinstitut, Munich. https://doi.org/10.1594/PANGAEA.864046 (Open Access)

Sośnica K (2015) Impact of the atmospheric drag on Starlette, Stella, Ajisai, and Lares orbits. Artif. Satell. 50(1):1–18. https://doi.org/10.1515/arsa-2015-0001

Tapley BD, Bettadpur S, Watkins M, et al (2004) The gravity recovery and climate experiment: mission overview and early results. Geophys Res Lett 31:L09607. https://doi.org/10.1029/2004GL019920

Vallado DA, Finkleman D (2014) A critical assessment of satellite drag and atmospheric density modeling. Acta Astronaut 95:141–165. https://doi.org/10.1016/j.actaastro.2013.10.005

Xiong C, Lühr H, Schmidt M, Bloßfeld M, Rudenko S (2018) An empirical model (CH-Therm-2018) of the thermospheric mass density derived from CHAMP. Ann Geophys Discuss. https://doi.org/10.5194/angeo-2018-25, in review

Geodetic Remote Sensing of Ionosphere in Relation to Space Weather and Seismic Activity in B&H

Randa Natras and Medzida Mulic

Abstract

Total electron content (TEC), along GNSS signal's path in the ionosphere, is spatially and temporally highly variable. In addition, sudden disturbances in the ionosphere may occur on the global, regional or local level from external sources, such as space weather and seismic activity. Results of TEC investigation for mid-latitude ionosphere over B&H (Bosnia and Herzegovina) during seismic activity of medium intensity ($4 < M < 5$ Richter) and severe geomagnetic storm (St. Patrick's Day in 2015) are presented. Analyses of relevant parameters such as solar wind, interplanetary magnetic field and geomagnetic activity are performed. Different analyses of TEC variations are carried out. Lower and upper bounds (LB and UB) are determined by 15-day running TEC median prior the day of consideration $\pm$ 2*standard deviation. TEC values which exceeded LB and UB are marked as anomalies. TEC_{QUIET} is calculated as mean TEC for five quietest days in a month regarding geomagnetic conditions to observe TEC residuals due to enhanced geomagnetic activity. Direct comparison of TEC values at different stations is also conducted. TEC deviations were in better agreement concerning GNSS stations located close to the epicentre. Both positive and negative anomalies were registered 2 weeks before the earthquake, with higher deviations during 7 days before, at stations located inside the earthquake preparation zone. The potential causes of these anomalies are discussed. Analysis of TEC response to the strongest geomagnetic storm in solar cycle 24 shows TEC deviations from 50% to even 150% compared to TEC_{QUIET}, where "positive ionospheric storm" is observed in the main phase and "negative ionospheric storm" in the recovery phase of the geomagnetic storm.

Keywords

Earthquake · Geomagnetic storm · Ionosphere · Lithosphere-ionosphere coupling · Space weather · Total electron content (TEC)

Abbreviations

B&H	Bosnia and Herzegovina
BiHPOS	Bosnia and Herzegovina Positioning Service
CME	Coronal mass ejection
EPN	EUREF Permanent Network
EQ	Earthquake
GNSS	Global Navigation Satellite System
GS	Geomagnetic storm
LB	Lower bound
SC	Solar cycle
SW	Space weather
TEC	Total electron content
TECU	TEC units
UB	Upper bound
VTEC	Vertical total electron content

R. Natras (✉) · M. Mulic
Department of Geodesy, Faculty of Civil Engineering, University of Sarajevo, Sarajevo, Bosnia and Herzegovina
e-mail: randa.natras@hotmail.com; randa.natras1@gmail.com; randa.natras@tuwien.ac.at; medzida_mulic@gf.unsa.ba

J. T. Freymueller, L. Sanchez (eds.), *International Symposium on Advancing Geodesy in a Changing World*, International Association of Geodesy Symposia 149, https://doi.org/10.1007/1345_2018_49

1 Introduction

Total electron content (TEC) is a complex parameter, which values depend on local time, latitude and longitude, season, geomagnetic conditions, solar activity and 11-year solar cycle. Additional manifestations can introduce sudden TEC disturbances on the global, regional or local level. Rapid global changes of TEC can be caused by space weather, which can lead to scintillations of signals of Global Navigation Satellite Systems (GNSS). Space weather (SW) refers to the dynamic conditions in the space environment between the Sun and Earth (and throughout the solar system) that can affect performance and reliability of space-borne and ground-based technological systems (U.S. National Space Weather Strategy 2015). It can be characterized by several parameters like solar wind, interplanetary magnetic field (IMF), geomagnetic Kp and equivalent Ap indices (Chapman and Bartels 1940), geomagnetic auroral electrojet (AE) index, Dst (disturbance storm time) index (Sugiura 1964). Based on the above-mentioned indices, disturbances in the geomagnetic field, known as geomagnetic storms, can be grouped into weak, moderate or great (Sugiura and Chapman 1960) and severity of storm can be determined (Gonzalez et al. 1994).

The strongest geomagnetic storm (class G4) in the solar cycle (SC) 24 occurred during St. Patrick's Day in 2015 (on 17th March). Several papers studied St. Patrick's Day storm's impact by multi-instrument approach on global level (Astafyeva et al. 2015), different longitudinal sectors (Asian, African, American and Pacific) at middle and low latitudes (Nava et al. 2016), effects on positioning techniques in Norway (Jacobsen and Andalsvik 2016), to mention few.

On the other hand, regional/local disturbances in the ionosphere can be connected to the source of regional/local character. Papers, published during last decades, reported anomalies in electron densities of the ionospheric F2 layer and/or anomaly TEC during preparatory phase (several days before the earthquake) and/or shortly after strong earthquakes (from few minutes to several hours after the earthquake) (Afraimovich et al. 2004; Gulyaeva and Arikan 2016; Gousheva et al. 2008; Liu et al. 2009), to mention few. One of the proposed explanations for this phenomena is the lithosphere-atmosphere-ionosphere coupling mechanism (Pulinets and Boyarchuk 2004; Pulinets and Ouzounov 2011), where an increased emanation of radon (and other gases) from the Earth's crust of an active fault produces the chain of physical processes above the active tectonic fault, which leads to additional ionization in the atmosphere and increase of air temperature. To detect possible ionosphere anomalies due to a seismic activity the running 15-day median (or mean) for TEC is calculated for 15 days preceding the day of consideration (Liu et al. 2006), where positive and negative deviations may be observed.

The previous studies of ionosphere variability over Bosnia and Herzegovina (B&H) include investigation of TEC variations for the period 2014–2015 using GNSS measurements of EUREF Permanent Network (EPN) station SRJV in Sarajevo and sudden TEC anomalies prior and after moderate earthquakes (EQs) around Sarajevo (Mulic and Natras 2018). To analyze TEC anomalies, EPN station ZADA in Croatia located at the similar latitude as SRJV, but outside the earthquake preparation zone, was introduced. The impact of ionosphere variations induced by two strong geomagnetic storms in SC 24 (17th March 2015 and 08th September 2017) on accuracy of precise point positioning of EPN station SRJV was investigated (Horozovic et al. 2018) and first precise ionosphere TEC model for the region of B&H is under development (Natras et al. 2018).

Objectives of the present study were to examine ionosphere variations during a seismic activity and the strongest geomagnetic storm in SC 24. The investigation covers a period before and after a shallow-depth earthquake of medium intensity with magnitude $4 < M < 5$ Richter and St. Patrick's Day geomagnetic storm in 2015. Selected GNSS stations are located near and far away from the epicentre. Some improvements from the previous study (Mulic and Natras 2018) are achieved. More GNSS stations in B&H are used in the present study, as well as indices of solar winds, IMF and geomagnetic activities. GNSS stations are located inside and outside the earthquake preparation zone in order to separate local disturbances in the ionosphere which could be introduced by seismic activity. The last question was to examine the impact of severe space weather event on the ionosphere over B&H during St. Patrick's Day's geomagnetic storm in 2015.

2 Methods and Data

GNSS dual-frequency observation data (GPS + GLONASS) from permanent stations of Bosnia and Herzegovina Positioning Service (BiHPOS) (stations FOCA and BIHA) and EUREF Permanent Network (EPN) in Bosnia and Herzegovina (station SRJV) were used for TEC estimation. Data of solar wind, interplanetary magnetic field and geomagnetic indices were applied to characterize their effect on the Earth as well as space weather-induced disturbances in the ionosphere. For TEC estimation, the ionosphere was approximated with the single-layer model (Schaer 1999) with the assumption that all free electrons were concentrated in an infinitely thin layer at a fixed height of 400 km above the Earth's surface. Carrier phase GNSS measurements of GPS and GLONASS satellite systems were applied. Biases were estimated and reduced from the measurements. TEC calibra-

tion was performed by the Ciraolo methodology (Ciraolo et al. 2007) for every 15 min.

2.1 VTEC Analysis

Study of the lithosphere-ionosphere coupling is presented for medium-intensity earthquakes with epicentre at mountain Treskavica (latitude 43° 37′ 12″ N, longitude 18° 26′ 60″ E) that occurred on 28th February 2015. The first earthquake happened at 09:24 am LT (local time) with the magnitude of 4.2 Richter, the intensity of VI on Mercalli scale (MCS) and shallow deep of 2 km. It was followed by an earthquake of 3.1 Richter and intensity of IV MCS at 10:17 am LT with same shallow deep (Source: the Federal Hydrometeorological Institute Sarajevo). The radius of the earthquake preparation zone (EPZ) was 71 km, estimated by formula (Dobrovolsky et al. 1979):

$$\rho = 10^{0.43M}\text{km} \tag{1}$$

where ρ is radius of the earthquake preparation zone in km, and M is magnitude of earthquake, on Richter scale.

GNSS stations were selected by their distance from the earthquake's epicentre in order to have stations inside and outside the EPZ (Table 1). Two GNSS stations SRJV and FOCA were distributed around earthquake's epicentre (distance ca 30 km), while GNSS station BIHA was in the different part of the country, where earthquake's effects were not felt (ca 250 km from the epicentre). Because two GNSS stations were located in the area of the earthquake's impact and shallow deep was only 2 km, a question was raised up if GNSS-derived VTEC values may reveal anomalies generated by seismic activity in the ionosphere above the earthquake's epicentre. Second study period covered the strongest geomagnetic storm in SC 24 St. Patrick's Day storm, occurred on 17th March 2015.

Different VTEC analyses were performed. To investigate EQ-induced ionosphere anomalies, common statistical analysis was applied (Liu et al., 2006) using lower (LB) and upper bounds (UB) ($\mu \pm 2\sigma$) to detect VTEC anomalies with confidence level of 95%, where μ represents running 15-day VTEC (vertical TEC) mean for 15 days preceding the day of consideration and σ is standard deviations of VTEC. To analyze SW-induced ionosphere anomalies, VTEC variations were compared to non-disturbed VTEC, estimated as mean VTEC for the five quietest days of the month related to geomagnetic activities. In addition, a comparison of VTEC values between different stations was carried out to detect possible local ionosphere anomalies. All of these analyses were applied in both study cases (seismic activity and severe geomagnetic storm) in order to distinguish different anomalies, especially because of a fact that some geomagnetic activity was presented around the period of earthquake's occurrence.

2.2 Data Acquisition

Data of solar wind speed (Vsw) and the vertical component of the interplanetary magnetic field (IMF) Bz were collected from OmniWeb interface of Goddard Space flight centre of NASA: https://omniweb.gsfc.nasa.gov/. Indices of geomagnetic field (GMF) Kp and Ap were obtained from the German Research Centre for Geosciences: ftp://ftp.gfz-potsdam.de/pub/home/obs/kp-ap/wdc/. AE and Dst indices are computed at and obtained from the World Data Center for Geomagnetism in Kyoto together with the list of the international most disturbed and quietest days of a month: http://wdc.kugi.kyoto-u.ac.jp.

3 Results

3.1 Space Weather Indices and Ionosphere TEC Variations for Studied Period

The entire period of investigation is mostly characterized with quiet and moderate conditions in IMF and GMF, followed by few storms, which are more pronounced in the second half of March (from 03/17) (Fig. 1a). Variations of maximum daily VTEC values (around local noon) show variations from 20 to more than 40 TECU at all stations (Fig. 1c). They are more variable during 2 weeks before the EQ (02/28) and on a day of strongest GS occurrence (03/17) as well as few days after it. Direct comparison of VTEC values is presented in Fig. 2. List of the international 10 quietest and 5 most disturbed days in February and March 2015 is given in Table 2.

Table 1 Used GNSS stations, latitude and longitude, distance from EQ epicentre and radius of EPZ

Station	Latitude	Longitude	Distance from EQ epicenter [km]	EPZ [km]
EPN SRJV	43° 51′ 22″ N	18° 22′ 59″ E	27	70
BiHPOS FOCA	43° 30′ 27″ N	18° 46′ 25″ E	29	70
BiHPOS BIHA	44° 48′ 50″ N	15° 52′ 08″ E	245	70

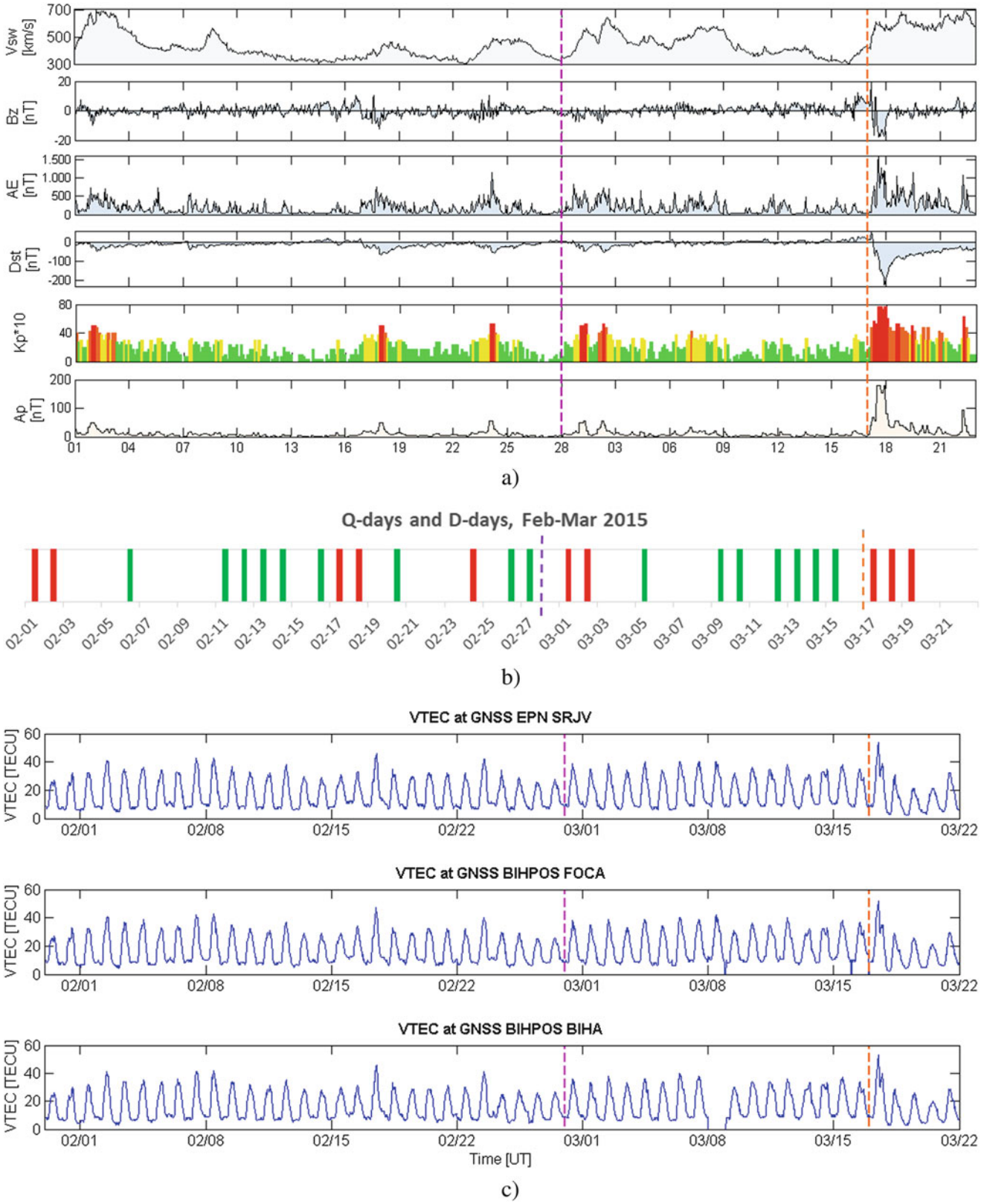

Fig. 1 (**a**) SW indices: Vsw (solar wind speed), Bz component of IMF, AE (auroral electrojet), Dst (disturbance storm time), Kp (Quiet K<3, Moderate 3≤K<4, Active 4≤K<5, Storm 5≤K) and its equivalent Ap. (**b**) International disturbed (D-) and quiet (Q-) days. (**c**) VTEC values estimated from GNSS measurements at stations SRJV, FOCA and BIHA for the study period. Purple line presents the occurrence of EQ Treskavica and orange line presents the occurrence of St. Patrick's GS (when CME hit the Earth)

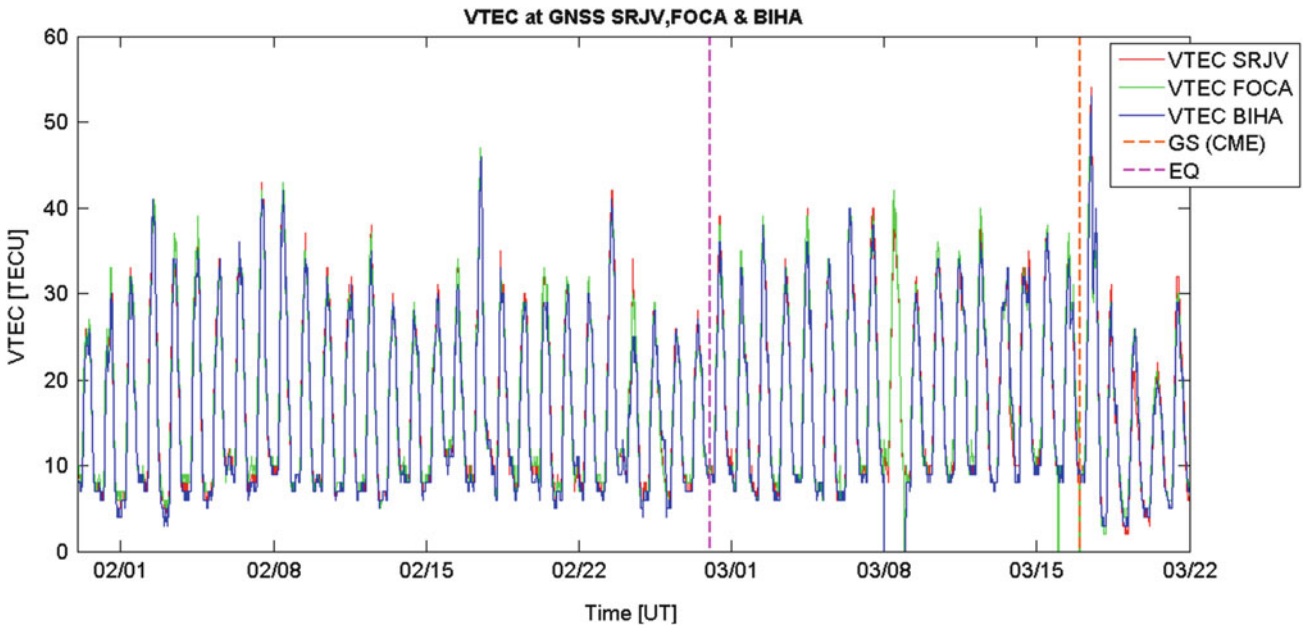

Fig. 2 Direct comparison of VTEC values of three GNSS station (purple line: EQ occurrence, orange line: St. Patrick's GS occurrence, when CME hit the Earth). Some deviations are observed (02/20, 02/24, 02/28, 03/04), which are more visible around EQ occurrence (VTEC at BIHA is smaller than VTEC at FOCA and latter is smaller than VTEC at SRJV during 2 weeks before the EQ and on the day of the EQ occurrence). Data gaps detected at BiHPOS BIHA on 03/08 and at BiHPOS FOCA on 03/15 and 03/17

Table 2 List of the quietest (Q-) days and most disturbed (D-) days, February–March 2015

YYYY	MM	Q1	Q2	Q3	Q4	Q5
2015	02	13	27	14	26	12
		Q6	Q7	Q8	Q9	Q10
		20	16	6	11	15
		D1	D2	D3	D4	D5
		2	24	17	1	18

YYYY	MM	Q1	Q2	Q3	Q4	Q5
2015	03	10	30	5	14	9
		Q6	Q7	Q8	Q9	Q10
		15	13	27	26	12
		D1	D2	D3	D4	D5
		17	18	2	19	1

3.2 VTEC Analysis Before and After Earthquake Treskavica

SW indices (Fig. 3) revealed some moderate and active geomagnetic conditions with storms on the 11th and 10th day (02/17–02/18) as well as on 5th and 4th day (02/23–02/24) before the EQ and after the EQ on 03/01–03/02. Those days were followed by quiet periods. Previously mentioned geomagnetic active days (02/24, 03/01, 03/02) were classified as the most disturbed (Table 2), while 2 days before the EQ were classified as the quietest days of the month.

VTEC variations for 15 days preceding and 7 days after the earthquake of EPN station SRJV and BiHPOS stations FOCA and BIHA are presented on Fig. 4 with calculated upper and lower bounds (UB and LB). Sudden VTEC increase observed on 11th (02/17, D-day) and 5th (02/23) before the earthquake and on the day of the earthquake (D-day) as well as during a night between 13th and 12th day (02/15–02/16, Q-days) when VTEC values exceeded UB. VTEC reached LB on the 4th day (02/24, D-day) before the EQ, during the night from 4th to 3th day (02/24–02/25) and again in the night from 8th to 7th day (02/20–02/21, Q-day). Mentioned variations are recorded on all three stations. Compared to space weather indices moderate geomagnetic activity followed by a storm is recorded on the 11th and 5th day before the EQ and on a day of the EQ. During a night between 13th and 12th day, it was quiet. A day before it, some moderate activity in GMF and IMF was observed for short time and 14th, 13th and 12th day (02/14–02/16) before the EQ was among the quietest days (Q-days) of February 2015 (Table 2). On the 4th day, a storm was presented, while during a night from 8th (Q-day) to 7th before the EQ it was quiet in GMF and IMF.

Differences between VTEC at SRJV, BIHA and FOCA are presented in Fig. 5. Comparison between VTECs of stations FOCA and SRJV (both stations inside EPZ) show better agreement, then when they are compared to VTEC at station BIHA (outside EPZ). Higher variations are observed 4 days before the EQ, when VTEC at FOCA and SRJV showed higher values than VTEC

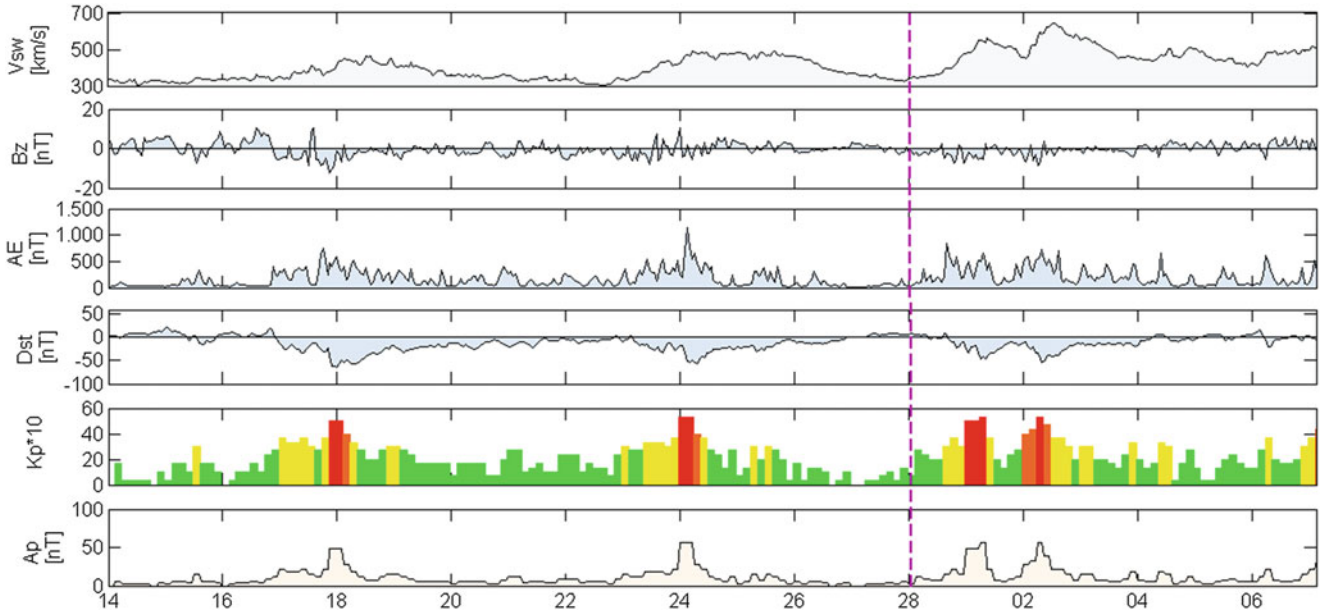

Fig. 3 SW indices for the period 02/14–03/06: Vsw, Bz, AE, Dst, Kp (Quiet K<3, Moderate 3≤K<4, Active 4≤K<5, Storm 5≤K) and Ap. GSs detected on 10th and 4th before the EQ (both D-days) with moderate conditions on 11th, 5th and 3rd day before the EQ. On a day of the EQ moderate conditions are presented followed by GSs on 2nd and 3rd day after. Until the end of a week (to 03/06) moderate conditions are observed

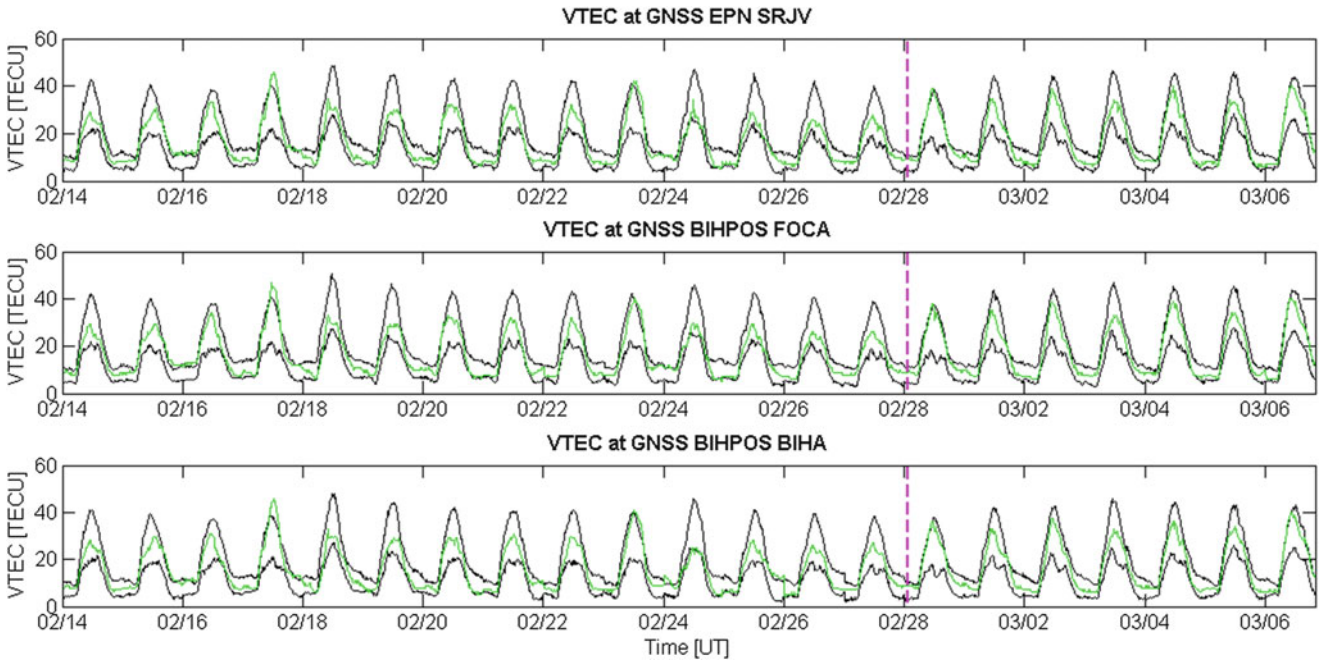

Fig. 4 UB and LB ($\mu \pm 2\sigma$) with VTEC values at GNSS stations SRJV, BIHA and FOCA for 2 weeks before and 1 week after the EQ Treskavica

at BIHA on 02/24 (maximum $VTEC_{(FOCA\text{-}BIHA)} = 7$ TECU and $VTEC_{(FOCA\text{-}BIHA)} = 9$ TECU), followed by VTEC decrease at FOCA and SRJV the following day (differences of VTEC compared to BIHA was −6 TECU in both cases). This represents a change of more than 10 TECU in just 2 days. However, 02/24 was one of the most D-days of the month, thus geomagnetic storm had effects on these significant VTEC variations. Other days with higher VTEC differences are 02/20–02/21 (8th and 7th day before the EQ) ($VTEC_{(FOCA\text{-}BIHA)} = 7$ TECU, $VTEC_{(SRJV\text{-}BIHA)} = 4$ TECU), during quiet conditions in GMF and IMF; 02/16 (12th day before the EQ)

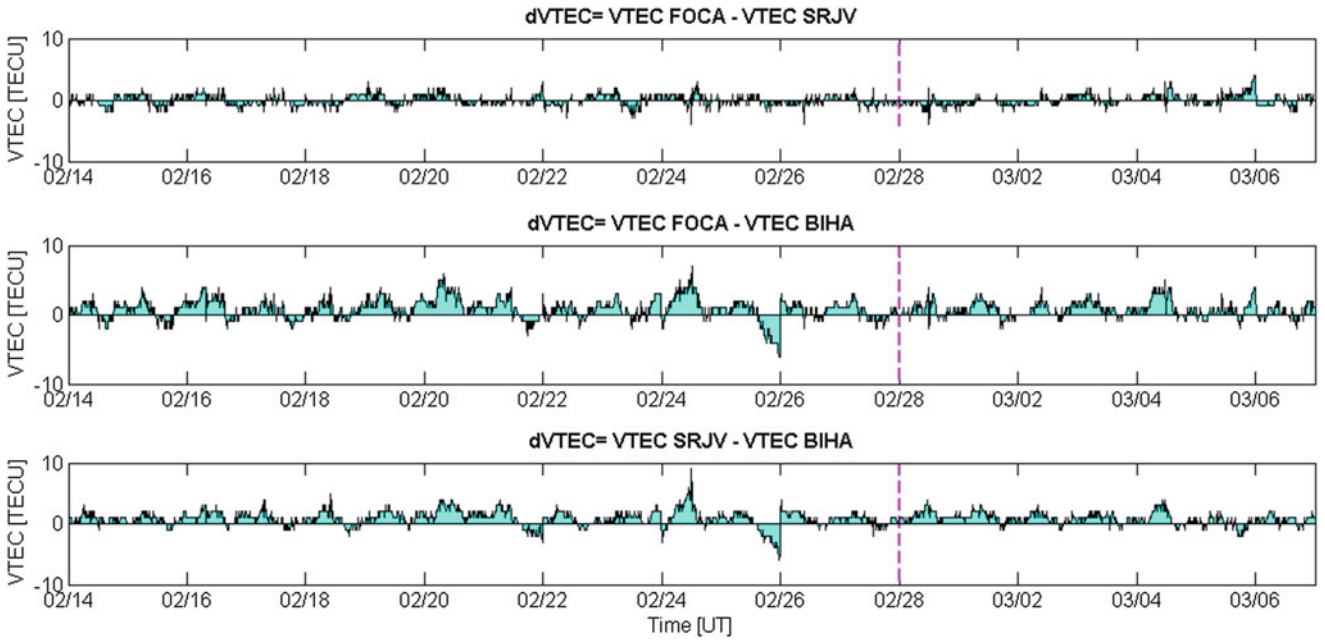

Fig. 5 Mutual differences of VTEC at SRJV, BIHA and FOCA. Better agreement observed between VTEC variations at stations FOCA and SRJV (both stations inside EPZ), but bigger differences are presented if comparing VTEC of those two stations with BIHA (outside EPZ)

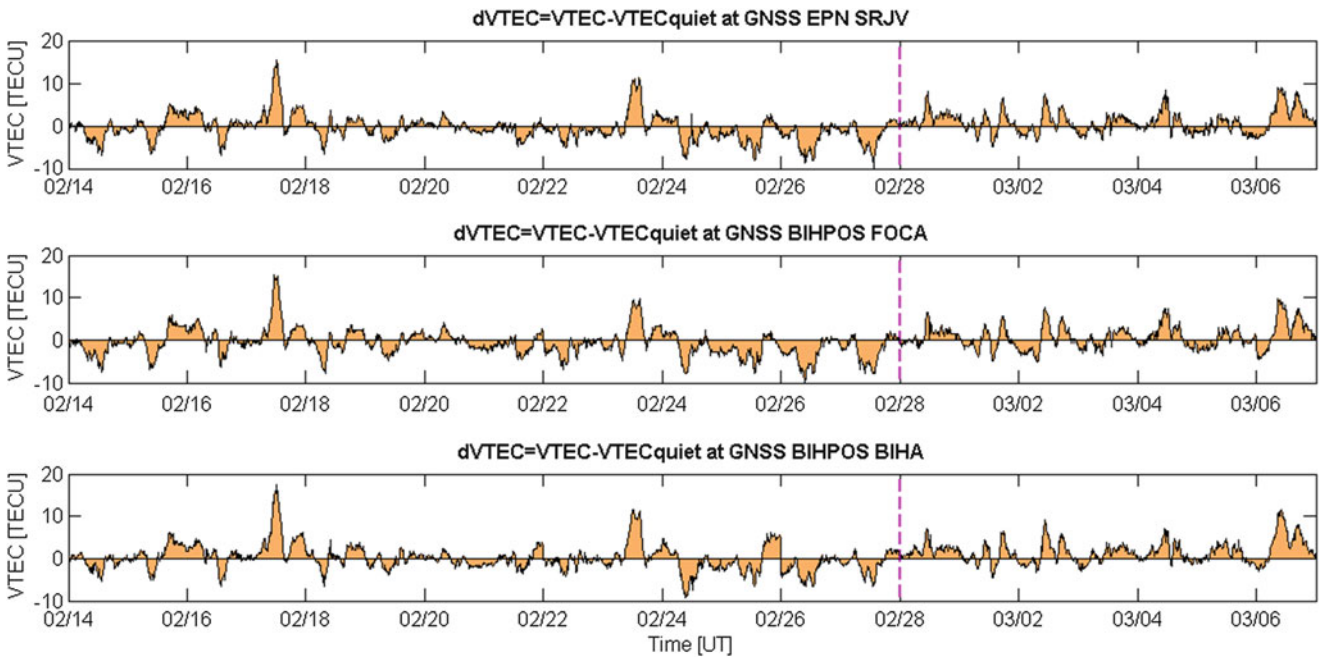

Fig. 6 Differences between observed VTEC and average VTEC calculated for the 5 quietest days ($VTEC_{QUIET}$) for all three stations, which represent VTEC residuals from VTEC variations during the geomagnetic quiet period. Similar residuals indicate that VTEC variations are registered on a wider area, probably caused by the same source such as a geomagnetic storm. However, some differences can be observed, especially 7 days before the EQ

($VTEC_{(FOCA\text{-}BIHA)} = 5$ TECU) one of the quietest day in a month.

Differences between observed VTEC and average VTEC calculated for the 5 quietest days ($VTEC_{QUIET}$) (Table 2) are presented in Fig. 6. These differences represent deviations of VTEC values from VTEC regular variations (without geomagnetic storm impact). Anomalies due to other external sources, such as seismic activity, are not taken in account in this approach, i.e. VTEC mean is calculated based on a list of geomagnetic quiet days without taking in consideration

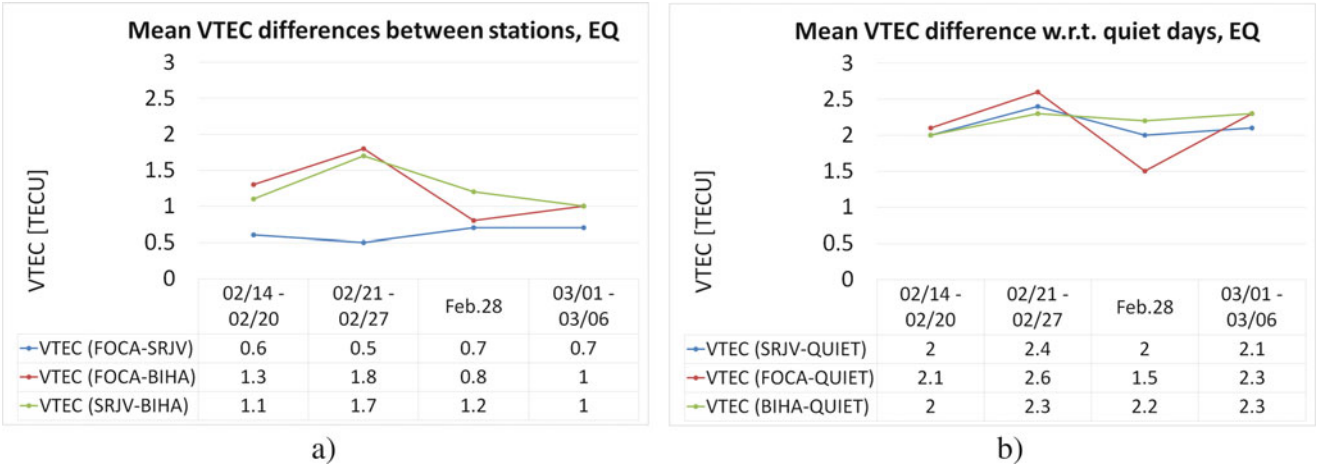

Fig. 7 Statistics: (**a**) mean differences between stations and (**b**) mean differences between observed VTEC and $VTEC_{QUIET}$. Study period (02/14–03/06): the 2nd week before the EQ (02/14–02/20), 1st before the EQ (02/21–02/27), the EQ (02/28) and 1 week after the EQ (03/01–03/06)

were those days affected by other local-induced ionosphere variations. Similar residuals indicate that VTEC anomalies are registered in a wider area, which covered all three stations. Such anomalies can be caused by the same source, such as geomagnetic storm, e.g. 02/17–02/18, 02/23 and 03/01–03/06, which correspond to moderate, active and storm conditions in the geomagnetic field. However, some differences can be observed, e.g. 02/24–02/28 VTEC residuals are for about 3–4 TECU different at BIHA, compared to maximum VTEC residuals at FOCA and SRJV.

During the 2nd week before the earthquake (02/14–02/20) mean VTEC differences between stations FOCA and SRJV were 0.6 TECU, while their mean differences from station BIHA were twice higher, about 1.2 TECU (Fig. 7a). Higher average differences ($VTEC_{(FOCA-BIHA)}$ and $VTEC_{(SRJV-BIHA)}$) were recorded during 1 week before the EQ (of about 1.8 TECU), which is about three times higher than $VTEC_{(FOCA-SRJV)}$ (mutual average difference of about 1 TECU). On the day of the EQ the highest mean differences are between stations SRJV and BIHA (1.2 TECU), but smaller than during a week before. A week after the EQ, mutual average differences are smaller between all stations (0.7–1 TECU). Differences of observed VTEC and mean VTEC during a geomagnetic quiet period (Fig. 7b) show similar mean values at all three station in 2 weeks before and 1 week after the EQ (from 2 to 2.5 TECU). On the day of the EQ, mean VTEC residual at station FOCA decreased to 1.5 TECU. The week after the EQ mean VTEC deviations from $VTEC_{QUIET}$ were again similar (2 to 2.4 TECU). It should be noted that in this approach mean VTEC during quiet conditions in geomagnetic field ($VTEC_{QUIET}$) was calculated without taking in the account which days are containing possible VTEC variations due to other sources, such as seismic activity.

3.3 VTEC Analysis for St. Patrick's Day Geomagnetic Storm

From 17th March expressive increase of wind speed was recorded, from 400 km/s to a maximum of nearly 700 km/s on 18th March (Fig. 8). Except for a brief interruption, the vertical component of the IMF Bz was consistently southward (about −20 nT, 17/03). As a result, severe geomagnetic storm (Kp = 8) lasted the most of the second half of 17/03. Dst index reached −228 nT, representing so far the strongest geomagnetic storm in SC 24. Afterwards, the recovery phase began and lasted few days (from 03/18 to 03/21). Periods of the main and the recovery phase of this intense storm were classified as the most disturbed in the March (17th–19th) (Table 2). Seven days before the GS it was relatively quiet in GMF and IMF, with few moderate conditions.

Before the storm VTEC values are mostly inside LB and UB (Fig. 9), except during night from 03/13 to 03/14, when moderate activity in GMF and IMF was observed in daytime on 03/13. VTEC values exceeded UB for more than 10 TECU during the main phase of the St. Patrick's GS (03/17) and LB during the recovery phase (until 03/20). Gaps of observation data on 03/15 and 03/17 during the night were detected at BiHPOS FOCA.

Higher VTEC differences between stations (Fig. 10) are visible on 03/12 and 03/13 during active conditions in IMF and GMF on all three diagrams, which are more pronounced when compared to BiHPOS BIHA. During the recovery phase, higher VTEC differences (>5 TECU) are detected at stations located on the relatively close distance (FOCA and SRJV, about 50 km) on 03/19, when ionosphere was still under the influence of the strongest GS. Data gaps detected at BiHPOS FOCA are responsible for significant differences on the 1st and 2nd day before the GS, which can also be the

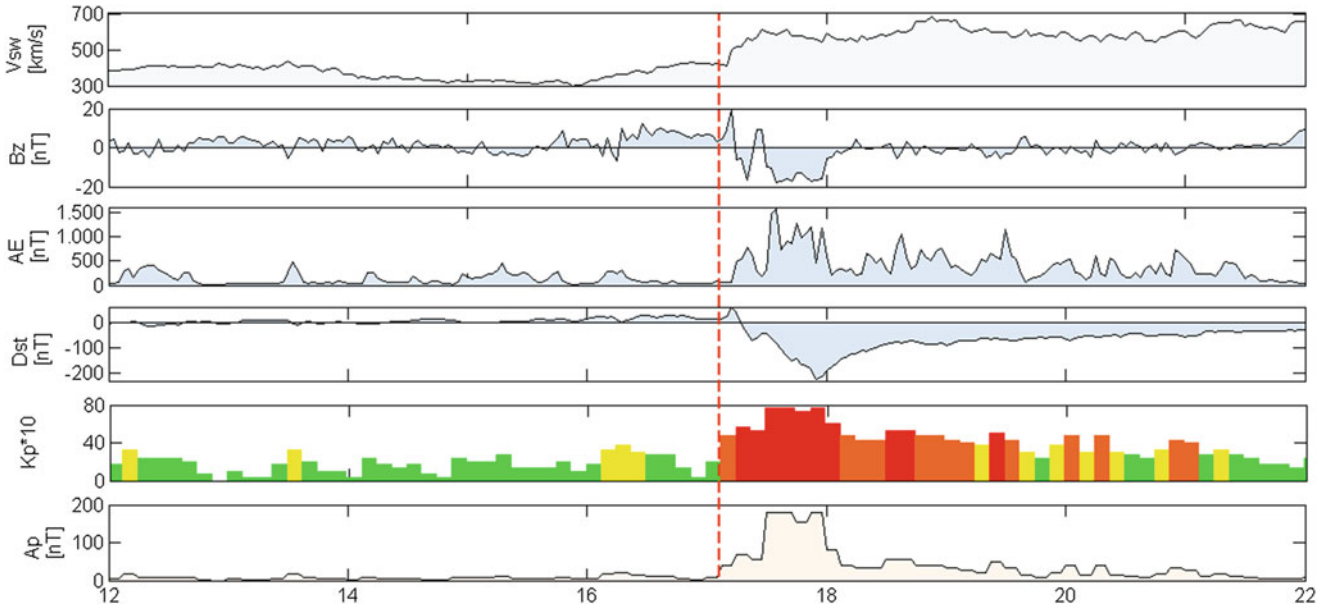

Fig. 8 SW indices for the period 03/12–03/21: Vsw, Bz, AE, Dst, Kp (Quiet K<3, Moderate 3≤K<4, Active 4≤K<5, Storm 5≤K) and Ap. The huge increase of SW speed, AE, Kp (to 8) and Ap indices, decrease of Dst (<−200 nT) and southward Bz component, characterize the main phase of the strongest GS in SC 24 on 03/17, followed by the recovery phase from 03/18 to 03/21

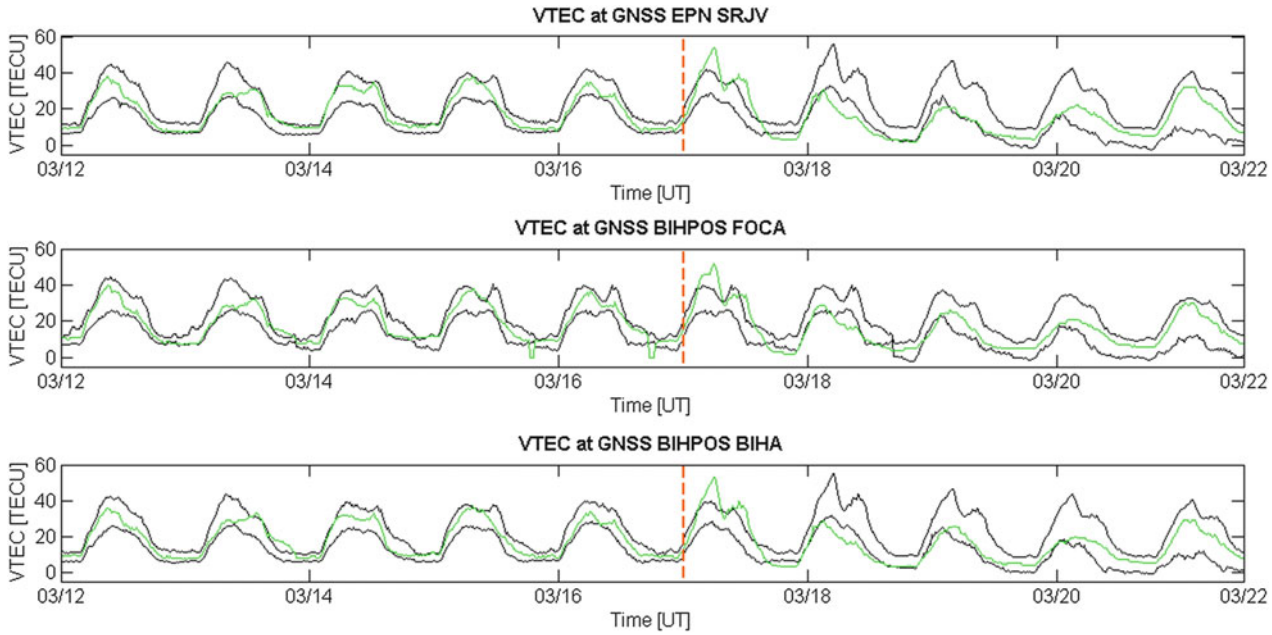

Fig. 9 UB and LB ($\mu \pm 2\sigma$) and VTEC values at GNSS SRJV, BIHA and FOCA for the period of St. Patrick's GS (03/17 arrival of the CME in GMF)

reason for deviations at FOCA observed on 03/17 (VTEC calibration is affected by data gaps).

Differences between observed VTEC and average VTEC calculated for the 5 quietest days ($VTEC_{QUIET}$) (Table 2) for all three stations are presented in Fig. 11. Analysis showed significant changes in VTEC after the arrival of CME in Earth's magnetic field (03/17, 04:30 UTC), which triggered severe geomagnetic storms. During the main phase of St. Patrick's storm (03/17) the "positive ionospheric storm" was registered. Maximum increase, compared to $VTEC_{QUIET}$, was slightly above 20 TECU around local noon and again in the evening (18 h). Following days (until 21/03) "negative" storm effects were presented (to about −15 TECU around local noon), which correspond to the recovery phase.

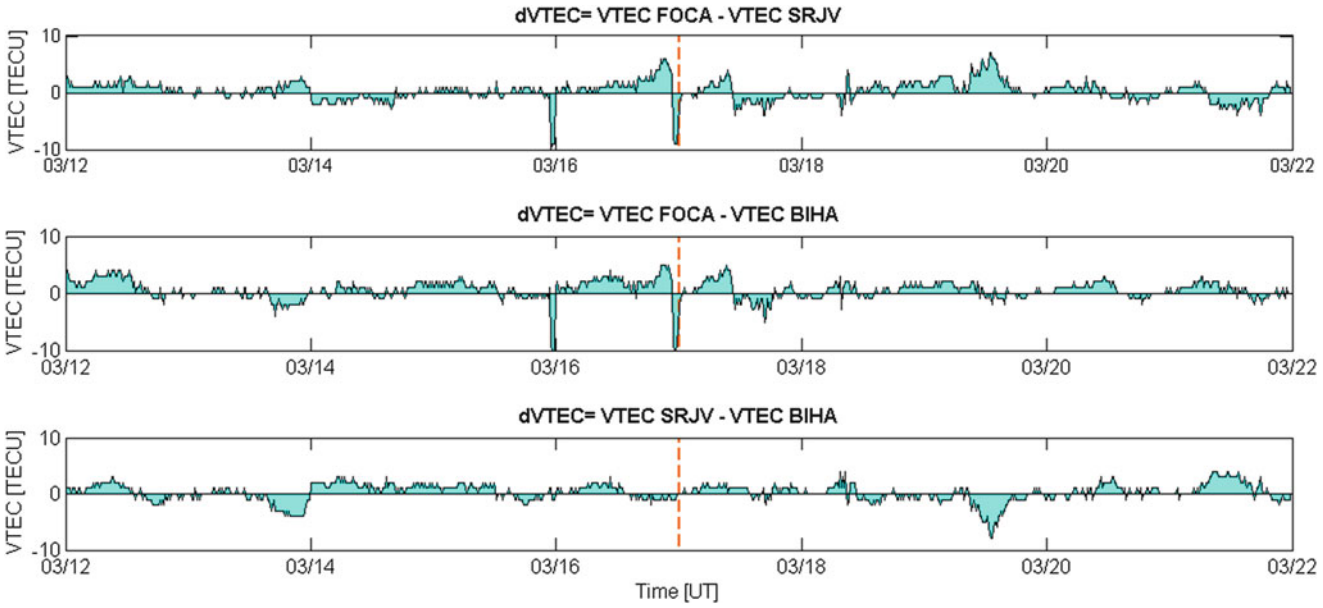

Fig. 10 Mutual differences of VTEC at SRJV, BIHA and FOCA. Differences between all three stations are under 10 TECU. Data gaps at BiHPOS FOCA, on the 1st and 2nd day before the GS, affected VTEC calibration

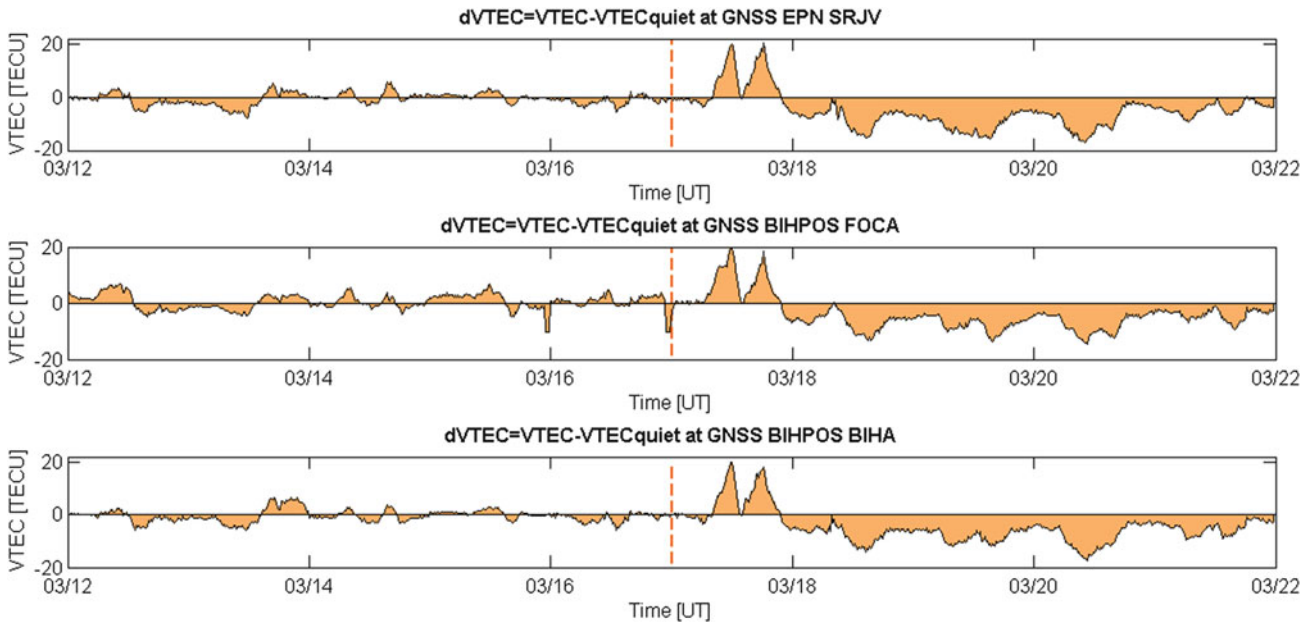

Fig. 11 Differences between observed VTEC and average $VTEC_{QUIET}$ for the quietest days for the case of St. Patrick's Day storm. Very similar residuals' pattern is observed on all three stations. "Positive ionospheric storm" is during the main phase of St. Patrick's storm (>20 TECU), while "negative ionospheric storm" is seen during the recovery phase (up to −20 TECU)

Changes in VTEC occurred during the night as well, with a decrease of more than 5 TECU from $VTEC_{QUIET}$. When comparing to the Fig. 10 variations are detected on same days. Exceptions are VTEC differences at FOCA before and after the CME arrival when GNSS data gaps affected VTEC calibration.

The week before St. Patrick's geomagnetic storm, mean VTEC differences between stations are similar (1–1.3 TECU) (Fig. 12a). During the main phase of the strong geomagnetic storm, differences are bigger when VTEC at stations SRJV and BIHA are compared to VTEC values at station FOCA (to 1.5 TECU). Station FOCA had data gaps shortly before 03/17, which affected VTEC calibration, while between station SRJV and BIHA mean difference was 0.8 TECU. During the recovery phase, smaller and similar variations are observed (0.9–1.2 TECU). Differences from

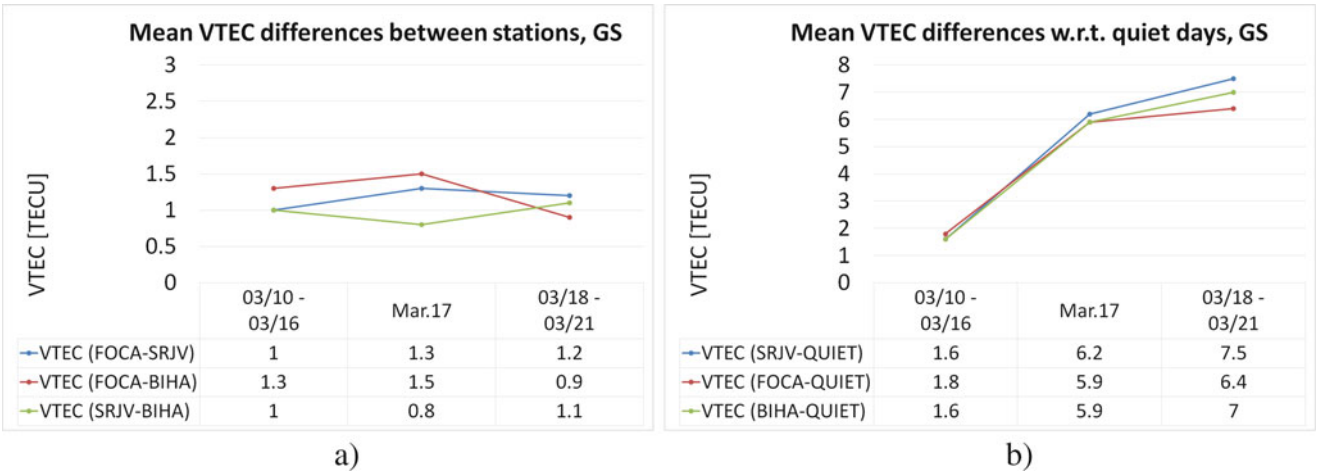

Fig. 12 Statistics: (**a**) mean differences between stations and (**b**) mean differences between observed VTEC and $VTEC_{QUIET}$. Study period (03/12–03/21): a week before the GS (03/10–03/16), the main phase of the GS (03/17) and recovery phase of the GS (03/18–03/21)

VTEC mean for the quiet period (Fig. 12b) show similar values during a week before the geomagnetic storm at all station of about 1.7 TECU. VTEC residuals are higher during the main phase of the storm (6 TECU) and even more during the recovery phase (6.4–7.5 TECU). When VTEC residuals are compared between stations, the average difference is about 0.3 TECU during the main phase, while in the recovery phase (03/18–03/21) mutual differences between stations FOCA, BIHA, SRJV are about 0.5 TECU respectively. These results show that especially high variability in the ionosphere is presented during the recovery phase, taking into account that St. Patrick's GS was the strongest storm in SC 24. Ionosphere variability was more than 3 times higher during the geomagnetic disturbed period than during a week before the storm.

4 Conclusion

This paper represents the study of VTEC variations during the period of seismic activity of medium intensity (M = 4.2 Richter) and severe space weather effects (the strongest geomagnetic storm in SC 24) using GNSS observations of Positioning Service of Bosnia and Herzegovina (BiHPOS) and EUREF Permanent Network (EPN). VTEC values were calibrated for every 15 min and the ionosphere height was kept fixed at 400 km above the Earth's surface. Conditions in the solar wind, interplanetary and geomagnetic field were also investigated to obtain information about space weather's impact on the state of the ionosphere on the global level.

Ionosphere VTEC variations were investigated in the period of the moderate earthquake with epicentre at mountain Treskavica, magnitude 4.2 Richter and shallow deep of 2 km. Selected GNSS stations from BiHPOS and EPN network in Bosnia and Herzegovina are located inside and outside the earthquake preparation zone, which has a radius of 71 km from the earthquake's epicentre. A second case study was the strongest geomagnetic storm in SC 24 so far, St. Patrick's Day geomagnetic storm. Significant VTEC variations were visible 2 weeks before the earthquake as well as on the St. Patrick's storm occurrence (the main phase) and during its recovery phase.

Analyses commonly used in studies of seismic-induced variations (estimation of UB and LB as a 15-day running mean of VTEC $\pm$ 2σ) and space weather-induced variations (average VTEC estimated for the 5 quietest days regarding geomagnetic activity) were applied to analyze both cases (the earthquake at Treskavica and St. Patrick's geomagnetic storm). Also, direct comparison of VTEC values between different stations was performed. The aim was to analyze the response of the ionosphere to different phenomena and to distinguish VTEC variations induced by different sources. If only one of the mentioned methods was applied, it could lead to wrong conclusions. That is especially needed in a case where more possible sources of VTEC variability exist.

Results showed that during 2 weeks before the earthquake, conditions in IMF and GMF were quiet to unsettled. Geomagnetic storms occurred on 10th and 4th day before the earthquake, as well as 3 days in a row after the earthquake occurrence, which induced additional variations in the ionosphere. Therefore, space weather-induced variations were studied as well, in order to determine sources of VTEC anomalies before and after seismic activity. Obtained results indicate that space weather-induced ionosphere anomalies make detection of seismo-ionosphere anomalies more difficult. Direct comparison between stations 2 weeks before the earthquake showed higher variations in VTEC values when stations located inside EPZ are compared to the station outside EPZ, especially during 1 week before the seismic shock (at least 2 times higher VTEC differences). On a day of the

seismic shock and during a week after it, differences between stations are smaller and similar. Reasons for these higher differences can be due to a local source of ionization, such as seismic activity, which could produce different variability in the ionosphere above EQ epicentre, i.e. inside EPZ. However, other possible reasons of those variations can be effects of local ionosphere variability dependable on a geographical location of GNSS receiver or uncertainties/biases induced in data pre-processing and TEC calibration. In the second case study (St. Patrick's Day storm) mean VTEC difference between stations was about 0.3 TECU, except when VTEC at station FOCA was affected by gaps in GNSS data. In case of the earthquake Treskavica, mean VTEC difference between stations located inside and outside the EPZ was about 1 TECU 1 week before the earthquake. It is important to note that the medium-intensity earthquake was examined. Thus if VTEC anomalies were produced by the seismic activity they probably could not be huge. During 2 weeks before the earthquake, VTEC values exceeded limit values of LB and/or UB several times, where some of the cases happened during disturbances in IMF and GMF and some cases during quiet conditions. When comparing to mean VTEC value for the 5 geomagnetic quietest days ($VTEC_{QUIET}$), higher VTEC residuals are observed a week before the earthquake. On a day of the earthquake, the smallest VTEC residuals were seen at station FOCA, near the epicentre, while residuals for other stations maintained similar to the previous week.

In the second case study, so far the strongest geomagnetic storm in SC 24, huge variations of ionosphere VTEC above B&H was observed after the CME's arrival in Earth's atmosphere (03/17). Significant variations continued during the following days. Analysis showed that VTEC values exceeded UB during the main phase (VTEC increase), while LB was reached in the recovery phase (VTEC decrease). Mutual VTEC differences between stations show smaller VTEC deviation in days before the severe geomagnetic storm and during the recovery phase (about 0.3 TECU), with higher deviations on the day of geomagnetic storm occurrence (compared to station FOCA, where TEC calibration was affected by data gaps). When compared to the average VTEC for the quietest days ($VTEC_{QUIET}$) "positive ionospheric storm" is detected in the main phase (VTEC geomagnetic storm-induced variations up to 60% after local noon and to even 150% in the evening compared to $VTEC_{QUIET}$), followed by "negative ionospheric storm" in the recovery phase (VTEC geomagnetic storm-induced variations of 50% in daytime and to 80% in night-time compared to $VTEC_{QUIET}$). Mean VTEC differences from the $VTEC_{QUIET}$ were at least three times higher in the main and the recovery phase of the geomagnetic storm compared to a period shortly before it. A similar pattern of variations is observed at all stations. Exceptions are deviations in VTEC values detected at station FOCA shortly before the geomagnetic storm and on 03/17, which was affected by data gaps. Intensive variations of ionosphere VTEC during the main and recovery phase of the storm at all stations can have a significant impact on the accuracy of GNSS measurements. Therefore, the effects of space weather cannot be ignored in the study of the ionosphere, as well as in the applications that depend on the state of the ionosphere. In the next stage of this study impact of severe space weather events on positioning accuracy are investigated, regarding the network, PPP static and kinematic positioning techniques.

Acknowledgements Authors are sincerely grateful to International Association of Geodesy (IAG) for providing travel grant to the first author to deliver oral presentation at IAG-IASPEI Assembly 2017 in Kobe, Japan. Authors also thank International Center of Theoretical Physics Abdus Salam in Trieste and Dr. Luigi Ciraolo for the TEC calibration programme. Many thanks to institutions and organizations, which kindly provided their data: German Research Centre for Geosciences; NASA OmniWeb; World Data Center for Geomagnetism at Kyoto University Japan; EUREF Permanent Network; Geodetic Administration of Federation Bosnia and Herzegovina. Authors are grateful to reviewers for their valuable comments and suggestions to improve the quality of the manuscript.

References

Afraimovich EL, Astafieva EI, Gokhberg MB, Lapshin VM, Permyakova VE, Steblov GM, Shalimov SL (2004) Variations of the total electron content in the ionosphere from GPS data recorded during the Hector Mine earthquake of October 16, 1999, California. Russ J Earth Sci 6(5):339–354

Astafyeva E, Zakharenkova I, Forster M (2015) Ionospheric response to the 2015 St. Patrick's day storm: a global multi-instrumental overview. J Geophys Res Space Phys 120:9023–9037. https://doi.org/10.1002/2015JA02629

Chapman S, Bartels J (1940) Geomagnetism, vol 1, chapter IX. Clarendon, Oxford

Ciraolo L, Azpilicueta F, Brunini C, Meza A, Radicella SM (2007) Calibration error on experimental slant total electron contents (TEC) determined with GPS. J Geod 81(2):111–120

Dobrovolsky IR, Zubkov SI, Myachkin VI (1979) Estimation of the size of earthquake preparation zones. Pure Appl Geophys 117:1025–1044

Gonzalez WD, Joselyn JA, Kamide Y, Kroehl HW, Rostoker G, Tsurutani BT, Vasyliunas VM (1994) What is a geomagnetic storm? J Geophys Res 99:5771–5792. https://doi.org/10.1029/93JA02867

Gousheva M, Danov D, Hristov P, Matova M (2008) Quasi-static electric fields phenomena in the ionosphere associated with pre- and post earthquake effects. Nat Hazards Earth Syst Sci 8(1):101–107. https://doi.org/10.5194/nhess-8-101-2008

Gulyaeva T, Arikan F (2016) Statistical discrimination of global post-seismic ionosphere effects under geomagnetic quiet and storm conditions. Geomat Nat Haz Risk 8:509–524. https://doi.org/10.1080/19475705.2016.1246483

Horozovic D, Natras R, Mulic M (2018) Impact of geomagnetic storms and ionospheric disturbances on mid-latitude station's coordinates using static and kinematic PPP; Poster: European Geosciences Union, General Assembly 2018 (EGU 2018), Vienna; 2018-04-09 - 2018-04-13. In: EGU general assembly 2018, Geophysical research abstracts, vol 20 . ISSN: 1029-7006, p 9009

Jacobsen KS, Andalsvik YL (2016) Overview of the 2015 St. Partick's day storm and its consequences for RTK and PPP positioning in Norway. J Space Weather Space Clim 6. https://doi.org/10.1051/swsc/2016004

Liu JY, Chen YI, Chuo YJ, Chen CS (2006) A statistical investigation of preearthquake ionospheric anomaly. J Geophys Res 111:A05304. https://doi.org/10.1029/2005JA011333

Liu JY, Chen YI, Chen CH, Liu CY, Chen CY, Nishihashi M, Li JZ, Xia YQ, Oyama KI, Hattori K, Lin CH (2009) Seismoionospheric GPS total electron content anomalies observed before the 12 May 2008 Mw7.9 Wenchuan earthquake. J Geophys Res 114(A4). https://doi.org/10.1029/2008JA013698

Mulic M, Natras R (2018) Ionosphere TEC variations over Bosnia and Herzegovina using GNSS data. In: Cefalo R, Zieliński J, Barbarella M (eds) New advanced GNSS and 3D spatial techniques. Lecture notes in geoinformation and cartography. Springer, Cham, pp 271–283. https://doi.org/10.1007/978-3-319-56218-6_22

Natras R, Magnet N, Boisits J, Weber R (2018) GNSS-based regional ionosphere modeling over Bosnia and Herzegovina, Poster: European Geosciences Union, General Assembly 2018 (EGU 2018), Vienna; 09.04.2018 - 13.04.2018. In: EGU general assembly 2018, Geophysical research abstracts, vol 20 . ISSN: 1029-7006, p 661

Nava B, Rodríguez-Zuluaga J, Alazo-Cuartas K, Kashcheyev A, Migoya-Orué Y, Radicella SM, Amory-Mazaudier C, Fleury R (2016) Middle- and low-latitude ionosphere response to 2015 St. Patrick's day geomagnetic storm. J Geophys Res Space Phys 121:3421–3438. https://doi.org/10.1002/2015JA022299

Pulinets S, Boyarchuk K (2004) Ionospheric precursors of earthquakes. Springer, Berlin, p 315

Pulinets S, Ouzounov D (2011) Lithosphere-atmosphere-ionosphere coupling (LAIC) model: an unified concept for earthquake precursors validation. J Asian Earth Sci 41(4–5):371–382

Schaer S (1999) Mapping and predicting the Earth's ionosphere using the Global Positioning System. PhD thesis, Bern University, Bern

Sugiura M (1964) Hourly values of equatorial Dst for IGY. In: Annals of the international geophysical year, vol 35. Pergamon Press, Oxford, pp 945–948

Sugiura M, Chapman S (1960) The average morphology of geomagnetic storm with sudden commencement. Abandl Akad Wiss Gottingen Math Phys K1(4):1

US National Space Weather Strategy, Product of National Science and Technology Council, Space weather operations, research and mitigation (SWORM) task force, USA, 2015

Comparing the Nigerian GNSS Reference Network's Zenith Total Delays from Precise Point Positioning to a Numerical Weather Model

A. O. Mayaki, T. Nikolaidou, M. Santos, and C. J. Okolie

Abstract

As a pivotal infrastructure for the socio-economic development of Nigeria, the Nigerian Global Navigation Satellite Systems (GNSS) Reference Network – NIGNET – can serve as a tool for weather and climate monitoring, by obtaining and analyzing the neutral atmospheric Zenith Total Delays (ZTD) from processed GNSS data. With the use of surface meteorological measurements, the ZTD can be transformed to the integrated water vapor content in the neutral atmosphere, which is an essential parameter in weather forecasting, and climate change and variability analysis. The focus of this research is to assess the adaptability of the NIGNET for meteorological applications using the global positioning system precise point positioning (PPP) derived ZTD at the stations. ZTD estimates are derived from daily data obtained from the NIGNET and International GNSS Service (IGS) stations spanning the years 2011–2016. These estimates are compared with ray-traced delay estimates from the National Centre for Environmental Prediction Reanalysis II (NCEP II) global Numerical Weather Model (NWM) and the IGS zenith path delay products. A comprehensive analysis is performed to assess the level of agreement of the different ZTD estimates and to identify possible systematic effects from the different sources. Comparisons between the PPP and NCEP II NWM ZTD estimates show a range of mean offsets from −6.4 to 23.9 mm, and standard deviations from 33.1 to 44.9 mm. With the PPP and IGS ZTD estimates, mean offsets of −2.4 and −0.1 mm, and standard deviations of 9.9 and 13.8 mm are obtained.

Keywords

Global Positioning System · Nigerian GNSS Reference Network · Numerical Weather Model · Precise Point Positioning · Zenith Total Delay

1 Introduction

Dry gases and water vapour affect the accuracy of point positions on Earth by delaying the Global Navigation Satellite Systems (GNSS) signals propagating through the neutral atmosphere (UCAR 2011) to ground receivers. This delay, called the neutral atmospheric or total delay, depends on the neutral atmosphere's refractive index which is a function of temperature, pressure and humidity. In GNSS analysis, the neutral atmospheric delay consists of a modelled hydrostatic delay and an estimated wet delay. At the line of sight, these

A. O. Mayaki (✉) · T. Nikolaidou · M. Santos
Department of Geodesy and Geomatics Engineering, University of New Brunswick, Fredericton, NB, Canada
e-mail: omayaki@unb.ca; Thalia.Nikolaidou@unb.ca; msantos@unb.ca

C. J. Okolie
Surveying and Geoinformatics Department, University of Lagos, Lagos, Nigeria
e-mail: cokolie@unilag.edu.ng

J. T. Freymueller, L. Sanchez (eds.), *International Symposium on Advancing Geodesy in a Changing World*, International Association of Geodesy Symposia 149, https://doi.org/10.1007/1345_2018_43

delays are usually referred to the zenith direction by means of mapping functions used to convert the slant delays at the actual elevation angle of satellite observations to the zenith (Isioye et al. 2015).

Many countries in the world employ networks of Continuously Operating Reference Stations (CORS) for multidisciplinary applications such as surveying, mapping, navigation and meteorology (Isioye et al. 2016). In Nigeria, the Nigerian GNSS Reference Network (NIGNET) CORS serve as the fiducial network that defines the national spatial reference framework based on modern space geodesy techniques. NIGNET also contributes to the African Geodetic Reference Frame (AFREF) project (Jatau et al. 2010; Farah 2009). However, NIGNET can also be used as a weather and climate monitoring tool through the processing of its data and the analyses of the derived neutral atmospheric parameters, such as the zenith total delay (ZTD), the zenith wet delays (ZWD) and the gradients. The ZTD and the integrated water vapor (which is derived from the ZWD) can be assimilated into local/regional and global numerical weather models (NWM), to improve weather forecasting and climate monitoring (Ahmed et al. 2014, 2015). This would aid, for example, in the identification of potential severe weather activity in the country and the tracking of weather fronts. In this work, however, we concentrate on the ZTD.

Precise Point Positioning (PPP) is a well-known technique that utilizes precise satellite orbit and clock information in the processing of observations produced by a single GNSS receiver, to determine its 3-D position along with other parameters such as the receiver clock error, the ambiguities and the ZTD (Zumberge et al. 1997; Leandro et al. 2010). Therefore, this technique renders GNSS suitable for meteorological studies by providing information about the atmospheric water vapour from the determined ZTD (Isioye et al. 2016).

In this chapter, we compare the ZTDs obtained from the GNSS PPP technique with those from an NWM and from the International GNSS Service (IGS). GNSS observations for 16 NIGNET and IGS stations in and around Nigeria were obtained. These observations were processed with the GNSS Analysis and Positioning Software (GAPS) PPP package of the University of New Brunswick (Urquhart et al. 2014). We calculated ZTD using the National Centre for Environmental Prediction Reanalysis II (NCEP II) global NWM (Kanamitsu et al. 2002) for all the stations employed in the study. NCEP II was chosen because of its quality and tested performance for geodetic applications[1] (Urquhart and Santos 2011) as well as its free data availability.[2] We also used the zenith path delay (ZPD) products, as generated by the IGS for its stations (Byun and Bar-Sever 2009), for the validation of the GAPS ZTD estimates of those stations. For simplicity, in this work, the ZTD estimates from GAPS, IGS and NCEP II NWM are referred to as "GAPS", "IGS" and "NCEP II", respectively.

The chapter is structured as follows. The data used, and the methodology employed are discussed in Sect. 2. Section 3 presents the results with discussion and analysis about the statistical and graphical comparisons between the GAPS, IGS and NCEP II ZTD estimates. Conclusions finalize the chapter.

2 Data and Methodology

A map of the study area and the distribution of the stations is shown in Fig. 1. Daily NIGNET and IGS observation files, spanning the years 2011–2016, with a data logging interval of 30 s, of 14 CORS and 2 IGS stations, were processed using GAPS. The observations used are the ionosphere-free linear combinations of the GPS undifferenced L1 and L2 carrier-phase and pseudo range measurements. For the processing, which was done in static mode, the IGS final orbit (sampled at 15-min intervals) and 30-s clock products were utilized in a sequential least-squares filter, with the Vienna Mapping Functions 1 – VMF1 – (Boehm et al. 2006) as the a priori hydrostatic delay model and mapping function, and an elevation angle cut-off of 10°. Satellites and receivers' antennae were corrected for phase centre offsets and phase centre variations. The coordinates of the stations were determined based on the International Terrestrial Reference Frame (ITRF) 2008 solution (Altamimi et al. 2011), and the ambiguities were estimated as real numbers. The ZTD estimates, together with their horizontal gradients, were estimated at every epoch. The horizontal gradients model the asymmetry of the delay in the north-south and east-west directions, and its estimation has shown to improve the position of stations (Balidakis et al. 2018) especially under the presence of extreme weather events (Nikolaidou et al. 2018). It should be noted that the use of the final orbit and clock products is to ensure high quality ZTD estimation useful for climate monitoring but not for weather forecasting due to its latency.

The ZPD products of the IGS stations are also produced through PPP with the same process noise as used in GAPS but sampled at 5-min intervals. The full list of the processing options is given in Byram and Hackman (2014). These ZPDs have a nominal accuracy of 4 mm and a latency of less than 4 weeks (www.igs.org/products).

The NCEP II ZTD estimates were retrieved from ray-tracing using the University of New Brunswick's in-house software developed by Nievinski and Santos

[1] http://unb-vmf1.gge.unb.ca/About.html.

[2] https://www.esrl.noaa.gov/psd/data/gridded/data.ncep.reanalysis2.html.

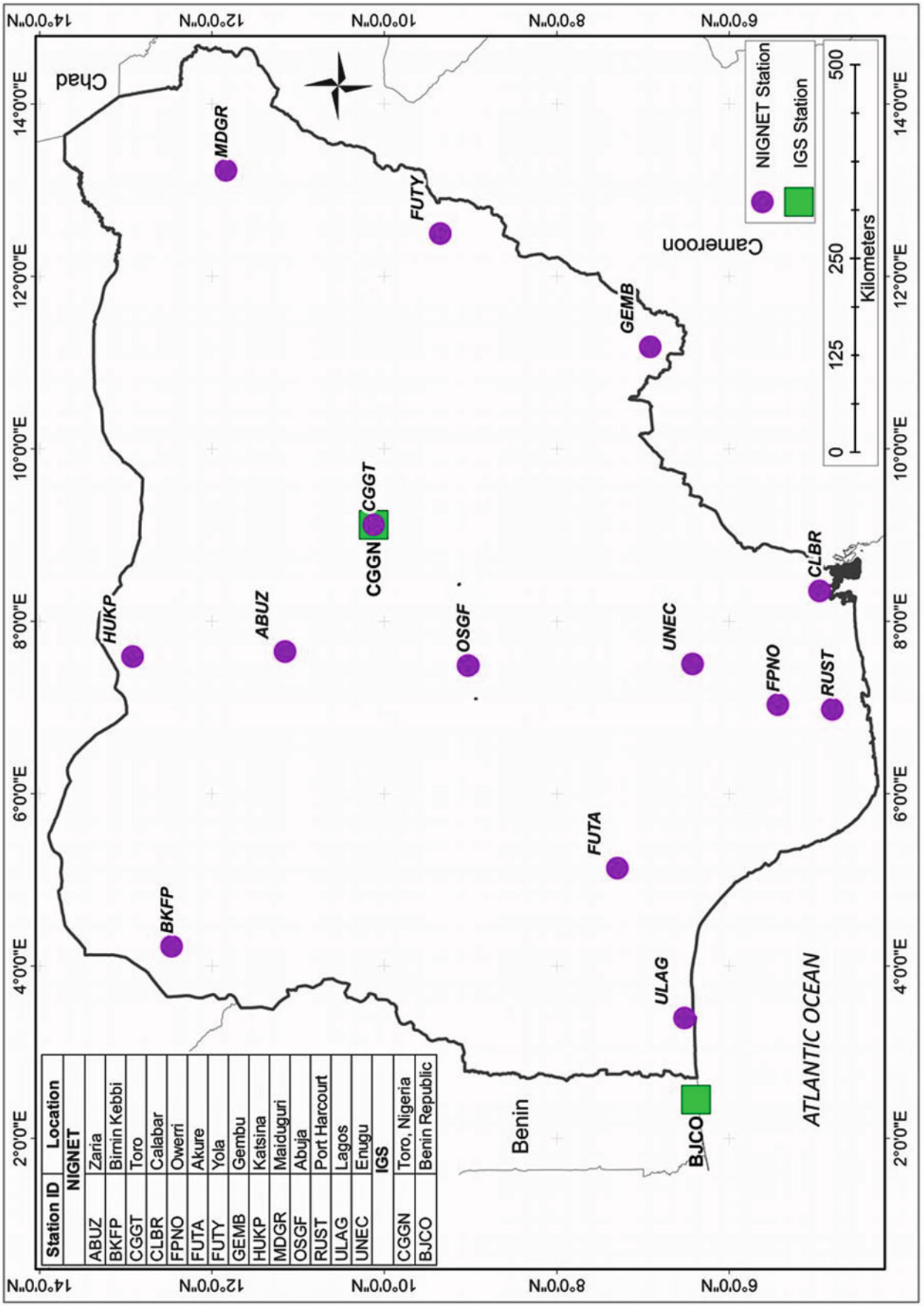

Station ID	Location
NIGNET	
ABUZ	Zaria
BKFP	Birnin Kebbi
CGGT	Toro
CLBR	Calabar
FPNO	Owerri
FUTA	Akure
FUTY	Yola
GEMB	Gembu
HUKP	Katsina
MDGR	Maiduguri
OSGF	Abuja
RUST	Port Harcourt
ULAG	Lagos
UNEC	Enugu
IGS	
CGGN	Toro, Nigeria
BJCO	Benin Republic

Fig. 1 Map of study area with GNSS reference stations

(2010), with computed station-specific zenith hydrostatic and wet delays, and horizontal gradients. A 2-D ray-tracing was performed at the initialization intervals of 0, 6, 12, and 18 h (temporal resolution) of the NCEP Reanalysis II global NWM, with a horizontal resolution of 2.5° × 2.5°.

In PPP static post-processing, it takes the first few hours for the 3-D coordinate of a point to become accurate to the centimetre level (Abdallah 2015; Bolbol et al. 2017). Because of this, the initial 2 h of the GAPS estimates were not considered for the analysis. Consequently, the first daily estimates (0-h ZTD estimates) of the NCEP II, and the initial 2 h of the IGS ZPDs were also neglected in the analysis. For comparing GAPS with NCEP II, daily 6-, 12- and 18-h GAPS values, averaged over 5-min windows centred around the exact 6-, 12- and 18-h estimates, were used. The same 5-min averaging was done for the comparison between GAPS and the IGS ZTDs to match the IGS interval. Statistic of values (the mean offsets (μ), standard deviations (σ) and root mean square (rms) values of the differences) of GAPS with respect to NCEP II and IGS values for each station, were determined.

3 Results and Discussion

3.1 Comparison Between GAPS and NCEP II

In this section, the quality of the ZTD estimates from GAPS is evaluated in comparison to those from NCEP II. Figure 2a–f show the GAPS and NCEP II estimates for six stations across the country in the year 2012. As shown in the plots, GAPS is generally in agreement with NCEP II; the statistics for the six stations (CLBR, ULAG, ABUZ, FUTY, BJCO and CGGN) is given in Table 1. The other stations in other years show a similar behaviour.

According to Eludoyin et al. (2014), the two major seasons in Nigeria are the rainy season (April to October) and the dry season (November to March). The quantity of atmospheric water vapor is typically higher in the rainy season, and lower in the dry season. Disregarding altitude, higher amounts of atmospheric water vapor are related to higher ZTD estimates and vice versa. Examples of these are seen in Fig. 2a–f; higher ZTD estimates typically occur within the days of year (DOY) 100–300, which coincides with the months April to October. The lower ZTD estimates, which mean lower amounts of atmospheric water vapor, are typically found in the dry season months November to March (around DOY 300–365/366 and 1–100). Studies by Olusola et al. (2015) and Willoughby et al. (2002) indicate that because the southern part of Nigeria is closer to a coastline of the Atlantic Ocean, its atmosphere is more humid (more water vapor content) than the atmosphere in the northern part of the country. In both the GAPS and the NCEP II plots, the southern stations have estimates as high as 2.75 m (Fig. 2a, b, e). However, the estimates in the northern stations (Fig. 2c, d, f) generally do not exceed 2.65 m.

Portrayed within DOY 200–250 (mid of July to early September), is a decrease in the GAPS estimates for the stations ULAG and BJCO (Fig. 2b, e). This decrease coincides with a phenomenon known as the "August break" (Ogungbenro et al. 2014), which is characteristic of the precipitation pattern in the southern part of the country and is consistent with the findings of Willoughby et al. (2002). Rapid changes in the GAPS and NCEP II estimates can be attributed to rapid changes in the humidity around the stations. Observed gaps at certain epochs in the plots are due to the non-availability of observations from the NIGNET stations.

Overall, for all the years combined, and for each NIGNET and IGS station, the differences between GAPS and NCEP II have mean offsets varying between −6.4 and 23.9 mm, and standard deviations between 33.1 and 44.9 mm. Table 2 gives the overall statistics for all the stations for all the years of study.

3.2 Comparison Between GAPS and IGS

In this comparison, the year 2016 is considered because of the substantial amount of ZPD products available for the station CGGN. Figure 3a, b show the 2016 GAPS and IGS estimates for the stations CGGN and BJCO, indicating very good agreement. The observed gaps at certain epochs in the plots are due to the non-availability of observations from the NIGNET station and the non-availability of ZPD products from the IGS.

For the combination of all years, Table 3 gives the statistics of the comparison between GAPS and IGS for the stations BJCO and CGGN.

3.3 Comparison Between GAPS, IGS and NCEP II

The comparisons here are only done for the IGS stations and are restricted to the epochs which have ZTD estimates from all three sources between 2011 and 2016. Figure 4a–c show the histograms for the offsets between NCEP II and GAPS, NCEP II and IGS, as well as IGS and GAPS.

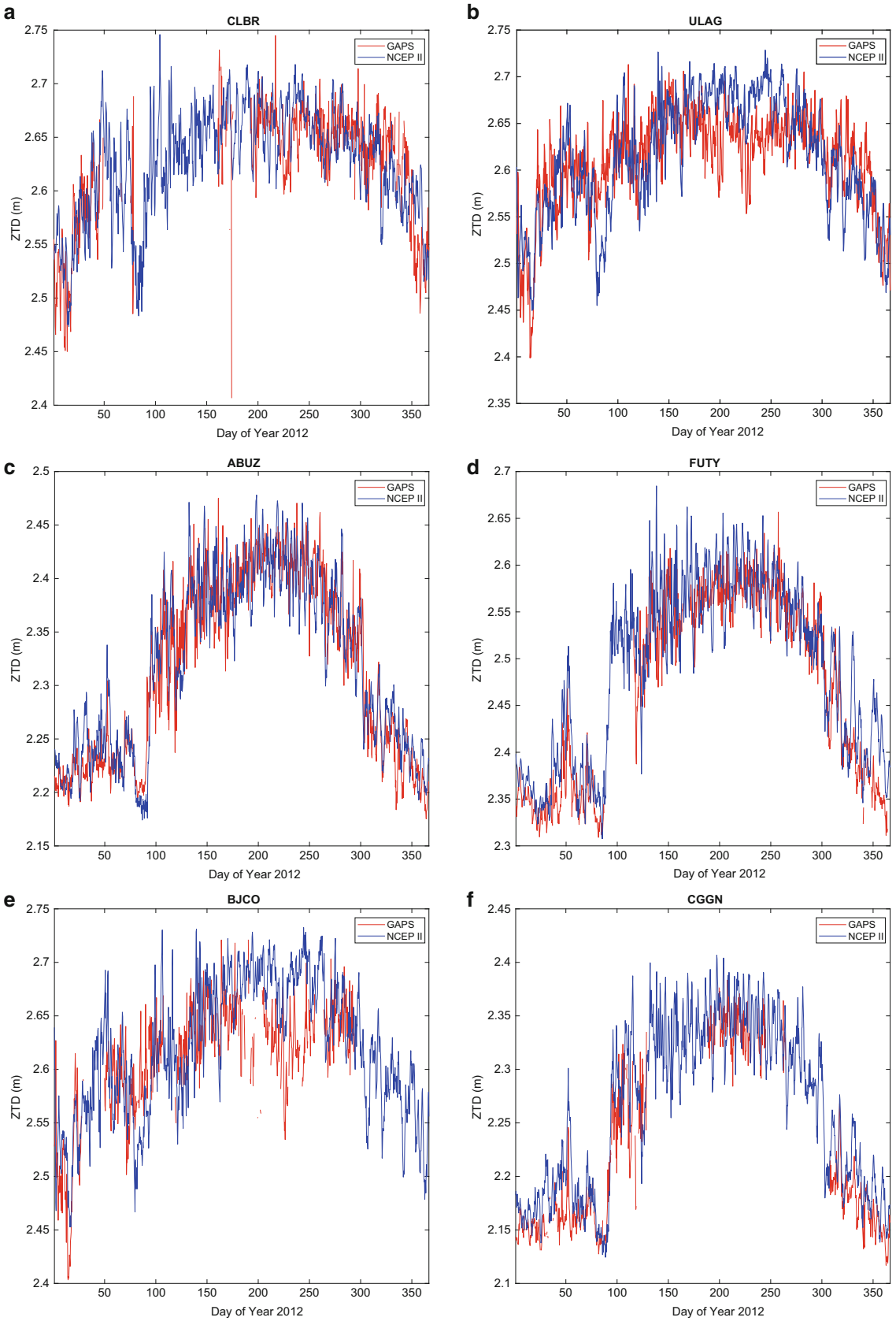

Fig. 2 (**a**) GAPS and NCEP II ZTD for CLBR in 2012. (**b**) GAPS and NCEP II ZTD for ULAG in 2012. (**c**) GAPS and NCEP II ZTD for ABUZ in 2012. (**d**) GAPS and NCEP II ZTD for FUTY in 2012. (**e**) GAPS and NCEP II ZTD for BJCO in 2012. (**f**) GAPS and NCEP II ZTD for CGGN in 2012

Table 1 2012 ZTD difference between GAPS and NCEP II

Stations	μ (mm)	σ (mm)	rms (mm)
ABUZ	4.9	31.3	31.7
BJCO	17.9	48.2	51.4
CGGN	20.8	29.3	35.9
CLBR	3.1	39.4	39.5
FUTY	17.5	37.3	41.2
ULAG	2.5	45.9	46.0

For the comparisons of NCEP II between GAPS and IGS (Fig. 4a, b), the large standard deviations may be attributed to the variability and the higher concentration of atmospheric water vapour at the lower latitudes/equatorial regions as stated in Li et al. (2015) and Dousa and Bennitt (2013). It could also be due to insufficient amounts of atmospheric observations assimilated into the NCEP II NWM from this part of the world, resulting in estimations with larger errors than in, for example, North America and Europe. The closer agreement between IGS and GAPS (Fig. 4c) can be attributed to both being obtained through the same technique, except for differences in the elevation cut-off angles (10° for GAPS and 7° for IGS) and a priori tropospheric models and mapping functions (VMF1 for GAPS and Niell model and Global Mapping Functions for IGS) used. The precision of the IGS and GAPS comparison agrees well with the result of Guo (2015).

Table 2 ZTD difference between GAPS and NCEP II (NIGNET and IGS stations)

Stations (years of data used)	μ (mm)	σ (mm)	rms (mm)
ABUZ (2011–2014, 2016)	3.4	36	36.2
BKPF (2011–2016)	17.7	41.7	45.3
CGGT (2011–2013)	9.5	38	39.2
CLBR (2011–2016)	−6.4	40.2	40.7
FPNO (2012–2014, 2016)	16	34.6	38.1
FUTA (2012–2013)	23.9	38.2	45.1
FUTY (2011–2016)	16	44	46.8
GEMB (2012–2013, 2015)	−4.3	33.1	33.3
HUKP (2012–2015)	10.1	35.8	37.2
MDGR (2011, 2013–2014)	18.3	36	40.3
OSGF (2011–2014, 2016)	14.1	44.4	46.6
RUST (2011–2013)	−3	40.9	41
ULAG (2011–2013)	4.5	37.7	38
UNEC (2011–2014, 2016)	3.9	43.8	44
BJCO[a] (2011–2016)	6.6	40.9	41.4
CGGN[a] (2011–2016)	11.9	44.9	46.5

[a]IGS stations

Table 3 ZTD difference between GAPS and IGS (IGS stations)

Stations (years of data used)	μ (mm)	σ (mm)	rms (mm)
BJCO (2011–2016)	−2.4	13.8	14
CGGN (2015–2016)	−0.1	9.9	9.9

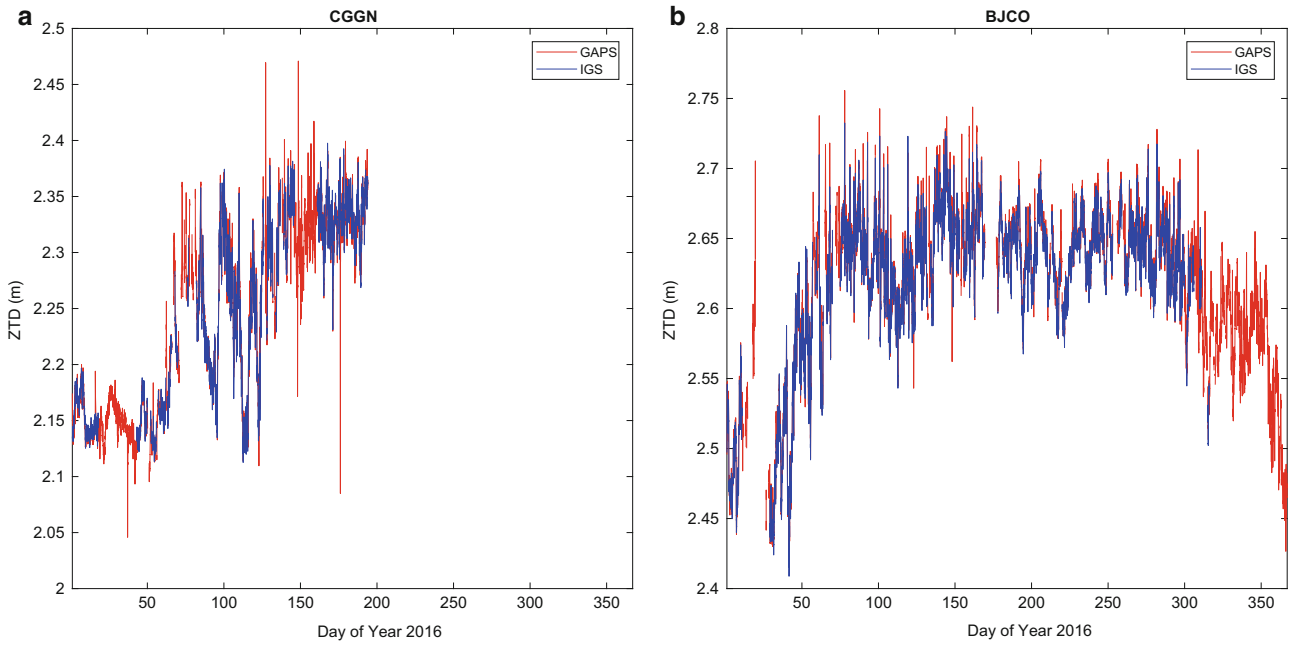

Fig. 3 (**a**) GAPS and IGS ZTD for CGGN in 2016. (**b**) GAPS and IGS ZTD for BJCO in 2016

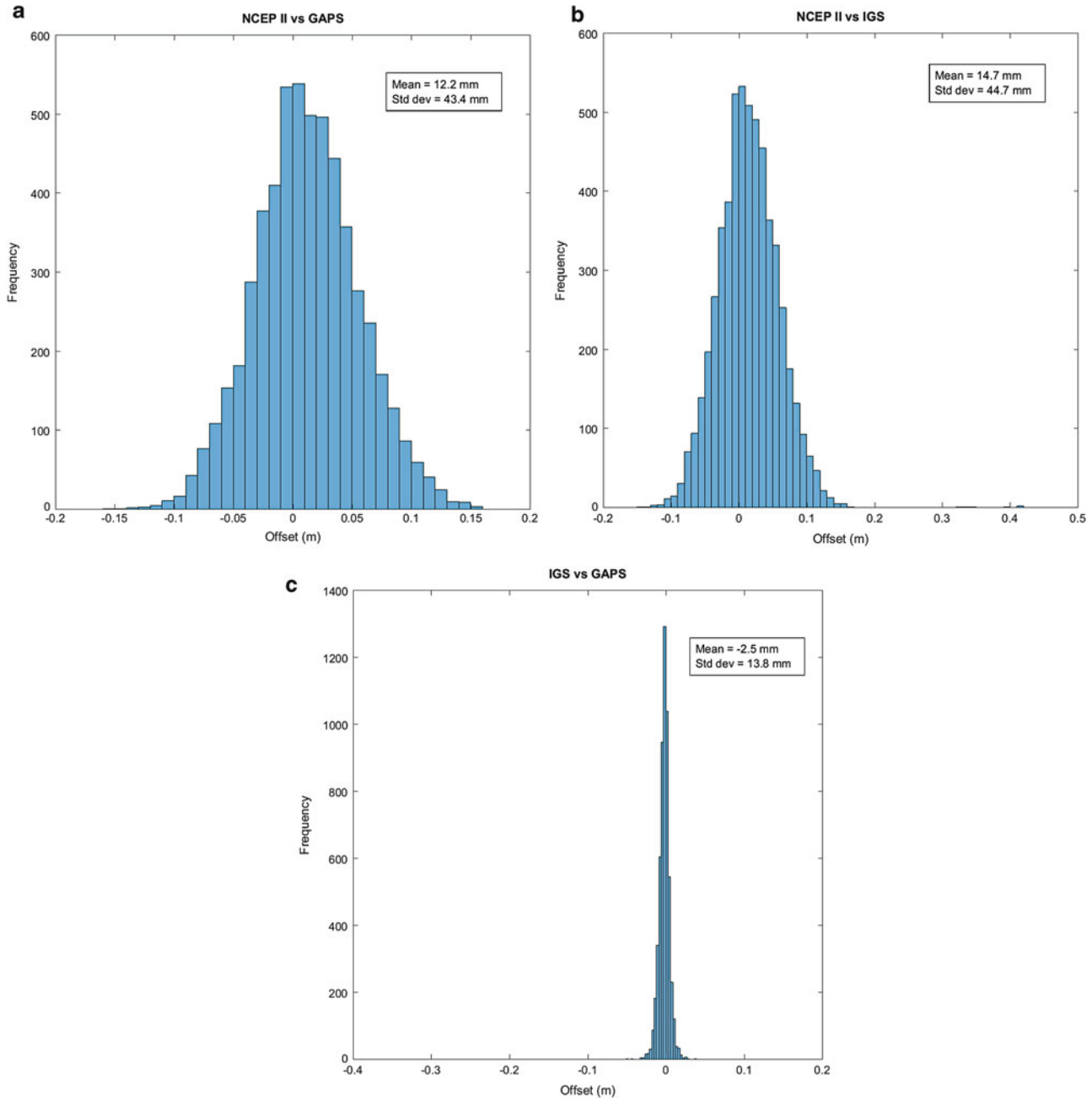

Fig. 4 (**a**) NCEP II and GAPS offset histogram for the IGS stations. (**b**) NCEP II and IGS offset histogram for the IGS stations. (**c**) IGS and GAPS offset histogram for the IGS stations

4 Conclusion

The adaptability of the NIGNET for meteorological studies in Nigeria was assessed using the ZTD estimates from the PPP processing of GPS observations. The precision of these estimates was assessed with comparisons to ray-traced ZTDs from NCEP Reanalysis II NWM and IGS ZPD products. The estimated ZTD for the NIGNET stations depict known latitudinal and seasonal variations. In comparing the ZTD estimates from the different sources, the results show that the mean offsets between the GAPS PPP and the NCEP II estimates for all the NIGNET and IGS stations, for the 6-year duration, vary between −6.4 and 23.9 mm, with their standard deviations between 33.1 and 44.9 mm. The difference between the GAPS PPP and the IGS estimates gives mean offsets of −2.4 and −0.1 mm, with standard deviations of 9.9 and 13.8 mm. The comparisons of the GAPS and the IGS estimates between the NCEP II estimates for the IGS stations have similar results, with standard deviations just

under 45 mm, perhaps indicating deficiencies with NCEP II around the country.

With proper management and maintenance of the NIGNET infrastructure, near real-time ZTD estimates can be produced using PPP with the IGS ultra-rapid orbit and real-time clock products. The near real-time ZTD estimates, if made publicly available, could then be assimilated into regional and global NWM to enhance the quality of their forecasts for Nigeria and the surroundings countries.

The continuation of this project includes an assessment of the inherent uncertainty of the PPP derived neutral atmospheric parameters in the computation of integrated water vapor. Also, a least-squares spectral analysis of the ZTD and its components (hydrostatic and wet delays, and horizontal gradients) is prepared to study other spatial and temporal (seasonal) trends that may be intrinsic in the data, in comparison to precipitation trends studies in the country.

References

Abdallah A (2015) The effect of convergence time on the static-PPP solution. Presented at 2nd international workshop on "Integration of point- and area-wise geodetic monitoring for structures and natural objects", Stuttgart, 23–24 Mar 2015

Ahmed F, Teferle N, Bingley R, Hunegnaw A (2014) A comparative analysis of tropospheric delay estimates from network and precise point positioning processing strategies. Poster presented at: IGS workshop, Pasadena, 23–27 June 2014

Ahmed F, Teferle FN, Bingley RM, Laurichesse D (2015) The status of GNSS data processing systems to estimate integrated water vapour for use in numerical weather prediction models. In: Rizos C, Willis P (eds) IAG 150 years, International Association of Geodesy symposia. Springer, Cham, p 143

Altamimi Z, Collileux X, Métivier L (2011) ITRF2008: an improved solution of the International Terrestrial Reference Frame. J Geod 85(8):457–473. https://doi.org/10.1007/s00190-011-0444-4

Balidakis K, Nilsson T, Zus F, Glaser S, Heinkelmann R, Deng Z, Schuh H (2018) Estimating integrated water vapor trends from VLBI, GPS, and numerical weather models: sensitivity to tropospheric parameterization. J Geophys Res Atmos 123:6356–6372. https://doi.org/10.1029/2017JD028049

Boehm J, Werl B, Schuh H (2006) Troposphere mapping functions for GPS and very long baseline interferometry from European Centre for Medium-Range Weather Forecasts operational analysis data. J Geophys Res 111. https://doi.org/10.1029/2005JB003629

Bolbol S, Ali AH, El-Sayed MS, Elbeah MN (2017) Performance evaluation of precise point positioning (PPP) using CSRS-PPP online service. Am J Geographic Inform Syst 6(4):156–167. https://doi.org/10.5923/j.ajgis.20170604.03

Byram S, Hackman C (2014) IGS final troposphere product update. Poster presented at IGS workshop 2014, Pasadena, 23–27 June 2014

Byun SH, Bar-Sever YE (2009) A new type of troposphere zenith path delay product of the International GNSS Service. J Geod 83:367–373

Dousa J, Bennitt GV (2013) Estimation and evaluation of hourly updated global GPS Zenith Total Delays over ten months. GPS Solutions 17(4):453–464. https://doi.org/10.1007/s10291-012-0291-7

Eludoyin OM, Adelekan IO, Webster R, Eludoyin AO (2014) Air temperature, relative humidity, climate regionalization and thermal comfort of Nigeria. Int J Climatol 34:2000–2018

Farah H (2009) The African Reference Frame (AFREF) project: a fundamental geodetic tool for Africa. Geophys Res Abstr 11:EGU2009–EG13950

Guo Q (2015) Precision comparison and analysis of four online free PPP services in static positioning and tropospheric delay estimation. GPS Solutions 19(4):537–544. https://doi.org/10.1007/s10291-014-0413-5

Isioye OA, Combrinck L, Botai J (2015) Performance evaluation of Blind Tropospheric delay correction models over Africa. S Afr J Geom 4(4):502–525. https://doi.org/10.4314/sajg.v4i4.10

Isioye OA, Combrinck L, Botai J (2016) Modelling weighted mean temperature in the West African region: implications for GNSS meteorology. Meteorol Appl 23:614–632. https://doi.org/10.1002/met.1584

Jatau B, Fernandes R, Adebomehin A, Gonçalves N (2010) NIGNET – the new permanent GNSS network of Nigeria. In: Proceedings of FIG congress 2010, Sydney

Kanamitsu M, Ebisuzaki W, Woollen J, Yang SK, Hnilo JJ, Fiorino M, Potter GL (2002) NCEP-DOE AMIP-II reanalysis (R-2). Bull Am Meteorol Soc 83:1631–1643

Leandro R, Santos M, Langley R (2010) Analyzing GNSS data in precise point positioning software. GPS Solutions 15(1):1–13. https://doi.org/10.1007/s10291-010-0173-9

Li X, Zus F, Lu C, Dick G, Ning T, Ge M, Wickert J, Schuh H (2015) Retrieving of atmospheric parameters from multi-GNSS in real time: validation with water vapor radiometer and numerical weather model. J Geophys Res Atmos 120:7189–7204. https://doi.org/10.1002/2015JD023454

Nievinski FG, Santos MC (2010) Ray-tracing options to mitigate the neutral atmosphere delay in GPS. Geomatica 64(2):191–207

Nikolaidou T, Nievinski F, Balidakis K, Schuh H, Santos M (2018) PPP without troposphere estimation: impact assessment of regional versus global numerical weather models and delay parametrization. International Association of Geodesy symposia. Accepted manuscript submitted for publication

Ogungbenro SB, Eniolu T, Morakinyo TE (2014) Rainfall distribution and change detection across climatic zones in Nigeria. Weather Clim Extrem 5:1–6

Olusola O, Kayode A, Israel E (2015) Spatial analysis of rainfall in the climatic regions of Nigeria using insitu data. J Environ Earth Sci 5(18):64–73

UCAR (2011) The troposphere – overview. https://scied.ucar.edu/shortcontent/troposphere-overview. Accessed 1 Sept 2017

Urquhart L, Santos M (2011) Development of VMF1-like service. White paper, Department of Geodesy and Geomatics, University of New Brunswick, New Brunswick

Urquhart L, Santos MC, Garcia CA, Langley RB, Leandro RF (2014) Global assessment of UNB's online precise point positioning software. IAG Symp Ser 139:585–592. https://doi.org/10.1007/978-3-642-37222-3_77

Willoughby AA, Aro TO, Owolabi IE (2002) Seasonal variations of radio refractivity gradients in Nigeria. J Atmos Sol Terr Phys 64:417–425

Zumberge JF, Heflin MB, Jefferson DC, Watkins MM, Webb FH (1997) Precise point positioning for the efficient and robust analysis of GPS data from large networks. J Geophys Res 102(B3):5005–5017. https://doi.org/10.1029/96JB03860

Part V

Global Geodetic Observing System (GGOS) and Earth Monitoring Services

GGOS Bureau of Products and Standards: Recent Activities and Future Plans

Detlef Angermann, Thomas Gruber, Michael Gerstl, Robert Heinkelmann, Urs Hugentobler, Laura Sánchez, and Peter Steigenberger

Abstract

This paper presents a summary of the activities of the Bureau of Products and Standards (BPS) to support IAG's Global Geodetic Observing System (GGOS) in its goal to provide observations and consistent geodetic products needed to monitor, map, and understand changes in the Earth's shape, rotation, and mass distribution. As a key activity the BPS has compiled an inventory of the standards and conventions currently adopted and used by the IAG and its components for the processing of geometric and gravimetric observations as the basis for the generation of IAG products. The outcome of the BPS inventory concerning numerical standards and the product-based review is summarized and recommendations for future improvements are provided. Finally, an overview about the ongoing and planned activities of the BPS is given.

Keywords

BPS inventory · Bureau of Products and Standards (BPS) · Geodesy · GGOS · IAG products · Standards and conventions

1 Introduction

The Bureau of Products and Standards (BPS) is a redefinition of the former Bureau for Standards and Conventions (BSC), which was established as a component of the Global Geodetic Observing System (GGOS) of the International Association of Geodesy (IAG) in 2009. This redefinition was a consequence of a restructuring of the GGOS organization in 2014. The organizational structure of GGOS and a description of its components is given in Kutterer and Neilan (2016) and on the GGOS webpage at www.ggos.org.

The work of the BPS is primarily built on the IAG Services and the products they derive on an operational basis for Earth monitoring making use of various space geodetic observation techniques such as Very Long Baseline Interferometry (VLBI), Satellite and Lunar Laser Ranging (SLR/LLR), Global Navigation Satellite Systems (GNSS), Doppler Orbitography and Radiopositioning Integrated on Satellite (DORIS), satellite altimetry, gravity satellite missions, gravimetry, etc. In order to fully benefit from the ongoing technological improvements of the geodetic observing systems, it is essential that the analysis of the observations is based on the definition and application of common standards and conventions and a consistent representation and parameterization of the relevant quantities. This is also a prerequisite for the integration of geometric and gravimetric observations as the basis for a consistent estimation of geodetic parameters describing the time-varying shape, rotation

D. Angermann (✉) · M. Gerstl · L. Sánchez
Deutsches Geodätisches Forschungsinstitut, Technische Universität München (DGFI-TUM), Munich, Germany
e-mail: detlef.angermann@tum.de

T. Gruber · U. Hugentobler
Institute for Astronomical and Physical Geodesy (IAPG), Technische Universität München, Munich, Germany

R. Heinkelmann
Helmholtz Centre Potsdam, German Research Centre for Geosciences (GFZ), Potsdam, Germany

P. Steigenberger
Deutsches Zentrum für Luft- und Raumfahrt (DLR), Oberpfaffenhofen, Germany

J. T. Freymueller, L. Sánchez (eds.), *International Symposium on Advancing Geodesy in a Changing World*, International Association of Geodesy Symposia 149, https://doi.org/10.1007/1345_2018_28

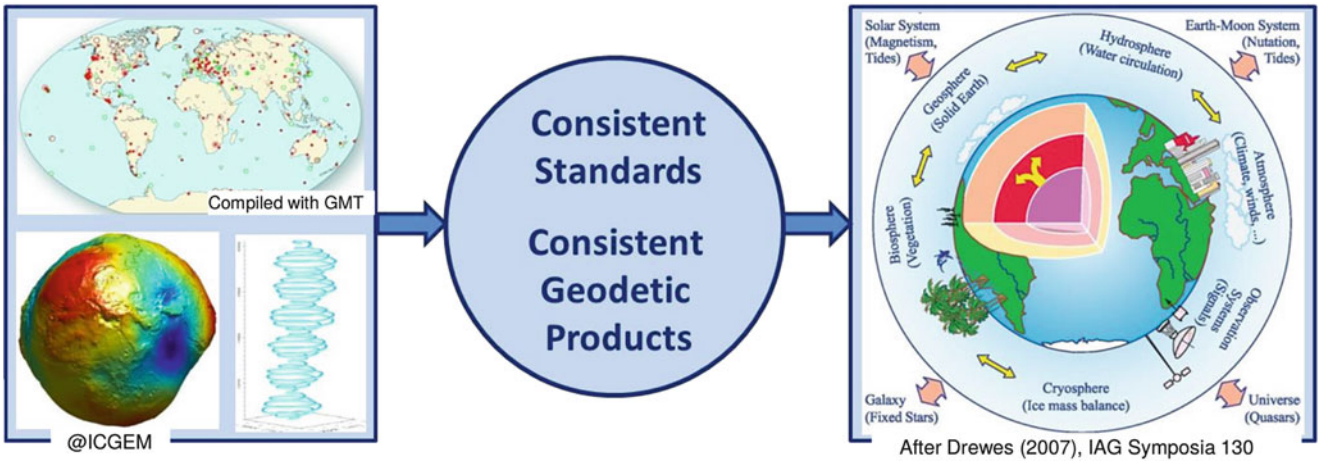

Fig. 1 The key role of standards and conventions for consistent geodetic products as the basis for Earth system research, for studying interactions between its sub-components and for precisely quantifying global change phenomena

and gravity field of the Earth. The results should refer to a highly-precise global reference frame, stable over decades in time, as a requirement for reliably monitoring global change phenomena (e.g., global sea level rise) and for providing the meteorological basis for Earth system sciences. Figure 1 illustrates the integration of the "three pillars" geometry, Earth rotation and gravity field to obtain consistent geodetic products as the basis for studying the Earth system and the interactions between its sub-components and the outer space (e.g., Rummel 2000; Drewes 2007; Plag and Pearlman 2009).

According to the GGOS Terms of Reference, the BPS acts as contact and coordinating point for the IAG Services regarding homogenization of standards and products. The IAG Services keep their full visibility and responsibility to manage their supporting data, products and information systems. The BPS shall ensure that common standards and conventions are implemented and adopted by all IAG components as a fundamental basis for the generation of consistent products. Another key task is the evaluation of the current status of IAG/GGOS products, including an accuracy assessment with respect to the GGOS requirements as specified in the GGOS 2020 book (Gross et al. 2009). The BPS also initiates the development of new products required for important geophysical questions and societal needs.

Most of these tasks cannot be fulfilled by the BPS alone and thus cooperations within the geoscientific community are essential. Towards this aim, the IAG Services and other entities involved in standards and geodetic products are represented in the BPS by means of associated members who support the Bureau business and ensure the interaction between the different components.

The purpose of this paper is to give a summary of recent and future activities of the BPS. The following section gives an overview about the Bureau, including its mission, objectives and the organizational structure. Section 3 addresses some of the key activities of the BPS, such as the compilation of an inventory on the standards and conventions currently adopted and used by IAG and its components for the generation of IAG products (Angermann et al. 2016a). Some examples of this inventory are highlighted. Finally, a summary of the ongoing and planned activities is provided.

2 GGOS Bureau of Products and Standards

The BPS is hosted and supported by the Deutsches Geodätisches Forschungsinstitut (DGFI-TUM) and the Institute for Astronomical and Physical Geodesy (IAPG) of the Technische Universität München, within the Forschungsgruppe Satellitengeodäsie (FGS). The BPS supports GGOS in its key goal to obtain consistent products describing geometry, rotation and gravity field of the Earth along with its variations in time.

The main objectives of the BPS are:

- to serve as contact and coordinating point for the homogenization of IAG standards and products;
- to keep track of the adopted geodetic standards and conventions across all IAG components, and to initiate steps to close gaps and deficiencies;
- to focus on the integration of geometric and gravimetric parameters and to develop new geodetic products, needed for Earth sciences and society.

The present BPS staff members are D. Angermann (director), T. Gruber (deputy director), M. Gerstl, R. Heinkelmann, U. Hugentobler, L. Sánchez and P. Steigenberger. In its current structure the following GGOS entities are associated with the BPS:

- Committee "Contributions to Earth System Modelling", Chair: M. Thomas (Germany),

Table 1 Representatives of IAG services and other entities (status: October 2017)

	G. Petit (until 2016)	BIPM (France)
IERS Conventions Center	N. Stamatakos (since 2017)	USNO (USA)
IERS Analysis Coordinator	T. Herring	MIT (USA)
IGS Representative	U. Hugentobler (BPS staff)	TUM (Germany)
ILRS Analysis Coordinator	E. Pavlis	UMBC/NASA (USA)
IVS Analysis Coordinator	J. Gipson	GSFC/NASA (USA)
IDS Analysis Coordinators	J.-M. Lemoine, H. Capdeville	CNES/GRGS (France)
IDS Representatives	F. Lemoine, J. Ries	GSFC, CSR (USA)
IGFS Chair	R. Barzaghi	Politecnico Milano (Italy)
BGI Chair	S. Bonvalot	IRD (France)
ISG President	M. Reguzzoni	Politecnico Milano (Italy)
ICGEM Chair	F. Barthelmes	GFZ (Germany)
IDEMS Director	K. Kelly	ESRI (USA)
IGETS Director	H. Wziontek	BKG (Germany)
Gravity Community (corresponding member)	J. Kusche	University Bonn (Germany)
IAG Representative to ISO	J. Ihde (until 2016)	BKG, now GFZ (Germany)
IAG Communication and Outreach	J. Adam	University Budapest (Hungary)
IAU Commission A3 Representative	C. Hohenkerk	HMNAO (United Kingdom)
IAU Representative	R. Heinkelmann (BPS staff)	GFZ (Germany)
	M. Craymer (Chair)	NRCan (Canada)
Control Body for ISO Geodetic Registry	L. Hothem (Vice Chair)	USA

– Joint Working Group "Establishment of the Global Geodetic Reference Frame (GGRF)",
  Chair: U. Marti (Switzerland),
– Working Group "ITRS Standards for ISO TC211", Chair: C. Boucher (France).

The Bureau comprises the staff members, the chairs of the associated GGOS components as well as representatives of the IAG Services and other entities. The present status of the associated members as BPS representatives is summarized in Table 1.

As regards the development of standards, there is a link with the Conventions Center of the International Earth Rotation and Reference Systems Service (IERS), the Commission A3 "*Fundamental Standards*" of the International Astronomical Union (IAU), the IAU Working Group "*Numerical Standards for Fundamental Astronomy*", the Bureau International de Poids et Mesures (BIPM), the Committee on Data for Science and Technology (CODATA), and the International Organization for Standardization (ISO) with its Technical Committee ISO/TC211.

As specified in the BPS Implementation Plan, a communication plan has been setup for a regular exchange of information. In addition to regular GGOS Coordinating Board Meetings (twice per year) and GGOS Consortium Meetings (once per year) monthly telecons of the GGOS Executive Committee take place to manage the day-to-day business of GGOS. Extended Bureau meetings of the BPS take place twice per year to coordinate and manage the BPS work, to monitor progress against schedule, and to redefine tasks and responsibilities in case of need. Regular meetings of the BPS team take place in Munich every 2 months to perform the operational Bureau business.

More information on the BPS can be found in the literature (e.g., Hugentobler et al. 2012; Angermann et al. 2016a,b) and on the GGOS website (www.ggos.org).

3 BPS Inventory on Standards and Conventions

The BPS has compiled an inventory of standards and conventions used for the generation of IAG products (Angermann et al. 2016a). This inventory gives a brief introduction into GGOS, including its mission and objectives and an overview about its structure. It presents some general information on standards and conventions and summarizes the current standards, standardized units, fundamental physical constants, resolutions, and conventions that are relevant for geodesy. Section 3.1 summarizes the outcome of the evaluation of numerical standards used within IAG and its components, and Sect. 3.2 focuses on the product-based inventory.

3.1 Status and Recommendations on Numerical Standards

Currently, different numerical standards are in use within the geodetic community (see Table 2). The values of the Geodetic Reference System 1980 (GRS80, Moritz 2000) are still used as official ellipsoid parameters, although it

Table 2 Comparison of numerical standards used within IAG

	Semi-major axis a (m)	Geocentric Grav. Constant GM (10^{12} m^3 s^{-2})	Dyn. form factor J_2 (10^{-6})	Earth's rotation ω (rad s^{-1})	Normal potential U_0 or W_0 (m^2 s^{-2})
GRS80 (1979)	6,378,137	398.6005	1,082.63	7.292115	62,636,860.850
EGM2008	6,378,136.3	398.6004415[a]	1,082.6359	7.292115	62,636,856.0 (1998)
IERS Conv. (2010)	6,378,136.6[b]	398.6004418[c]	1,082.6359	7.292115	62,636,856.0 (1998)
IERS Conv. (update 2017)	6,378,136.6[b]	398.6004418[c]	1,082.6359	7.292115	62,636,853.4 (2015)
IAG Resol. No. 1 (2015)					62,636,853.4 (2015)

[a]TT-compatible value
[b]Value given in zero-tide system
[c]TCG-compatible value

represents the scientific status of the 1970s. In the concept of GRS80, the tidal systems and relativistic theories are not considered (Ihde et al. 2017). The numerical standards of the IERS Conventions 2010 (Petit and Luzum 2010), which are based on the best estimates of Groten (2004), are commonly used for the processing of the geometric observations and for the generation of IERS products. The fact that the semi-major axis between GRS80 and IERS Conventions 2010 differs by 0.4 m is critical and has to be considered correctly for users of geodetic products. Table 2 also shows the numerical standards of the Earth Gravitational Model 2008 (EGM2008; Pavlis et al. 2012), which are partly different from the numerical standards given in the IERS Conventions. In cooperation between the IERS Conventions Center and the BPS, the conventional value $W_0 = 62{,}636{,}853.4\,\mathrm{m^2\,s^{-2}}$ for the geopotential at mean sea level issued in the IAG (2015) Resolution No. 1 (Drewes et al. 2016; Ihde et al. 2017; Sánchez and Sideris 2017) has recently been updated in Chapter 1 of the IERS Conventions (Stamatakos 2017). Thus, the former difference between the IERS Conventions 2010 value and the new IAG 2015 value of about $-2.6\,\mathrm{m^2\,s^{-2}}$ (equivalent to a level difference of about 27 cm) has been resolved recently. In order not to affect current definitions of time scale, W_0 is no longer related to L_G, the conventional conversion factor between the scale of terrestrial time (TT) and the geocentric coordinate time (TCG).

The current situation concerning numerical standards and the different use of time and tide systems is a potential source for inconsistencies and even errors of geodetic products. Thus, it is essential for a correct interpretation and use of geodetic results and products that the underlying numerical standards are clearly documented. Moreover, if geodetic results are combined that are expressed in different time or tide systems, transformations have to be performed to get consistent results.

The following recommendations on numerical standards have been specified in the BPS inventory, also endorsed as recommendations of the Unified Analysis Workshop 2017 (Gross and Herring 2017).

- **Recommendation 1**: The used numerical standards including time and tide systems must be clearly documented for all geodetic products.
- **Recommendation 2**: The geopotential value $W_0 = 62{,}636{,}853.4\,\mathrm{m^2\,s^{-2}}$ issued by the IAG resolution No. 1 (2015) should be used as the conventional reference value for geodetic work.
- **Recommendation 3**: The development of a new Geodetic Reference System GRS20XX based on best estimates of the major parameters related to a geocentric level ellipsoid is desired.

3.2 Product-Based Review of Standards and Conventions

In the product-based evaluation of standards and conventions the following major topics were addressed:

- Celestial reference systems and frames
- Terrestrial reference systems and frames
- Earth orientation parameters
- GNSS satellite orbits
- Gravity and geoid
- Height systems and their realizations.

IAG products exist for the celestial and terrestrial reference frame as well as for the EOP which are provided by the responsible Product Centers of the IERS (see www.iers.org). These products are derived from the data of the space geodetic observation techniques GNSS, SLR, VLBI and DORIS provided by the International GNSS Service (IGS; Dow et al. 2009), the International Laser Ranging Service (ILRS; Pearlman et al. 2002), the International VLBI Service (IVS; Schuh and Behrend 2012) and the International DORIS Service (IDS; Willis et al. 2010), respectively. These technique-specific Services and the IERS are in charge of the data analysis and combination issues for the generation of the reference frame products and the EOP. The BPS inventory gives an overview about the present status concerning the IERS products, it identifies gaps and deficiencies

and provides recommendations for further improvements for each product (Angermann et al. 2016a). The work of the BPS should be considered as a supplement to the extensive activities performed within the technique-specific IAG Services and the IERS. The present issues concerning the analysis and combination of the geometric space-techniques were discussed during the Unified Analysis Workshop 2017, which was co-organized by GGOS and the IERS. Detailed recommendations were provided in the minutes of the workshop (Gross and Herring 2017).

Some general recommendations of the BPS inventory (Angermann et al. 2016a) concerning the IERS products are provided below:

- At present, the celestial and the terrestrial reference frame and their integral EOP solutions are not fully consistent with each other as they are computed independently by separate IERS Product Centers. The Resolution No. 3 (2011) of the International Union of Geodesy and Geophysics (IUGG) recommends, that the highest consistency between the ICRF, the ITRF and the EOP as observed and realized by IAG and its components such as the IERS should be a primary goal in all future realizations of the ICRS.
- The processing standards and models should be consistently applied by all the analysis centers of the IAG Services providing data for the generation of the IERS products.
- The station networks and the spatial distribution of high quality co-location sites should be improved as a fundamental requirement to achieve the GGOS accuracy requirements as specified in chapter 7 of the GGOS 2020 book (Gross et al. 2009).

The GNSS satellite orbits are a technique-specific product provided by the IGS. It was included in the inventory, since the GNSS orbits are used for a wide range of applications. Recommendations were provided on further studies of the impact of analysis strategies on the orbit parameters and the satellite operators were asked to provide detailed information about satellite dimensions, surface properties, attitude models, antenna offsets, antenna phase patterns, and radio emission power. The European GNSS Service Center provided information about the Galileo In-Orbit Validation (IOV) and Full Operational Capability (FOC) satellites in December 2016 and October 2017, respectively (GSA 2017). The Cabinet Office, Government of Japan (CAO) published satellite property information for the first two satellites of the Quasi-Zenith Satellite System (QZSS) as well as operational history information for QZS-1 in 2017 (Cabinet Office 2017). Satellite property information for QZS-3 and -4 as well as operational history information for QZS-2 are currently in preparation.

The International Gravity Field Service (IGFS) is responsible to coordinate the gravity-related IAG Services (BGI, ISG, IGETS, ICGEM, IDEMS) and its overall goal is to coordinate the provision of gravity field related data, software and information for the scientific community (Barzaghi and Vergos 2016). The IGFS Central Bureau has recently been established at the Aristotle University of Thessaloniki providing an updated IGFS website (www.igfs.topo.auth.gr), including a dedicated products portal for the download of data and products generated by the IGFS Services (Vergos et al. 2017). As an example, about 170 models of the global gravity field of the Earth are made available to the public via the ICGEM website (icgem.gfz-potsdam.de; Barthelmes 2016). A recommendation is that a conventional global gravity field model might be useful as a reference model to be used for the generation of official IAG products, whereas scientific users should be free to use any preferred model for their particular purposes.

The last topic of the product-based inventory focuses on the height systems and their realizations. Currently, a formal GGOS height system product or an IAG Height Systems Service does not exist. An important step oriented to the establishment of a worldwide unified (standardized) vertical reference system was the release of the IAG resolution No. 1 (2015) for the definition and realization of an International Height Reference System (IHRS) and the adoption of the conventional value $W_0 = 62{,}636{,}853.4\,\mathrm{m^2\,s^{-2}}$ for the geopotential at the geoid (Drewes et al. 2016; Ihde et al. 2017; Sánchez and Sideris 2017). A proposal for the IHRF reference network with about 170 stations co-located with geometric techniques, absolute gravity and tide gauges has been prepared by the GGOS Focus Area "Unified Height System" (Sánchez 2017) and the IAG JWG 0.1.2 "Strategy for the Realization of the IHRS".

4 Ongoing and Planned Activities

An ongoing activity of the BPS is to keep track of the geodetic standards and conventions adopted by IAG and its components for the generation of IAG products. The contents of the BPS inventory (Angermann et al. 2016a) presents the status of January 15, 2016, and thus it needs to be regularly updated if new IAG products are released (e.g., ITRF2014, IERS EOP 14 C04 series, upcoming ICRF3) or if there are any other changes in the field of standards and conventions or the generation of IAG products. It is planned to provide an updated electronic version of the BPS inventory by early 2018. Concerning the recommendations given in the BPS inventory a lot of progress has already been achieved and several activities have been initiated by the responsible IAG components. The BPS has taken over a coordinating role to initiate steps how to proceed with the recommendations that require further activities. Together with the representatives of the IAG Services and other involved entities (see Table 1) an

action plan should be compiled, including a task description, specification of responsibilities and a time schedule.

The BPS also supports the development of new products derived from a combination of geometric and gravimetric observations. Towards this aim various activities have been initiated and dedicated GGOS entities have been established to focus on the development of integrated products, such as the Focus Area "Unified Height System", the newly established Focus Area "Geodetic Space Weather Research" and the Joint IAG Working Group "Establishment of the Global Geodetic Reference Frame (GGRF)" to support the activities of the United Nations (UN) in context with the UN resolution on a Global Geodetic Reference Frame for Sustainable Development (A/RES/69/266) adopted on February 26, 2015. The BPS contributed to an IAG position paper for the GGRF description (iag.dgfi.tum.de/fileadmin/IAG-docs/GGRF_description_by_the_IAG_V2.pdf), which includes the geometry, gravity field and physical heights as well as the Earth's orientation with respect to the celestial reference frame. The director of the BPS has been nominated by the IAG Executive Committee as the IAG Representative to the UN Global Geospatial Information Management (UN-GGIM) Subcommittee "Geodesy" (the former GGRF Working Group) for the Focus Group "Data Sharing and Development of Geodetic Standards". Thus, the BPS is involved in the definition and establishment of the GGRF.

The BPS activities also focus on celestial reference systems and frames and on the contributing VLBI data as well as on the relevant standards, conventions and resolutions. The IVS, as a joint service of IAU and IAG, interacts closely with the IERS, which is tasked by IAU and IUGG with maintaining the ICRF and ITRF, respectively. Within IAU, the Division A Commission A3 "Fundamental Standards" (www.iau.org/science/scientific_bodies/commissions/A3/), the Division Working Group "Numerical Standards in Fundamental Astronomy (NSFA)" (Luzum et al. 2011), and the IAU's Standards of Fundamental Astronomy (SOFA) service (www.iausofa.org) are directly involved in standards. A close link has been established between IAU and the BPS to ensure the interaction between the different components and to enable regular exchange of information.

Another external relation exists between the BPS and the International Standards Organization Technical Committee 211 (ISO/TC211) "Geographic Information/Geomatics", M. Craymer and L. Hothem were appointed as associated members of the BPS (see Table 1). The ISO/TC211 has taken responsibility for establishing the ISO Geodetic Registry, a registry of international geodetic reference systems and transformations (Craymer and Hothem 2017). In 2016, the BPS acted as the proposer for the "New Work Item Proposal" ISO/TC211: Revision of ISO 19111 "Geospatial Information – Spatial references by coordinates".

Finally, the BPS should initiate steps to identify user needs and requirements for products that are currently not provided by the IAG Services, but required to address important geophysical questions and user needs. This task should be supported by the GGOS Science Panel, the Focus Areas and representatives of the IAG Services. Such a task fits well into the Work Programme of the Group on Earth Observation (GEO), which has defined an assessment of "User Needs and Gap Analysis" as a key task. Towards this aim the contributing Global Ocean Observing System (GOOS) and the Global Climate Observing System (GCOS) have defined so-called Essential Ocean and Climate Variables (EOC/ECVs), needed to understand and predict the evolution of climate and oceans. As discussed during the IAG-IASPEI Joint Scientific Assembly in Kobe 2017 and during the GGOS Days 2017 in Vienna (October 31–November 2, 2017) it has been discussed that GGOS should also propose such variables (e.g., Essential Geodetic Variables, EGV). First ideas on this subject were presented by R. Gross during the GGOS Days 2017 (see meeting notes at www.ggos.org). Together with the GGOS Science Panel and representatives of the IAG Services the BPS should take over a leading role for such an activity.

References

Angermann D, Gruber T, Gerstl M, Heinkelmann R, Hugentobler U, Sánchez L, Steigenberger P (2016a) GGOS Bureau of Products and Standards: inventory of standards and conventions used for the generation of IAG products. In: Drewes H, Kuglitsch F, Adám J, Rozsa S (eds) The geodesist's handbook 2016. J Geod 90(10):1095–1156. https://doi.org/10.1007/s00190-016-0948-z

Angermann D, Gerstl M, Sánchez L, Gruber T, Hugentobler U, Steigenberger P, Heinkelmann R (2016b) GGOS Bureau of Products and Standards: inventory of standards and conventions for geodesy. In: Rizos C, Willis P (eds) IAG 150 years. IAG symposia, vol 143, pp 571–577. https://doi.org/10.1007/1345_2015_165

Barthelmes F (2016) International Centre for Global Earth Models (ICGEM). In: Drewes H, Kuglitsch F, Adám J, Rozsa S (eds) The geodesist's handbook 2016. J Geod 90(10):1177–1180. https://doi.org/10.1007/s00190-016-0948-z

Barzaghi R, Vergos G (2016) International Gravity Field Service (IGFS). In: Drewes H, Kuglitsch F, Adám J, Rozsa S (eds) The geodesist's handbook 2016. J Geod 90(10):1175–1176. https://doi.org/10.1007/s00190-016-0948-z

Cabinet Office (2017) QZSS Satellite information. qzss.go.jp/en/technical/qzssinfo/index.html

Craymer M, Hothem L (2017) The ISO Geodetic Registry and Related Standards. Poster presented at Joint Scientific Assembly of IAG/IASPEI in Kobe, 30 July–04 August 2017

Dow J, Neilan R, Rizos C (2009) The international GNSS service in a changing landscape of global navigation satellite systems. J Geod 83(3–4):191–198. https://doi.org/10.1007/s00190-008-0300-3

Drewes H (2007) Science rationale of the Global Geodetic Observing System (GGOS). In: Tregoning P, Rizos C (eds) Dynamic planet. IAG Symposia, vol 130. Springer, Berlin, pp 703–710. https://doi.org/10.1007/978-3-540-49350-1_101

Drewes H, Kuglitsch F, Adám J, Rozsa S (eds) The geodesist's handbook 2016. J Geod 90(10):1095–1156. https://doi.org/10.1007/s00190-016-0948-z

Gross R, Herring T (2017) Report of the GGOS/IERS Unified Analysis Workshop. Paris (2017/07/10-12). 176.28.21.212/media/filter_public/71/81/718149fd-b295-43dd-b82e-d01cacc8363e/uaw2017_report_v4.pdf

Gross R, Beutler G, Plag H-P (2009) Integrated scientific and societal user requirements and functional specifications for the GGOS (chapter 7). In: Global geodetic observing system – meeting the requirements of a global society on a changing planet in 2020. Springer, Berlin. https://doi.org/10.1007/978-3-642-02687-4

Groten E (2004) Fundamental parameters and current (2004) best estimates of the parameters of common relevance to astronomy, geodesy, and geodynamics. J Geod 77(10–11):724–731. https://doi.org/10.1007/s00190-003-0373-y

GSA (2017) Galileo Satellite Metadata. www.gsc-europa.eu/support-to-developers/galileo-satellite-metadata

Hugentobler U, Gruber T, Steigenberger P, Angermann D, Bouman J, Gerstl M, Richter B (2012) GGOS Bureau for Standards and Conventions: integrated standards and conventions for geodesy. In: Kenyon S, Pacino M C, Marti U (eds) Geodesy for planet earth. IAG symposia, vol 136, pp 995–998. https://doi.org/10.1007/978-3-642-20338-1

Ihde J, Sánchez L, Barzaghi R, Drewes H, Foerste Ch, Gruber T, Liebsch G, Marti U, Pail R, Sideris M (2017) Definition and proposed realization of the International Height Reference System (IHRS). Surv Geophys 38(3):549–570. https://doi.org/10.1007/s10712-017-9409-3

Kutterer H, Neilan R (2016) Global Geodetic Observing System (GGOS). In: Drewes H, Kuglitsch F, Adám J, Rozsa S (eds) The geodesist's handbook 2016. J Geod 90(10):1079–1094. https://doi.org/10.1007/s00190-016-0948-z

Luzum B, Capitaine N, Fienga A, Folkner W, Fukushima T, Hilton J, Hohenkerk C, Krasinski G, Petit G, Pitjeva E (2011) The IAU 2009 system of astronomical constants: report of the IAU working group on numerical standards for fundamental astronomy. Celest Mech Dyn Astron 110(4):293

Moritz H (2000) Geodetic reference system 1980. J Geod 74(1):128–162. https://doi.org/10.1007/s001900050278

Pavlis NK, Holmes SA, Kenyon SC, Factor JK (2012) The development of the Earth Gravitational Model 2008 (EGM2008). J Geophys Res 117(B04406). https://doi.org/10.1029/2011JB008916

Pearlman M, Degnan J, Bosworth J (2002) The international laser ranging service. Adv Space Res 30(2):135–143

Petit G, Luzum B (2010) IERS conventions 2010. IERS Technical Note No. 36, Frankfurt am Main

Plag H-P, Pearlman M (2009) Global geodetic observing system – meeting the requirements of a global society on a changing planet in 2020. Springer, Berlin. https://doi.org/10.1007/978-3-642-02687-4

Rummel R (2000) Global Integrated Geodetic and Geodynamic Observing System (GIGGOS); In: Rummel R, Drewes H, Bosch W, Hornik H (eds) Towards an integrated global geodetic observing system (IGGOS). IAG symposia, vol 120, pp 253–260. https://doi.org/10.1007/978-3-642-59745-9_53

Sánchez L (2017) Focus Area 1: Unified Height System. In: Drewes H, Kuglitsch F, Adám J, Rozsa S (eds) The geodesist's handbook 2016. J Geod 90(10):1091. https://doi.org/10.1007/s00190-016-0948-z

Sánchez L, Sideris MG (2017) Vertical datum unification for the International Height Reference System (IHRS). Geophys J Int 209(2):570–586. https://doi.org/10.1093/gji/ggx025

Schuh H, Behrend D (2012) VLBI: a fascinating technique for geodesy and astrometry. J Geodyn 61:68–80. https://doi.org/10.1016/j.jog.2012.07.007

Stamatakos N (2017) Update IERS Conventions Chapter 1, November 2017. iers-conventions.obspm.fr/2010/2010_update/chapter1/icc1.pdf. maia.usno.navy.mil/conventions/2010/2010_update/chapter1/icc1.pdf

Vergos G, Grigoriadis V, Barzaghi R, Carrion D, Bonvalot S, Barthelmes F, Reguzzoni M, Wziontek H, Kelly K (2017) IGFS geoportal development for gravity, geoid, GGM and DEM data. Poster presented at Joint Scientific Assembly of IAG/IASPEI in Kobe, 30 July–04 August 2017

Willis P et al. (2010) The International DORIS Service: toward maturity. Adv Space Res 45(12):1408–1420. https://doi.org/10.1016/j.asr.2009.11.018

Recent Activities of the GGOS Standing Committee on Performance Simulations and Architectural Trade-Offs (PLATO)

Benjamin Männel, Daniela Thaller, Markus Rothacher, Johannes Böhm, Jürgen Müller, Susanne Glaser, Rolf Dach, Richard Biancale, Mathis Bloßfeld, Alexander Kehm, Iván Herrera Pinzón, Franz Hofmann, Florian Andritsch, David Coulot, and Arnaud Pollet

Abstract

The Standing Committee on Performance Simulations and Architectural Trade-Offs (PLATO) was established by the Bureau of Networks and Observations of the Global Geodetic Observing System (GGOS) in order to support – by prior performance analysis – activities to reach the GGOS requirements for the accuracy and stability of the terrestrial reference frame. Based on available data sets and simulated observations for further stations and satellite missions the committee studies the impact of technique-specific improvements, new stations, and additional co-locations in space on reference frame products. Simulation studies carried out so far show the importance of the individual station performance and additional stations for satellite laser ranging, the perspectives for lunar laser ranging assuming additional stations and reflectors, and the significant impact of the new VGOS antennas. Significant progress is achieved in processing VLBI satellite tracking data. New insights in technique-specific error sources were derived based on real data from short baselines. Regarding co-location in space PLATO members confirmed that E-GRASP could fulfill the GGOS requirements with reaching a geocenter and scale accuracy and stability of 1 mm and 0.1 mm/year, respectively.

Keywords

Co-location · DORIS · GGOS · GNSS · Reference frames · SLR · VLBI

B. Männel (✉)
GFZ German Research Center for Geosciences, Potsdam, Germany
e-mail: benjamin.maennel@gfz-potsdam.de

D. Thaller
Bundesamt für Kartographie und Geodäsie, Frankfurt am Main, Germany

M. Rothacher · I. Herrera Pinzón
Institut für Geodäsie und Photogrammetrie, ETH Zürich, Zurich, Switzerland

J. Böhm
Technische Universität Wien, Vienna, Austria

J. Müller · F. Hofmann
Institut fur Erdmessung, Leibniz Universität Hannover, Hanover, Germany

R. Biancale
CNES/GRGS, Toulouse, France

M. Bloßfeld · A. Kehm
Deutsches Geodätisches Forschungsinstitut der Technischen Universität München (DGFI-TUM), Munich, Germany

R. Dach · F. Andritsch
Astronomical Institute of the University of Bern, Bern, Switzerland

S. Glaser
Institute of Geodesy and Geoinformation Science, Technical University of Berlin, Berlin, Germany

GFZ German Research Center for Geosciences, Potsdam, Germany

D. Coulot · A. Pollet
IGN/LAREG, Marne la Vallee, France

J. T. Freymueller, L. Sánchez (eds.), *International Symposium on Advancing Geodesy in a Changing World*,
International Association of Geodesy Symposia 149, https://doi.org/10.1007/1345_2018_30

1 Purpose and Scope of PLATO

The International Terrestrial Reference Frame (ITRF) is commonly used as realization of the terrestrial reference system and is generated by combining the observations of Global Navigation Satellite Systems (GNSS), Very Long Baseline Interferometry (VLBI), Satellite Laser Ranging (SLR), and Doppler Orbitography and Radiopositioning Integrated by Satellite (DORIS) based on terrestrial measured local ties. Despite of the fact the reference frame realizations are being constantly improved, even the recent realization named ITRF2014 does not reach the GGOS requirements of 1 mm station coordinate accuracy and 0.1 mm/year stability (Altamimi et al. 2016). The reasons for today's limitations are technique-specific error sources, inhomogeneous network distributions, and the small number of accurate local ties. Consequently the following improvements are discussed to reach the GGOS requirements: (1) developing next generation space-geodetic stations with improved technology and system performance, (2) improving the ground network configuration in view of global coverage and co-locations, (3) improving the number and accuracy of surveys between co-located stations, and (4) deploying, improving and optimizing space-based co-locations. In the framework of the GGOS Bureau of Network and Observations (GGOS BNO) the Standing Committee on Performance Simulations and Architectural Trade-Offs (PLATO) was formed to support ongoing and future activities in the four topics mentioned above. From the viewpoint of reference frame products PLATO aims to estimate the dependency of such products:

- on ground station architectures,
- on new co-location and core stations which fill gaps in the current station networks (especially in the southern hemisphere),
- on the quality and number of local ties (at ground sites) and space ties (on-board satellites),
- on additional satellites, especially in the SLR space segment (e.g., cannonball satellites, LEO, GNSS constellations) and additional lunar reflectors,
- on additional co-locations in space, e.g., on-board existing GNSS and LEO satellites or on-board dedicated co-location satellites like E-GRASP/Eratosthenes.

Twelve groups from institutions in Europe and the US contribute currently to PLATO (Table 1). Since 2015, PLATO acts also as Joint Working Group 1.1.2 under IAG's Sub-Commission 1.1.

Table 1 PLATO members (as of August 2017)

Institution	Country	Participants
AIUB, Uni Bern	Switzerland	R. Dach, F. Andritsch
BKG	Germany	D. Thaller
CNES	France	R. Biancale
DGFI-TUM	Germany	M. Bloßfeld, A. Kehm
ETH Zurich	Switzerland	M. Rothacher, I Herrera Pinzón
GFZ/TU Berlin	Germany	B. Männel, S. Glaser
GSFC/JCET	United States	E. Pavlis
IfE, Uni Hannover	Germany	J. Müller, F. Hofmann
IGN France	France	D. Coulot, A. Pollet
JPL	United States	R. Gross
NMA	Norway	E. Mysen, G. Hjelle
TU Vienna	Austria	J. Böhm, A. Hellerschmied

2 Activities and Recent Achievements

Since PLATO's kickoff meeting in April 2013, several projects were initiated by the PLATO members and became funded by national science foundations, e.g., "DIrect GEocentric Realization of the American reference frame by combination of geodetic observation TechnIques" (DIGERATI, DGFI-TUM), "Satellite Observations by Radio Telescopes for Superior Reference Frame Interconnections" (SORTS, TU Wien and Bonn University), "GGOS-SIM" (GFZ/TU Berlin), or "KoKoRef" (BKG). In addition, major efforts were carried out to implement required simulating and processing tools into existing software packages, like a VLBI satellite tracking mode in VieVS, in GINS and in the Bernese GNSS Software and SLR simulation capabilities in DOGS and Bernese GNSS Software. In the following, selected activities carried out by the PLATO members and preliminary results are described related to laser ranging, fundamental sites, and co-location in space.

2.1 Studies Related to Satellite and Lunar Laser Ranging

Driven by the inhomogeneously distributed SLR station network and LAGEOS-dominated observation statistics simulations for improved global SLR solutions were carried out. By simulating up to eight additional SLR stations the group of DGFI-TUM showed improvements of up to 20% in terms of WRMS for Helmert transformation parameters with respect to SLRF2008. However, they considered also an increase in the performance of the existing stations, where performance

is defined as relationship between actually observed satellite arcs and the maximum possible number of observable satellite arcs. Assuming a performance of at least 20% for each SLR site, while current performances of SLR stations typically range between 4 and 51%, the scale was improved by 49% and the pole coordinates by 10% (Bloßfeld et al. 2018; Kehm et al. 2017). Another interesting improvement for the ERP was found at AIUB in a dedicated simulation study. They assumed that 10% of the current measurements of LAGEOS were done to ETALON. Without any degradation in the estimated station coordinates and LAGEOS orbits they found an improvement in the ERP recovery of 8% with respect to the original observation scenario (Andritsch et al. 2017). Simulations at TU Berlin/GFZ taking the total cloud coverage for the planned SLR stations into account demonstrate that American Samoa, Easter Island, Haleakala, and Hartebeesthoek are very important stations for polar motion estimates (improvements up to 56% in y_p in case of Easter Island (Glaser et al. 2017b)).

Simulations related to Lunar Laser Ranging (LLR) were carried out by the group in Hannover. Results from Lunar solutions with two new ground stations and three new single-prism reflectors on the Moon were compared against a solution containing the recent measurement configuration (basically two ground stations and five reflector arrays). Assuming future millimeter ranging accuracies they estimated lunar reflector coordinates, the mass of the Earth-Moon system, the temporal variation of the gravitational constant and tested the equivalence principle with Earth and Moon as test bodies. While two additional stations improve the accuracy of the estimated parameters up to a factor of two, three additional single-prism reflectors on the lunar surface would lead to an improvement of up to a factor of six over a decade of new measurements (Hofmann 2017; Hofmann et al. 2014).

2.2 Studies Related to Fundamental Sites

The PLATO members contributed to several station proposals by extended simulations, e.g. the French groups carried out extensive simulations for a new fundamental site in Tahiti.

Investigations of technique-specific error sources were carried out at ETH Zurich with the analysis of GNSS and VLBI short baselines. The GNSS baselines show repeatabilities better than 2 mm for most of the considered sites. However, their comparison with terrestrial local ties shows differences surpassing the centimetre level. These analyses also revealed the presence of unusual seasonal signals at Irkutsk and Obninsk (Russia), with periods of ∼4 months, which have to be further clarified (Herrera Pinzón and Rothacher 2018). Studies of the short baseline between the legacy Radio Telescope Wettzell (RTW) and the first Twin Telescope (TTW1) in Wettzell show a satisfactory agreement w.r.t. a terrestrial two-way time transfer system, at the level of ±50 ps. Additionally, these results show that differences of VLBI-based baselines w.r.t. terrestrial measurements are below 1 mm. A comparison of the tropospheric zenith delays for VLBI and a co-located GNSS antenna shows again a fair agreement, with a bias of around 1 mm attributed to height differences between the reference points of the techniques. VLBI simulations performed at GFZ and TU Berlin for a network of VGOS telescopes which is expected to be operational in 2020 by using next generation broadband VLBI technology, show that the GGOS requirements of 1 mm accuracy can be achieved for the VLBI reference frame. In addition, the impact of systematically wrong local ties on the reference frame products was studied. By falsifying the local ties connected to one technique at one station by 1 cm in the height component the technique and the station with the largest impact on the Helmert parameters (up to 0.5 mm in the height component) were analyzed. The derived results indicate Hartebeesthoek, Hobart, Tahiti, and Kokee Park as important local tie sites (Glaser et al. 2017a).

2.3 Studies Related to Co-location in Space

Linking the space geodetic techniques on-board satellites using space ties is seen as a challenging but promising addition to the ground-based local ties approach. Several members of PLATO contributed simulation studies to the E-GRASP/Eratosthenes proposal submitted to ESA answering the Earth-Explorer-9 call (Biancale et al. 2017). GPS, SLR, VLBI, and DORIS simulations carried out at IGN and CNES confirmed that reference frame solutions combined using solely E-GRASP's space ties could fulfill the GGOS requirement for geocenter and scale including their rates within the envisaged mission duration of 5 years. DGFI-TUM found a significant improvement of up to 60% for the Stokes coefficients (especially for the C_{20} and C_{40} coefficients) derived from simulated SLR measurements containing E-GRASP, LAGEOS, LARES, and ETALON. VLBI observations of GNSS satellites and the Chinese APOD cube-satellite by the Australian VLBI antennas were processed by the groups at TU Wien and ETH Zurich. The derived results, currently with residuals at the ns-level, show the potential of VLBI satellite tracking but also the necessity of further developments in VLBI satellite tracking (Plank et al. 2017).

3 Preliminary Recommendations

So far PLATO can give preliminary recommendations related mainly to laser ranging. For SLR, firstly, a coordinated increase of ETALON observations should be further con-

sidered at the expense of LAGEOS observations. Secondly, in addition to building new SLR stations, existing laser telescopes should be encouraged and supported to increase their performance, if possible, to the proposed level of 20%. In terms of LLR additional stations capable to perform measurements to (new) lunar reflectors are highly important to achieve highest accuracy. Despite technique-specific advice, simulations performed by PLATO members showed impressively the benefits of the proposed E-GRASP mission. Therefore, we recommend to strive by all means for a satellite mission dedicated to co-location in space.

4 Future Plans

PLATO's goals for the next 2 years are defined in the current GGOS BNO implementation plan (Pearlman et al. 2017). First of all, it is planned to define a list of trade-off options for station deployment and closure as well as technology upgrades. The ongoing simulation studies will be continued with the focus on network configuration, technique and technology mix, and local tie accuracy for the ground network and with the focus on space tie accuracy and mission scenarios for co-location satellites. As the recent achievements are based on different software packages, an "analysis campaign" with exchanged simulated observations is envisaged. This analysis experiment will lead to a review of recent analysis methods for reference frame products by including all existing data and available co-locations.

References

Altamimi Z, Rebischung P, Metivier L, Collilieux X (2016) ITRF2014: a new release of the international terrestrial reference frame modeling nonlinear station motions. J Geophys Res 121(8):6109–6131. https://doi.org/10.1002/2016JB013098. 2016JB013098

Andritsch F, Grahsl A, Dach R, Jäggi A (2017) Comparing tracking scenarios to LAGEOS and Etalon by simulating realistic SLR observations. In: EGU general assembly, geophysical research abstracts, vol 19. EGU2017-16642

Biancale R, Pollet A, Coulot D, Mandea M (2017) E-GRASP/Eratosthenes: a mission proposal for millimetric TRF realization. In: EGU general assembly, geophysical research abstracts, vol 19. EGU2017-8752

Bloßfeld M, Rudenko S, Kehm A, Panafidina N, Müller H, Angermann D, Hugentobler U, Seitz M (2018) Consistent estimation of geodetic parameters from SLR satellite constellation measurements. J Geod (under review)

Glaser S, König R, Ampatzidis D, Nilsson T, Heinkelmann R, Flechtner F, Schuh H (2017a) A global terrestrial reference frame from simulated VLBI and SLR data in view of GGOS. J Geod 91(7):723–733. https://doi.org/10.1007/s00190-017-1021-2

Glaser S, König R, Neumayer KH, Nilsson T, Heinkelmann R, Schuh H, Flechtner F (2017b) Simulated multi-technique TRFs for GGOS with focus on enhanced SLR and VLBI ground network architecture. In: IAG-IASPEI 2017, Abstract. G07-2-04

Herrera Pinzón I, Rothacher M (2018) Assessment of local GNSS baselines at fundamental sites. J Geod. https://doi.org/10.1007/s00190-017-1108-9

Hofmann F (2017) Lunar laser ranging - verbesserte Modellierung der Monddynamik und Schätzung relativistischer parameter. PhD thesis, Leibniz Universität Hannover. Deutsche Geodätische Kommission bei der Bayerischen Akademie der Wissenschaften, Reihe C, Nr. 797

Hofmann F, Müller J, Biskupek L, Currie D (2014) Benefit of the next generation corner cubes for lunar laser ranging analysis. In: EGU general assembly conference abstracts, vol 16, p 3299

Kehm A, Bloßfeld M, Pavlis E, Seitz F (2017) Future global SLR network evolution and its impact on the terrestrial reference frame. J Geod. https://doi.org/10.1007/s00190-017-1083-1

Pearlman M, Ma C, Neilan R, Noll C, Pavlis E, Saunier J, Schöne T, Barzaghi R, Thaller D, Bergstrand S, Müller J (2017) The GGOS bureau of networks and observations: an update on the space geodesy network and the new implementation plan for 2017-18. In: EGU general assembly, geophysical research abstracts, vol 19. EGU2017-10814-1

Plank L, Hellerschmied A, McCallum J, Böhm J, Lovell J (2017) VLBI observations of GNSS-satellites: from scheduling to analysis. J Geod 91(7):867–880. https://doi.org/10.1007/s00190-016-0992-8

IGFS Metadata for Gravity. Structure, Build-up and Application Module

G. S. Vergos, V. N. Grigoriadis, R. Barzaghi, and D. Carrion

Abstract

Gravity field related products have been the focus of almost all geosciences in the sense that they give a realistic representation of the physical properties of system Earth. The rigorous documentation and archiving of gravity field related data (e.g., absolute gravity, gravity anomalies etc.), either irregularly distributed and on a grid, has become mandatory in order to ensure coherent and unambiguous utilization by users and archiving in related data management servers and services. Given the above, the International Gravity Field Service (IGFS) has taken steps in order to generate metadata for gravity field related data so that fragmentation of databases at national and international level as well as user needs can be addressed. To that respect, a new ISO19115-1 profile for gravity field metadata has been prepared, describing all necessary fields that the metadata should have, while an online PHP-based (PHP: Hypertext Preprocessor) web application (XML generator) has been developed and became available as an IGFS product to assist users to generate compliant metadata. In this work, we describe the main characteristics of the metadata structure and give details on the developed web application. Finally, the dedicated IGFS application server, igfsapps.topo.auth.gr, is described and details on the incorporation of the gravity metadata application as an online IGFS service are provided.

Keywords

Gravity · International Gravity Field Service · ISO19115 · Metadata

1 Introduction

Before the digital era and the exchange of information through the internet, available datasets were usually accompanied by proper documentation in order to describe their characteristics, standards, collection and generation methods, and applications. In many cases, the exchange of datasets did not include the documentation because either it was deemed unnecessary, it was lost or became missing. Moreover, as these datasets were processed, the documentation, when available, was not necessarily updated or redistributed. This is also the case with historic gravity observations, both marine and land, for which little or no information is available. When historic gravity datasets become available, they come with little documentation on their gravity and spatial reference system, tide conventions, accuracy, processing methodology, type of gravity anomaly, instrumentation, etc. In the digital era where all historical data begun to be digitized, the absence of information about what the data really describe lead to significant uncertainties, where in the worst case rendered them unusable. With respect to the modern datasets created, although the process of preparing the supplemental data description is much simpler,

G. S. Vergos (✉) · V. N. Grigoriadis
GravLab, Department of Geodesy and Surveying, Faculty of Rural and Surveying Engineering, Aristotle University of Thessaloniki, Thessaloniki, Greece
e-mail: vergos@topo.auth.gr

R. Barzaghi · D. Carrion
DICA, Politecnico di Milano, Piazza Leonardo da Vinci, Milan, Italy

J. T. Freymueller, L. Sanchez (eds.), *International Symposium on Advancing Geodesy in a Changing World*, International Association of Geodesy Symposia 149, https://doi.org/10.1007/1345_2018_38

this is usually restrained by lack of time, personnel costs, complicated requirements and other factors (Giuliani et al. 2016). Without the necessary supplemental information the exchange of datasets may be problematic.

In the last two decades, Spatial Data Infrastructures (SDI) have played a significant role in archiving, discovering, delivering and exchanging geospatial data. One of the key components necessary for SDI to operate is the availability of metadata (Masó et al. 2012), i.e., data that describe the geospatial datasets. The metadata may include various information such as owner of the data, distributor, license and usage rights, spatial reference, area coverage and format as well as other more specific details. These details usually depend on the type and the purpose of the dataset as well as the usage of the metadata. Moreover, the metadata may include information that allows assessing whether the dataset is suitable for the needs of the end-user. In many cases, the metadata adhere to standards provided by the issuer, working groups or international organizations, e.g., the International Organization for Standardization (ISO). When the existing standards do not cover the needs of a specific community, agency or organization then there is the option to further develop an existing one or in rare cases create a new one. For standards prepared by ISO, when an existing standard is further extended, the new standard is called a profile. It should be noted that the profile must also adhere to certain rules set by ISO, like, for example, retaining the name, definition and data type of existing elements, include all mandatory elements and sections, etc.

In gravity field studies, where both absolute and relative gravity data are concerned, there currently exists no standard for describing the datasets produced and distributed. In order to fulfill this need, the International Gravity Field Service (IGFS) prepared such a metadata standard. The IGFS standard for gravity metadata is a profile of ISO19115-1:2014 (ISO 2014), where the latter provides the fundamental metadata information for describing datasets that have geographic extents. The present paper aims to present this new standard along with the online application developed specifically for creating compliant gravity metadata in XML format.

2 Metadata Structure

As an extension of the ISO19115-1, the IGFS standard includes apart from the standard fields of information, additional ones for describing gravity data. These fields of information contained in the IGFS standard may be grouped in five categories: (a) Metadata reference information, (b) Identification information, (c) Distribution information, (d) Standards and Conventions and (e) Data and data quality information. The first three categories (a, b and c) contain

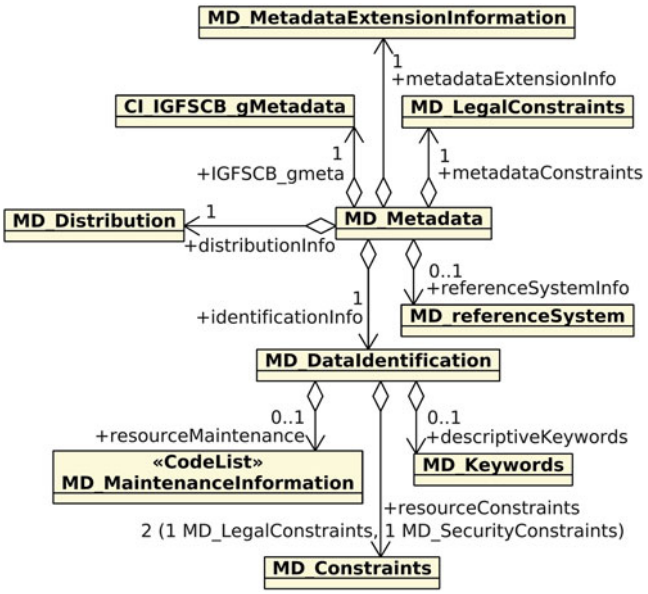

Fig. 1 Top-level classes and associations in the new profile

information only found in the ISO19115-1 standard while the other two (d) and (e) are an extension to the ISO standard specifically for gravity data. Figure 1 shows the top-level classes of the profile and their associations (without their attributes). All classes in the new standard include in their name the abbreviation "IGFSCB". It should be noted that the MD_Metadata class is the root class of the standard, while the CI_IGFSCB_gMetadata is the class that defines the additional gravity specific metadata.

The three default categories of ISO19115-1 received a small number of modifications that pertain mainly to changing the necessity of some elements, i.e., changing their requirement from optional to mandatory. For example, in the metadata profile it is required to provide information for restrictions on the access and use of the metadata. Moreover, it is mandatory to include information about the distributor of the referred gravity data and options for obtaining it. As far as the domain of values for the reference system is concerned, it was limited to the code values provided by the International Association of Oil and Gas Producers (IOGP) EPSG Geodetic Parameter Dataset in order to facilitate interoperability (IOPG 2012).

Of importance was maintaining balance between the number of mandatory and optional fields. As the number of mandatory fields increases, users tend to move away from such a standard in order to avoid the complexity as well as the time loss. On the other hand, too many optional fields may lead users who create the metadata to provide the minimum possible information. In order to make sure that the new standard meets the requirements of the geodetic community, a different approach was followed for its preparation.

First, a new standard was prepared independently of the existing ones by defining the necessary classes and properties for gravity data. In a next step, the newly compiled standard was examined against ISO19115-1. After the differences and inadequacies were identified, modifications were made in order to make it compatible with ISO19915-1, while any additional metadata elements were included in new classes that formed the final profile. It should be noted though that there is still work in progress to enhance the structure of the extension. Therefore, the end-users should be aware that the specifications are subject to change. Figure 2 presents the new metadata classes included in the IGFS metadata standard profile of ISO19115-1.

The main class CI_IGFSCB_gMetadata is composed of two parts. The first part (CI_IGFSCB_gStandardsConventions) deals with describing standards and conventions, including the adopted values used while obtaining the original gravity observations or during processing gravity data (see Fig. 2a). The second part deals mainly with their quality in terms of accuracy (CI_IGFSCB_dataQuality), referring to both the accuracy of the acquired or processed gravity observation as well as that of the position and height. The main class has been designed to fit the needs of single station observations as is the case for example of absolute gravimetry. In the case of a single gravity observable at a measurement station, an optional class (CI_IGFSCB_stationCoordinatesAbsGravity) may be used for specifying the coordinates of the station as well as more detailed information like, for example, density value, vertical gravity gradient and air pressure corrections (see Fig. 2b). On the other hand, it incorporates also the case where gravity data have been processed and a gravity database has become available, either as gridded or irregularly distributed point values.

A significant number of classes (see Fig. 2c) are available for providing detailed information related to tides (solid earth tides, tidal ocean loading, tide system, wave groups, vertical gravity gradient used, atmosphere admittance function, etc.). It should be noted though that the tidal information is optional as in the past it was seldom to provide such information. Nevertheless, for the user and/or agency who wish to provide such detailed information for future reference, the

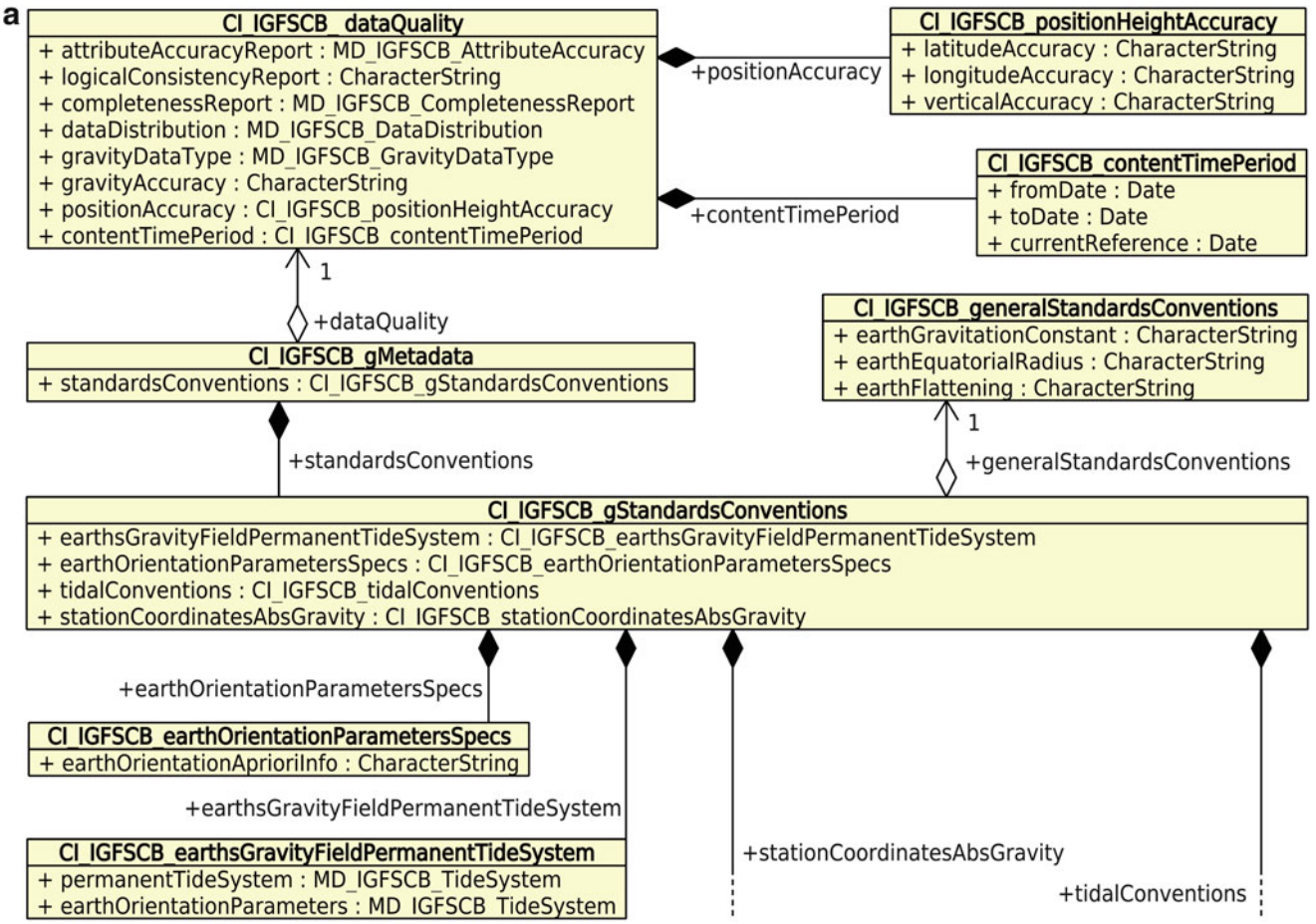

Fig. 2 (**a**) New classes and associations included in the new profile for data quality and standards and conventions. (**b**) g-metadata on gravity data coordinates. Vertical gradient and corrections. (**c**) g-metadata classes and associations for tidal conventions

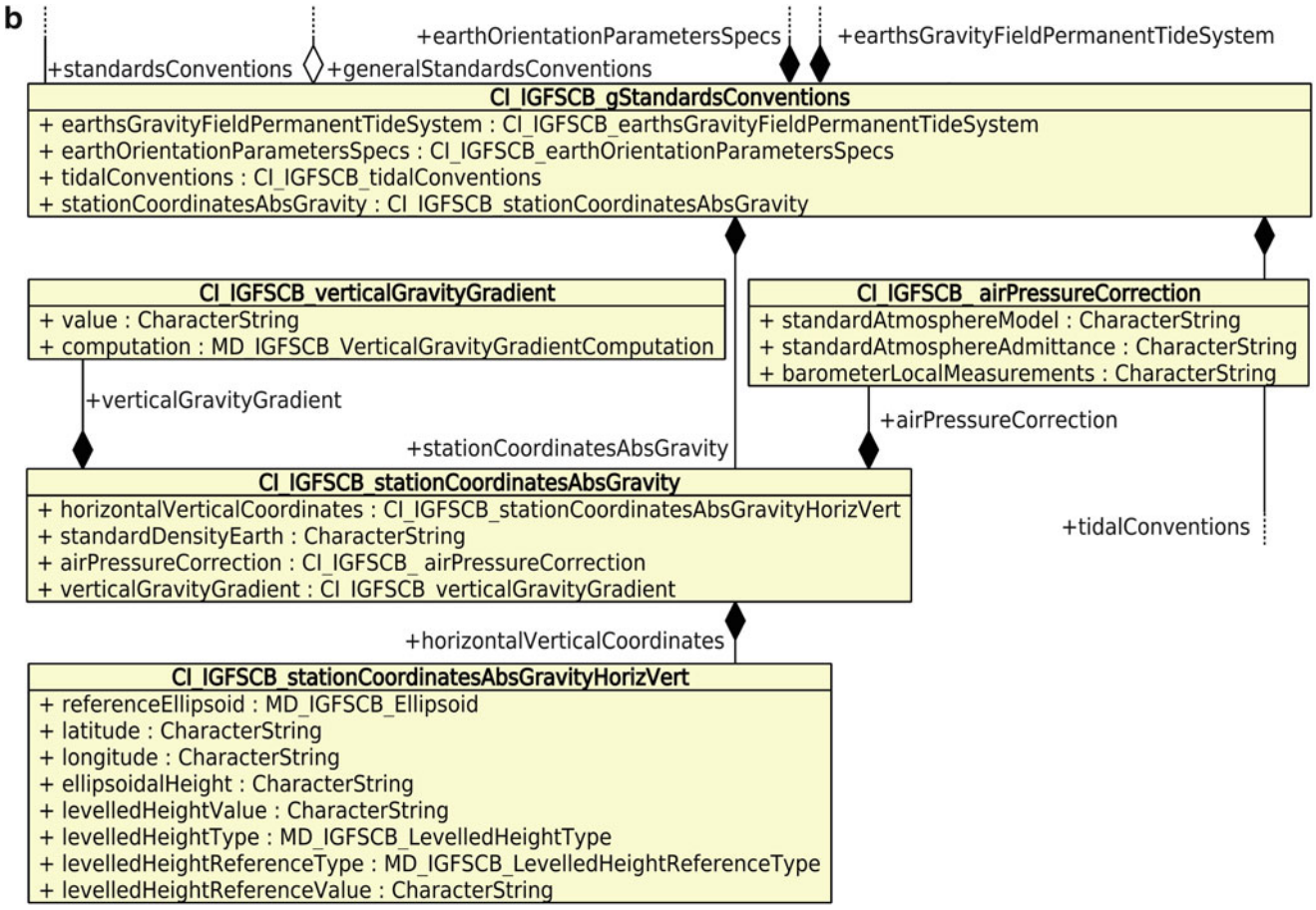

Fig. 2 (continued)

current IGFS metadata standard facilitates input for all available specifications. As far as the data quality is concerned, the corresponding class (CI_IGFSCB_dataQuality) contains information pertaining to the accuracy of the gravity data, i.e., the positional accuracy (horizontal and vertical/height component) and the accuracy of the gravity values. As the accuracy is usually examined along with the time period the data were collected, it was decided to include also the so-called content time period, i.e., the period during which the data have been acquired and/or processed.

The new classes are also accompanied by nine newly specified Code Lists whose names are self explanatory. Code lists are practically predefined lists that are usually based on commonly accepted set of values and include the reference ellipsoid used, the tide conventions, the type of levelled height, the way the vertical gravity gradient was computed and the type of gravity data, its accuracy (e.g., variable or constant) and its distribution (e.g., on a grid). Table 1 lists the new Code Lists included in the profile along with some of their values. From the provided lists, the Code List for defining the reference ellipsoid used in the gravity data (MD_IGFSCB_Ellipsoid) is based on the EPSG Geodetic Parameter Dataset (IOPG 2012).

Table 1 New Code Lists declared in the new standard

Code List	Sample values
MD_IGFSCB_TideSystem	Mean, tide free, zero tide
MD_IGFSCB_LevelledHeightType	Physical, Helmert, normal
MD_IGFSCB_LevelledHeightReference Type	Local geoid, local MSL, IHRS/IHRF
MD_IGFSCB_VerticalGravityGradient Computation	Model or own measurements
MD_IGFSCB_Ellipsoid	GRS 1980, International 1924, WGS 84
MD_IGFSCB_AttributeAccuracy	Variable accuracy provided with the data
MD_IGFSCB_CompletenessReport	Data available for parts of the area
MD_IGFSCB_DataDistribution	Irregular point data, on a grid, single station
MD_IGFSCB_GravityDataType	Absolute gravity, free-air gravity anomaly

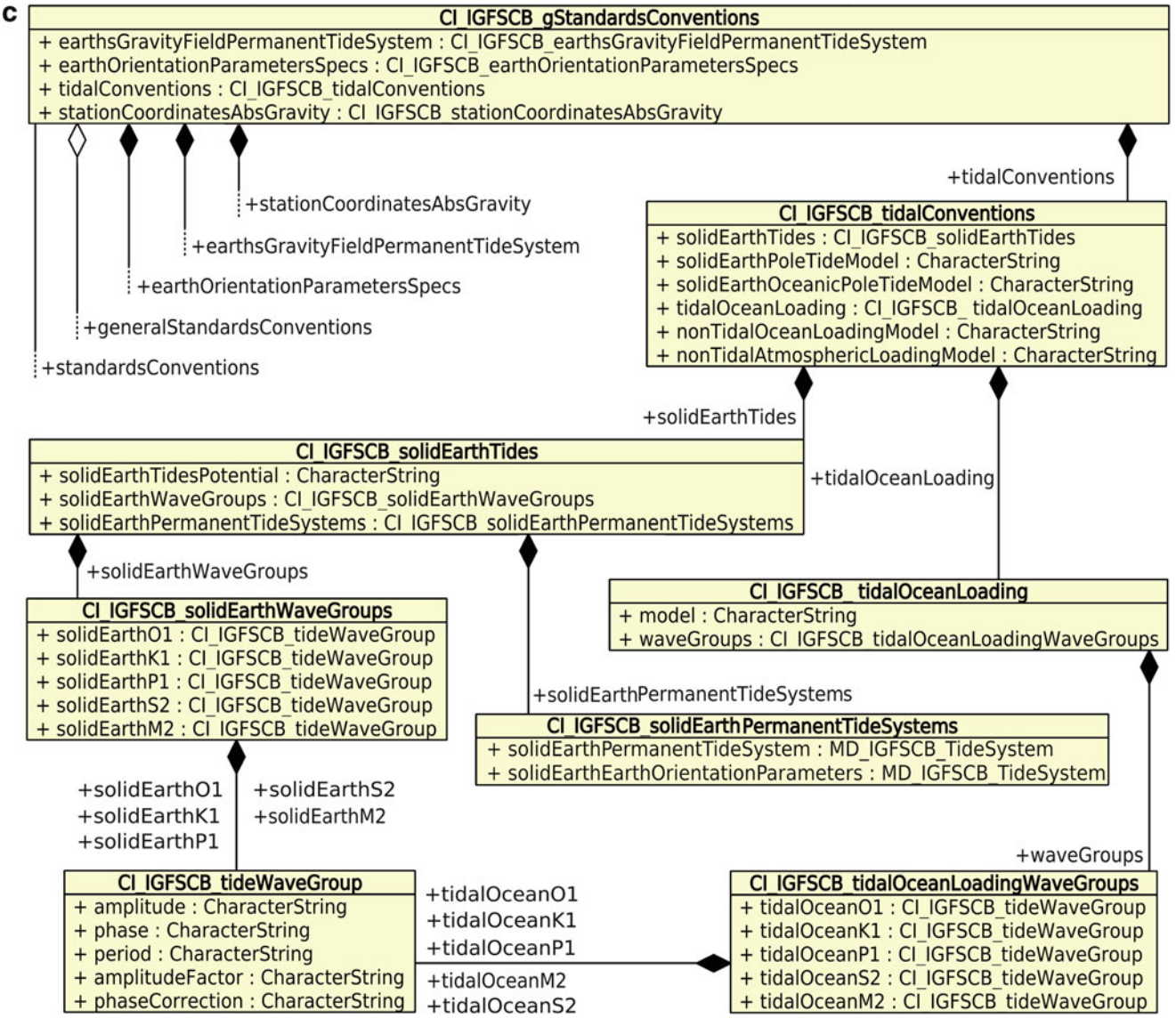

Fig. 2 (continued)

3 Web Application deployment

From the initial concept of the gravity metadata creation, the IGFS Central Bureau (CB) has targeted on the development of online apps through a web interface. Open-source and free to use technologies have been adopted for the deployment both of the web server and the development of the applications. The web server is currently deployed as a virtual machine at the Aristotle University of Thessaloniki virtual machine host, which offers minimum downtime, automatic server backup and most importantly, security as all virtual machines are constantly monitored for threats. It should be noted that this decision could be reconsidered in case the generated traffic and requirements increase, although this is not expected in the near future. On the virtual machine, a Debian Linux server has been installed while the website is hosted on an Apache HTTP Server. The aforementioned software selection was based on four criteria: (a) no or minimum cost, (b) reliability, (c) stability and (d) community acceptance.

Two online apps for the creation of metadata (g-μeta for metadata related to gravity datasets and N-μeta for metadata related to geoid models and geoid heights) are currently under development. g-μeta is currently on a beta-testing stage while N-μeta is on an alpha stage (its standard is still under consideration) and hence not yet been released. Both apps use HTML5 and CSS3 for their interface, JavaScript, jQuery, Modernizr and PHP for their functionality while Oracle NetBeans was used as the development environment.

The most important criteria, apart from using free and open-source technologies, was compatibility. As the online apps aim to be used by different users, each adopting a variety of devices and means for accessing the IGFS CB online-apps website, it was necessary to ensure that all of them will share the same experience. Moreover, the developed applications have been designed to be lightweight but self-contained and user-friendly. The size of the g-μeta apps is about 3MiB including all the necessary libraries.

g-μeta produces as output an XML file based on the user supplied information in accordance to the new profile discussed in the previous section. This can be achieved through the user interface of the application. The interface (see Fig. 3) consists of five sections where each section provides the optional and necessary information for creating the final metadata XML file. For each quantity, units are provided on the interface although they are not recorded in the XML file and hence the end-users should consult the standard specifications. The app users have also the ability to hide some subsections, therefore skip entering this information, and consequently exclude them from the XML file. By hiding complete subsections, the app users can better focus on the main fields of information that concern them and for which they can provide input. Upon filling in information in all five sections, the users move on to the Finalize section where all information is being validated. If the validation succeeds the app users may choose to prepare the final metadata file and then be provided with a link for downloading the produced XML file. Each XML file produced has a unique filename (and URL address for download) and therefore privacy of the app users information is guaranteed. The produced XML files are deleted on a daily basis although it has been predicted to include in the future the option for the users to choose to make the metadata publicly available through the IGFS CB platform. This functionality, though not included yet, refers to the case that the users wish to submit

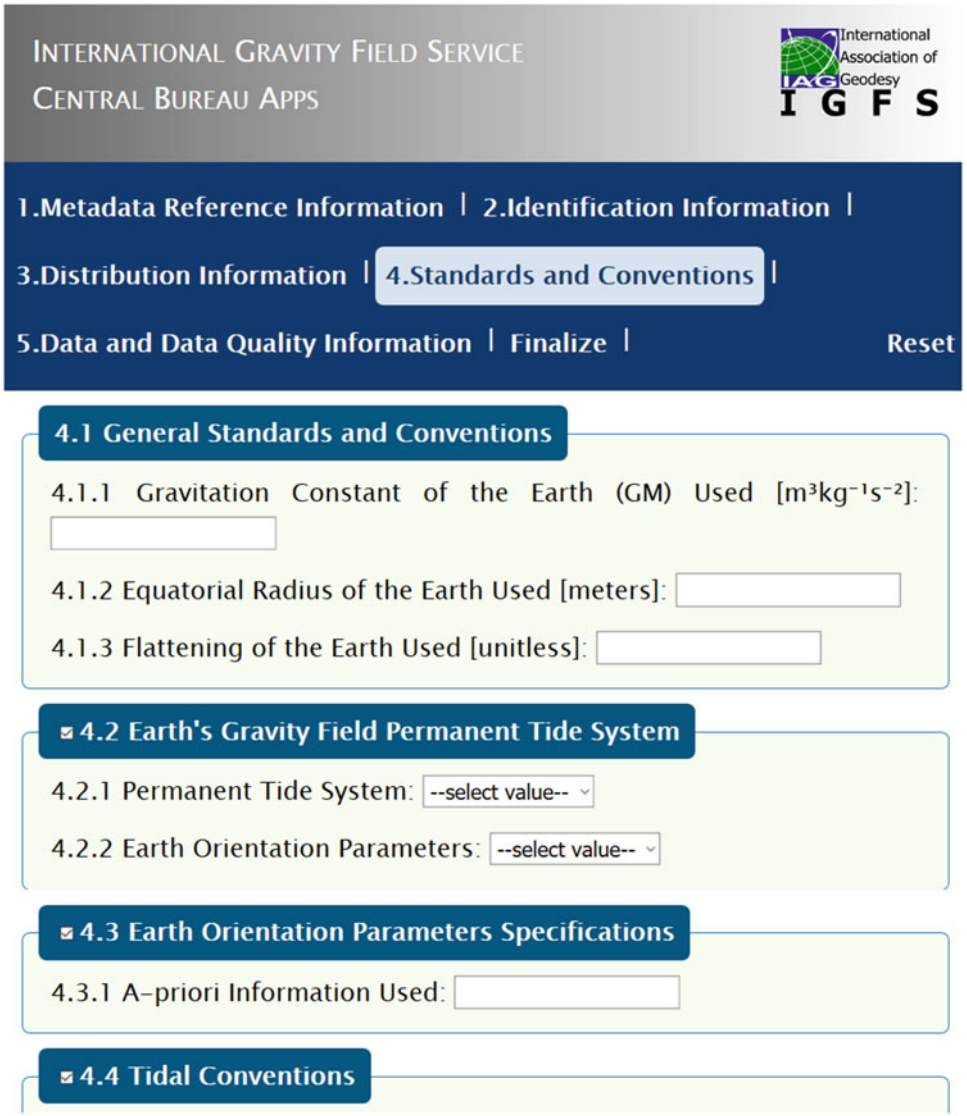

Fig. 3 The g-μeta interface

the data, for which the XML has been created, to the IGFS CB so that it will show up in the dedicated geoportal that is still under development. Another option to be included will be the archiving to another IGFS Service like Bureau Gravimétrique International (BGI), so that once the XML has been created, the users will have the option to submit the data together with their metadata information. The latter option would significantly enhance the discovery of existing gravity data, but will in no case be obligatory, i.e., the g-μeta and N-μeta applications are and will always be free to use without any obligation for the users to submit any data unless they wish so.

With the already developed g-μeta application, a strong validation engine has been included, in the sense that if the user enters a wrong type of value, this is readily indicated on-the-fly. For example, if a numeric value is expected in field and the user enters an alphanumeric one, then a prompt message appears instantly asking for correct input. It should be noted that no range checks have been yet included for the numerical values. Finally, at the stage of finalizing the XML metadata, and if some fields which are deemed necessary by the app and/or were selected by the user as necessary, are left blank an error message is created. If all fields are created in good order, then the validation step passes and the final XML is produced for the user to download.

Access to the online g-μeta app is currently available only through the following URL: http://igfsapps.topo.auth.gr, and when the specifications are finalized and the apps have been thoroughly tested access will also be provided through the main website of the IGFS (http://igfs.topo.auth.gr).

4 Future Work

The new ISO19115-1 profile prepared by IGFS for gravity metadata aims to cover the needs of geodesists, geophysicists and other geoscientists to describe their gravity-filed related data and prepare them for archiving, exchange and inclusion in other databases. Currently, it is possible to prepare gravity metadata according to the new profile by using the g-μeta online application provided by the IGFS CB. IGFS urges all interested individuals and parties to test the available application and submit their feedback to the IGFS CB or participate in the discussion by joining the IGFS Standards mailing list (http://igfs.topo.auth.gr/mailing-lists/). End-user feedback is necessary for improving both the standard specifications and the provided application in order to fit the community needs.

Future work includes the preparation of schema files, an online viewer, export of the metadata in a human-readable format and improvements in the data entry forms for the metadata, like, for example, range checks for numerical data etc. In a second stage, in order to support the dissemination and adoption of the new standard, the IGFS CB will examine the need for providing to the community libraries (code) in selected programming languages in order to facilitate its inclusion in existing software.

References

Giuliani G, Guigoz Y, Lacroix P, Ray N, Lehmann A (2016) Facilitating the production of ISO-compliant metadata of geospatial datasets. Int J Appl Earth Obs Geoinf 44:239–243. https://doi.org/10.1016/j.jag.2015.08.010

IOPG (2012) Using the EPSG geodetic parameter dataset. OGP Publication 373-7-1. Geomatics Guid Note 7(1):41

ISO (2014) Geographic information – Metadata – Part 1: Fundamentals (ISO 19115-1:2014)

Masó J, Pons X, Zabala A (2012) Tuning the second-generation SDI: theoretical aspects and real use cases. Int J Geogr Inf Sci 26(6):983–1014. https://doi.org/10.1080/13658816.2011.620570

Part VI

Multi-Signal Positioning: Theory and Applications

Assessment of GNSS and Map Integration for Lane-Level Applications in the Scope of Intelligent Transportation Location Based Services (ITLBS)

Emerson Pereira Cavalheri and Marcelo Carvalho dos Santos

Abstract

To enable safe and robust Intelligent Transportation Systems (ITS) applications, the integration of different sensors and techniques will certainly be a common reality. One application in this context is the lane-keeping techniques for autonomous driving systems. These systems normally use imagery sensors for lane identification, however imagery systems always depend on light and well-structured roads. One potential worldwide autonomous driving technique without any other lane and road detection/identification sensor would be GNSS positions along with accurate map information. However, this fusion depends on the accuracy and reliability of both GNSS positions and map information. The positioning accuracy that Intelligent Transportation Location Based Services (ITLBS) requires for where-in-lane and active control applications are 0.5 m and 0.1 m, respectively. To evaluate the potential of fusion, this work proposes an integration of GNSS and map information in the attempt to address the lane-keeping problem. This integration is performed by merging a GNSS solutions and lane centerline positions, acquired from aerial orthophotos, into a Kalman Filter and a simple map matching approach. To measure the positioning error, or off-track performance, a conversion of positions to the road space is necessary. To evaluate the results, a positioning accuracy limit, considering the road, vehicle dimensions, and the requirements for ITLBS is also proposed. The results showed that 95% of the time the proposed methodology off-track performances were within 1.89 m, in an average of 4 runs. Half of the runs were within 0.75 m, in average, at 95% of the time. Compared to an accurate GNSS Post Processed Kinematic (PPK) mode, an improvement of 10% was achieved.

Keywords

GNSS · ITLBS · Lane-level positioning · Maps

1 Introduction

Intelligent Transportation Systems (ITS) applications are rapidly emerging and efforts are being made in order to set appropriate standards. For example, positional accuracy standards for Intelligent Transportation Location Based Services (ITLBS) technologies. A complete review on the accuracy for ITLBS was carried by Stephenson et al. (2011), where four main classes of accuracy categories were outlined: which road (5.0 m); which lane (1.5 m); where in lane (0.5 m); and active control (0.1 m).

GNSS has been the main system for providing consistent global positions in several applications. However, there are major issues limiting the ITLBS application requirements, such as availability, continuity, and integrity. It is conceivable that GNSS positions along with accurate map information

E. P. Cavalheri (✉) · M. C. dos Santos
Department of Geodesy and Geomatics Engineering, University of New Brunswick, Fredericton, NB, Canada
e-mail: e.cavalheri@unb.ca; msantos@unb.ca

J. T. Freymueller, L. Sánchez (eds.), *International Symposium on Advancing Geodesy in a Changing World*, International Association of Geodesy Symposia 149, https://doi.org/10.1007/1345_2018_45

offers a potential worldwide autonomous driving without any other lane and road detection/identification sensors (Bishop 2005; Hillel et al. 2014).

When it comes to vehicle autonomous navigation systems and related applications, GNSS and maps are normally used separately for distinct purposes. One of the primary challenge in autonomous systems is the navigation, which basically requires an accurate knowledge of the vehicle's position in the environment. Current developments have mostly been using imagery sensors to identify the lanes. However, imagery systems always depend on light and well structured roads to correctly identify the edges of roads, leading to failures in dark or to bright environments (Hillel et al. 2014; Li et al. 2014).

Therefore, this work proposes an integration of GNSS and road map information to address this problem. This integration is performed by merging a GNSS position solution and lane centerline positions, from aerial orthophotos, into a Kalman Filter and a map matching algorithm. To measure the positioning error with respect to the reference lanes, a conversion of positions to the road space is necessary. To evaluate the results, a positioning accuracy limit, considering the road, vehicle dimensions, and the requirements for ITLBS is also proposed. In the following section, methodology, a satellite positions and map centerline approach using Kalman filter and a map matching algorithm will be outlined. In the sequence, in the section experiment and results, a study case describes the performance of the methodology followed by an statistical analysis of the off-track solutions, in the section analysis. And then, the conclusions of this work are discussed.

2 Methodology

This proposition integrates positions, from a satellite positioning technique, with the centerline position of the lanes, into a Kalman Filter, with the objective of keeping the estimated solutions in the center of lanes. At every satellite position solution (z_k), a map matching algorithm is executed to correctly identify where the vehicle is likely to be in the reference lanes (x_{ref}). By using this map-matched point (x_{mm}) and the lanes orientation, the filter prediction step ($\hat{\mathbf{x}}_{k/k-1}$) is constrained to keep the next position and velocity state, estimated in the filter update step ($\hat{\mathbf{x}}_k$), in the lane. The flowchart in Fig. 1 describes this procedure.

In the sequence, the map matching and kalman filter algorithms are detailed.

2.1 Map Matching

The main purpose of a map matching algorithm is to identify the correct road segments that a vehicle is travelling and its correct position on that segment (Quddus et al. 2003). Quddus et al. (2007) presented a complete review on the different MM algorithms and its performances. To mention a few techniques, map matching algorithms can range from simple geometric searching techniques, to complexes ones using fuzzy logic, Extended Kalman Filter (EKF), and Belief Theory. These techniques can be categorized into four main groups: geometric, topological, probabilistics, and advanced algorithms.

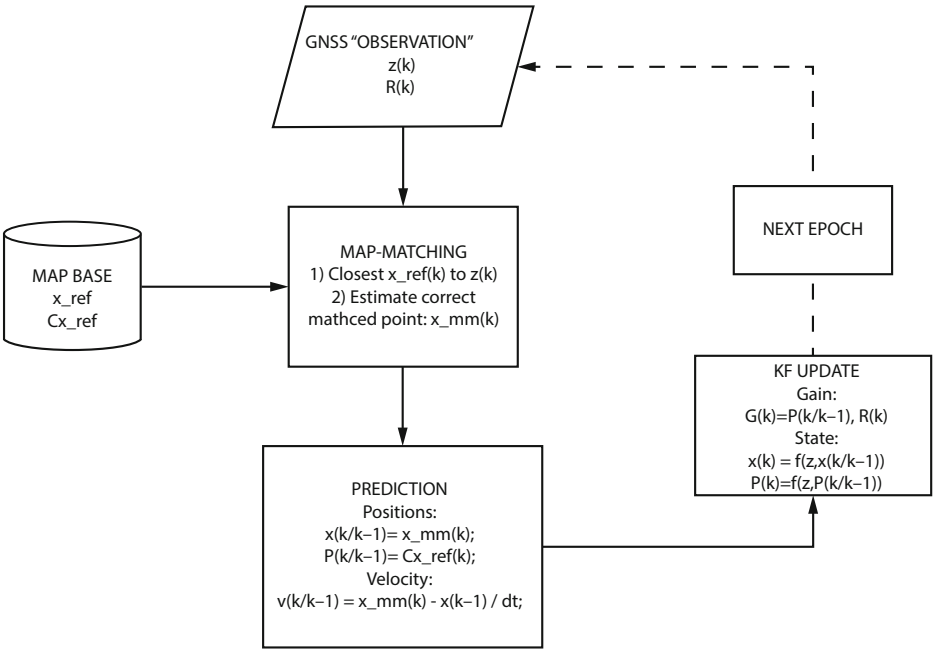

Fig. 1 Filter flowchart

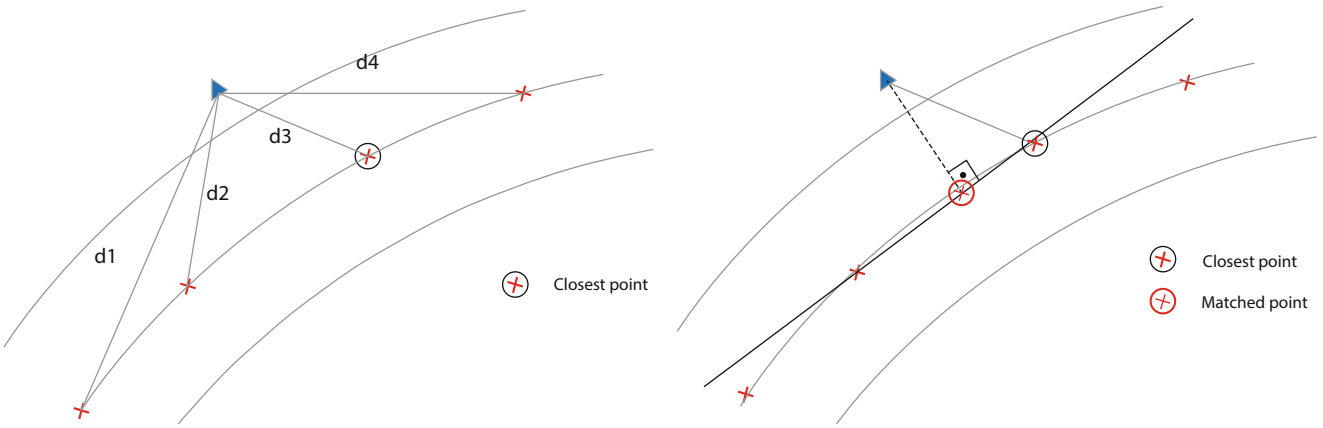

Fig. 2 Map matching step 1 (left) and step 3 (right)

The type of algorithm may be chosen depending on the type of data fed to the map matching process. In this work, positions coming from either the vehicle and the lane are used, therefore a simple geometric map matching is selected and explained in the sequence.

The first step of the map matching is to determine a position in the reference lane that is closest to the satellite position solution. This situation is depicted on the left side of Fig. 2, where the satellite position is represented as a blue triangle, the reference lane candidates as red crosses. The candidate with the shortest distance ($\mathbf{d_i}$) to the satellite position is chosen as the closest point. Then, the second step is to fit a line equation in the reference lane neighbouring candidates so that a perpendicular projection of the satellite position can be made onto this line. The intersection of the projection in this line gives the map-matched position x_{mm}. The right side of Fig. 2 depicts this second step. For the sake of illustration the line fit is made over a well spaced candidate points, which results on a line being not in the lane centerline, however in the experiments, on a real scenario, the points spacing are close enough to consider the line as the adjusting geometry.

From this step, the map-matched position and line orientation, or azimuth, are used in the navigation filter, as it explained in the sequence.

It should be noted that in the experiments the map contains only the lanes where the vehicle navigated, thus road identification is not necessary in this map matching approach. This way, there is no concerns with road ambiguous selection, for instance in intersections.

2.2 Navigation Algorithm

The information extracted from the lanes are used to constrain the navigation filter. The mathematical model uses local coordinates and the horizontal position and the velocity are the states to be estimated:

$$\begin{aligned} n_k &= n_{k-1} + v \cdot dt \cdot cos(\theta) \\ e_k &= e_{k-1} + v \cdot dt \cdot sin(\theta) \\ v_k &= v_{k-1} + w_k \end{aligned} \tag{1}$$

where, n, e are the local north and east components, v is the vehicle horizontal velocity, θ is the azimuth, w_k is the velocity process noise, and dt is the time between observations.

The Kalman Filter (KF) is an optimal estimation framework to solve the dynamic system presented in Eq. (1) (Grover and Hwang 1992). This system and measurement models can be represented in the following form, respectively:

$$\begin{aligned} \mathbf{x}_k &= \mathbf{F}_{k-1}\mathbf{x}_{k-1} + \mathbf{v}_{k-1} \\ \mathbf{z}_k &= \mathbf{H}_{k-1}\mathbf{x}_k + \mathbf{w}_k \end{aligned} \tag{2}$$

where $\mathbf{x}_k$ is the state vector, $\mathbf{F}_{k-1}$ and $\mathbf{H}_{k-1}$ are the Jacobian matrices of the functions with respect to the state vector $\mathbf{x}_k$, of the state and measurement functions, respectively. The noise sequences $\mathbf{v}_{k-1}$ and $\mathbf{w}_k$ are assumed to be white with known probability density function and mutually independent, with respectively covariance matrices: $\mathbf{Q}_{k-1}$ and $\mathbf{R}_k$.

The Kalman filter is a recursive process with the prediction and update steps. In the prediction step, the state and error covariance are estimated from previous timestep:

$$\begin{aligned} \hat{\mathbf{x}}_{k/k-1} &= \mathbf{F}_{k-1}\hat{\mathbf{x}}_{k-1} + \mathbf{v}_{k-1} \\ \mathbf{P}_{k/k-1} &= \mathbf{Q}_{k-1} + \mathbf{F}_{k-1}\mathbf{P}_{k-1}\mathbf{F}_{k-1}^T \end{aligned} \tag{3}$$

where $\mathbf{P}_k$ is the state error covariances.

In this proposition, the state vector prediction is provided by the map matching (x_{mm}). The navigation orientation (θ), which will impact the matrix $\mathbf{F}_{k-1}$, is obtained from the map. This quantities along with the measurements ($\mathbf{z}_k$), the vehicle positions in this case, are the inputs for the Kalman

filter update:

$$\begin{aligned}\hat{\mathbf{x}}_k &= \hat{\mathbf{x}}_{k/k-1} + \mathbf{K}_k(\mathbf{z}_k - \mathbf{H}_k\hat{\mathbf{x}}_{k/k-1}) \\ \mathbf{P}_k &= (\mathbf{I} - \mathbf{K}_k\mathbf{H}_k)\mathbf{P}_{k/k-1}\end{aligned} \tag{4}$$

where $\mathbf{K}_k = \mathbf{P}_{k/k-1}\mathbf{H}_k^T(\mathbf{H}_k\mathbf{P}_{k/k-1}\mathbf{H}_k^T + \mathbf{R}_k)^{-1}$ is the Kalman gain.

The dynamics of the problem is a car navigating in the streets of a city and according to tests made by Hu et al. (2003), 0.1 m/s^2 were the best dynamic noise for this situation and is the value considered in this work. For details on the application of the Kalman filter several textbooks or papers provides its flow (Miller and Leskiw 1987; Hu et al. 2003; Ristic et al. 2004).

2.3 Positioning Accuracy Limit

The position errors with respect to the lane centerline should be within a limit to evaluate the methodology. An accuracy threshold that considers the vehicle (v_w) and lane (l_w) dimensions is proposed and depicted in Fig. 3.

Considering the average lane sizes where vehicle navigates and the vehicle lateral widths, the following lane threshold can be developed,

$$\sigma_{lim} = (l_{w/2}) - (v_{w/2}) \tag{5}$$

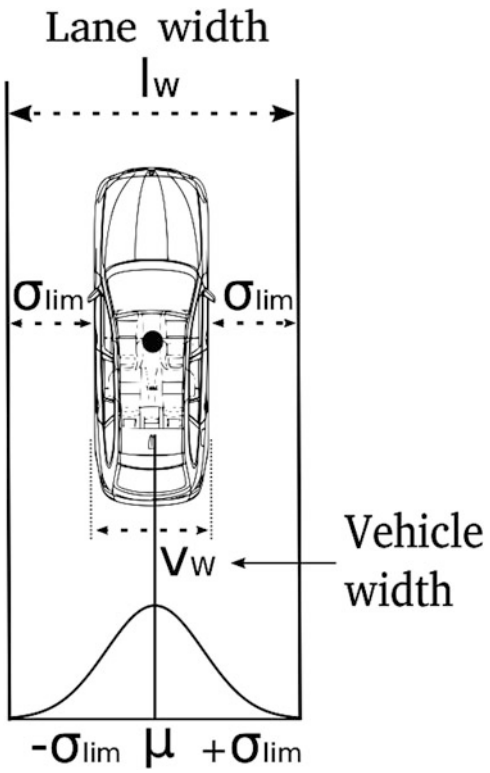

Fig. 3 Vehicle navigation threshold

The threshold σ_{lim} represents the very limit of the lane, to be more conservative, an appropriate value for a safer limit would be $\sigma_{lim/2}$. For this experiment, the accuracy threshold value is $\sigma_{lim/2} = 0.49$ m.

3 Experiment and Results

A satellite dataset was collected in the streets of Fredericton, New Brunswick, Canada. Two geodetic dual-frequencies receivers were mounted on the roof of a vehicle for the collections. The position solution was obtained from a post-processed kinematic (PPK) technique with a short baseline station (<8 km). The data was processed using the open source RTKlib package for satellite positioning, details can be seen at Takasu (2018). The road centerlines positions were digitized from a 15-cm resolution orthophotos provided by the city of Fredericton. The positions representing the trajectory were generated at every 0.5 m in the road centerline. The dataset was processed separately for each receiver thus the solutions are seen separately.

In a first moment, position performances will be visualized during GNSS outages. In Figs. 4 and 5, the estimated positions of the vehicle using the Kalman filter (as green stars) and the PPK solution (colored circles) are visualized along with the reference lane centerlines (yellow dots). The same stretch of the road are seen for receiver 1 and 2 respectively at the left and right side of the figures.

Figure 4 show the filter performance after a complete and quick outage when the vehicle passed underneath a walking bridge. The direction of navigation is from the bottom to the upper part of the figures. After the complete outage, the PPK solution suffers a quick reconvergence and can only determine a position using the low accurate pseudorange observable, also known as single point positioning (SPP, represented as red circles). The KF solution showed a better performance where it kept the position correctly on the lane before and even after the outage.

Figure 5 shows the vehicle coming from the upper part and taking the exit ramp and passing underneath the bridge. Both receiver solutions have similar behaviours. The RTK and KF solutions are practically together before passing under the bridge. After the complete signal blockage, PPK solutions went away of the lane of navigation while the KF solutions were mostly in right lane of navigation. It is observed when PPK solutions are float the filter trusts more the road centerline information. However, when the PPK solution fix ambiguities, thus with a small standard deviation, the filter trusts more the GNSS positions.

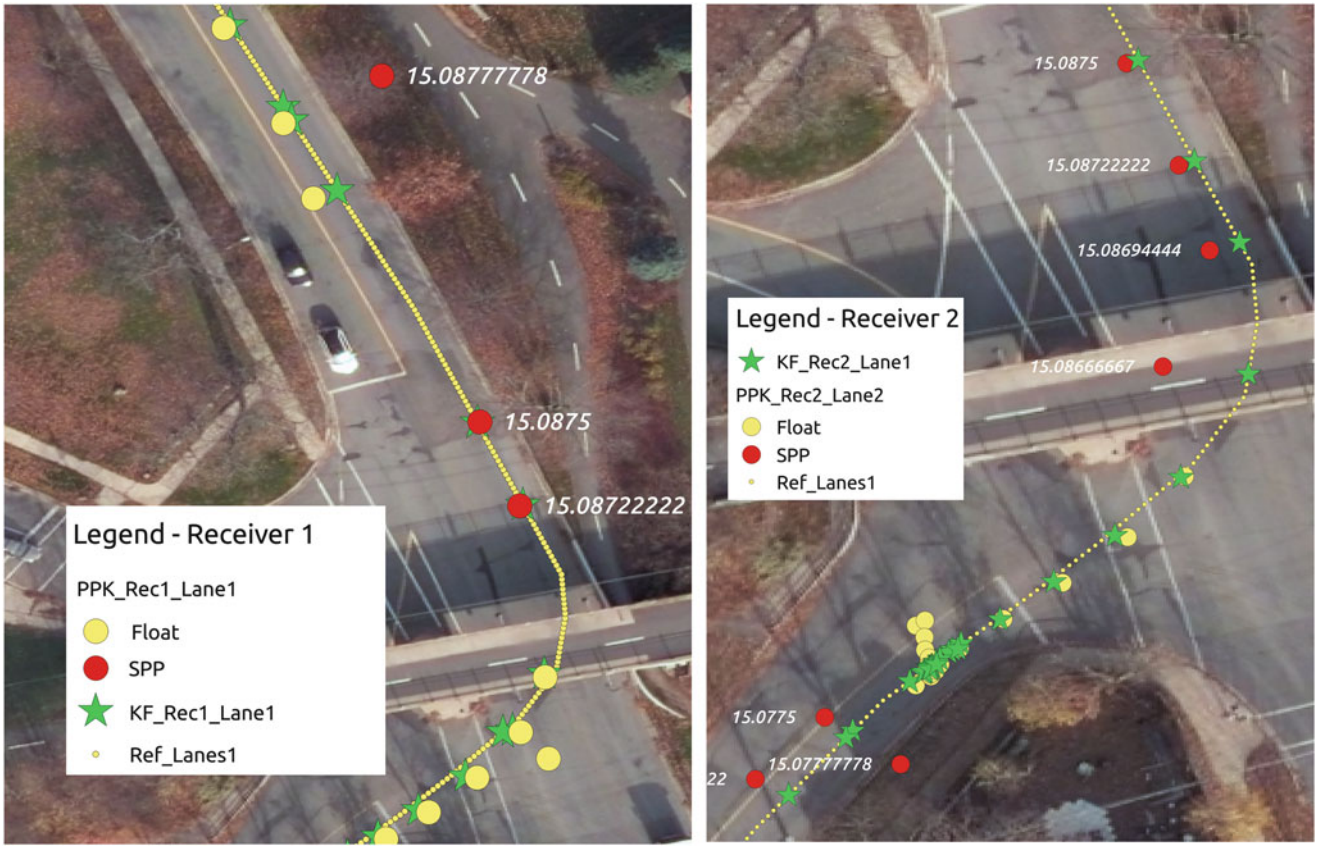

Fig. 4 Receivers 1 (left) and 2 (right) KF (green stars) and PPK (circles) performances passing underneath a walking bridge

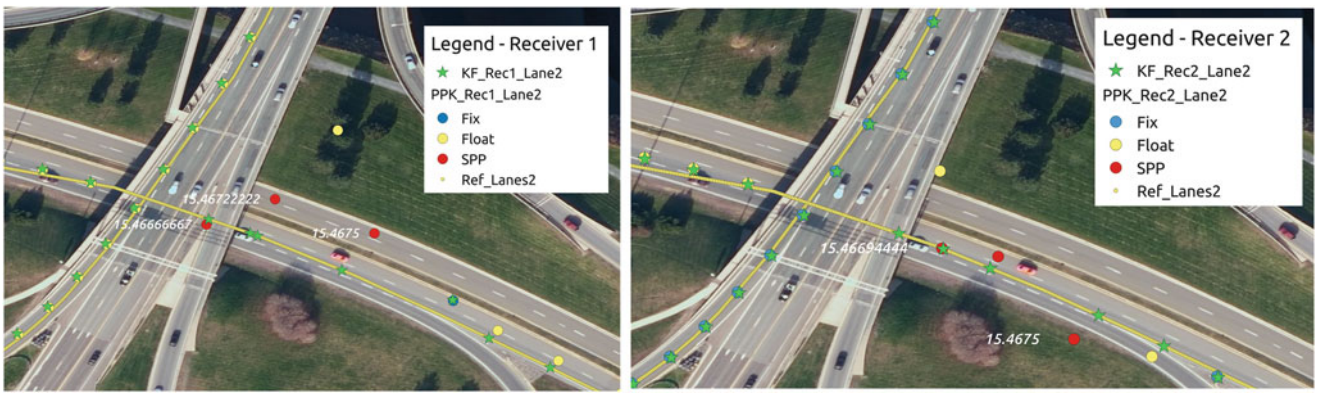

Fig. 5 Receivers 1 (left) and 2 (right) KF (green stars) and PPK (circles) performances passing underneath a walking bridge

One delicate situation was noticed when the vehicle passed inside a urban canyon where the occurrence of multipath was high. During this situation the receiver observes measurements from reflected signals which makes the filter to determine with confidence a wrong position. This situation in seen in Fig. 6, in which a wrong PPK fix mislead the Kalman filter solution, which judged the position as being correct.

4 Analysis

The methodology is assessed by determining the off-track of PPK and KF solutions to the reference lanes, for both receivers 1 and 2. The processing was separated by the navigation direction, going to the halfway trajectory point (Lanes 1) and coming back to the starting point (Lanes 2), visualized in Fig. 7.

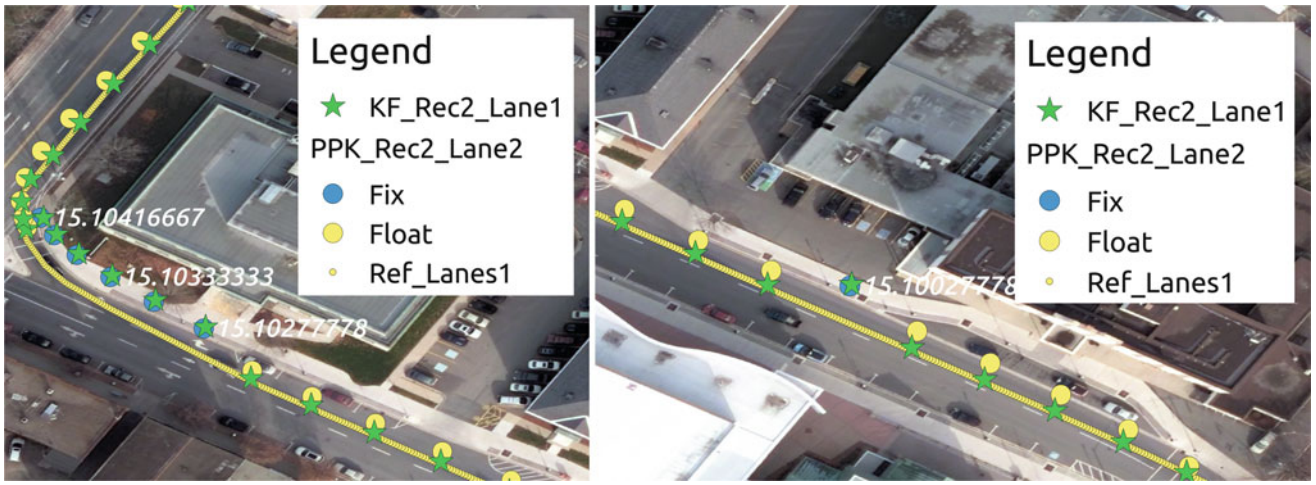

Fig. 6 Wrong filter positioning due to a wrong GNSS position fixes on a urban canyon

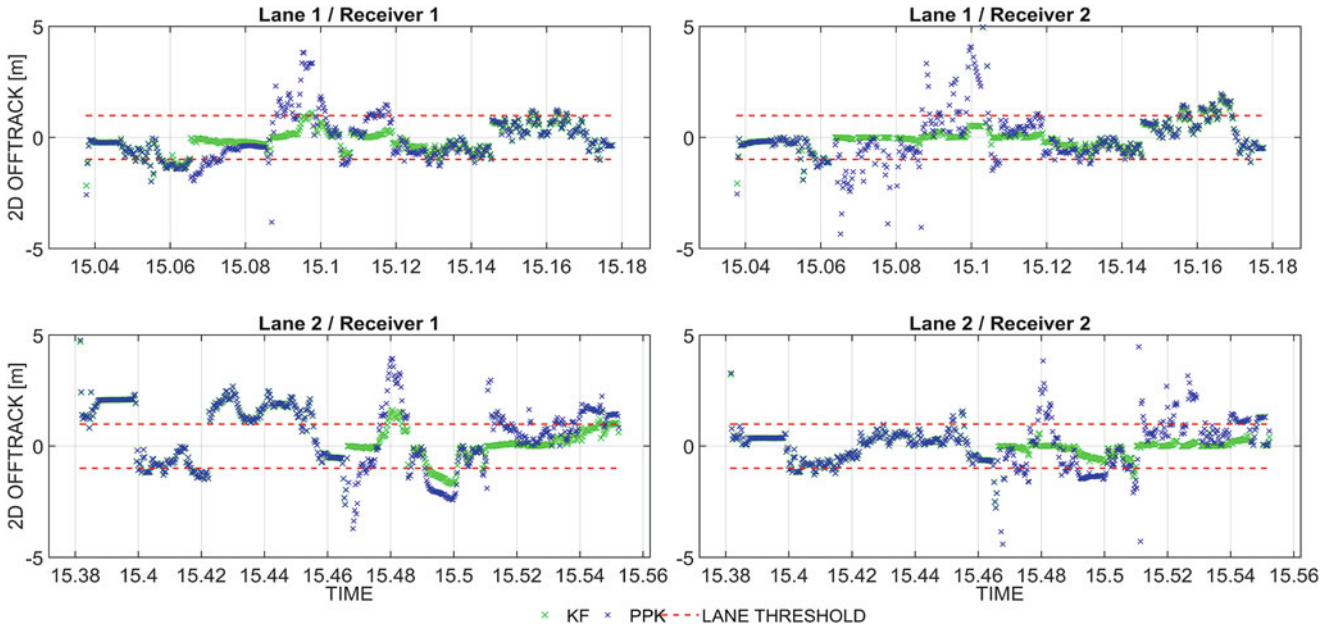

Fig. 7 Off-track for receivers 1 (left) and 2 (right) in the lanes 1 (top) and 2 (bottom)

Table 1 Off-track accuracy analysis

PPK			KF		
avg (m)	std (m)	95% (m)	avg (m)	std (m)	95% (m)
0.74	0.70	2.10	0.56	0.58	1.89

Statistics of the off-track measure were grouped for both receivers into one, and are shown as the average off-track (avg), its standard deviation (std), at 95% confidence level for PPK and KF solutions, in Table 1. Satellite obstructions were disregarded in the statistics due to the great impact in the PPK solutions.

The results showed that 95% of the time the KF off-track performances were within 1.89 m in average for the 4 runs, while PPK had an average of 2.10 m. An improvement of 10% KF had over the PPK off-track performances. Considering the lane threshold standard deviation proposed in this work for the off-track evaluation, $\sigma_{lim} = +/-0.49$ m, the KF average performance was 0.56 m, only 7 cm above the limit. However, when considering 95% of the data, the KF solutions were 1.88 m, more than 3 times the limit. The PPK mean was above the limit for 25 cm. And, 95% of the data were under 2.09 m. This way, for the required limit of 0.49 m, the proposed methodology did not achieve the active control limit 95% of the time.

5 Conclusion

This work proposed an integration of GNSS positions and lane centerlines into a Kalman Filter and map matching approach, with the main objective of keeping the vehicle position in the lane center. Mostly, the KF off-track performances follows the PPK solution. The main limiting points are the long periods of GNSS outages affecting the quality of the KF positions and wrong PPK fixed positions due to multipath. The improvements obtained by the approach are during short and complete signal outages where the map aids the filter with the satellite observations blockages making a continuous solution while keeping it in the correct lane.

The concern from the community towards low-cost single frequency navigation systems was reasonable few years ago, however, in a few years from now, the cost versus performance of dual frequencies against single frequency receivers will be justified as the prices lower and the need for performance increases especially for safety of life navigation applications.

The main challenges for future tests is to develop a filter that integrates the map information with satellite measurements to exclude wrong fixes due to multipath signals and improve the solution continuity in any duration of satellite outages.

Acknowledgements To the CNPq (Conselho Nacional de Desenvolvimento Científico e Tecnológico) agency, which through the Brazilian Sciences without borders program provided the necessary funds for the development of this research.

References

Bishop R (2005) Intelligent vehicle technology and trends. Artech House, Boston

Grover R, Hwang PYC (1992) Introduction to random signals and applied Kalman filtering. Wiley, New York

Hillel AB, Lerner R, Levi D, Raz G (2014) Recent progress in road and lane detection: a survey. Mach Vis Appl 25(3):727–745

Hu C, Chen W, Chen Y, Liu D (2003) Adaptive Kalman filtering for vehicle navigation. J Glob Positioning Syst 2(1):42–47

Li Q, Chen L, Li M, Shaw SL, Nuchter A (2014) A sensor-fusion drivable-region and lane-detection system for autonomous vehicle navigation in challenging road scenarios. 63(2):540–555

Miller KS, Leskiw DM (1987) An introduction to Kalman Filtering with applications. Riverside Research Institute, New York

Quddus MA, Ochieng WY, Zhao L, Noland RB (2003) A general map matching algorithm for transport telematics applications. GPS Solut 7(3):157–167

Quddus MA, Ochieng WY, Noland RB (2007) Current map-matching algorithms for transport applications: state-of-the art and future research directions. Transp Res Part C: Emerg Technol 15(5):312–328

Ristic B, Arulampalam S, Gordon N (2004) Beyond the Kalman filter: particle filters for tracking applications. Artech House, Boston

Stephenson S, Meng X, Moore T, Baxendale A, Ford T (2011) Accuracy requirements and benchmarking position solutions for intelligent transportation location based services. In: Proceedings of the 8th international symposium on location-based services

Takasu, T (2018) RTKLIB: An open source program package for GNSS positioning (2018-07-11). http://www.rtklib.com

Improving Low-Cost GNSS Navigation in Urban Areas by Integrating a Kinect Device

C. I. De Gaetani, D. Pagliari, E. Realini, M. Reguzzoni, L. Rossi, and L. Pinto

Abstract

In the last decades, low-cost GNSS receivers have been widely used for navigation purposes. Some of them deliver also raw data, allowing for a more sophisticated processing, such as the double-difference approach, and therefore a more accurate positioning, typically at the decimeter level. However, these accuracies can be generally achieved only with a good sky visibility, that is a critical issue in urban areas even using low-cost receivers equipped with a high-sensitive antenna. In this respect, a significant contribution comes from the use of digital images or dense point clouds which provides an estimate of the sensor kinematic position. To maintain the low-cost target, the Kinect device, endowed with RGB and depth cameras, can be used. In this work, we have first processed the GNSS raw data from a u-blox receiver by using the free and open source goGPS software. Then, we have studied the integration of the Kinect device by a proper Kalman filter. An outdoor experiment has been arranged with the aim of testing the hardware and software system.

Keywords

GNSS · Kalman filter · Kinect · Low-cost system · Multi-sensor navigation · Photogrammetry

1 Introduction

The task of precise navigation in urban areas is quite complex and it is not fully exploited yet, especially when low-cost devices are used. Concerning outdoor navigation, the GNSS is widespread, thanks to its easiness of use. However, its accuracy decays in urban areas, because of the presence of obstacles in the sky visibility. To overcome this drawback, the classical approach is to use Inertial Navigation Systems (INS), basically integrating GNSS data with information provided by accelerometers and gyroscopes (Hofmann-Wellenhof et al. 2003). When optical sensors are also integrated into the platform, one gets the so-called Mobile Mapping Systems (MMS) that have been used for decades to solve urban position problems (Tao et al. 2001; Hassan et al. 2006). However, these platforms could be very expensive, especially when high accuracies are required. Nowadays alternative low-cost systems are available, e.g. supporting GNSS receivers with MEMS devices (Noureldin et al. 2009; Tomaszewski 2017), reduced inertial sensor systems (Georgy et al. 2010) or radio-frequency wireless technologies (Nur et al. 2013). Image-based techniques can also be used to complement GNSS observations and represent an interesting and suitable low-cost alternative to overcome the limitation of the GNSS-only solution. The use of photogrammetry for GNSS outage bridging was already discussed by several authors (Chaplin 1999; Da Silva et al. 2003). The task of image-based navigation is quite common in Computer Vision (CV), especially for autonomous robot navigation. In this

C. I. De Gaetani (✉) · D. Pagliari · M. Reguzzoni · L. Rossi · L. Pinto
Department of Civil and Environmental Engineering (DICA), Politecnico di Milano, Milan, Italy
e-mail: carloiapige.degaetani@polimi.it

E. Realini
GReD srl, Lomazzo, CO, Italy
http://www.g-red.eu

J. T. Freymueller, L. Sánchez (eds.), *International Symposium on Advancing Geodesy in a Changing World*, International Association of Geodesy Symposia 149, https://doi.org/10.1007/1345_2018_27

case, the problem is faced by retrieving simultaneously the robot location and the model of the surrounding environment (Simultaneous Location And Mapping). Since this solution is always computed incrementally, its quality quickly decreases over time. To mitigate this problem, laser range systems are commonly used to add information to the pure visual-based solutions, but resulting in a high increment of the costs. The launch on the market of the Microsoft Kinect device allowed to have both active and passive sensors in the same device, thus maintaining the low-cost target and having a device that can be easily used for both mapping and navigation purposes, see e.g. Suarez et al. (2012), Omara et al. (2015), Frankhauser et al. (2015). The aim of this work is to develop an algorithm based on an extended Kalman filter to retrieve the trajectory of a rover by means of a low-cost GNSS receiver integrated by a Kinect device.

2 Kinect Device and Its Calibration

The Microsoft Kinect device was released on the market in 2010 for gaming and entertainment purposes. It is composed by a RGB camera, an IR camera and an IR projector, see Fig. 1a, and it is capable of acquiring coloured and depth images with a frame rate up to 30 fps. The complementarity of RGB and depth images attracted researchers from different fields, especially from CV, where it is commonly used to solve navigation and mapping tasks (Endres et al. 2012; Oliver et al. 2012). In 2014, Microsoft released a second generation (v2) of the device. The main difference with respect to the first generation is the principle used for the depth measurements, making the v2 device capable of acquiring data even under sunlight radiations in an outdoor environment. The accuracy of the outdoor acquisition is comparable to the one obtained in an indoor environment, even if it is noisier (Pagliari et al. 2016). Nevertheless, the depth measurements could not be acquired at all in case of direct sunlight radiation. The imaging sensors of the Kinect v2 deliver high resolution images, i.e. 1280×1090 pixels for the RGB camera and 512×424 pixels for the IR camera. Note that the latter delivers different output images: (1) gray scale images dependent on the ambient lighting, (2) active gray scale images independent from the ambient lighting and (3) depth images, namely images where the value of the distance between the object and the sensor is stored into each pixel.

3 Low-Cost GNSS Receivers and goGPS Software

In the last decade, raw data access was enabled by some mass-market GNSS chipset manufacturers, such as u-blox, Fastrax, SkyTraq, NVS, SiRF/Qualcomm, STMicroelectronics and Broadcom. In some cases, it is made particularly easy for users to enable and read timing, code and phase observations from a GNSS module by providing a dedicated evaluation kit (as in the case of u-blox, Fastrax, SkyTraq and NVS), while in other cases users are required to interface the GNSS module with a circuit board of their own design to configure the module and access the data (as in the case of SiRF/Qualcomm, STMicroelectronics and Broadcom). Of course, the companies providing evaluation kits also sell GNSS chipsets/modules to be integrated in the users' own designs. Among the evaluation kits currently available on the market, u-blox ones stand out for the completeness and clarity of the documentation, as well as for the broad configuration options. For this reason, the u-blox evaluation kit EVK-6T is used in this work together with the patch antenna ANN-MS-0-005, see Fig. 1b. This is a GPS L1-only receiver providing raw code and phase data in u-blox UBX binary format, through a COM port. The free and open-source goGPS software (Realini et al. 2013; Herrera et al. 2016) is used to record the data stream from the receiver and to process it. goGPS is a software package designed and initially developed at Politecnico di Milano. The development is now carried out mostly by GReD srl, with the contributions of users from several institutions, at international level. goGPS is written in MATLAB programming language, and is designed to process single-frequency code and phase observations, either by undifferenced or double-difference approach. The processing can be performed either epoch-by-epoch, or by applying an extended Kalman filter. goGPS can read RINEX files (both versions 2 and 3) and SP3 files in input. Algorithms to decode binary formats by

Fig. 1 The devices used in this work: (**a**) Kinect v2 device with underlined the three imaging sensors, (**b**) low-cost u-blox GNSS receiver

u-blox, Fastrax, NVS and SkyTraq are included, returning data files in RINEX format. The software core functionalities are implemented in a Java version as well.

4 The Proposed Solution

The proposed solution is based on the following procedure. First of all a calibration is performed to determine the geometry, the initial position and attitude of the vehicle. Then the Kinect images and the GNSS raw data are separately post-processed. The two independent estimates are merged into a unique solution by an extended Kalman filter.

4.1 Calibration

The system requires two calibration steps. The former has to be performed once and for all "at home" to determine the position and the attitude of the sensors with respect to the vehicle reference frame. In practice, the aim of this step is to estimate the coordinates of both the GNSS antenna phase centre and the Kinect RGB camera projection centre in the vehicle reference frame, as well as the rotation matrix between the Kinect and the vehicle reference frames. The second calibration step is needed to determine the initial position and attitude of the vehicle and has to be performed "on the field". The aim of this step is to estimate the parameters that allow the transformation between the reference frame in which the trajectory will be determined and the vehicle reference frame at the initial time. In practice, a translation vector and a rotation matrix (or three Cardan angles in a 3D system) have to be determined.

4.2 RGB-D Kinect Solution

The Kinect v2 is used to acquire both depth and RGB images. The former are pre-processed, following the procedure presented in Pagliari et al. (2014) and Pagliari and Pinto (2015). Then, all the images are corrected for lens distortions by the camera calibration app embedded in MATLAB. Since the resolution of depth images is lower, they are interpolated at the same resolution of the RGB images (sampling rate 4:1). Finally, RGB-D images are created by adding three channels to the original RGB ones, containing the coordinates of the point cloud computed from the depth images.

The Relative Orientation (RO) between each subsequent couple of RGB-D images is computed according to Xiao et al. (2013). This procedure consists of firstly computing the RO by using the SIFT keypoints (Lowe 2004) detected on the RGB images and then refining it by applying the ICP algorithm (Zhengyou 1994) to the three-dimensional information of the point clouds.

4.3 Low-Cost GNSS Solution

The u-blox data processing by goGPS consists in applying code and phase double differences with respect to a permanent station. In our experiment we use the MILA station located about 500 m far from the experiment area. The adjustment procedure is carried out by means of an extended Kalman filter on double-differenced L1 observations, at 1 Hz, with float phase ambiguities (Realini et al. 2013). The effect of the filter dynamics is disabled by setting the model error standard deviation to a value significantly higher than the observation error standard deviation. This is basically equivalent to performing a kinematic solution based on phase-smoothed code observations. Satellite orbits and clocks are modelled by broadcast ephemeris data, the elevation angle cut-off is set to 15° and observations are weighted based on the sine of the elevation, squared.

4.4 Extended Kalman Filter

The trajectory of the vehicle, i.e. its position in space and time, can be described by six degrees of freedom, e.g. the position of the barycenter O at the epoch t and the attitude of the vehicle at the same time. The position of the barycenter is expressed in Cartesian coordinates with respect to a local East-North-Up frame. Therefore, assuming no vertical movements (flat field), the motion of the vehicle is just in the East-North plane and its attitude is described by a single angle (three degrees of freedom). Moreover, the dynamics of the system can be modelled assuming a uniform rectilinear motion and a constant attitude between two consecutive epochs. Under these hypotheses, the state of the system can be defined by the following variables at discrete epochs t_i ($i = 1, 2, \ldots$):

- $\boldsymbol{x}_O^{\mathrm{EN}}(t_i) = [E_O(t_i),\ N_O(t_i)]^{\mathsf{T}}$, the position of O in the East-North system,
- $\dot{\boldsymbol{x}}_O^{\mathrm{EN}}(t_i) = \left[\dot{E}_O(t_i),\ \dot{N}_O(t_i)\right]^{\mathsf{T}}$, the velocity of O in the East-North system,
- $\alpha_{\mathrm{V}}^{\mathrm{EN}}(t_i)$, the rotation angle from the vehicle system to the East-North system (see Fig. 2).

The dynamics of this system is described by:

$$\boldsymbol{x}_O^{\mathrm{EN}}(t_{i+1}) = \boldsymbol{x}_O^{\mathrm{EN}}(t_i) + (t_{i+1} - t_i)\,\dot{\boldsymbol{x}}_O^{\mathrm{EN}}(t_i) \tag{1}$$

$$\dot{\boldsymbol{x}}_O^{\mathrm{EN}}(t_{i+1}) = \dot{\boldsymbol{x}}_O^{\mathrm{EN}}(t_i) + \boldsymbol{\varepsilon}_{\dot{\boldsymbol{x}}}(t_{i+1}) \tag{2}$$

$$\alpha_{\mathrm{V}}^{\mathrm{EN}}(t_{i+1}) = \alpha_{\mathrm{V}}^{\mathrm{EN}}(t_i) + \varepsilon_{\alpha}(t_{i+1}) \tag{3}$$

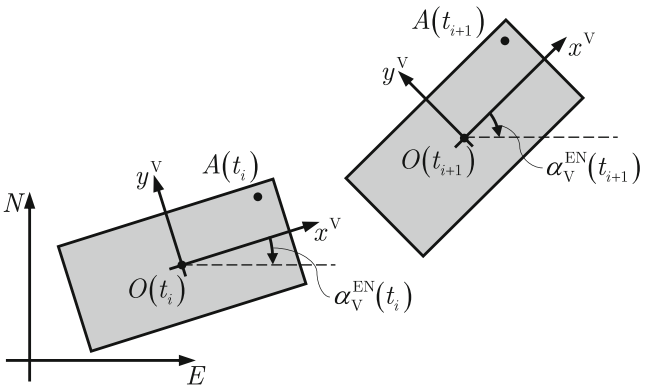

Fig. 2 Vehicle at epochs t_i and t_{i+1}. The observation point A and the vehicle barycenter O are highlighted

where suitable model errors $\boldsymbol{\varepsilon}_{\dot{\boldsymbol{x}}}$ and ε_α are introduced to allow smooth changes in velocity and direction of motion, respectively. In matrix notation, the system is fully described by the following state vector:

$$\boldsymbol{X}(t_i) = \left[\boldsymbol{x}_O^{\mathrm{EN}}(t_i),\, \dot{\boldsymbol{x}}_O^{\mathrm{EN}}(t_i),\, \alpha_{\mathrm{V}}^{\mathrm{EN}}(t_i)\right]^{\mathsf{T}} \tag{4}$$

and the dynamics by:

$$\boldsymbol{X}(t_{i+1}) = \mathbf{T}(t_i, t_{i+1})\, \boldsymbol{X}(t_i) + \boldsymbol{\varepsilon}(t_{i+1}) \tag{5}$$

where $\mathbf{T}$ is the non-stationary transition matrix:

$$\mathbf{T}(t_i, t_{i+1}) = \begin{bmatrix} 1 & 0 & t_{i+1} - t_i & 0 & 0 \\ 0 & 1 & 0 & t_{i+1} - t_i & 0 \\ 0 & 0 & 1 & 0 & 0 \\ 0 & 0 & 0 & 1 & 0 \\ 0 & 0 & 0 & 0 & 1 \end{bmatrix} \tag{6}$$

and $\boldsymbol{\varepsilon}$ is the model error vector:

$$\boldsymbol{\varepsilon}(t_{i+1}) = \left[0,\, 0,\, \varepsilon_{\dot{E}}(t_{i+1}),\, \varepsilon_{\dot{N}}(t_{i+1}),\, \varepsilon_\alpha(t_{i+1})\right]^{\mathsf{T}} . \tag{7}$$

The proposed extended Kalman filter aims at integrating two kinds of observations, respectively acquired by the GNSS receiver and by the Kinect device at different epochs and at a different sampling rate. We call t_i^{G} $(i = 1, 2, \dots)$ the GNSS receiver observation epochs and t_i^{K} $(i = 1, 2, \dots)$ the Kinect device ones; their union is the set of epochs t_i at which the state vector is evaluated. Furthermore, the acquisition points of the instruments are not generally at the same location of the barycenter O of the vehicle, i.e. the point which the state variables refer to. We only assume that the GNSS antenna (phase center) and the Kinect device (camera projection center) are located at a point A with the same planimetric coordinates. In particular, in our experiment the u-blox antenna is just above the Kinect device and the possible misalignment between antenna phase center and camera projection center is neglected. The vector

$$\boldsymbol{x}_{AO}^{\mathrm{V}} = \boldsymbol{x}_O^{\mathrm{V}} - \boldsymbol{x}_A^{\mathrm{V}} = \left[x_{AO}^{\mathrm{V}},\, y_{AO}^{\mathrm{V}}\right]^{\mathsf{T}} \tag{8}$$

links the acquisition point A and the vehicle barycentric point O in the vehicle local reference system V and therefore it is constant in time.

Regarding the GNSS observations, sampled at epochs t_i^{G}, we consider as observations the antenna coordinates estimated by goGPS in the East-North frame, instead of the observed pseudo-ranges. Therefore the GNSS observation equations are:

$$\boldsymbol{x}_A^{\mathrm{EN}}(t_i^{\mathrm{G}}) = \boldsymbol{x}_O^{\mathrm{EN}}(t_i^{\mathrm{G}}) + \boldsymbol{x}_{AO}^{\mathrm{EN}}(t_i^{\mathrm{G}}) + \boldsymbol{v}_{\boldsymbol{x}}(t_i^{\mathrm{G}}) \tag{9}$$

where $\boldsymbol{v}_{\boldsymbol{x}}$ is the observation error described by the covariance matrix of the estimated coordinates of A by goGPS. Differently from $\boldsymbol{x}_{AO}^{\mathrm{V}}$, the components of vector $\boldsymbol{x}_{AO}^{\mathrm{EN}}$ change in time according to changes of the vehicle attitude, therefore Eq. 9 can be rewritten as:

$$\boldsymbol{x}_A^{\mathrm{EN}}(t_i^{\mathrm{G}}) = \boldsymbol{x}_O^{\mathrm{EN}}(t_i^{\mathrm{G}}) - \mathbf{R}\left(\alpha_{\mathrm{V}}^{\mathrm{EN}}(t_i^{\mathrm{G}})\right) \boldsymbol{x}_{AO}^{\mathrm{C}} + \boldsymbol{v}_{\boldsymbol{x}}(t_i^{\mathrm{G}}) \tag{10}$$

where $\mathbf{R}(\cdot)$ stands for the two-dimensional rotation matrix of a given rotation angle. Note that Eq. 10 is not linear in the angle $\alpha_{\mathrm{V}}^{\mathrm{EN}}(t_i^{\mathrm{G}})$ describing the vehicle attitude. After linearization around $\widetilde{\alpha}_{\mathrm{V}}^{\mathrm{EN}}(t_i^{\mathrm{G}}) = \alpha_{\mathrm{V}}^{\mathrm{EN}}(t_\ell)$ with $t_\ell = \max\left(t_j : t_j < t_i^{\mathrm{G}},\ j = 1, 2, \dots\right)$, Eq. 10 becomes:

$$\boldsymbol{x}_A^{\mathrm{EN}}(t_i^{\mathrm{G}}) - \boldsymbol{h}_{\mathrm{G}}(t_i^{\mathrm{G}}) = \mathbf{H}_{\mathrm{G}}(t_i^{\mathrm{G}})\, \boldsymbol{X}(t_i^{\mathrm{G}}) + \boldsymbol{v}_{\boldsymbol{x}}(t_i^{\mathrm{G}}) \tag{11}$$

where $\boldsymbol{h}_{\mathrm{G}}$ is the known term:

$$\boldsymbol{h}_{\mathrm{G}}(t_i^{\mathrm{G}}) = -\mathbf{R}\left(\widetilde{\alpha}_{\mathrm{V}}^{\mathrm{EN}}(t_i^{\mathrm{G}})\right) \left\{ \boldsymbol{x}_{AO}^{\mathrm{V}} + \widetilde{\alpha}_{\mathrm{V}}^{\mathrm{EN}}(t_i^{\mathrm{G}}) \begin{bmatrix} y_{AO}^{\mathrm{V}} \\ -x_{AO}^{\mathrm{V}} \end{bmatrix} \right\} \tag{12}$$

and $\mathbf{H}_{\mathrm{G}}$ is the GNSS transformation matrix:

$$\mathbf{H}_{\mathrm{G}}(t_i^{\mathrm{G}}) = \left[\mathbf{I}\ \mathbf{0}\ \mathbf{0}\ \mathbf{R}\left(\widetilde{\alpha}_{\mathrm{V}}^{\mathrm{EN}}(t_i^{\mathrm{G}})\right) \begin{bmatrix} y_{AO}^{\mathrm{V}} \\ -x_{AO}^{\mathrm{V}} \end{bmatrix} \right] . \tag{13}$$

Regarding the Kinect observations, the displacement and the rotation between two subsequent epochs t_{i-1}^{K} and t_i^{K} are acquired. First of all, these observations have to be transformed into the vehicle reference frame V, since the Kinect device can be mounted with an arbitrary attitude on the vehicle. For example, in our experiments it was rotated by about 30° around the x axis of the vehicle reference frame. After that, dividing the resulting displacements by the time lag $t_i^{\mathrm{K}} - t_{i-1}^{\mathrm{K}}$, the velocity $\dot{\boldsymbol{x}}_A^{\mathrm{EN}}$ is obtained in the vehicle reference frame at the epoch t_i^{K}. Note that, since $t_i^{\mathrm{K}} - t_{i-1}^{\mathrm{K}}$

is the time difference between two Kinect acquisitions, the average velocity and not the instantaneous one at time t_i^{K} is actually computed. The Kinect observation equations can be written as:

$$\dot{\boldsymbol{x}}_A^{\mathrm{EN}}\left(t_i^{\mathrm{K}}\right) = \dot{\boldsymbol{x}}_O^{\mathrm{EN}}\left(t_i^{\mathrm{K}}\right) + \left[\mathbf{I} - \mathbf{R}\left(\alpha_{\mathrm{V}\left(t_{i-1}^{\mathrm{K}}\right)}^{\mathrm{V}\left(t_i^{\mathrm{K}}\right)}\right)\right] \boldsymbol{x}_{AO}^{\mathrm{V}} + \boldsymbol{v}_{\dot{\boldsymbol{x}}}\left(t_i^{\mathrm{K}}\right) \tag{14}$$

$$\alpha_{\mathrm{V}\left(t_{i-1}^{\mathrm{K}}\right)}^{\mathrm{V}\left(t_i^{\mathrm{K}}\right)} = \alpha_{\mathrm{V}}^{\mathrm{EN}}\left(t_i^{\mathrm{K}}\right) - \alpha_{\mathrm{V}}^{\mathrm{EN}}\left(t_{i-1}^{\mathrm{K}}\right) + v_\alpha\left(t_i^{\mathrm{K}}\right) . \tag{15}$$

In these equations the variances of the observation noise $\boldsymbol{v}_{\dot{\boldsymbol{x}}}$ and v_α are empirically estimated on the basis of the velocity and rotation variability in the trajectory rectilinear stages. In these stages, in fact we expect the velocity is constant and the vehicle rotation is absent. In matrix notation, Eqs. 14 and 15 can be rewritten as:

$$\boldsymbol{y}^{\mathrm{K}}\left(t_i^{\mathrm{K}}\right) = \mathbf{H}_{\mathrm{K}} \boldsymbol{X}\left(t_i^{\mathrm{K}}\right) + \boldsymbol{v}_{\boldsymbol{y}^{\mathrm{K}}}\left(t_i^{\mathrm{K}}\right) \tag{16}$$

where the observation vector $\boldsymbol{y}^{\mathrm{K}}\left(t_i^{\mathrm{K}}\right)$ is given by:

$$\boldsymbol{y}^{\mathrm{K}}\left(t_i^{\mathrm{K}}\right) = \begin{bmatrix} \dot{\boldsymbol{x}}_A^{\mathrm{EN}}\left(t_i^{\mathrm{K}}\right) - \left[\mathbf{I} - \mathbf{R}\left(\alpha_{\mathrm{V}\left(t_{i-1}^{\mathrm{K}}\right)}^{\mathrm{V}\left(t_i^{\mathrm{K}}\right)}\right)\right] \boldsymbol{x}_{AO}^{\mathrm{V}} \\ \alpha_{\mathrm{V}\left(t_{i-1}^{\mathrm{K}}\right)}^{\mathrm{V}\left(t_i^{\mathrm{K}}\right)} + \alpha_{\mathrm{V}}^{\mathrm{EN}}\left(t_{i-1}^{\mathrm{K}}\right) \end{bmatrix} , \tag{17}$$

the observation error vector $\boldsymbol{v}_{\boldsymbol{y}^{\mathrm{K}}}\left(t_i^{\mathrm{K}}\right)$ is:

$$\boldsymbol{v}_{\boldsymbol{y}^{\mathrm{K}}}\left(t_i^{\mathrm{K}}\right) = \begin{bmatrix} \boldsymbol{v}_{\dot{\boldsymbol{x}}}\left(t_i^{\mathrm{K}}\right) \\ v_\alpha\left(t_i^{\mathrm{K}}\right) \end{bmatrix} \tag{18}$$

and the stationary transformation matrix $\mathbf{H}_{\mathrm{K}}$ is:

$$\mathbf{H}_{\mathrm{K}} = \begin{bmatrix} 0\,0\,1\,0\,0 \\ 0\,0\,0\,1\,0 \\ 0\,0\,0\,0\,1 \end{bmatrix} . \tag{19}$$

Note that the velocity and rotation observations in Eqs. 14 and 15 are correlated to one another, even if this correlation is neglected in the noise modelling.

Once the transition and transformation matrices are given for any acquisition time, along with the model and observation error covariance matrices, the Kalman filter can iteratively update the state vector providing the estimated trajectory and its error estimate (Kalman 1960).

A comment is due about the proposed Kalman filter. Displacements and attitude variations of the vehicle are directly observed by the Kinect device and therefore an additional and predefined dynamics, like the one introduced in Eqs. 1, 2, and 3, is not strictly required. This dynamics is useful when only GNSS observations are available or when the Kinect errors are larger than the expected variability of the vehicle position and attitude. It can be also used to reduce the effect of possible outliers in the Kinect observations.

5 Experimental Test

The kinematic test was realized by moving a cart at crawl velocity around Cascella's fountain (Milan, Italy). As shown in Fig. 3, the test cart was equipped with a Kinect v2 and a u-blox receiver both mounted on a pole in the point A. Moreover, a 360° reflective prism (P1) and three double-frequency Leica GPS1200 (G1, G2, G3) receivers were installed on the cart and used to validate the results. Note that the prism was mounted on the same pole of the u-blox and Kinect devices and was tracked by means of a Leica MS-60 Multistation (MS).

During the survey, the RGB and depth images of the Kinect v2 and the GNSS data of the u-blox receiver were acquired at about 750 ms and 1 s sampling rate, respectively. Since the instruments were controlled by the same PC, the observations could be correctly synchronized through its internal time.

Before the kinematic test execution, the system was calibrated in order to determine the vector between the cart barycenter O and the acquisition point A, as well as the attitude of the cart and the RGB Kinect camera with respect to the local East-North reference system. This calibration was based on a set of images acquired by both a Nikon D800 reflex camera and the Kinect camera. These images were processed together with 15 Ground Control Points (GCPs) acquired by the MS in a bundle-block adjustment. Note that to correctly georeference both the GCPs and the P1 trajectory, the MS station points were also surveyed by a double-frequency GNSS receiver.

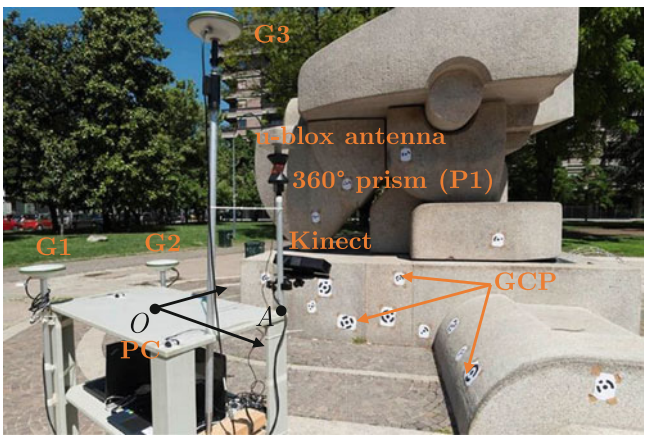

Fig. 3 Cart setup. The instruments mounted on-board are highlighted. The picture was taken during the calibration phase

The reference trajectory of the cart barycenter O and the reference attitude were retrieved by combining the trajectory observed by G1, G2, G3 and P1. This is possible since during the calibration phase also the relative position of this instruments with respect to the cart reference system was estimated. A remark is that these observations were synchronized with the low-cost devices by means of the GPS time.

6 Results

The developed Kalman filter is applied to estimate the trajectory of the point O by exploiting the spatial information acquired in A. Three tests are presented, they are based on different data combinations in the filtering process, i.e. GNSS-only, Kinect-only, and GNSS-Kinect combination. GNSS error standard deviation is different position by position, but it is always of the order of 25 cm (Eq. 9). Kinect error standard deviation is set for all the epochs to 4.1 cm/s for the velocity (Eq. 14) and to 1.4° for the attitude variation (Eq. 15).

For all the tests the same dynamics is used in the Kalman filter. Its error is divided into two groups, providing a different variance for the straight and curved sections of the trajectory. In particular the velocity error standard deviation (Eq. 2) is set to 4 cm/s and 8 cm/s, while the attitude error standard deviation (Eq. 3) to 1.0° and 10°, respectively. These values depend on the user expectation and are here calibrated on the basis of the reference trajectory.

The GNSS-only solution is not able to reconstruct the attitude variation of the cart during its motion, because a single antenna does not bear any information on it. Even with this lack of information, the Kalman filter predicts a cart attitude by minimizing the variations of the cart barycenter velocity and attitude. The results however are not satisfactory (see Fig. 5) and consequently the estimated trajectory mismatches the reference one (see Fig. 4). This happens because the reconstruction of the motion of O from the position of A requires the knowledge of the relative position between them in the East-North frame.

The Kinect-only solution is able to update the cart attitude during its motion (see Fig. 5), but the estimated trajectory is getting farther away from the reference one (see Fig. 4). This is due to a drift when cumulating the observed displacements of the point A, as well as the cart attitude variations. The Kalman filter can only limit strong variations between two consecutive epochs, but it cannot prevent the overall drift effect. This could be overcome by adding some GCPs during the path, e.g. extracted from existing cartography (Barzaghi et al. 2016), at the cost of making the procedure less automatic.

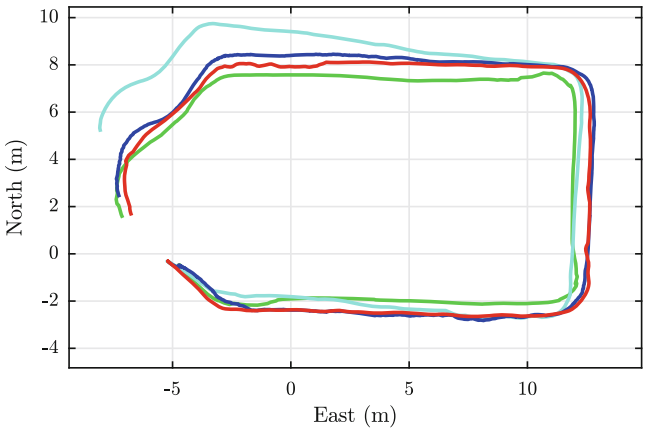

Fig. 4 Estimated and reference cart trajectory: GNSS-only solution (green), Kinect-only solution (cyan), GNSS-Kinect combination (blue), reference (red)

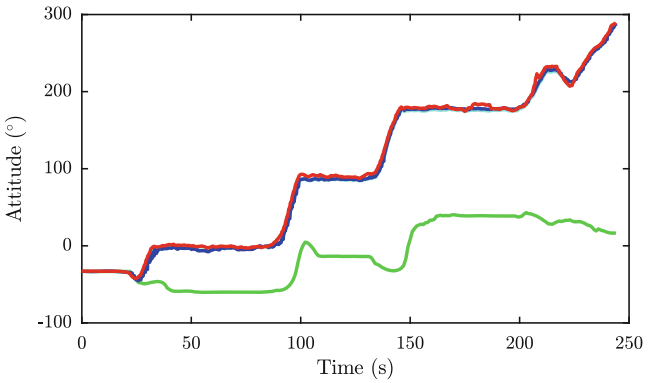

Fig. 5 Estimated and reference cart attitude: GNSS-only solution (green), Kinect-only solution (cyan), GNSS-Kinect combination (blue), reference (red)

The best results are obtained by the combined GNSS-Kinect solution. The two kinds of observation can be considered complementary to one another and definitely improve the capability of the filter to reconstruct the trajectory of O (see Fig. 4) and the cart attitude (see Fig. 5). Note that the drift in the cart attitude is not corrected by the GNSS integration, since there are no absolute observations of the cart attitude with respect to the East-North frame.

Statistics of the difference between the estimated trajectory and the reference one, in terms of Euclidean distance between points at the same epoch, are illustrated in the upper part of Table 1, while the difference in the estimated cart attitude are reported in the lower part of the same table.

Table 1 Statistics of the differences between the estimated trajectory and attitude with respect to the reference ones, see also Figs. 4 and 5

		GNSS only	Kin. only	GNSS + Kin.
Trajectory	mean (m)	0.61	1.02	0.45
	std (m)	0.14	0.79	0.13
	rms (m)	0.62	1.29	0.47
Attitude	mean (°)	98.5	4.1	3.5
	std (°)	52.9	2.7	2.8
	rms (°)	111.8	4.9	4.5

7 Conclusions

Two different kinds of observation, acquired with low-cost instruments such a u-blox GNSS receiver and a Kinect device, have been combined in order to estimate the trajectory of a moving cart in an urban environment through an extended Kalman filter. The GNSS data have been processed by the free and open source goGPS software to provide the cart positions, while the Kinect images have been considered in pairs to provide the cart displacements and attitude variations by photogrammetric techniques using automatically detected tie points. The trajectory estimated by the Kalman filter refers to a barycentric point of the cart, whose position is different with respect to the acquisition point of the two on board instruments. This makes crucial the joint knowledge of the cart position and attitude. In fact, the trajectory is not well determined when using GNSS-only observations, because of the lack of information about changes in the cart attitude. On the other hand, the use of Kinect-only observations without the support of ground control points leads to a less accurate estimated trajectory because of the drift in the reconstructed positions. Thanks to their complementarity, combining both the observations improves the quality of the estimated trajectory, resulting in an overall accuracy of 50 cm in position and 5° in attitude, even using low-cost devices.

References

Barzaghi R, Cazzaniga NE, Pagliari D, Pinto L (2016) Vision-based georeferencing of GPR in urban areas. Sensors 16(1):132

Chaplin B (1999) Motion estimation from stereo image sequences for a mobile mapping system. MSc Thesis, Department of Geomatics Engineering, University of Calgary

Da Silva JF, de Oliviera Carmago P, Gallis RBA (2003) Development of a low-cost mobile mapping system: a South American experience. Photogramm Rec 18(101):5–26

Endres F, Hess J, Engelhard N, Sturn J, Cremer D, Burgard W (2012) An Evaluation of RGB-D SLAM system. In: 2012 IEEE international conference on robotics and automation. River Centre, Saint Paul, MN

Fankhauser P, Bloesch M, Rodriguez D, Kaestner E, Hutter M, Siegwart R (2015) Kinect v2 for mobile robot navigation. In: International conference on evaluation and modeling. Advanced Robotics (ICAR), Istanbul, Turkey, pp 388–394

Georgy J, Noureldin A, Korenberg MJ, Bayoumi MM (2010) Low-cost three-dimensional navigation solution for RISS/GPS integration using mixture particle filter. IEEE Trans Veh Technol 59(2):599–615

Hassan T, Ellum C, El-Sheimy N (2006) Bridging land-based mobile mapping using photogrammetric adjustments. In: ISPRS Commission I symposium. From sensors to imagery. Marne-la-Vallèe, France

Herrera AM, Suhandri HF, Realini E, Reguzzoni M, de Lacy MC (2016) goGPS: open source MATLAB software. GPS Solutions 20(3):595–603

Hofmann-Wellenhof B, Legat K, Wieser M (2003) Navigation: principles of positioning and guidance. Springer, Vienna

Kalman RE (1960) A new approach to linear filtering and prediction problems. Trans ASME J Basic Eng 82:35–45

Lowe D (2004) Distinctive image feature from scale-invariant. Int J Comput Vis 60(2):91–110

Noureldin A, Karamat TB, Eberts MD, El-Shafie A (2009) Performance enhancement of MEMS-based INS/GPS integration for low-cost navigation applications. IEEE Trans Veh Technol 58(3):1077–1096

Nur K, Feng S, Ling C, Ochieng W (2013) Integration of GPS with a WiFi high accuracy ranging functionality. Geospat Inform Sci 16(3):155–168

Oliver A, Kong S, Wünsche B, MacDonald B (2012) Using the Kinect as a navigation sensor for mobile robotics. In: 27th conference on image and vision computing, Dunedin, New Zealand, pp 505–514

Omara HIMA, Sahari KSM (2015) Indoor mapping using kinect and ROS. In: 2015 international symposium on agents, multi-agent systems and robotics (ISAMSR), Putrajaya, Malaysia, pp 110–116

Pagliari D, Pinto L (2015) Calibration of Kinect for Xbox One and comparison between the two generations of Microsoft sensors. Sensors 15:27569–27589

Pagliari D, Menna F, Roncella R, Remondino F, Pinto L (2014) Kinect Fusion improvement using depth camera calibration. Int Arch Photogramm Remote Sens Spat Inf Sci XL-5:479–485

Pagliari D, Pinto L, Reguzzoni M, Rossi L (2016) Integration of kinect and low-cost GNSS for outdoor navigation. Int Arch Photogramm Remote Sens Spat Inf Sci XLI-B5:565–572

Realini E, Reguzzoni M (2013) goGPS: open source software for enhancing the accuracy of low-cost receivers by single-frequency relative kinematic positioning. Meas Sci Technol 24(11):115010

Suarez J, Murphy RR (2012) Using the Kinect for search and rescue robotics. In: 2012 IEEE international symposium on safety, security, and rescue robotics (SSRR), College Station, TX, pp 1–2

Tao CV, Chapman MA, Chaplin BA (2001) Automated Processing of Mobile Mapping Image Sequences. ISPRS J Photogramm Remote Sens 55:330–346

Tomaszewski D (2017) Concept of INS/GPS integration algorithm designed for MEMS based navigation platform. In: 10th international conference on environmental engineering. Vilnius Gediminas Technical University, Lithuania

Xiao J, Owens A, Torralba A (2013) SUN3D: a database of big spaces reconstructed using SfM and object labels. In: 2013 IEEE international conference on computer vision, Sydney, Australia, pp 1625–1632

Zhengyou Z (1994) Iterative point matching for registration of free-form curves and surfaces. Int J Comput Vis 13(12):119–152

Part VII

Geodesy and Seismology General Contributions

Crustal Deformation and Fault Models of the 2016 Kumamoto Earthquake Sequence: Foreshocks and Main Shock

Tomokazu Kobayashi, Hiroshi Yarai, Satoshi Kawamoto, Yu Morishita, Satoshi Fujiwara, and Yohei Hiyama

Abstract

We explored crustal deformation associated with the foreshocks and the main shock of the 2016 Kumamoto earthquake sequence. We conducted kinematic-Global Navigation Satellite System analysis for the foreshocks, and succeeded in separately retrieving the coseismic crustal deformation for the two M6-class events that occurred nearly contemporaneously (within 3 h). Our fault model shows that the first seismic event occurred in the northern part of the Takano-Shirahata segment of the Hinagu Fault, while the second occurred in the southern part of the segment. For the main shock, we mapped the widely distributed ground displacements in and around the Futagawa Fault zone by conducting an Interferometric Synthetic Aperture Radar analysis. The obtained displacement field shows clear displacement boundaries linearly along the Futagawa and the Hinagu faults, across which the sign of the displacement component turns to the opposite, suggesting that the two faults were intimately involved with the main shock. The previously known fault trace of the Futagawa Fault terminates at the western edge of the Aso Caldera, but the intense deformation implying fault ruptures clearly appears within the caldera. Our fault model suggests that the main rupture occurred on the Futagawa Fault in a right-lateral fashion with normal faulting. The rupture on the Futagawa Fault extends into the Aso Caldera, and the fault plane dips oppositely toward the southeast, suggesting that the rupture propagates eastward on a conjugate fault against the main fault. The rupture on the Hinagu Fault shows a right-lateral fault motion on a plane dipping west.

Keywords

Crustal deformation · Fault model · InSAR · Kinematic-GNSS · Kumamoto earthquake

1 Introduction

The 2016 Kumamoto earthquake sequence started with an event of a Japan Meteorological Agency (JMA) magnitude (M_j) of 6.5 at 12:25 (Coordinated Universal Time: UTC) on April 14, 2016, followed by an M_j 6.4 event ~2.5 h later at 14:06 (UTC). After the M6-class foreshocks, the main shock of M_j 7.3 occurred at 16:25 (UTC) on April 15, 2016. The foreshocks ruptured the Takano-Shirahata segment of the Hinagu Fault, which connects with the Futagawa Fault, while the main shock ruptured mainly the Futagawa Fault as well as other faults in a complex manner (Fig. 1). The detailed source properties provide fundamental information for better understanding of the 2016 Kumamoto earthquake sequence. However, a few points remain unclear: (1) The two M6 foreshocks occurred within a few hours of each other; hence, conventional geodetic data cannot retrieve the individual coseismic deformation separately because of the

T. Kobayashi (✉) · H. Yarai · S. Kawamoto · Y. Morishita · S. Fujiwara
Geospatial Information Authority of Japan, Tsukuba, Ibaraki, Japan
e-mail: kobayashi-t96dv@mlit.go.jp

Y. Hiyama
Ministry of Land, Infrastructure, Transport and Tourism, Chiyoda-ku, Tokyo, Japan

J. T. Freymueller, L. Sanchez (eds.), *International Symposium on Advancing Geodesy in a Changing World*, International Association of Geodesy Symposia 149, https://doi.org/10.1007/1345_2018_37

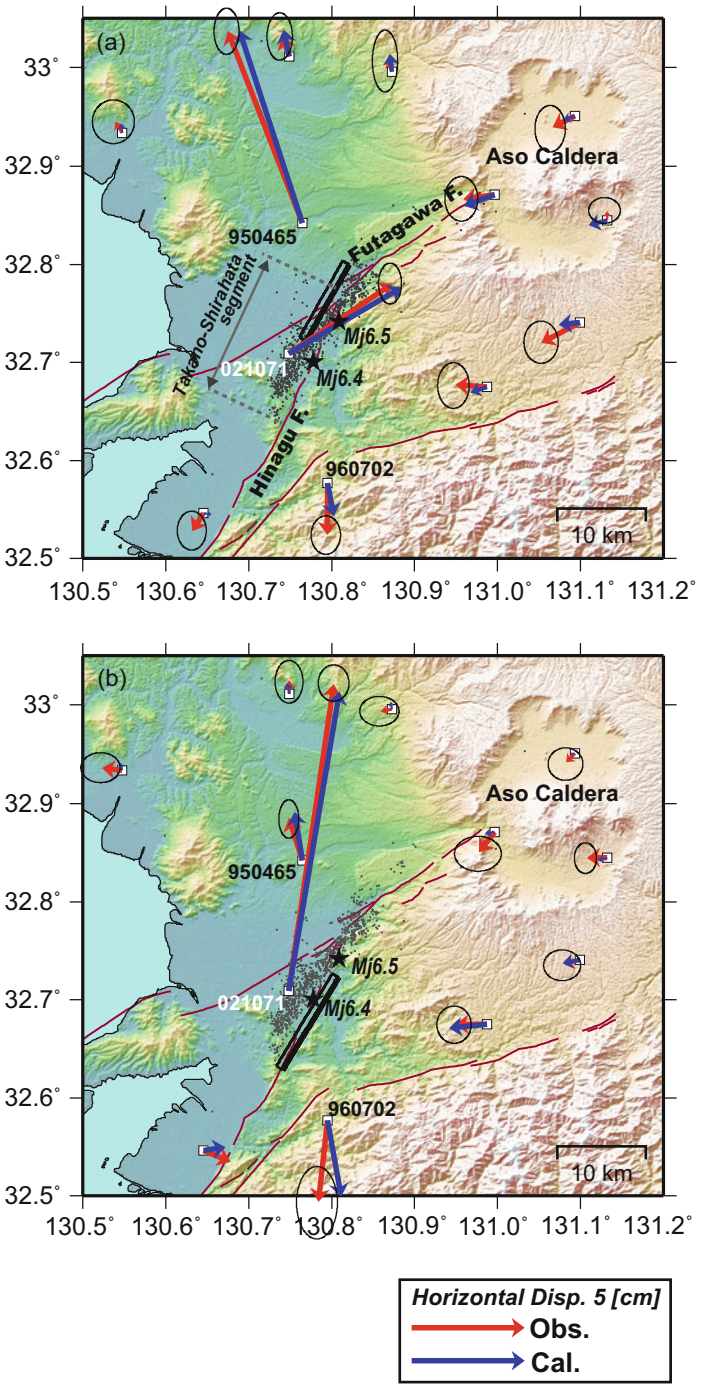

Fig. 1 Coseismic displacements due to (**a**) the M_j6.5 event and (**b**) the M_j6.4 event estimated from kinematic-GNSS positioning data, respectively. Arrows represent horizontal displacement. Red and blue represent the observed and the model-predicted displacement, respectively. Error ellipses show the standard deviation (1σ) for the observed displacements. Stars indicate epicenters of the Mj6.5 and Mj6.4 events. The frames indicate surface projections of the fault plane for modeling and the thick line represents the upper edges. Red lines indicating active faults are from the Headquarters for Earthquake Research Promotion (2013)

limited temporal resolution, which prevents construction of each fault model. (2) A number of fault models for the main shock have been proposed from seismological and/or geodetic analyses, but there are few that elaborately consider fault ruptures in the Aso Caldera. Crustal deformation data with high temporal and spatial resolution will be useful to clarify the unclear source properties of the foreshocks and the main shock, respectively.

This study consists of (1) fault modeling of the M_j6.5 and Mj6.4 foreshocks and (2) fault modeling of the main shock. For the analyses, we used kinematic-GNSS data to separately retrieve the coseismic displacement of the two individual foreshocks, and for the main shock we used Interferometric Synthetic Aperture Radar (InSAR) data to map the complicated ground displacement field.

2 Foreshocks: M_j6.5 and M_j6.4

2.1 Crustal Deformation Derived by Kinematic-GNSS

The Geospatial Information Authority of Japan (GSI) releases some types of Global Navigation Satellite System (GNSS) positioning data. Q3 data, which is the fastest-derived static positioning data, are calculated every 3 h with a 6-h data window (Nakagawa et al. 2009). However, the time interval between the M_j6.5 and M_j6.4 events is less than 3 h; hence, we cannot separate the coseismic displacement caused by the two events that occurred in temporal proximity. Thus, to overcome the issue of the temporal resolution, we used kinematic-GNSS data to retrieve the coseismic crustal deformation of the two individual foreshocks separately. We obtained post-processed kinematic positioning results using the International GNSS Service (IGS) final orbit and an elevation cutoff angle of 15°. The data are the same coseismic data presented in Kawamoto et al. (2016).

Figure 1a, b show coseismic horizontal displacement vectors for the M_j6.5 and the M_j6.4 events, respectively. Red is GNSS-observed displacement. The hypocenters are close to each other, but there is a clear difference in the spatial pattern of the crustal deformation. The displacement recorded at the GNSS site 021071 reaches 5.5 cm during the M_j6.5 event, while it increases to ∼13.5 cm during the M_j6.4 event. The orientation of the ground movement changes from NE-SW to NNE-SSW. We also recognize a difference at 950465 where the displacement reaches 9.0 cm for the M_j6.5 event, while for the M_j6.4 event it decreases to 1.9 cm. These differences strongly suggest that the main slip areas and/or slip mechanisms are different.

2.2 Fault Models

We next constructed a fault model assuming a single rectangular fault plane with a uniform slip (Okada 1985). We estimated the model parameters using a simulated annealing method (Metropolis et al. 1953; Cervelli et al. 2001). To estimate the individual confidence of the inferred parameters, we employed a bootstrap method (Efron 1979). For the analysis, the strike was assumed to run along the Hinagu Fault (search range: 200–220° in strike angle), but both the east- and west-dipping planes were searched.

The frames in Fig. 1a, b show the estimated fault positions for the M_j6.5 and the M_j6.4 events, respectively. Blue vectors represent the model-predicted displacements. The fault model can account for the observation data well. The estimated fault parameters are listed in Table 1. For the M_j6.5 event, the depth (fault center) is estimated to be approximately 2.5 km at fault top, while for the M_j6.4 event, the depth is estimated to be 0.2 km at fault top. The M_j6.4 event occurred shallower than M_j6.5 event. Also, there is a significant difference in the horizontal position. As seen in Fig. 1, the M_j6.5 event occurred in the northern part of the Takano-Shirahata segment of the Hinagu Fault, which is near the junction of the Futagawa Fault and the Hinagu Fault, while the M_j6.4 event is estimated to have occurred south of the M_j6.5 event.

Matsuda (1975) proposed an empirical relation between a magnitude M and a fault length L; Log $L = 0.6\ M-2.9$. According to the formulation, the foreshocks for the Kumamoto earthquake should have fault lengths less than 10 km. On the other hand, the fault lengths estimated in the modeling are ∼10 km for both the events. The inconsistency may suggest that the relation does not always meet nature of fault rupture, which could be a controversial issue in future work because the formulation has been often used in discussion regarding potential of inland earthquake.

Kobayashi (2017) showed the distributed slip model for the foreshocks using InSAR and GNSS (static solution) data, in which a deep north slip and a shallow south slip with almost pure right-lateral fault motion are estimated. The author suggested a possibility that the north and south slips correspond to the M_j6.5 and the M_j6.4 events, respectively, taking the spatial relation of the hypocenters into consideration. However, InSAR data includes contributions from both events, and cannot further separate the individual crustal deformation because of its temporal resolution. We here stress that the kinematic-GNSS data work well to derive the individual source properties for the two events that occurred within a few hours of each other. The kinematic-GNSS data will have an active part in fault modeling in the future.

Table 1 Fault parameters for M_j6.5 (upper) and M_j6.4 (lower) events inferred from kinematic-GNSS data

Event	Longitude	Latitude	Depth	Length	Width	Strike	Dip	Rake	Slip	M_w
12:25 Apr. 14	130.821 (0.011)	32.800 (0.013)	2.5 (0.8)	9.9 (2.5)	2.9 (1.6)	209.5 (4.6)	72.7 (10.2)	166.5 (21.3)	1.6 (0.3)	6.03
14:06 Apr. 14	130.809 (0.013)	32.723 (0.019)	0.2 (0.9)	12.2 (3.0)	3.6 (2.3)	211.3 (5.6)	76.0 (10.1)	157.9 (15.8)	0.9 (0.4)	5.98

The units of length, width, and depth are in kilometers; those of dip, strike, and rake are in degrees; and the unit of slip is meters. The position indicates the top-left corner of the fault plane. The parenthetical numbers are the standard deviation (1σ)

3 Main Shock

3.1 InSAR- and GNSS-Derived Complex Crustal Deformation

The Japan Aerospace Exploration Agency (JAXA) conducted emergency observations from the Advanced Land Observing Satellite 2 (ALOS-2) in response to the Kumamoto earthquake. We applied an InSAR method to the ALOS-2 data acquired on April 15, 2016 and on April 29, 2016 for which we can obtain InSAR images with two different view angles from ascending/left-looking and descending/left-looking orbit data. The master images were acquired before the main shock and after the two foreshocks; thus, the InSAR images do not include the crustal deformation due to the foreshocks. In addition to InSAR, we utilized GNSS data to identify the coseismic displacement. To obtain the coseismic displacement, we calculated a difference in the daily coordinate data corresponding to observation dates of the master and slave images. To achieve stable coordinate data for the master, we averaged Q3 data from 18:00 on April 14 to 14:59 on April 15 (UTC). On the other hand, for the slave, we took an average of F3 data, which are the finest solutions (Nakagawa et al. 2009), from April 25, 2016 to May 3, 2016 (10 days).

Figure 2a, b show the InSAR images for the ascending and descending orbit data, respectively. We can identify widely distributed crustal deformation in and around the Futagawa Fault zone. Intense fringes appear on the northern side of the Futagawa Fault. They are line-of-sight (LOS) lengthening phase changes for both orbit data, suggesting that the ground subsides significantly in this area. We can identify clear displacement discontinuities along the previously known fault traces of the Futagawa Fault. In addition to the Futagawa Fault, the discontinuity can be also identified on the Hinagu fault trace, suggesting that the Hinagu Fault is also involved in the fault rupture of the main shock. It is also noted that large displacements can be recognized within the Aso Caldera. The eastern edge of the previously known Futagawa Fault terminates at the western rim of the caldera; however, InSAR images obviously show that the fault rupture proceeds into the caldera.

Figure 3a, b show the GNSS-derived deformation data. Red vectors and bars represent observed horizontal and vertical displacements, respectively. The horizontal displacement pattern surrounding the Futagawa Fault is consistent with a right-lateral slip motion. However, at site 021071 northeastward movement was detected where southward movement should be observed if right-lateral slip occurred on the Futagawa Fault, suggesting that non-negligible fault slip also occurred on the Hinagu Fault. The spatial pattern in the Aso Caldera is complicated. Although the horizontal component shows uniform westward movement, for the vertical component, ground subsidence is dominant in the central part of the caldera, while ground uplift is observed at its western edge.

3.2 Fault Model

We next constructed a fault model for the main shock to obtain the source properties. We utilized derived InSAR data of both ascending and descending orbits as well as GNSS data. The interferograms have ground surface changes over a range of several tens of kilometers, producing too many values to be easily assimilated in a modeling scheme. In order to reduce the amount of data for the modelling analysis, we resampled the InSAR data beforehand, using a quadtree decomposition method. Essentially, we followed an algorithm of Jónsson et al. (2002). For a given quadrant, if, after removing the mean, the residual is greater than a prescribed threshold, the quadrant is further divided into four new quadrants. The threshold was set to 2 cm. This process is iterated until either each block meets the specified criterion, or until the quadrant reaches a minimum block size of 16 × 16 pixels, equivalent to ∼30 × ∼30 m.

For the weight of modeling, we assigned standard deviations of 1.5 and 1.1 cm for the ascending and descending InSAR data, respectively, calculated using phase changes outside of the source region. For GNSS data, we provided the standard deviations of the time series data during the averaged period; 0.4, 0.5, and 0.9 cm for the EW, NS, and UD components, respectively. We estimated the model parameters using a simulated annealing method in nearly the same manner as the analysis for the foreshocks.

Here we set the fault planes for the Futagawa and Hinagu faults, whose strike angles are fixed to be 235° and 205° so as to fit the displacement discontinuities, respectively. In addition to the two faults, we set one more fault which is in the eastward extension of the Futagawa Fault within the Aso Caldera. For the modeling, both the NW- and SE-dipping fault planes are searched (strike angle: from 225° to 245°/from 45° to 65°), and neither the dip nor the rake were constrained. The fault planes for the Futagawa Fault, its eastward extension fault, and the Hinagu Fault are hereafter termed F1, F2, and F3.

Figure 4 shows the InSAR results calculated from the derived fault model. The model can account for the broad spatial pattern although there still remain residuals in the proximity of the faults (Fig. 2). The GNSS data are also reproduced well by the constructed model (Fig. 3). The estimated parameters are listed in Table 2. The total seismic moment is 4.76×10^{19} Nm (M_w 7.05) assuming a rigidity of 30 GPa, and the released moments for each fault are

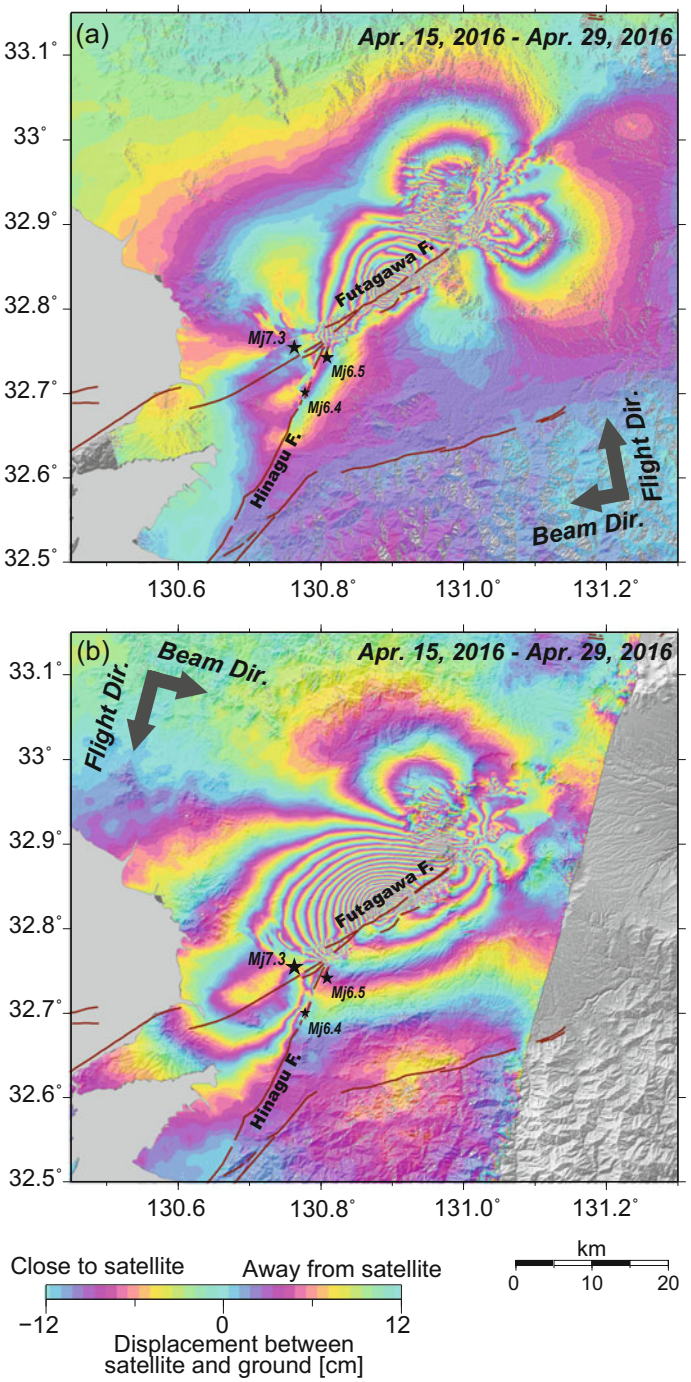

Fig. 2 Interferograms for (**a**) ascending/left-looking and (**b**) descending/left-looking orbit data, respectively. Stars indicate the epicenters of the main shock and the two foreshocks

estimated to be 2.84×10^{19} Nm (M_w 6.90), 3.37×10^{18} N m (M_w 6.28), and 1.58×10^{19} N m (M_w 6.73) for F1, F2, and F3, respectively. According to the results of the JMA CMT solution, the seismic moment is 4.06×10^{19} N m (M_w 7.0) (JMA 2016). Our result is in good agreement with this value.

For the F1 fault, right-lateral slip is predominant, but a normal fault motion is also included. The normal slip possibly produces the ground subsidence on the northern side of the Futagawa Fault. The dip angle is neither high nor low, but is moderate. Approximately 56% of the total seismic moment is released on this fault.

The F2 fault also has a right-lateral slip component. Of note, the fault was determined to be not NW-dipping but SE-dipping planes (Fig. 4). Unfortunately, the aftershock is in low level activity around the F2 as seen in Fig. 3, thus we

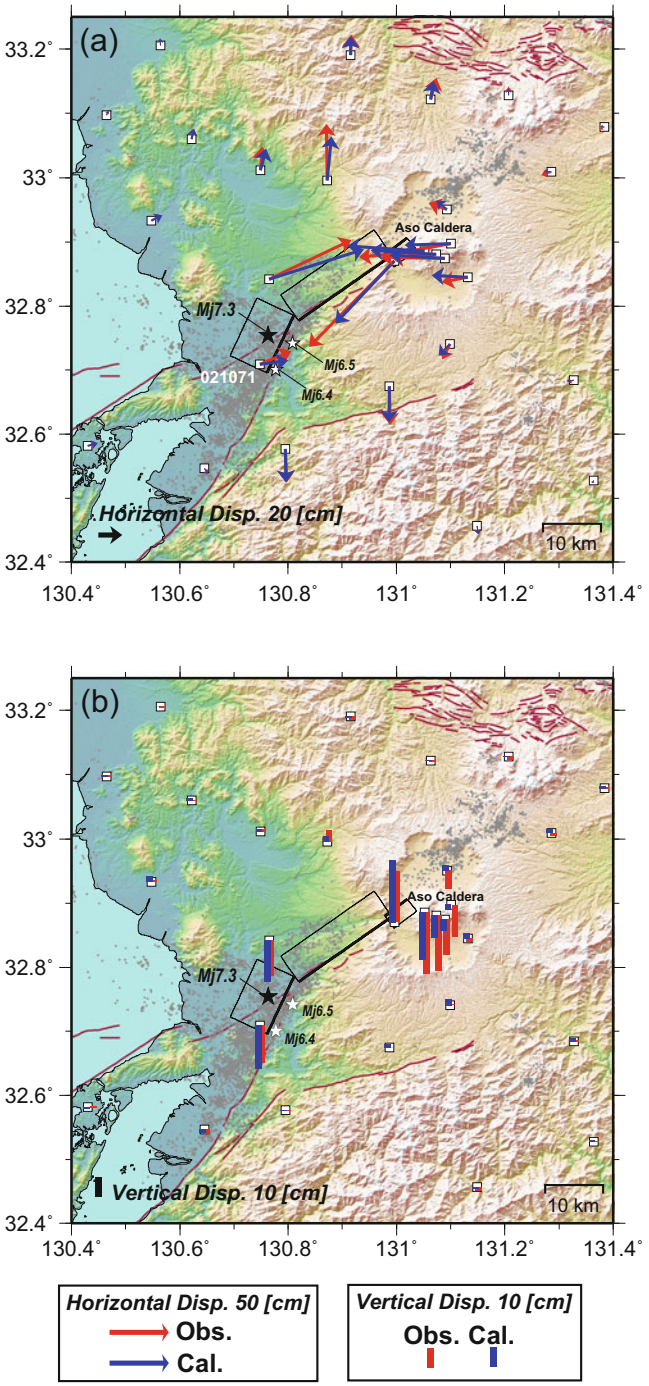

Fig. 3 Coseismic displacements of the main shock in (**a**) horizontal and (**b**) vertical components, respectively. Arrows and bars represent horizontal and vertical displacements, respectively. Red and blue represent the observed and the model-predicted displacement, respectively. Stars indicate epicenters of the main shock and the two foreshocks. Gray dots represent the epicenters of aftershocks

cannot confirm the fault dip from the hypocenter distribution. Hence, to confirm the reliability of the SE-dipping plane, we investigate root mean squares (RMSs) of residuals for various dip angles of F2. For the estimate, we assigned dip angles with an interval of 20°, and searched for the optimal parameters in the same manner. We here fixed the parameters of F1 and F3. For the NW-dipping model, the RMSs are estimated to be 15.7, 15.8, 17.0, and 16.4 cm for the dip angle of 20°, 40°, 60°, and 80° respectively. On the other hand, for the SE-dipping model, the RMSs are 15.6, 15.2, 15.1, and 15.5 cm for the dip angle of 20°, 40°, 60°, and 80°, respectively. We can find that the residuals systematically decrease with approaching to the moderate dip angle for the SE-dipping plane. The results suggest that the fault plane drastically changes to the opposite dip at the western margin of the Aso Caldera. The fault rupture probably proceeds on a conjugate fault against the main fault.

The F3 fault has a nearly pure right-lateral motion. If there were no slip on the Hinagu Fault, the GNSS site

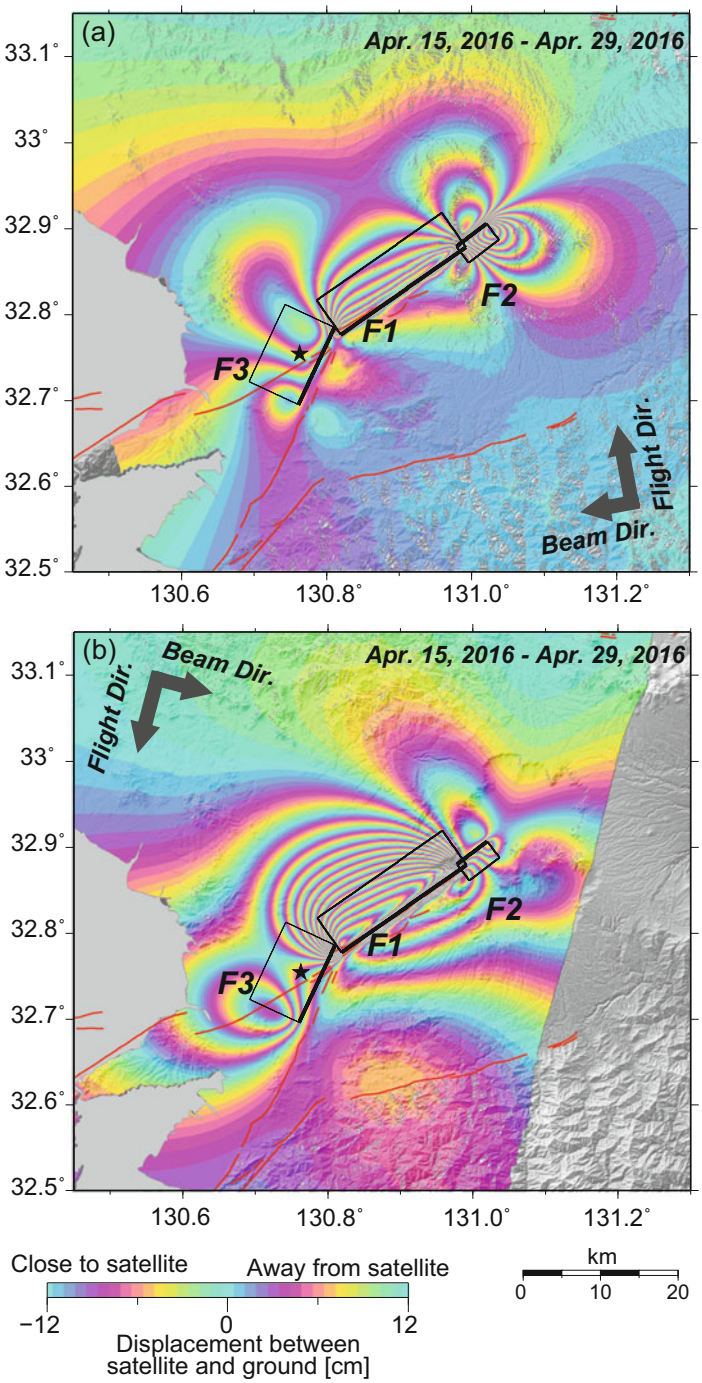

Fig. 4 Same as Fig. 2 but for the LOS displacements calculated by the fault model. The frames indicate surface projections of the fault plane for modeling and the thick line represents the upper edges

Table 2 Fault parameters for the main shock

Fault	Longitude	Latitude	Depth	Length	Width	Strike	Dip	Rake	Slip	M_w
F1	130.992 (0.011)	32.879 (0.002)	6.0 (0.2)	19.7 (0.8)	12.3 (0.5)	235	63.9 (4.2)	−151.0 (2.0)	3.9 (0.2)	6.90
F2	130.979 (0.013)	32.880 (0.009)	4.9 (0.9)	4.9 (1.6)	6.4 (4.8)	52.7 (4.0)	65.9 (18.2)	−169.9 (6.6)	3.6 (0.8)	6.28
F3	130.811 (0.010)	32.786 (0.010)	11.3 (0.8)	11.0 (1.0)	19.9 (5.3)	205	69.4 (8.8)	178.0 (7.5)	2.4 (0.1)	6.73

The units of length, width, and depth are in kilometers; those of dip, strike, and rake are in degrees; and the unit of slip is meters. The position indicates the top-left corner of the fault plane. The parenthetical numbers are the standard deviation (1σ)

021071 would move southward. This is why the slip of the Hinagu Fault is essential to account for the observed eastward motion.

Acknowledgements ALOS-2 data were provided by the Earthquake Working Group under a cooperative research contract with the Japan Aerospace Exploration Agency (JAXA). ALOS-2 data are owned by JAXA. Generic Mapping Tools (GMT) provided by Wessel and Smith (1998) were used to construct the figures. Hypocenter data processed by the Japan Meteorological Agency (JMA) were used. Part of the GNSS data was provided by the JMA. We thank the editor and two anonymous reviewers for their constructive comments.

References

Cervelli P, Murray MH, Segall P, Aoki Y, Kato T (2001) Estimating source parameters from deformation data, with an application to the March 1997 earthquake swarm off the Izu Peninsula, Japan. J Geophys Res 106:11217–11237

Efron B (1979) Bootstrap methods: another look at the jackknife. Ann Statis 7:1–26

Headquarters for Earthquake Research Promotion (2013) Evaluation of active faults to date. http://jishin.go.jp/main/chousa/katsudansou_pdf/93_futagawa_hinagu_2.pdf. Accessed 8 Oct 2017 (in Japanese)

Japan Meteorological Agency (2016) CMT catalog. http://www.data.jma.go.jp/svd/eqev/data/mech/cmt/fig/cmt20160416012505.html. Accessed 10 Oct 2017. (in Japanese)

Jónsson S, Zebker H, Segall P, Amelung F (2002) Fault slip distribution of the 1999 Mw 7.1 Hector mine, California, earthquake, estimated from satellite radar and GNSS measurements. Bull Seismol Soc Am 92:1377–1389

Kawamoto S, Hiyama Y, Ohta Y, Nishimura T (2016) First result from the GEONET real-time analysis system (REGARD): the case of the 2016 Kumamoto earthquakes. Earth Planets Space 68:190. https://doi.org/10.1186/s40623-016-0564-4

Kobayashi T (2017) Earthquake rupture properties of the 2016 Kumamotot earthquake foreshocks (Mj6.5 and Mj6.4) revealed by conventional and multiple-aperture InSAR. Earth Planets Space 69:7. https://doi.org/10.1186/s40623-016-0594-y

Matsuda T (1975) Magnitude and recurrence interval of earthquakes from a fault. J Seismol Soc Jpn, 2 28:269–283 (in Japanese with English abstract)

Metropolis N, Rosenbluth A, Rosenbluth M, Teller A, Teller E (1953) Equation of state calculations by fast computing machines. J Chem Phys 21:1087–1092

Nakagawa H, Toyofuku T, Kotani K, Miyahara B, Iwashita C, Kawamoto S, Hatanaka Y, Munekane H, Ishimoto M, Yutsudo T, Ishikura N, Sugawara Y (2009) Development and validation of GEONET new analysis strategy (Version 4). J Geogr Surv Inst 118:1–8 (in Japanese)

Okada Y (1985) Surface deformation due to shear and tensile faults in a halfspace. Bull Seismol Soc Am 75:1135–1154

Wessel P, Smith WH (1998) New, improved version of generic mapping tools released. Eos Trans AGU 79:579

Associate Editors

Allison Kealy	Carine Bruyninx	Detlef Angermann
Felipe Nievinski	Hussein A. Abd-Elmotaal	Janusz Bogusz
Johannes Boehm	Manabu Hashimoto	Matt A. King
Michael Schmidt	Pawel Wielgosz	Richard Gross
Roland Pail	Shuanggen Jin	Zuheir Altamimi

J. T. Freymueller, L. Sánchez (eds.), *International Symposium on Advancing Geodesy in a Changing World*,
International Association of Geodesy Symposia 149, https://doi.org/10.1007/978-3-030-12915-6

List of Reviewers

Andres Calabia
Arturo Villiger
Aurelien Hees
Benedikt Soja
Bernhard Heck
Bruno Meurers
Christoph Foerste
Claudio Abbondanza
Corné Kreemer
Daniel MacMillan
Dariusz Tomaszewski
Dirk Behrend
German Olivares-Pulido
Gino Tuccari
Guenther Retscher
Hana Krasna
Hanjiang Wen
Hao Zhou
Hartmut Wziontek
Henrik Vedel
Jamie McCallum
Jiuhou Lei
Jonas Ågren
Jose van den Ijssel
Karen Boniface
Kefei Zhang
Krzysztof Sośnica
Manabu Hashimoto
Maria Clara de Lacy
Martin Vermeer
Masato Furuya
Matthias Madzak
Mehdi Eshagh
Michael Moore
Mike Pearlman
Nicola Cenni
Oliver Francis
Paulo Sérgio de Oliveira
Pieter NAM Visser
Riccardo Barzaghi
Robert Heinkelmann
Roland Pail
Sanat K Biswas
Sean Bruinsma
Sergei Kopeikin
Severine Rosat
Srinivas Bettadpur
Tamara Gulyaeva
Thomas Gruber
Thomas Hobiger
Thomas Pany
Tomasz Hadas
Urs Marti
Vassilis Gikas
WenBin Shen
William Terry Petrachenko
Yan Ming Wang
Yoshiyuki Tanaka

J. T. Freymueller, L. Sánchez (eds.), *International Symposium on Advancing Geodesy in a Changing World*,
International Association of Geodesy Symposia 149, https://doi.org/10.1007/978-3-030-12915-6

Author Index

J. T. Freymueller, L. Sánchez (eds.), *International Symposium on Advancing Geodesy in a Changing World*,
International Association of Geodesy Symposia 149, https://doi.org/10.1007/978-3-030-12915-6